INTERNATIONAL DOCTORAL SCHOOL OF THE USC

Raquel
Martínez Pulleiro

PhD Thesis

Novel genetic and molecular approaches to Polycystic Kidney Disease: A way to diagnose inconclusive cases and find new possible treatments

Santiago de Compostela, 2025

Doctoral Programme in Molecular Medicine

ESCOLA DE DOUTORAMENTO
INTERNACIONAL DA USC

DOCTORAL THESIS

NOVEL GENETIC AND MOLECULAR APPROACHES TO POLYCYSTIC KIDNEY DISEASE: A WAY TO DIAGNOSE INCONCLUSIVE CASES AND FIND NEW POSSIBLE TREATMENTS

Author

Raquel Martínez Pulleiro

Supervisor/s: Catarina Allegue Toscano and Noa Carrera Cachaza

Tutor: Ángel María Carracedo Álvarez

PHD PROGRAMME IN MOLECULAR MEDICINE

SANTIAGO DE COMPOSTELA

ACKNOWLEDGEMENTS

Que difícil se me fai escribir isto, pero todas as persoas que vou a mencionar a continuación merecen que faga o esforzo, por estar dunha maneira ou outra ao meu carón durante estes anos de tese, dándome o seu apoio e consellos. Sodes marabillosos, tiven moita sorte por tervos atopado no meu camiño.

En primeiro lugar, quero expresar o meu agradecemento ás miñas directoras de tese Cata e Noa. Grazas por depositar en min a vosa confianza e polo voso apoio ao longo destes anos. Grazas tamén a Miguel por darme a oportunidade de traballar en ciencia, e por crer nas miñas capacidades.

Gracias a Ángel Carracedo, a todo o grupo de Medicina Xenómica e ao Servicio de Nefroloxía de Santiago por brindarme a vosa axuda e boa disposición cando o precisei.

Gracias a Susana Bravo por atenderme cada vez que asomaba pola túa porta, que non foron poucas. A Michael Köttgen e a todo o seu grupo, por facer que a miña estadía fose tan proveitosa, aprendín moito e levo un recordo magnífico deses meses en Friburgo.

Quero destacar o meu agradecemento ás persoas que me acompañaron no día a día. A María García por ser sempre tan positiva e alegre. A Eloísa, Pedro e Fernando por ser tan bos compañeiros. A María Pereira pola túa forza e determinación contaxiosa. A Marta e Adrián por ser referentes e mostrarme o camiño. A Ana e a Laura, admírovos moito. Sodes fortes, traballadoras, talentosas, divertidas e moi boas amigas. Entre todos os puntos positivos de ter feito a tese sodes o número 1.

Foi un gusto traballar con Elena e con Sara, gracias pola vosa axuda e motivación. Vin como o grupo foi medrando pouco a pouco e non podo estar máis orgullosa do equipo tan unido que se formou. A Alba, Lucía, Miguel e Marta gracias por acollerme nos meus períodos de cultivos.

Neste camiño de anos atopei grandes compañeiros científicos. Grazas a todo o laboratorio 13, sodes encantadores, en especial a Valentín e Pablo, sempre sabedes animarme con risas e excelentes consellos. Tamén a ao laboratorio 3, María Pardo, Nerea, Tamara e Adrián, encántame que exista a fusión de laboratorios que temos. Gracias a Alana, Adrián González, Raquel e Andrea, alégrome moito de tervos coñecido.

Coñecín xente incrible, pero tamén quero mencionar aos que estiveron sempre. Ás miñas amigas de toda a vida, Eva, Cris e Ana moitas gracias por estar e por conseguir desconectarme do mundo tese, que tanto me absorbeu.

Por último, agradecer ás persoas máis importantes da miña vida, meus pais. Gracias por educarme con tanto amor. A miña ética de traballo provén de vervos a vós. Agradezo ter un fogar ao que poder ir e descansar con vós, coa avoa e con Pipo e Xacobe.

Para min foron anos duros, non quero esquecelo, pero tamén foron anos de cambio, a mellor. A Raquel que comezou a tese non é a mesma a rematou. Estou moi orgullosa de min por todo o esforzo invertido, por todo a aprendido e por como conseguín saír adiante.

CONFLICT OF INTEREST STATEMENT

The doctoral candidate, Raquel Martínez Pulleiro DNI 45956118W, declares no conflict of interest related to her doctoral thesis.

FIGURES AUTHORSHIP STATEMENT

The doctoral candidate, Raquel Martínez Pulleiro, declares that all figures included in this document have been created by herself, are freely accessible, or have the necessary permissions (Figure 1**:** Licensed under License Number 5935570610988 by Elsevier /Figure 6: Licensed under License Number 5935581350212 by Springer Nature).

FUNDING

This work has been conducted with the support of several research projects, including two projects from the Health Research Fund (FIS) from the Carlos III Health Institute (ISCIII) (PI18/00378 and PI22/00227) co-financed by the European Union, two RICORS2040 projects from the Carlos III Health Institute (ISCIII) (RD21/0005/0020 and RD24/0004/0010) co-financed by the European Union, two projects funded by the Xunta de Galicia (IN607B2023/07 and ED431G 2019/02), and one project from the SENEFRO Foundation (SEN2021_2).

Additionally, the doctoral candidate received a one-year research initiation contract from the University of Santiago de Compostela, a three-year predoctoral support grant from the Xunta de Galicia (ED481A-2020/204), and is currently employed by the Public Foundation of the Galician Health Research Institute of Santiago de Compostela (FIDIS). In 2022, the doctoral candidate completed a three-month research stay at the Institute for Disease Modelling and Targeted Medicine (IMITATE) in Freiburg, Germany, supported by the predoctoral grant from the Xunta de Galicia.

RESUMO

A Poliquistose Renal Autosómica Dominante (ADPKD) é a enfermidade renal hereditaria máis común, cunha prevalencia estimada de 1: 400 a 1:1000. Esta doenza caracterízase polo desenvolvemento progresivo de quistes renais recheos de líquido ao longo da vida dos afectados, o que leva á perda de función renal e á necesidade de terapia renal substitutiva, como diálise ou transplante. Ademais, a ADPKD está asociada a diversas manifestacións extrarrenais, incluíndo hipertensión, aneurismas e quistes hepáticos. A maioría dos casos de ADPKD son causados por mutacións nos xenes *PKD1* (~80%) e *PKD2* (~15%), mentres que o resto dos casos están sen resolver xeneticamente ou son atribuíbles a mutacións noutros xenes que causan fenotipo quístico menos comúns. O fenotipo asociado a *PKD1* é máis severo que o de *PKD2*, cunha idade media de inicio de enfermidade renal terminal (ESRD, polas súas siglas en inglés) de 58 anos para *PKD1* e 79 anos para *PKD2*.

O diagnóstico clínico da ADPKD realízase rutineiramente mediante técnicas de imaxe, pero o diagnóstico xenético está gañando terreo debido ás súas vantaxes, como evitar probas máis caras e invasivas, resolver casos dubidosos, realizar diagnósticos pre-clínicos e posibilitar terapias preventivas, así como diagnóstico prenatal ou selección preimplantacional de embrións sans. Unha limitación do diagnóstico xenético é a detección de variantes de significado incerto (VUS, polas súas siglas en inglés), cuxo efecto sobre a funcionalidade da proteína non sempre se pode determinar. Para confirmar a sospeita, sería necesario realizar un estudo de segregación familiar amplo e exhaustivo, verificando que todos os individuos afectados posúen a variante e todos os individuos sans carecen dela. Outra opción sería realizar un estudo funcional a medida, deseñado especificamente tendo en conta as características do xene e da variante.

Existe un tratamento aprobado, tolvaptán, para tratar a ADPKD capaz de atrasar a progresión da enfermidade e preservar a función renal, pero a súa prescrición está indicada para pacientes que cumpren certas características. Actualmente, a enfermidade xestiónase con tratamentos destinados ao control dos síntomas.

O xene *PKD1* localízase no cromosoma 16 e codifica a proteína policistina 1 (PC1), mentres que *PKD2* localízase no cromosoma 4 e codifica a proteína policistina 2 (PC2). Sobre as policistinas e súa función segue habendo bastante descoñecemento; non sabemos exactamente cal é o seu papel nin por que a súa perda ou disfuncionalidade leva á formación de quistes. En ADPKD, todas as células renais teñen a mutación xerminal, pero non todas inician a formación de quistes. O modelo máis aceptado ata a data para explicar este feito é o do "limiar", que suxire que un quiste comeza a formarse cando a funcionalidade das policistinas cae por debaixo dun limiar mínimo, frecuentemente debido a unha segunda mutación somática no alelo san, coñecido como o modelo dos “dous golpes”. Outros procesos que reduzan a funcionalidade das policistinas tamén poden causar a formación de quistes. O modelo dos “tres golpes” propón que a aparición de quistes pode acelerarse por un terceiro evento, como un dano renal, e o efecto "bóla de neve" suxire que os quistes existentes exercen estrés nas células circundantes, iniciando a formación de novos quistes.

Múltiples vías de sinalización e metabólicas están alteradas en ADPKD. No que respecta ao metabolismo, o que se describe na literatura con máis frecuencia é que nas células quísticas ocorre un efecto Warburg, onde a glicólise é o principal proceso de produción de enerxía a pesar da presenza de osíxeno, mentres que a oxidación de ácidos

graxos e a fosforilación oxidativa están diminuídas. A glutaminólise aumenta como mecanismo compensatorio. A ADPKD tamén se asociou con dano mitocondrial, evidenciado por mitocondrias fragmentadas, alta produción de especies reactivas de osíxeno e potencial de membrana alterado en modelos animais e celulares. Existe unha relación directa entre as mitocondrias e as policistinas, xa que diferentes fragmentos C-terminais da PC1 foron localizados na mitocondria e relacionados co fenotipo quístico. A cilia, outra das localizacións das policistinas, ten un papel dos máis significativos en ADPKD. Descubriuse un mecanismo polo cal as policistinas inhiben un mecanismo cistoxénico dependente de cilia que controla a proliferación celular. Finalmente, mencionar que o balance entre autofaxia e apoptose pode ser beneficioso ou agravante para a cistoxénese, dependendo do estado fisiolóxico das células.

A pesar dos avances científicos na ADPKD nas últimas décadas, aínda existen desafíos significativos, como as limitacións diagnósticas e terapéuticas e o descoñecemento da patoxénese molecular da enfermidade.

Por unha banda, nesta tese, realizouse unha exploración xenética da ADPKD co obxectivo de mellorar o diagnóstico xenético, que ocasionalmente resulta inconcluso. O propósito principal foi diagnosticar xeneticamente casos inconclusos con variantes candidatas clasificadas como VUS. Comezamos estudando dúas familias da cohorte quística do laboratorio de xenética renal NefroCHUS, que comparten dúas variantes no xene *PKD1* (E3068Q e A1368V), ambas clasificadas como VUS. Estas variantes co-segregan coa enfermidade en ambas familias e hérdanse xuntas, suxerindo que están situadas no mesmo alelo, en posición *cis*. Tras descartar a presenza de duplicacións e inserción en *PKD1* e *PKD2* mediante a análise de MLPA (*Multiplex Ligation-dependent Probe Amplification* en inglés) e secuenciar outros xenes quísticos coñecidos, estas variantes foron as únicas candidatas para explicar a enfermidade. O estudo de segregación non puido descartar ningunha das variantes como causal, pero tampouco puido indicar cal delas podería ser a causal. Os casos de ambas familias foron inicialmente clasificados clinicamente como afectados por ADPKD. Propuxéronse varias hipóteses para explicar xeneticamente os casos: (1) Unha das variantes é causal, mentres que a outra simplemente se herda en conxunto. (2) As dúas variantes son causais por un efecto aditivo negativo que fai que a proteína sintetizada non supere o limiar de funcionalidade mínima. (3) Existe unha mutación causal aínda non detectada, que se herda en desequilibrio de ligamento coas dúas variantes.(4) A causante é unha mutación nun xene quístico diferente de *PKD1* ou *PKD2* non detectada ou non analizada, aínda que se considera o escenario menos probable dada a presentación clínica. Abordamos a situación comezando pola comprobación máis obvia. A variante E3068Q, situada no primeiro nucleótido do exón 26, foi estudada para avaliar o seu efecto no corte e empalme do RNAm, un proceso esencial para a correcta tradución da información xenética en proteínas. Utilizáronse distintos preditores de corte e empalme *in silico* (SpliceAI, SPIDEX, CADD e NNSplice) para avaliar a probabilidade de eventos de corte e empalme inducidos pola variante e mellorar a precisión do deseño experimental dun posterior ensaio de minixenes. Os resultados dos preditores suxerían que efectivamente podía haber un efecto sobre o corte e empalme.

Un ensaio de corte e empalme de minixenes é un experimento de validación funcional que pode reproducir o patrón de corte e empalme do ARNm *in vitro*. Chámase minixene porque se introduce nun vector parte da secuencia do xene en investigación, susceptible de ser afectada polo proceso de corte e empalme defectuoso. O fluxo de traballo completo ten tres pasos principais: (1) Construción do minixene: Obtención da

secuencia do minixene mediante PCR a partir do ADN xenómico dos pacientes, clonación no vector pCR 2.1-TOPO e amplificación en células competentes. A secuencia correctamente orientada foi cortada con enzimas de restricción e ligada no vector de expresión pcDNA5/FRT/TO. (2) Expresión do minixene: Transfección de células HEK 293 cos plásmidos de expresión e indución da expresión mediada polo promotor CMV con tetraciclina. (3) Recollida de ARN e análise do patrón de corte e empalme: Lise das células, extracción de ARN total, transcrición inversa a ADNc, amplificación da secuencia de ADNc por PCR e observación do patrón de bandas nun xel de agarosa. Tamén se secuenciaron as bandas obtidas no xel de agarosa. Observouse que se a variante E3068Q estaba presente no cDNA, o transcrito canónico estaba ausente, o que suxire que a variante inflúe no proceso de corte e empalme e, posteriormente, na proteína sintetizada. As ferramentas de interpretación de variantes Varsome e Franklin cambiaron o seu veredicto a "Patoxénico" ao engadir a información funcional *in vitro*.

Por outra banda, a nivel molecular, realizamos unha análise proteómica comparativa utilizando un modelo celular inmortalizado, a liña celular mIMCD3 (*Inner Medullary Collecting Duct*), que se emprega habitualmente no estudo de enfermidades renais e ADPKD. Estas células son monoclonais, o que reduce a variabilidade dentro do cultivo. Traballamos con células mIMCD3 WT e con células mIMCD3 *Pkd1* KO (*Knock-out*). Despois de sementalas, deixáronse medrar durante 10 días sen facer subcultivos. O medio completo foi cambiado nos días 3 e 6, e as células foron privadas de nutrientes no día 8. Recollemos o pellet celular o día 10 e levamos as mostras ao servizo de proteómica do Instituto de Investigación Sanitaria de Santiago de Compostela, onde se encargaron de todo o protocolo asociado á cromatografía líquida acoplada a espectrometría de masas en tándem (LC-MS/MS).

A análise comparativa SWATH (Adquisición Secuencial de Ventás de Todos os Espectros de Masa Teóricos) identificou un total de 334 proteínas diferencialmente reguladas entre as condicións *Pkd1* KO e WT tras aplicar filtros (p valor < 0.05 e cambio múltiple (fold-change en inglés) > 1.5). Entre estas, 165 proteínas estaban reguladas á alza na condición KO, 118 estaban regulada á baixa e 51 proteínas estaban presentes exclusivamente na condición KO. Utilizando a ferramenta STRING, fixemos unha análise de enriquecemento destas proteínas, que revelou un enriquecemento en termos relacionados co metabolismo mitocondrial e o ARN, así como o enriquecemento de localizacións como a mitocondria, o ribosoma e o núcleo. A análise suxire que a célula mutante experimenta un cambio global, con moitos procesos afectados e a mitocondria xogando un papel central.

A análise proteómica revelou unha gran cantidade de información, incluíndo unha listaxe extensa de proteínas desreguladas con múltiples funcións en diversos procesos. Debido á complexidade de analizar cada vía específica a partir do mapa global de proteínas, decidimos realizar unha análise manual de certas vías específicas. Isto permitiunos comparar os nosos achados cos xa publicados e aprender máis sobre o noso modelo.

Referente ao metabolismo enerxético, a análise proteómica detectou só dúas proteínas glicolíticas: unha regulada á alza (GAPDH, Gliceraldehido-3-fosfato deshidroxenasa) e outra á baixa (PGK1, fosfoglicerato quinasa 1), polo que non se pode determinar claramente como se altera a glicólise. A oxidación de ácidos graxos parece estar regulada á alza nas células *Pkd1* KO. Isto suxire un aumento na degradación de ácidos graxos para a produción de enerxía. Interpretar os eventos no ciclo dos ácidos

tricarboxílicos (TCA) é máis complexo debido a datos contraditorios. Algunhas enzimas están reguladas á alza, mentres que outras están reguladas á baixa, o que dificulta a comprensión completa do funcionamento deste ciclo. A fosforilación oxidativa parece máis sinxela de interpretar, xa que moitas proteínas, subunidades dos complexos da cadea de transporte electrónico, están reguladas á alza, indicando unha alta demanda de enerxía nas células. Isto suxire que, baixo as condicións aplicadas, as células mIMCD3 son capaces de usar lípidos como fonte de enerxía e de usar osíxeno para xerar enerxía, a pesar das alteracións noutras vías metabólicas.

En canto ao estrés parece estar aumentado, especialmente nas mitocondrias. As enzimas SODM (Superóxido dismutasa mitocondrial) e PRDX3 (Peroxirredoxina-3) están reguladas á alza, suxerindo unha resposta activa ao estrés oxidativo, mentres que SODC (Superóxido dismutasa citosólica) e PRDX5 (Peroxirredoxina-5) están reguladas á baixa. A glutatión S-transferase Mu 1 é a proteína máis regulada á baixa, implicada na desintoxicación. Tamén se atoparon proteínas relacionadas coa apoptose, con proteínas pro-apoptóticas reguladas á alza e anti-apoptóticas á baixa, aínda que non podemos inferir que está pasando coa apoptose xa que estas proteínas teñen múltiples funcións.

Estudamos experimentalmente o estado da mitocondria mediante ensaios de citometría de fluxo e microscopía utilizando as células mIMCD3. Tinguimos as células con Mitotracker Green, un tinte que marca mitocondrias, e con TMRM (Éster metílico de tetrametilrodamina perclorato), que marca mitocondrias activas, é dicir, é un marcador de potencial de membrana mitocondrial. Comprobamos que nas células *Pkd1* KO había unha maior masa mitocondrial e que presentaban unha tendencia a maior potencial de membrana mitocondrial. Tamén se tinguiron as mitocondrias con Mitotracker Green para examinar a súa morfoloxía e localización subcelular por microscopía confocal. Nas células mIMCD3 WT, a alta confluencia dificultou a observación detallada das mitocondrias. En contraste, nas células mIMCD *Pkd1* KO, observáronse células de diferente tamaño con mitocondrias con morfoloxía normal, fragmentadas e con diferentes intensidades de sinal. Ademais, a tinción con DAPI revelou células multinucleadas.

Por citometría de fluxo, observouse que as células mutantes teñen unha segunda poboación celular claramente identificable. As diferenzas entre WT e *Pkd1* KO céntranse principalmente no tamaño celular. Nun histograma que mide no eixo Y o número de células e no eixo X o tamaño de células (parámetro FCS), podemos observar que as células WT seguen unha curva de Gauss (poboación principal) cunha cola á dereita que consideraremos como a poboación secundaria de maior tamaño, mentres que as células mutantes mostran unha curva bimodal, cun pico maior que representa a poboación principal e un pico menor que representa a poboación secundaria de maior tamaño. A poboación principal comprende o 70% das células WT e o 57% das células mutantes, mentres que a poboación secundaria comprende o 30% das células WT e o 43% das células mutantes. Esta información coincide co observado por microscopía.

Ademais, determinamos as diferenzas no ciclo celular entre células WT e *Pkd1* KO, utilizando ioduro de propidio para medir o contido de ADN mediante citometría de fluxo. Isto permitiu identificar células nas fases G_1, S e G_2/M. Observouse unha diminución significativa das células na fase S na condición mutante, así como unha tendencia a unha diminución das células na fase G_1 e un aumento nas fases G_2/M. A acumulación de células en fase G_2/M podería deberse á actividade dos puntos de control do ciclo celular que detectan dano no ADN e bloquean o ciclo ou indicar un estado pre-proliferativo, aínda que as células confluentes non contan con espazo na placa para seguir

dividíndose. Ademais, observouse unha maior porcentaxe de células poliploides nas células *Pkd1* KO en comparación coas WT, o que apoia a presenza de inestabilidade xenética nas células mutantes e que podería estar relacionado coas células multinucleadas que vimos por microscopía.

Co obxectivo de atopar unha proteína ou vía na que centrar o noso estudo, comparamos o estudo proteómico celular con outro feito sobre mostras de ril de ratos C57/BL6J *Pkd1*$^{flox/flox}$; TamCre, inactivados a día 10-11 e sacrificados a día postnatal 18 e 30. Identificáronse 228 proteínas compartidas entre o SWATH das células e os SWATHs renais de ratos. Delas, 109 proteínas mostraron un comportamento oposto e 119 proteínas mostraron un comportamento consistente co observado no SWATH das células, das cales 101 estaban reguladas á alza e 18 reguladas á baixa. Das proteínas reguladas á baixa, 17 eran mitocondriais, 10 eran enzimas metabólicos, 3 eran proteínas estruturais, 2 estaban relacionadas coa xestión do estrés e 4 estaban asociadas coa mitofaxia. Consideramos que investigar a mitofaxia en ADPKD é unha liña de estudo prometedora que merece ser profundizada.

A mitofaxia é un proceso especializado encargado da eliminación de mitocondrias defectuosas ou innecesarias. Todas as proteínas pasan o filtro de significancia, sendo os cambios altamente significativos tanto en células como en ratos. Con todo, non se considerou un filtro de cambio múltiplo mínimo para a comparación célula-rato, e varias das proteínas non alcanzan un cambio múltiplo mínimo de 1.5. As proteínas reguladas á baixa relacionadas coa mitofaxia son as seguintes: (1) NIPS1(Proteína NipSnap homóloga1): Expresada principalmente no cerebro, ril e fígado. É unha proteína da matriz mitocondrial que se acumula na superficie das mitocondrias en resposta á despolarización mitocondrial, actuando como un sinal para recrutar proteínas implicadas na autofaxia selectiva. (2) FIS1(Proteína de fisión mitocondrial 1): Participa na fragmentación da rede mitocondrial e no seu agrupamento perinuclear. Tamén está implicada no desenvolvemento, estrés oxidativo e metabolismo. (3) PHB1 (Prohibitina-1): Forma complexos con PHB2 (Prohibitina-2) na membrana mitocondrial interna. Estes complexos marcan as mitocondrias para a degradación lisosomal e son esenciais para o mantemento da función mitocondrial. (4) MIC60 (Subunidade MIC60 do complexo MICOS): Forma parte do complexo MICOS, encargado de manter as cristas mitocondriais e a estrutura da membrana mitocondrial interna. Esta subunidade, en particular, bloquea a mitofaxia en resposta a altos niveis de estrés.

A validación de proteínas relacionadas coa mitofaxia (NISP1, PHB1 e FIS1), só se puido facer en mostras de rato por qPCR (PCR cuantitativa) e Western Blot. Validouse a regulación á baixa de PHB1 e FIS1, e outras proteínas como PINK e Parkin (unhas das proteínas máis e mellor coñecidas asociadas á mitofaxia) tamén se atoparon reguladas á baixa. A regulación á baixa do xene NISP1 foi validada por qPCR, pero para Western Blot usouse un xel 2D SDS-PAGE debido a que o anticorpo recoñecía proteínas doutros pesos distintos ao de referencia para NIPS1, 30KDa. Aínda que se podería tratar de bandas inespecíficas, consideramos que tamén se podería tratar de isoformas da proteína e do efecto de cambios postraducionais. Os resultados do xel 2D mostraron diferenzas entre as mostras WT e mutantes. Sería interesante investigar as modificacións diferenciais que sofre NISP1 e o seu papel na mitofaxia.

Hipotetizamos que a mitofaxia nas células e nos riles de ratos ADPKD podía estar bloqueada por altos niveis de estrés celular e quixemos comprobar este feito no modelo celular mIMCD3. Para medir o nivel de mitofaxia utilizamos mt-mKeima, unha proteína

fluorescente sensible ao pH. Esta proteína entra nas mitocondrias e, dependendo do pH, cambia a súa lonxitude de onda de excitación, permitindo distinguir entre mitocondrias intactas e degradadas. Nun ambiente neutro (pH 7), como a matriz mitocondrial, mt-mKeima é predominantemente excitado a 440 nm. Non obstante, cando as mitocondrias son degradadas nos lisosomas, o ambiente vólvese ácido (pH 4), e mt-mKeima é predominantemente excitado a 585 nm. Os resultados preliminares mostraron que a mitofaxia estaba aumentada en células *Pkd1* KO, pero que o nivel de activación era similar ao de células WT. Este campo de investigación necesita aínda máis profundización, porque hai varios factores que poden influír significativamente no resultado, o máis importante o nivel de estrés.

Os resultados en conxunto indican unha profunda desregulación metabólica en ADPKD, sobre todo a nivel mitocondrial, e ofrecen unha oportunidade para investigar máis e buscar alternativas terapéuticas que teñan como diana o estrés celular ou a mitofaxia. Ademais, os datos de proteómica teñen aínda potencial que explorar para atopar novas proteínas ou vías relevantes en ADPKD.

RESUMEN

La Poliquistosis Renal Autosómica Dominante (ADPKD) es la enfermedad renal hereditaria más común, con una prevalencia estimada de 1:400 a 1:1000. Esta enfermedad se caracteriza por el desarrollo progresivo de quistes renales llenos de líquido a lo largo de la vida de los afectados, lo que lleva a la pérdida de función renal y a la necesidad de terapia renal sustitutiva, como diálisis o trasplante. Además, la ADPKD está asociada a diversas manifestaciones extrarrenales, incluyendo hipertensión, aneurismas y quistes hepáticos. La mayoría de los casos de ADPKD son causados por mutaciones en los genes *PKD1* (80%) y *PKD2* (15%), mientras que el resto de los casos están sin resolver genéticamente o son atribuibles a mutaciones en otros genes que causan fenotipos quísticos menos comunes. El fenotipo asociado a *PKD1* es más severo que el de *PKD2*, con una edad media de inicio de enfermedad renal terminal (ESRD, por sus siglas en inglés) de 58 años para *PKD1* y 79 años para *PKD2*.

El diagnóstico clínico de la ADPKD se realiza rutinariamente mediante técnicas de imagen, pero el diagnóstico genético está ganando terreno debido a sus ventajas, como evitar pruebas más caras e invasivas, resolver casos dudosos, realizar diagnósticos preclínicos y posibilitar terapias preventivas, así como diagnóstico prenatal o selección preimplantacional de embriones sanos. Una limitación de este proceso es la detección de variantes de significado incierto (VUS, por sus siglas en inglés), cuyo efecto sobre la funcionalidad de la proteína no siempre se puede determinar. Para confirmar la sospecha, sería necesario realizar un estudio de segregación familiar amplio y exhaustivo, verificando que todos los individuos afectados poseen la variante y todos los individuos sanos carecen de ella. Otra opción sería realizar un estudio funcional a medida, diseñado específicamente teniendo en cuenta las características del gen y de la variante.

Existe un tratamiento aprobado, tolvaptán, para tratar la ADPKD que puede retrasar la progresión de la enfermedad y preservar la función renal, pero su prescripción está indicada para pacientes que cumplen ciertas características. Actualmente, la enfermedad se maneja con tratamientos destinados al control de los síntomas.

El gen *PKD1* se localiza en el cromosoma 16 y codifica la proteína policistina 1 (PC1), mientras que *PKD2* se localiza en el cromosoma 4 y codifica la proteína policistina 2 (PC2). Sobre las policistinas y su función sigue habiendo bastante desconocimiento; no sabemos exactamente cuál es su papel ni por qué su pérdida o disfuncionalidad lleva a la formación de quistes. En ADPKD, todas las células renales tienen la mutación germinal, pero no todas inician la formación de quistes. El modelo más aceptado hasta la fecha para explicar este hecho es el del "umbral", que sugiere que un quiste comienza a formarse cuando la funcionalidad de las policistinas cae por debajo de un umbral mínimo, frecuentemente debido a una segunda mutación somática en el alelo sano, conocido como el modelo de los “dos golpes”. Otros procesos que reduzcan la funcionalidad de las policistinas también pueden causar la formación de quistes. El modelo de los “tres golpes” propone que la aparición de quistes puede acelerarse por un tercer evento, como un daño renal, y el efecto "bola de nieve" sugiere que los quistes existentes ejercen estrés en las células circundantes, iniciando la formación de nuevos quistes.

Múltiples vías de señalización y metabólicas están alteradas en ADPKD. En lo que respecta al metabolismo, lo que se describe en la literatura con más frecuencia es que en las células quísticas ocurre un efecto Warburg, donde la glucólisis es el principal proceso de producción de energía a pesar de la presencia de oxígeno, mientras que la

oxidación de ácidos grasos y la fosforilación oxidativa están disminuidas. La glutaminólisis aumenta como mecanismo compensatorio. La ADPKD también se ha asociado con daño mitocondrial, evidenciado por mitocondrias fragmentadas, alta producción de especies reactivas de oxígeno y potencial de membrana alterado en modelos animales y celulares. Existe una relación directa entre las mitocondrias y las policistinas, ya que diferentes fragmentos C-terminales de la PC1 fueron localizados en la mitocondria y relacionados con el fenotipo quístico. La cilia, otra de las localizaciones de las policistinas, tiene un papel de los más significativos en ADPKD. Se ha descubierto un mecanismo por el cual las policistinas inhiben un mecanismo cistogénico dependiente de cilia que controla la proliferación celular. Finalmente, mencionar que el balance entre autofagia y apoptosis puede ser beneficioso o agravante para la cistogénesis, dependiendo del estado fisiológico de las células.

A pesar de los avances científicos en la ADPKD en las últimas décadas, aún existen desafíos significativos, como las limitaciones diagnósticas y terapéuticas y el desconocimiento de la patogénesis molecular de la enfermedad.

Por un lado, en esta tesis, se realizó una exploración genética de la ADPKD con el objetivo de mejorar el diagnóstico genético, que ocasionalmente resulta inconcluso. El propósito principal fue diagnosticar genéticamente casos inconclusos con variantes candidatas clasificadas como VUS. Comenzamos estudiando dos familias de la cohorte quística del laboratorio de genética renal NefroCHUS, que comparten dos variantes en el gen *PKD1* (E3068Q y A1368V), ambas clasificadas como VUS. Estas variantes co-segregan con la enfermedad en ambas familias y se heredan juntas, sugiriendo que están situadas en el mismo alelo, en posición *cis*. Tras descartar la presencia de duplicaciones e inserciones en *PKD1* y *PKD2* mediante el análisis de MLPA (Multiplex Ligation-dependent Probe Amplification en inglés) y secuenciar otros genes quísticos conocidos, estas variantes fueron las únicas candidatas para explicar la enfermedad. El estudio de segregación no pudo descartar ninguna de las variantes como causal, pero tampoco pudo indicar cuál de ellas podría ser la causal. Los casos de ambas familias fueron inicialmente clasificados clínicamente como afectados por ADPKD. Se propusieron varias hipótesis para explicar genéticamente los casos: (1) Una de las variantes es causal, mientras que la otra simplemente se hereda en conjunto. (2) Las dos variantes son causales por un efecto aditivo negativo que hace que la proteína sintetizada no supere el umbral de funcionalidad mínima. (3) Existe una mutación causal aún no detectada, que se hereda en desequilibrio de ligamiento con las dos variantes. (4) La causante es una mutación en un gen quístico diferente de *PKD1* o *PKD2* no detectada o no analizada, aunque se considera el escenario menos probable dada la presentación clínica. Abordamos la situación comenzando por la comprobación más obvia. La variante E3068Q, situada en el primer nucleótido del exón 26, fue estudiada para evaluar su efecto en el corte y empalme del RNAm, un proceso esencial para la correcta traducción de la información genética en proteínas. Se utilizaron distintos predictores de corte y empalme *in silico* (SpliceAI, SPIDEX, CADD y NNSplice) para evaluar la probabilidad de eventos de corte y empalme inducidos por la variante y mejorar la precisión del diseño experimental de un posterior ensayo de minigenes. Los resultados de los predictores sugerían que efectivamente podía haber un efecto sobre el corte y empalme.

Un ensayo de corte y empalme de minigenes es un experimento de validación funcional que puede reproducir el patrón de corte y empalme del ARNm *in vitro*. Se llama minigen porque se introduce en un vector parte de la secuencia del gen en investigación, susceptible de ser afectada por el proceso de corte y empalme defectuoso. El flujo de

trabajo completo tiene tres pasos principales: (1) Construcción del minigen: Obtención de la secuencia del minigen mediante PCR a partir del ADN genómico de los pacientes, clonación en el vector pCR 2.1-TOPO y amplificación en células competentes. La secuencia correctamente orientada fue cortada con enzimas de restricción y ligada en el vector de expresión pcDNA5/FRT/TO. (2) Expresión del minigen: Transfección de células HEK 293 con los plásmidos de expresión e inducción de la expresión mediada por el promotor CMV con tetraciclina. (3) Recogida de ARN y análisis del patrón de corte y empalme: Lisis de las células, extracción de ARN total, transcripción inversa a ADNc, amplificación de la secuencia de ADNc por PCR y observación del patrón de bandas en un gel de agarosa. También se secuenciaron las bandas obtenidas en el gel de agarosa. Se observó que si la variante E3068Q estaba presente en el ADNc, el transcrito canónico estaba ausente, lo que sugiere que la variante influye en el proceso de corte y empalme y, posteriormente, en la proteína sintetizada. Las herramientas de interpretación de variantes Varsome y Franklin cambiaron su veredicto a "Patogénico" al añadir la información funcional *in vitro*.

Por otra parte, a nivel molecular, realizamos un análisis proteómico comparativo utilizando un modelo celular inmortalizado, la línea celular mIMCD3 (*Inner Medullary Collecting Duct*), que se emplea habitualmente en el estudio de enfermedades renales y ADPKD. Estas células son monoclonales, lo que reduce la variabilidad dentro del cultivo. Trabajamos con células mIMCD3 WT y con células mIMCD3 *Pkd1* KO (*Knock-out*). Después de sembrarlas, se dejaron crecer durante 10 días sin hacer subcultivos. El medio completo fue cambiado en los días 3 y 6, y las células fueron privadas de nutrientes en el día 8. Recogimos el pellet celular el día 10 y llevamos las muestras al servicio de proteómica del Instituto de Investigación Sanitaria de Santiago de Compostela, donde se encargaron de todo el protocolo asociado a la cromatografía líquida acoplada a espectrometría de masas en tándem (LC-MS/MS).

El análisis comparativo SWATH (Adquisición Secuencial de Ventanas de Todos los Espectros de Masa Teóricos) identificó un total de 334 proteínas diferencialmente reguladas entre las condiciones *Pkd1* KO y WT tras aplicar filtros (p valor < 0.05 y cambio múltiple (*fold-change* en inglés) > 1.5). Entre estas, 165 proteínas estaban reguladas al alza en la condición KO, 118 estaban reguladas a la baja y 51 proteínas estaban presentes exclusivamente en la condición KO. Utilizando la herramienta STRING, hicimos un análisis de enriquecimiento de estas proteínas, que reveló un enriquecimiento en términos relacionados con el metabolismo mitocondrial y el ARN, así como el enriquecimiento de localizaciones como la mitocondria, el ribosoma y el núcleo. El análisis sugiere que la célula mutante experimenta un cambio global, con muchos procesos afectados y la mitocondria jugando un papel central.

El análisis proteómico reveló una gran cantidad de información, incluyendo una lista extensa de proteínas desreguladas con múltiples funciones en diversos procesos. Debido a la complejidad de analizar cada vía específica a partir del mapa global de proteínas, decidimos realizar un análisis manual de ciertas vías específicas. Esto nos permitirá comparar nuestros hallazgos con los ya publicados y aprender más sobre nuestro modelo.

Referente al metabolismo energético, el análisis proteómico detectó solo dos proteínas glucolíticas: una regulada al alza (GAPDH, Gliceraldehído-3-fosfato deshidrogenasa) y otra a la baja (PGK1, fosfoglicerato quinasa 1), por lo que no se puede determinar claramente cómo se altera la glucólisis. La oxidación de ácidos grasos parece

estar regulada al alza en las células *Pkd1* KO. Esto sugiere un aumento en la degradación de ácidos grasos para la producción de energía. Interpretar los eventos en el ciclo de los ácidos tricarboxílicos (TCA) es más complejo debido a datos contradictorios. Algunas enzimas están reguladas al alza, mientras que otras están reguladas a la baja, lo que dificulta la comprensión completa del funcionamiento de este ciclo. La fosforilación oxidativa parece más sencilla de interpretar, ya que muchas proteínas, subunidades de los complejos de la cadena de transporte electrónico, están reguladas al alza, indicando una alta demanda de energía en las células. Esto sugiere que, bajo las condiciones aplicadas, las células mIMCD3 son capaces de usar lípidos como fuente de energía y de usar oxígeno para generar energía, a pesar de las alteraciones en otras vías metabólicas.

En cuanto al estrés parece estar aumentado, especialmente en las mitocondrias. Las enzimas SODM (Superóxido dismutasa mitocondrial) y PRDX3 (Peroxirredoxina-3) están reguladas al alza, sugiriendo una respuesta activa al estrés oxidativo, mientras que SODC (Superóxido dismutasa citosólica) y PRDX5 (Peroxirredoxina-5) están reguladas a la baja. La glutatión S-transferasa Mu 1 es la proteína más regulada a la baja, implicada en la desintoxicación. También se encontraron proteínas relacionadas con la apoptosis, con proteínas pro-apoptóticas reguladas al alza y anti-apoptóticas a la baja, aunque no podemos inferir qué está pasando con la apoptosis ya que estas proteínas tienen múltiples funciones.

Estudiamos experimentalmente el estado de la mitocondria mediante ensayos de citometría de flujo y microscopía utilizando las células mIMCD3. Teñimos las células con Mitotracker Green, un tinte que marca mitocondrias, y con TMRM (Éster metílico de tetrametilrodamina perclorato), que marca mitocondrias activas, es decir, es un marcador de potencial de membrana mitocondrial. Comprobamos que en las células *Pkd1* KO había una mayor masa mitocondrial y que presentaban una tendencia a un mayor potencial de membrana mitocondrial. También se tiñeron las mitocondrias con Mitotracker Green para examinar su morfología y localización subcelular por microscopía confocal. En las células mIMCD3 WT, la alta confluencia dificultó la observación detallada de las mitocondrias. En contraste, en las células mIMCD3 *Pkd1* KO, se observaron células de diferente tamaño con mitocondrias con morfología normal, fragmentadas y con diferentes intensidades de señal. Además, la tinción con DAPI reveló células multinucleadas.

Por citometría de flujo, se observó que las células mutantes tienen una segunda población celular claramente identificable. Las diferencias entre WT y *Pkd1* KO se centran principalmente en el tamaño celular. En un histograma que mide en el eje Y el número de células y en el eje X el tamaño de células (parámetro FCS), podemos observar que las células WT siguen una curva de Gauss (población principal) con una cola a la derecha que consideraremos como la población secundaria de mayor tamaño, mientras que las células mutantes muestran una curva bimodal, con un pico mayor que representa la población principal y un pico menor que representa la población secundaria de mayor tamaño. La población principal comprende el 70% de las células WT y el 57% de las células mutantes, mientras que la población secundaria comprende el 30% de las células WT y el 43% de las células mutantes. Esta información coincide con lo observado por microscopía.

Además, determinamos las diferencias en el ciclo celular entre células WT y *Pkd1* KO, utilizando yoduro de propidio para medir el contenido de ADN mediante citometría de flujo. Esto permitió identificar células en las fases G_1, S y G_2/M. Se observó una disminución significativa de las células en la fase S en la condición mutante, así como

una tendencia a una disminución de las células en la fase G_1 y un aumento en las fases G_2/M. La acumulación de células en fase G_2/M podría deberse a la actividad de los puntos de control del ciclo celular que detectan daño en el ADN y bloquean el ciclo o indicar un estado pre-proliferativo, aunque las células confluyentes no cuentan con espacio en la placa para seguir dividiéndose. Además, se observó un mayor porcentaje de células poliploides en las células *Pkd1* KO en comparación con las WT, lo que apoya la presencia de inestabilidad genética en las células mutantes y que podría estar relacionado con las células multinucleadas que vimos por microscopía.

Con el objetivo de encontrar una proteína o vía en la que centrar nuestro estudio, comparamos el estudio proteómico celular con otro hecho sobre muestras de riñón de ratones C57/BL6J *Pkd1*$^{flox/flox}$; TamCre, inactivados a día 10-11 y sacrificados a día postnatal 18 y 30. Se identificaron 228 proteínas compartidas entre el SWATH de las células y los SWATHs renales de ratones. De ellas, 109 proteínas mostraron un comportamiento opuesto y 119 proteínas mostraron un comportamiento consistente con lo observado en el SWATH de las células, de las cuales 101 estaban reguladas al alza y 18 reguladas a la baja. De las proteínas reguladas a la baja, 17 eran mitocondriales, 10 eran enzimas metabólicas, 3 eran proteínas estructurales, 2 estaban relacionadas con la gestión del estrés y 4 estaban asociadas con la mitofagia. Consideramos que investigar la mitofagia en ADPKD es una línea de estudio prometedora que merece ser profundizada.

La mitofagia es un proceso especializado encargado de la eliminación de mitocondrias defectuosas o innecesarias. Todas las proteínas pasan el filtro de significancia, siendo los cambios altamente significativos tanto en células como en ratones. Sin embargo, no se consideró un filtro de cambio múltiple mínimo para la comparación célula-ratón, y varias de las proteínas no alcanzan un cambio múltiple mínimo de 1.5. Las proteínas reguladas a la baja relacionadas con la mitofagia son las siguientes: (1) NIPS1 (Proteína NipSnap homóloga 1): Expresada principalmente en el cerebro, riñón e hígado. Es una proteína de la matriz mitocondrial que se acumula en la superficie de las mitocondrias en respuesta a la despolarización mitocondrial, actuando como una señal para reclutar proteínas implicadas en la autofagia selectiva. (2) FIS1 (Proteína de fisión mitocondrial 1): Participa en la fragmentación de la red mitocondrial y en su agrupamiento perinuclear. También está implicada en el desarrollo, estrés oxidativo y metabolismo. (3) PHB1 (Prohibitina-1): Forma complejos con PHB2 (Prohibitina-2) en la membrana mitocondrial interna. Estos complejos marcan las mitocondrias para la degradación lisosomal y son esenciales para el mantenimiento de la función mitocondrial. (4) MIC60 (Subunidad MIC60 del complejo MICOS): Forma parte del complejo MICOS, encargado de mantener las crestas mitocondriales y la estructura de la membrana mitocondrial interna. Esta subunidad, en particular, bloquea la mitofagia en respuesta a altos niveles de estrés.

La validación de proteínas relacionadas con la mitofagia (NISP1, PHB1 y FIS1), solo se pudo hacer en muestras de ratón por qPCR (PCR cuantitativa) y Western Blot. Se validó la regulación a la baja de PHB1 y FIS1, y otras proteínas como PINK y Parkin (unas de las proteínas más y mejor conocidas asociadas a la mitofagia) también se encontraron reguladas a la baja. La regulación a la baja del gen NISP1 fue validada por qPCR, pero para Western Blot se usó un gel 2D SDS-PAGE debido a que el anticuerpo reconocía proteínas de otros pesos distintos al de referencia para NIPS1, 30KDa. Aunque se podría tratar de bandas inespecíficas, consideramos que también se podría tratar de isoformas de la proteína y del efecto de cambios postraduccionales. Los resultados del

gel 2D mostraron diferencias entre las muestras WT y mutantes. Sería interesante investigar las modificaciones diferenciales que sufre NISP1 y su papel en la mitofagia.

Hipotetizamos que la mitofagia en las células y en los riñones de ratones ADPKD podía estar bloqueada por altos niveles de estrés celular y quisimos comprobar este hecho en el modelo celular mIMCD3. Para medir el nivel de mitofagia utilizamos mt-mKeima, una proteína fluorescente sensible al pH. Esta proteína entra en las mitocondrias y, dependiendo del pH, cambia su excitación, permitiendo distinguir entre mitocondrias intactas y degradadas. En un ambiente neutro (pH 7), como la matriz mitocondrial, mt-mKeima es predominantemente excitado a 440 nm. Sin embargo, cuando las mitocondrias son degradadas en los lisosomas, el ambiente se vuelve ácido (pH 4), y mt-mKeima es predominantemente excitado a 585 nm. Los resultados preliminares mostraron que la mitofagia estaba aumentada en células *Pkd1* KO, pero que el nivel de activación era similar al de células WT. Este campo de investigación necesita aún más profundización, porque hay varios factores que pueden influir significativamente en el resultado, el más importante el nivel de estrés.

Los resultados en conjunto indican una profunda desregulación metabólica en ADPKD, sobre todo a nivel mitocondrial, y ofrecen una oportunidad para investigar más y buscar alternativas terapéuticas que tengan como diana el estrés celular o la mitofagia. Además, los datos de proteómica tienen aún potencial que explorar para encontrar nuevas proteínas o vías relevantes en ADPKD.

ABSTRACT

Autosomal Dominant Polycystic Kidney Disease (ADPKD) is the most common hereditary kidney disease, with an estimated prevalence of 1:400 to 1:1000. This condition is characterized by the progressive development of fluid-filled kidney cysts throughout the affected individuals' lives, leading to loss of kidney function and the need for renal replacement therapy, such as dialysis or transplantation. Additionally, ADPKD is associated with various extrarenal manifestations, including hypertension, aneurysms, and liver cysts. Most cases of ADPKD are caused by mutations in the *PKD1* (80%) and *PKD2* (15%) genes, while the remaining cases are genetically unresolved or attributable to mutations in other less common genes causing cystic phenotypes. The phenotype associated with *PKD1* is more severe than that of *PKD2*, with a median age of onset of end-stage renal disease (ESRD) of 58 years for *PKD1* and 79 years for *PKD2*.

The clinical diagnosis of ADPKD is routinely performed using imaging techniques, but genetic diagnosis is gaining ground due to its advantages, such as avoiding more expensive and invasive tests, resolving doubtful cases, performing pre-clinical diagnoses, and enabling preventive therapies, as well as prenatal diagnosis or preimplantation selection of healthy embryos. A limitation of this process is the detection of variants of uncertain significance (VUS), whose effect on protein functionality cannot always be determined. To confirm the suspicion, it would be necessary to conduct a broad and exhaustive family segregation study, verifying that all affected individuals possess the variant and all healthy individuals lack it. Another option would be to perform a tailored functional study, specifically designed considering the characteristics of the gene and the variant.

There is an approved treatment, tolvaptan, for treating ADPKD that can delay the progression of the disease and preserve kidney function, but its prescription is indicated for patients who meet certain characteristics. The disease is currently managed with treatments aimed at symptom control.

The *PKD1* gene is located on chromosome 16 and encodes the protein polycystin 1 (PC1), while *PKD2* is located on chromosome 4 and encodes the protein polycystin 2 (PC2). There is still considerable unknown about polycystins and their function; we do not know exactly what their role is or why their loss or dysfunction leads to cyst formation. In ADPKD, all kidney cells have the germline mutation, but not all initiate cyst formation. The most accepted model to date to explain this fact is the "threshold" model, which suggests that a cyst begins to form when polycystin functionality falls below a minimum threshold, often due to a second somatic mutation in the healthy allele, known as the "two-hit" model. Other processes that reduce polycystin functionality can also cause cyst formation. The "three-hit" model proposes that cyst formation can be accelerated by a third event, such as kidney damage, and the "snowball" effect suggests that existing cysts exert stress on surrounding cells, initiating the formation of new cysts.

Multiple signaling and metabolic pathways are altered in ADPKD**.** Regarding metabolism, the most frequently described in the literature is that in cystic cells, a Warburg effect occurs, where glycolysis is the main energy production process despite the presence of oxygen, while fatty acid oxidation and oxidative phosphorylation are diminished. Glutaminolysis increases as a compensatory mechanism. ADPKD has also been associated with mitochondrial damage, evidenced by fragmented mitochondria, high production of reactive oxygen species, and altered membrane potential in animal and cell

models. There is a direct relationship between mitochondria and polycystins, as different C-terminal fragments of PC1 have been located in the mitochondria and related to the cystic phenotype. Cilia, another location of polycystins, play a significant role in ADPKD. A mechanism has been identified by which polycystins inhibit a cilia-dependent cystogenic mechanism that controls cell proliferation. Finally, the balance between autophagy and apoptosis can be beneficial or aggravating for cystogenesis, depending on the physiological state of the cells.

Despite scientific advances in ADPKD in recent decades, significant challenges remain, such as diagnostic and therapeutic limitations and the lack of understanding of the molecular pathogenesis of the disease.

In this thesis, a genetic exploration of ADPKD was conducted with the aim of improving genetic diagnosis, which occasionally remains inconclusive. The main purpose was to genetically diagnose inconclusive cases with candidate variants classified as VUS. We began by studying two families from the cystic cohort of the NefroCHUS renal genetics laboratory, which share two variants in the *PKD1* gene (E3068Q and A1368V), both classified as VUS. These variants co-segregate with the disease in both families and are inherited together, suggesting they are located on the same allele, in *cis* position. After ruling out the presence of duplications and insertions in *PKD1* and *PKD2* through MLPA (Multiplex Ligation-dependent Probe Amplification) analysis and sequencing other known cystic genes, these variants were the only candidates to explain the disease. The segregation study could not rule out either variant as causal, but neither could it indicate which one might be causal. The cases in both families were initially clinically classified as affected by ADPKD. Several hypotheses were proposed to genetically explain the cases: (1) One of the variants is causal, while the other is simply inherited together. (2) Both variants are causal due to a negative additive effect that causes the synthesized protein to not exceed the minimum functionality threshold. (3) There is an undetected causal mutation, inherited in linkage disequilibrium with the two variants. (4) The cause is a mutation in a cystic gene other than *PKD1* or *PKD2*, undetected or unanalyzed, although this is considered the least likely scenario given the clinical presentation. We addressed the situation by starting with the most obvious check. The E3068Q variant, located at the first nucleotide of exon 26, was studied to evaluate its effect on mRNA splicing, an essential process for the correct translation of genetic information into proteins. Various *in silico* splicing predictors (SpliceAI, SPIDEX, CADD, and NNSplice) were used to assess the likelihood of splicing events induced by the variant and improve the experimental design accuracy of a subsequent minigene assay. The prediction results suggested that there could indeed be an effect on splicing.

A minigene splicing assay is a functional validation experiment that can reproduce the mRNA splicing pattern *in vitro*. It is called a minigene because part of the gene sequence under investigation, susceptible to defective splicing, is introduced into a vector. The complete workflow has three main steps: (1) Minigene construction: Obtaining the minigene sequence by PCR from the patients' genomic DNA, cloning into the pCR 2.1-TOPO vector, and amplification in competent cells. The correctly oriented sequence was cut with restriction enzymes and ligated into the pcDNA5/FRT/TO expression vector. (2) Minigene expression: Transfection of HEK 293 cells with the expression plasmids and induction of expression mediated by the CMV promoter with tetracycline. (3) RNA collection and splicing pattern analysis: Cell lysis, total RNA extraction, reverse transcription to cDNA, amplification of the cDNA sequence by PCR, and observation of the band pattern on an agarose gel. The bands obtained on the agarose gel were also

sequenced. It was observed that if the E3068Q variant was present in the cDNA, the canonical transcript was absent, suggesting that the variant influences the splicing process and subsequently the synthesized protein. The variant interpretation tools Varsome and Franklin changed their verdict to "Pathogenic" when adding the *in vitro* functional information

On the other hand, at the molecular level, we performed a comparative proteomic analysis using an immortalized cell model, the mIMCD3 (Inner Medullary Collecting Duct) cell line, which is commonly used in the study of kidney diseases and ADPKD. These cells are monoclonal, reducing variability within the culture. We worked with mIMCD3 WT cells and mIMCD3 *Pkd1* KO cells. After seeding, they were allowed to grow for 10 days without subculturing. The complete medium was changed on days 3 and 6, and the cells were deprived of nutrients on day 8. We collected the cell pellet on day 10 and took the samples to the proteomics service of the Health Research Institute of Santiago de Compostela, where they handled the entire protocol associated with liquid chromatography coupled to tandem mass spectrometry (LC-MS/MS).

The comparative SWATH analysis (Sequential Window Acquisition of All Theoretical Mass Spectra) identified a total of 334 differentially regulated proteins between the *Pkd1* KO and WT conditions after applying filters (p-value < 0.05 and fold-change > 1.5). Among these, 165 proteins were upregulated in the KO condition, 118 were downregulated, and 51 proteins were exclusively present in the KO condition. Using the STRING tool, we performed an enrichment analysis of these proteins, which revealed enrichment in terms related to mitochondrial metabolism and RNA, as well as enrichment of locations such as the mitochondria, ribosome, and nucleus. The analysis suggests that the mutant cell undergoes a global change, with many processes affected and the mitochondria playing a central role.

The proteomic analysis revealed a large amount of information, including an extensive list of dysregulated proteins with multiple functions in various processes. Due to the complexity of analyzing each specific pathway from the global protein map, we decided to manually analyze certain specific pathways. This will allow us to compare our findings with those already published and learn more about our model.

Regarding energy metabolism, the proteomic analysis detected only two glycolytic proteins: one upregulated (GAPDH, Glyceraldehyde-3-phosphate dehydrogenase) and one downregulated (PGK1, Phosphoglycerate kinase 1), so it is not possible to clearly determine how glycolysis is altered. Fatty acid oxidation appears to be upregulated in *Pkd1* KO cells. This suggests an increase in fatty acid degradation for energy production. Interpreting events in the tricarboxylic acid (TCA) cycle is more complex due to contradictory data. Some enzymes are upregulated, while others are downregulated, making it difficult to fully understand the functioning of this cycle. Oxidative phosphorylation seems easier to interpret, as many proteins, subunits of the electron transport chain complexes, are upregulated, indicating a high energy demand in the cells. This suggests that, under the applied conditions, mIMCD3 cells are capable of using lipids as an energy source and using oxygen to generate energy, despite alterations in other metabolic pathways.

Regarding stress, it appears to be increased, especially in the mitochondria. The enzymes SODM (Mitochondrial superoxide dismutase) and PRDX3 (Peroxiredoxin-3) are upregulated, suggesting an active response to oxidative stress, while SODC (Cytosolic

superoxide dismutase) and PRDX5 (Peroxiredoxin-5) are downregulated. Glutathione S-transferase Mu 1 is the most downregulated protein, involved in detoxification. Proteins related to apoptosis were also found, with pro-apoptotic proteins upregulated and anti-apoptotic proteins downregulated, although we cannot infer what is happening with apoptosis as these proteins have multiple functions.

We experimentally studied the state of the mitochondria through flow cytometry and microscopy assays using mIMCD3 cells. We stained the cells with Mitotracker Green, a dye that marks mitochondria, and with TMRM (Tetramethylrhodamine Methyl Ester Perchlorate), which marks active mitochondria, i.e., it is a marker of mitochondrial membrane potential. We found that *Pkd1* KO cells had a greater mitochondrial mass and exhibited a higher mitochondrial membrane potential. Mitochondria were also stained with Mitotracker Green to examine their morphology and subcellular location by confocal microscopy. In mIMCD3 WT cells, high confluence made detailed observation of mitochondria difficult. In contrast, in mIMCD *Pkd1* KO cells, cells of different sizes with normal, fragmented mitochondria and varying signal intensities were observed. Additionally, DAPI staining revealed multinucleated cells.

Flow cytometry showed that mutant cells have a clearly identifiable second cell population. The differences between WT and *Pkd1* KO are mainly focused on cell size. In a histogram measuring the number of cells on the Y-axis and cell size on the X-axis (FCS parameter), we can see that WT cells follow a Gaussian curve (main population) with a right tail considered as the secondary larger population, while mutant cells show a bimodal curve, with a larger peak representing the main population and a smaller peak representing the secondary larger population. The main population comprises 70% of WT cells and 57% of mutant cells, while the secondary population comprises 30% of WT cells and 43% of mutant cells. This information coincides with what was observed by microscopy.

Additionally, we determined the differences in the cell cycle between WT and *Pkd1* KO cells using propidium iodide to measure DNA content by flow cytometry. This allowed us to identify cells in the G_1, S, and G_2/M phases. A significant decrease in cells in the S phase was observed in the mutant condition, as well as a trend towards a decrease in cells in the G_1 phase and an increase in the G_2/M phases. The accumulation of cells in the G_2/M phase could be due to the activity of cell cycle checkpoints that detect DNA damage and block the cycle or indicate a pre-proliferative state, although confluent cells do not have space on the plate to continue dividing. Additionally, a higher percentage of polyploid cells was observed in *Pkd1* KO cells compared to WT cells, supporting the presence of genetic instability in mutant cells and possibly related to the multinucleated cells seen by microscopy.

To find a protein or pathway to focus our study on, we compared the cellular proteomic study with another done on kidney samples from C57/BL6J $Pkd1^{flox/flox}$; TamCre mice, inactivated on days 10-11 and sacrificed on postnatal days 18 and 30. A total of 228 proteins were identified as shared between the cell SWATH and the renal SWATHs of mice. Of these, 109 proteins showed opposite behavior and 119 proteins showed consistent behavior with that observed in the cell SWATH, of which 101 were upregulated and 18 downregulated. Of the downregulated proteins, 17 were mitochondrial, 10 were metabolic enzymes, 3 were structural proteins, 2 were related to stress management, and 4 were associated with mitophagy. We considered that

investigating mitophagy in ADPKD is a promising line of study that deserves to be further explored.

Mitophagy is a specialized process responsible for the elimination of defective or unnecessary mitochondria. All proteins pass the significance filter, with changes being highly significant in both cells and mice. However, a minimum fold-change filter was not considered for the cell-mouse comparison, and several proteins do not reach a minimum fold-change of 1.5. The downregulated proteins related to mitophagy are as follows: (1) NIPS1 (NipSnap homolog 1 protein): Expressed mainly in the brain, kidney, and liver. It is a mitochondrial matrix protein that accumulates on the surface of mitochondria in response to mitochondrial depolarization, acting as a signal to recruit proteins involved in selective autophagy. (2) FIS1 (Mitochondrial fission 1 protein): Involved in the fragmentation of the mitochondrial network and its perinuclear clustering. It is also implicated in development, oxidative stress, and metabolism. (3) PHB1 (Prohibitin-1): Forms complexes with PHB2 (Prohibitin-2) in the inner mitochondrial membrane. These complexes mark mitochondria for lysosomal degradation and are essential for maintaining mitochondrial function. (4) MIC60 (MICOS complex subunit MIC60): Part of the MICOS complex, responsible for maintaining mitochondrial cristae and inner mitochondrial membrane structure. This subunit, in particular, blocks mitophagy in response to high levels of stress.

The validation of proteins related to mitophagy (NISP1, PHB1, and FIS1) could only be done in mouse samples by qPCR (quantitative PCR) and Western Blot. The downregulation of PHB1 and FIS1 was validated, and other proteins such as PINK and Parkin (some of the best-known proteins associated with mitophagy) were also found to be downregulated. The downregulation of the NISP1 gene was validated by qPCR, but for Western Blot, a 2D SDS-PAGE gel was used because the antibody recognized proteins of different weights than the reference for NIPS1, 30KDa. Although these could be nonspecific bands, we considered that they could also be isoforms of the protein and the effect of post-translational changes. The 2D gel results showed differences between WT and mutant samples. It would be interesting to investigate the differential modifications that NISP1 undergoes and its role in mitophagy.

We hypothesized that mitophagy in ADPKD cells and mouse kidneys could be blocked due to high levels of stress and wanted to verify this in the mIMCD3 cell model. To measure the level of mitophagy, we used mt-mKeima, a pH-sensitive fluorescent protein. This protein enters the mitochondria and, depending on the pH, changes its excitation, allowing the distinction between intact and degraded mitochondria. In a neutral environment (pH 7), such as the mitochondrial matrix, mt-mKeima is predominantly excited at 440 nm. However, when mitochondria are degraded in lysosomes, the environment becomes acidic (pH 4), and mt-mKeima is predominantly excited at 585 nm. Preliminary results showed that mitophagy was increased in *Pkd1* KO cells, but the activation level was similar to that of WT cells. This field of research still needs further investigation, as several factors can significantly influence the result, the most important being the level of stress.

The results collectively indicate a profound metabolic dysregulation in ADPKD, especially at the mitochondrial level, and offer an opportunity to further investigate and seek therapeutic alternatives targeting cellular stress or mitophagy. Additionally, the proteomic data still have potential to explore to find new proteins or pathways relevant to ADPKD.

ABBREVIATIONS

ACMG/ATM: American College of Medical Genetics and Genomics/ Association for Molecular Pathology
ADPKD: Autosomal dominant polycystic kidney disease
ARPKD: Autosomal recessive polycystic kidney disease
CDCA: Cilia-dependent cyst activation
CKD: Chronic kidney disease
CT: Computerized Tomography
CTF: C-terminal fragment
CTT: C-terminal tail
DDA: Data-dependent acquisition
DEP: Differentially expressed protein
eGFR: Estimated Glomerular Filtration Rate
ER: endoplasmic reticulum
ESRD: End-stage renal disease
FBS: Fetal bovine serum
FCCP: Carbonyl cyanide-p-trifluoromethoxyphenylhydrazone
GC: Genetic counseling
GFR: Glomerular filtration rate
GPS: G-protein Proteolytic Site (GPS)
HBSS: Hanks' Balanced Salt Solution
htTKV: height-adjusted Total Kidney Volume
IMM: Inner mitochondrial membrane
KD: Gene knockdown
KO: Gene knockout
MAMs: Mitochondria-associated ER membranes
MEFs: Mouse Embryonic Fibroblasts
MLPA: Multiplex ligation-dependent probe amplification
MRI: Magnetic Resonance Imaging
NGS: Next generation sequencing
NMD: No Mutation Detected
OMM: Outer mitochondrial membrane
OXPHOS: Oxidative Phosphorilation
PBS: Phosphate-Buffered Saline
PCR: Polymerase Chain Reaction
PFA: Paraformaldehyde
PLD: Polycystic Liver Disease
RRT: Renal Replacement Therapy
SDS-PAGE: Sodium Dodecyl Sulfate Polyacrylamide Gel Electrophoresis
SWATH: Sequential Window Acquisition of All Theoretical Fragment Ion Mass Spectra
TMRM: Tetramethylrhodamine methyl ester perchlorate
VUS: Variant of Uncertain Significance
WT: Wild type

INDEX

1 INTRODUCTION

1.1. GENETIC POLYCYSTIC KIDNEY DISEASE

Genetically-based polycystic kidney disease is a general term for genetic diseases that can cause cysts in the kidneys. In some cases, like autosomal dominant or recessive polycystic kidney disease (ADPKD and ARPKD), the cysts are the main feature and physiological problem. However, in other cases of renal genetic disease, cysts are secondary in the disease's pathophysiology.

In this thesis, we will primarily focus on exploring ADPKD from various perspectives to contribute to the current understanding of the disease.

1.1.1. Autosomal Dominant Polycystic Kidney Disease (ADPKD)

Autosomal dominant polycystic kidney disease (ADPKD) (ORPHA:730) is the most common inherited renal disease, with an estimated prevalence of 1:400-1:1000. The prevalence varies according to the study consulted due to factors such as the geographical area studied, population composition and size of population or the diagnostic approach used (Lanktree et al., 2018; Suwabe et al., 2020; Willey et al., 2017).

1.1.1.1. Clinical description

The disease is characterized by the appearance and progressive growth of bilateral fluid-filled renal cysts. Renal function gradually declines and, usually, by the sixth decade of life end-stage renal disease (ESRD) is reached, implying the need for renal replacement therapy (RRT). Cyst development begins before birth and continues to initiate and grow throughout the patient's life (Reeders et al., 1986).

Cystic growth can lead to renal complications such as acute and chronic pain, haematuria, cyst infection and nephrolithiasis. Extrarenal manifestations are also frequent, the most common being hypertension, present in 50-70% of patients before glomerular filtration rate (GFR) decline (Bergmann et al., 2018). Other manifestations include cysts in other organs, particularly the liver and pancreas, intracranial aneurysms and dolichoectasias, abdominal hernias and heart valve lesions (Devuyst et al., 2025)

1.1.1.2. Etiology

ADPKD is a monogenic disease caused by pathogenic mutations in *PKD1* (chromosome 16p13.3) and *PKD2* (chromosome 4q22.1) genes, which are responsible for ~80% and ~15% of ADPKD cases respectively. The remaining cases are genetically unresolved or due to mutations in rarer polycystic disease-related genes (Cornec-Le Gall et al., 2018). Generally, the phenotype associated with *PKD1* is more severe than that associated with *PKD2*, with a median age of onset of ESRD of 58 years for *PKD1* and 79 years for *PKD2* (Gall et al., 2013). Patients with *PKD1* mutations also have lower GFR and larger kidney volumes. According to Heyer et al. the no mutation detected (NMD) group had a *PKD2*-like phenotype. Males had a more severe renal disease in both *PKD1* and *PKD2* populations while, females had larger liver cyst volume, demonstrating that sex influences disease expression (Heyer et al., 2016).

The phenotypic range of ADPKD can be certainly broad, with cases detected in utero or elderly patients without renal failure. Genetic (individual or familial) and environmental factors significantly affect the ADPKD phenotype.

1.1.1.3. Diagnosis

Clinicians follow specialized guidelines when addressing a potential diagnosis of ADPKD (Ars et al., 2022; Cornec-Le Gall et al., 2019; Devuyst et al., 2025). These guidelines may vary slightly in their recommendations due to factors such as resource availability or the target age group (Gimpel et al., 2019) but, in general, the directives are quite similar among all. It is recommended to adhere to the most up-to-date guidelines available. Therefore, when a patient presents with suspected polycystic kidney disease, it is important to investigate several aspects:

1) **Previous family history of ADPKD**. In most cases of ADPKD there is a family history (90%) and only 10% of cases are sporadic (Chapman et al., 2015)

2) **Cyst Presentation**: It is essential to assess the appearance and condition of the cysts. Imaging techniques are used for this purpose. The most commonly used method is ultrasonography, as it is quick, cost-effective, and comfortable for the patient. Other options include computed tomography (CT) and magnetic resonance imaging (MRI). Both of these techniques offer higher resolution and allow for the determination of Total Kidney Volume (TKV). However, they have disadvantages, such as exposing the patient to radiation (in the case of CT) and limited accessibility (in the case of MRI) (Ars et al., 2022).

3) **Presentation of associated extrarenal manifestations**. Extrarenal manifestations can guide the diagnosis of ADPKD, especially the identification of the most prevalent extrarenal manifestations such as hypertension (50-70%) (Bergmann et al., 2018) and hepatic cysts (83%)(Ratnam & Nauli, 2010). It is also important to inquire about recurrent urinary tract infections and hematuria.

4) **Evaluation of renal function status,** taking into account the patient's age, can give an idea of whether ADPKD is rapidly or slowly progressive. It is done by measuring the estimated glomerular filtration rate (eGFR) and several confounding factors must be taken into consideration (Ars et al., 2022).

5) **Differential diagnosis**. Other kidney diseases can create confusion about whether or not it is ADPKD, for example cystic disease caused by mutations in *GANAB*. In these cases, it is necessary to look for distinguishing signs and perform differentiating tests, such as genetic analysis of *GANAB* in the case example (Cornec-Le Gall et al., 2019).

6) **Genetic diagnosis**. Genetic diagnosis is the chosen option in unclear cases or for screening relatives of affected individuals. It should always be accompanied by genetic counseling (GC).

With all these data the clinician should be able to make a diagnosis of ADPKD. They should be able to calculate the stage of the disease, the risk of progression and the possibilities of treatment. Figure 1 presents an example flow chart detailing the steps to follow in case of suspected ADPKD.

The first KDIGO Clinical Practice Guideline for the Evaluation, Management, and Treatment of Autosomal Dominant Polycystic Kidney Disease (ADPKD) has been recently published. This guideline aims to assist clinicians, geneticists, and patients by providing recommendations based on rigorous and comprehensive information (Devuyst et al., 2025)

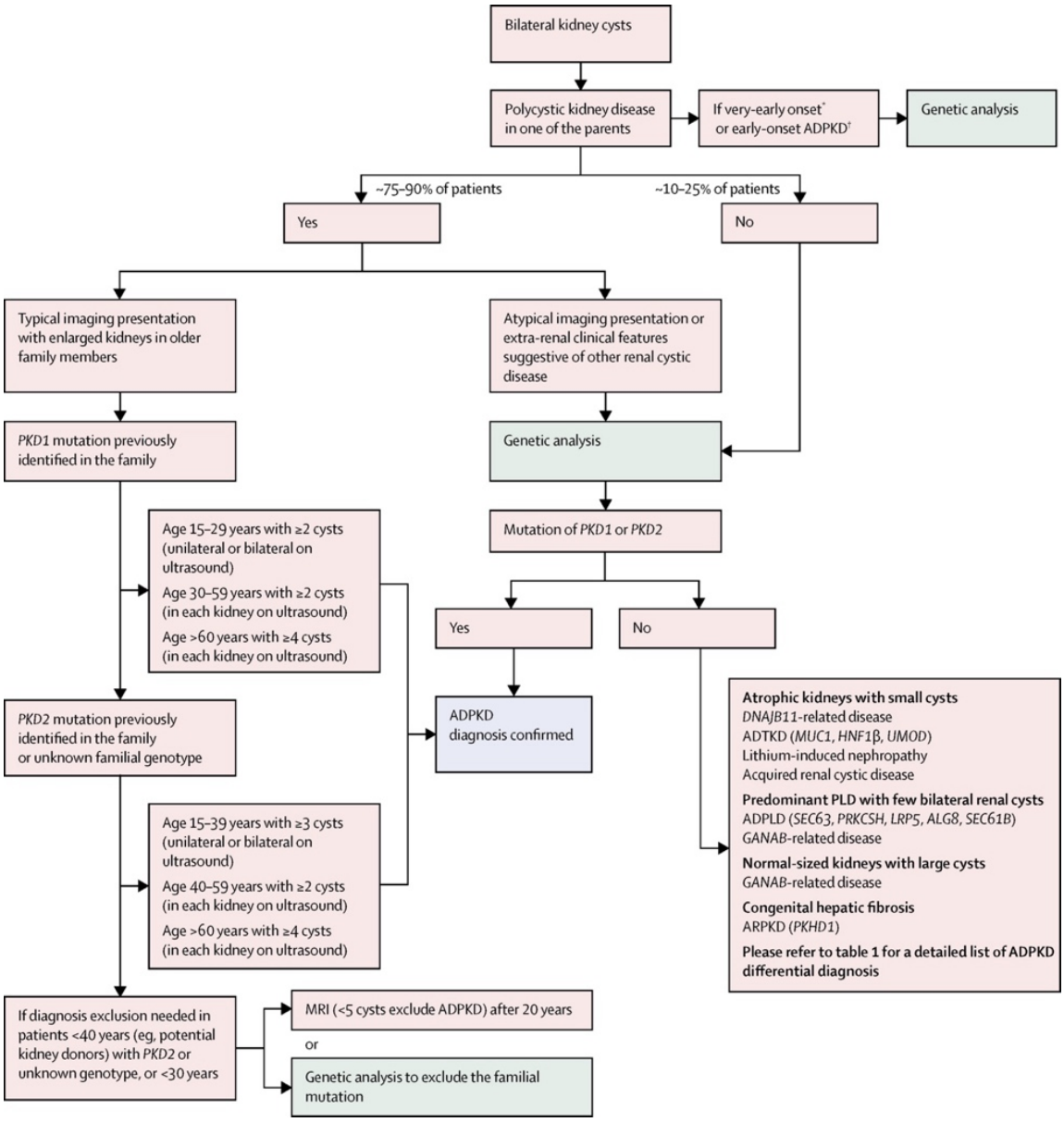

Figure 1. Flowchart for diagnostic of ADPKD. After finding bilateral cysts, the physician may start by reviewing the family history. If there is a positive family history, it is recommended to further investigate the clinical phenotype using imaging techniques. For differential diagnosis, guidelines recommend MRI or genetic testing. Following these instructions, genetic diagnosis is recommended in cases of negative family history, very early-onset or early-onset ADPKD, atypical imaging findings, or to exclude the presence of the mutation in a family donor candidate. The diagnosis can be confirmed either genetically or by age-related cystic findings. Image taken from Cornec-Le Gall et al., 2019 with usage rights granted by Elsevier.

1.1.1.3.1. Genetic diagnosis

Genetic analysis, as illustrated in Figure 1, is the preferred option in cases of clinical uncertainty. This includes scenarios such as: 1) young patients presenting with mild symptoms, 2) absence of a family history, 3) intrafamilial phenotypic variability, 4) atypical results from imaging tests, 5) discrepancy between the observed phenotype and the kidney's functional status or 6) very early onset of the disease. Genetic diagnosis is also recommended when considering a living donor candidate who is a young relative, and it is mandatory for family planning purposes (Figure 1).

Any genetic diagnosis should always be accompanied by **genetic counselling** (GC). In Spain, according to the Biomedical Research Law (LIB 14/2007), genetic counselling is defined as "the procedure aimed at informing an individual about the possible consequences of the results of a genetic analysis or screening for themselves or their offspring, including its advantages and risks. Additionally, it involves advising the individual on possible alternatives derived from the analysis". A multidisciplinary team of specialists should be in charge of genetic counselling**.** This approach ensures that the counselling is comprehensive and better able to address the patient's situation and potential concerns (Ars et al., 2022). Thus, the patient must be provided with all necessary information throughout the entire process, both before and after the genetic results, if it is decided to proceed with the genetic analysis.

Genetic analysis of ADPKD can be complicated, particularly when involving the *PKD1* gene due to certain peculiarities of the gene. It has a high mutation rate and a large size (approximately 13kb). It also contains very GC-rich regions and six pseudogenes on the same chromosome, which exhibit almost complete sequence homology from exon 1 to exon 33 (Gulati et al., 2023). In the past, deal with these challenges required the use of a specific protocol that involve long-range PCRs, sample dilution, and nested PCRs to avoid the amplification of pseudogenes. With the development and improvement of Next Generation Sequencing techniques, it is now possible to accurately differentiate between *PKD1* and its pseudogenes without extra steps. In cases where ADPKD is suspected, it is recommended to use a targeted Next Generation Sequencing (tNGS) panel. This panel should include all genes known to cause cystic disease (Table *1*). If the results are negative, it would be recommended to employ complementary techniques to investigate structural variations or copy number variations. The gold standard for ADPKD is Multiplex Ligation-dependent Probe Amplification (MLPA) (Carrera et al., 2016). Alternatively, an array CGH (comparative genomic hybridization) could be utilized (Audrézet et al., 2012) . If a pathogenic mutation is identified, genetically confirming the diagnosis and a family member also seeks testing, it would only be necessary to analyze the familial variant using Sanger sequencing (only for point mutations). Regarding variant interpretation, the *PKD1* gene presents significant challenges due to its high genetic variability. Numerous variants are detected, but determining their pathogenicity is complex. Consequently, many variants must be classified as variants of uncertain significance (VUS). Variant classification should be conducted in accordance with the guidelines established by the American College of Medical Genetics and Genomics (ACMG)/ Association for Molecular Pathology (AMP) (Richards et al., 2015). The KDIGO 2025 guidelines for ADPKD include recommendations on how genetic variants should be reported (Devuyst et al., 2025)

It is important to note that a negative genetic test does not exclude the presence of the disease. Despite significant advances in sequencing and analysis techniques in recent

years, **diagnostic challenges** remain, such as VUS or non-coding variants. In all genetic pathologies including ADPKD, VUS are a common finding, and they cannot be definitively classified as either pathogenic or benign without further evidence. An in-depth segregation study may help to clarify the VUS, if we can confirm in a large multi-generational family that the variant is present in all affected individuals and absent in all healthy members. Another option would be to perform a tailor-made functional study, specifically designed taking into account the characteristics of the gene and the variant(Fowler & Rehm, 2024). Recently, the role of non-coding variants, which are found in non-coding regions of the gene but still affect the function of the synthesized protein, has also been discussed (Hort et al., 2023). Efforts are being invested in establishing and reaching a consensus on how to interpret them. There are specialized working groups focused on studying certain types of variants, as well as groups investigating how to evaluate variants based on the gene under study (https://clinicalgenome.org/working-groups/).

Table 1. Currently known genes associated with a cystic phenotype. Most of the information has been sourced from the OMIM website (https://omim.org), with the exception of the collagenopathy genes, which have been included based on published references (Gulati et al., 2020; Pierides et al., 2009; Sevillano et al., 2014)

Phenotype	Genes
Polycystic Kidney Disease (PKD)	*PKD1, PKD2, PKHD1, LRP5, GANAB, DZIP1L, DNAJB11, ALG5*
Polycystic Liver Disease (PLD) with or without kidney cysts	*SEC63, SEC61B, PRKCSH, ALG8*
Congenital Disorder of Glycosylation (CDG)	*PMM2, ALG9, ALG8*
Renal Cysts and Diabetes Syndrome (RCAD)	*HNF1B*
Short Rib Thoracic Dysplasia with or without polydactyly	*NEK, DYNC2H1, IFT140*
Tubulointerstitial Kidney Disease (TKD)	*UMOD, SEC61A1, REN, MUC1*
Tuberous Sclerosis (TS)	*TSC1, TSC2*
Collagenopathy with or without kidney cysts	*COL4A3, COL4A4, COL4A5*

1.1.1.4. Treatment and management

In 2015, the European Medicines Agency (EMA) approved the use of **tolvaptan** (Jinarc®), a vasopressin-2 receptor antagonist, for the treatment of ADPKD in Europe. Tolvaptan has demonstrated to be an effective treatment to delay ADPKD progression and preserve renal function, with a sustained benefit in eGFR and an acceptable safety profile (Torres et al., 2016, 2017, 2018). Tolvaptan is only recommended for patients who are over 18 years of age, have a Chronic Kidney Disease (CKD) stage of 1-4 at the beginning of the treatment, and demonstrate rapid disease progression. In other countries where tolvaptan has also been approved, the criteria may vary slightly but are generally similar(Ars et al., 2022). While many potential treatments have been proposed and developed in animal models, none have yet advanced to clinical use in humans.

The disease is currently managed with treatments aimed at symptom control. Blood pressure should be monitored and maintained within a healthy range to prevent cardiovascular events. Aneurysms should be screened and followed-up, especially if there is a family history. Liver cysts typically do not cause functional issues but may require treatment for discomfort or complications. Women with polycystic liver disease (PLD) should seek specialist advice if they need estrogen treatment (Ars et al., 2022). It is

advised that the patient maintains a daily water intake of 2-3 liters and adheres to a healthy diet and lifestyle (Devuyst et al., 2025).

ADPKD represent approximately 7-10% of individuals undergoing dialysis or renal transplantation (Martínez et al., 2013). Thus, although patients can potentially be diagnosed decades before they begin to manifest symptoms, allowing for early intervention, the lack of effective treatments means they continue to experience the same pattern of progression and deterioration (Menezes & Germino, 2019).

1.1.1.5. Molecular biology of ADPKD

1.1.1.5.1. PKD1 and PKD2 genes

ADPKD is caused by mutations in *PKD1* (16p13.3) and *PKD2* (4q22.1) genes. Those genes encode polycystin-1 (PC1) and polycystin-2 (PC2) proteins, respectively.

PKD1 is a large protein coding gene located in chromosome 16 (GRCh37.p13-Chromosome 16: 2,138,711-2,185,899) and *PKD2* is in chromosome 4 (GRCh37.p13-Chromosome 4: 88,928,820-88,998,929) (Figure 2)

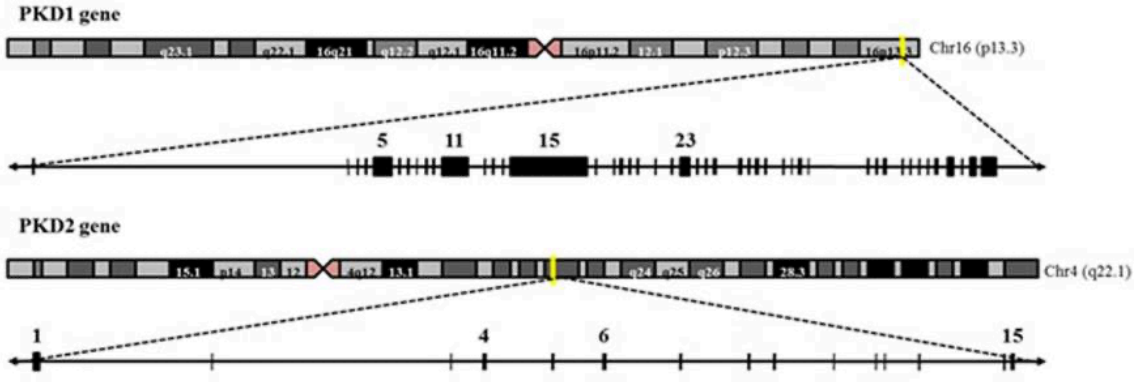

Figure 2. **Chromosomal location of the human *PKD1* and *PKD2* genes and their genetic structure.** Image taken from Cordido et al., 2017 an open-access article under the terms of the CC BY

By consulting the Genotype-Tissue Expression (GTEx) Portal (https://gtexportal.org/home/), it is possible to analyze the tissue-specific transcriptomic expression levels of the cystic genes. The RNA expression patterns of the two genes, *PKD1* and *PKD2*, differ significantly among all tissues (Figure *3*). *PKD1* is predominantly expressed in brain tissues, particularly in the cerebellum and cerebellar hemisphere. Its expression at the renal level is quite low, in fact it is one of the lowest across all tissues. *PKD2,* on the other hand, is mainly expressed in cardiovascular tissues and is also notably expressed in the uterus and other organs of the female reproductive system, such as the fallopian tubes, cervix, and ovaries. Although *PKD2* expression at the renal level is not prominent, it is still higher than that of *PKD1*.

Patients with ADPKD may or may not exhibit certain extrarenal manifestations. In animal models, the complete knockout of *Pkd1* or *Pkd2* results in embryonic mortality with severe abnormalities in other organs, such as the pancreas, liver, and cardiovascular system. Additionally, tissue-specific disruption of *Pkd1* or *Pkd2* in mice leads to hydrocephalus and lymphatic abnormalities (Bergmann et al., 2018).

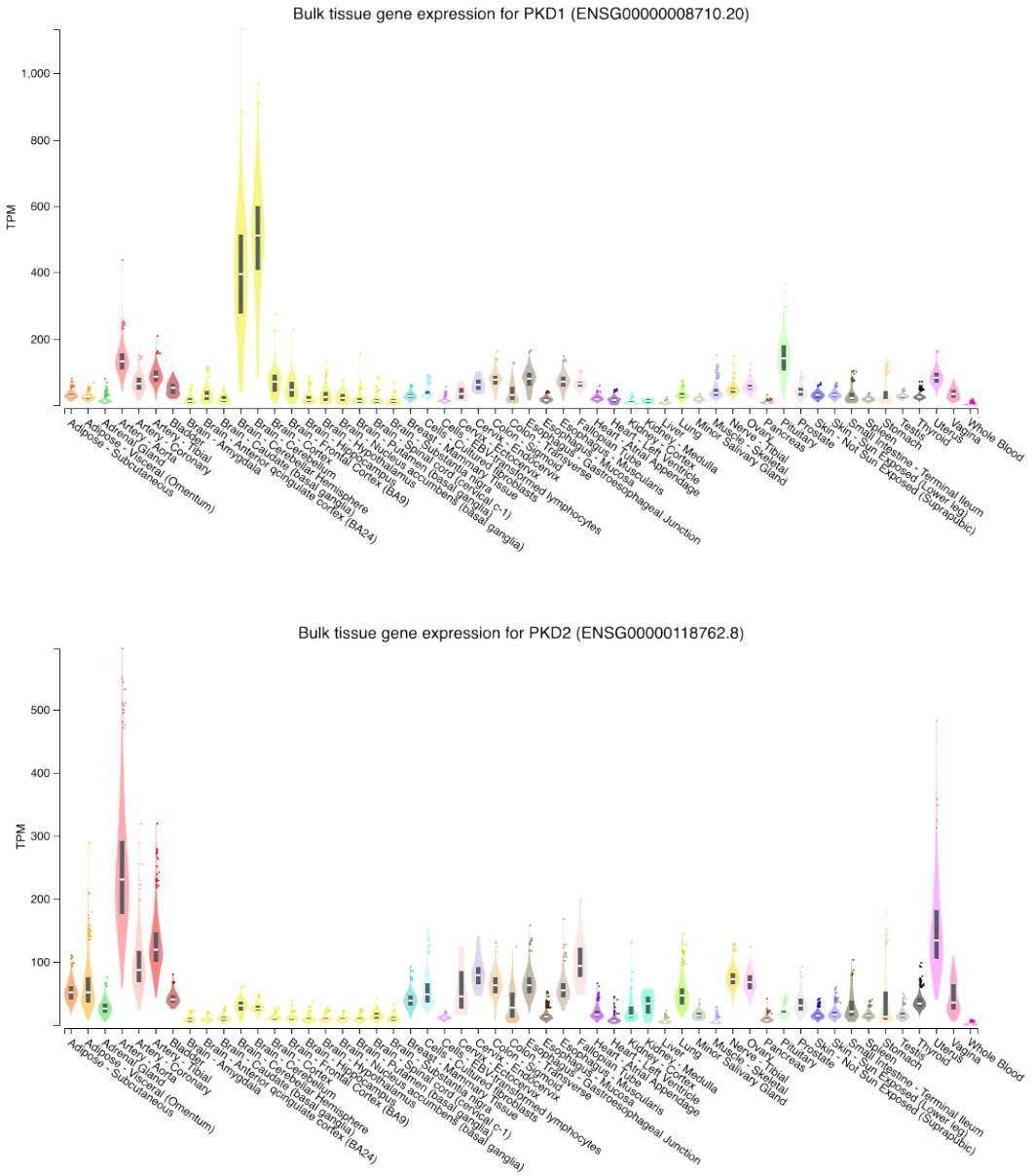

Figure 3. Tissue-specific gene expression profiles of Human *PKD1* and *PKD2* genes according to GTEx.

1.1.1.5.2. Polycystin-1 and polycystin-2

Polycystin-1 (PC1) is a protein composed of 4303 amino acid residues, characterized by a complex structure that includes an N-terminal extracellular region, 11 transmembrane helices (TMs), and a C-terminal coiled-coil domain (Figure 4). PC1 is found in the primary cilium, apical and basolateral membranes, the endoplasmic reticulum (ER), and mitochondria-associated membranes (MAMs). PC1 undergoes autocleavage at the G-protein proteolytic site, resulting in an N-terminal fragment of 3048 amino acids that remains anchored to the rest of the protein. The C-terminal fragment (CTF) contains 11 transmembrane segments and terminates with a 200-amino-acid cytoplasmic tail (CTT). Cleavage at the GPS is essential for ciliary trafficking. Additionally, the CTF undergoes cleavage, possibly mediated by γ-secretase, releasing the CTT, which then traffics to the nucleus and/or mitochondria (Kurbegovic et al., 2014; C. C. Lin et al., 2018; Qian, 2015).

Polycystin-2 (PC2) is a 110KDa membrane protein that forms a homotetramer in which each subunit contains a pore domain, composed of two pore helices and a selectivity filter, as well as a voltage sensor-like domain (VSD). PC2 is a member of the Transient Receptor Potential Protein (TRP). PC2 is much more abundant than PC1 and has been localized to the ER and primary cilium. PC1 requires PC2 to traffic to the primary cilium, and it might also be found alongside PC1 in other areas (Qiu et al., 2023).

The PC1 and PC2 form a heteromeric complex composed of one PC1 and three PC2 subunits (Q. Su et al., 2018)(Figure 4).

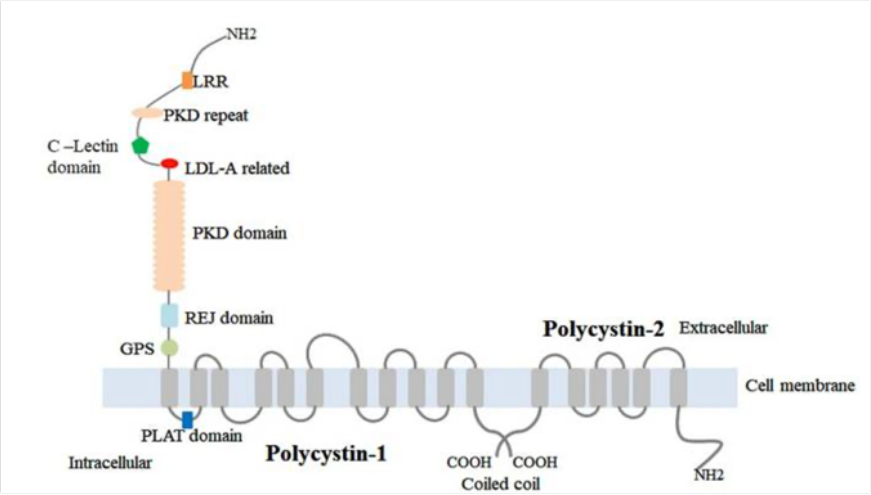

Figure 4. Structure of the polycystins. Image taken from Cordido et al., 2017 *an open-access article under the terms of the CC BY*

1.1.1.5.3. Cystogenesis. The functionality threshold and the two-hit hypothesis

ADPKD is an autosomal dominant inherited disease. Mutations in one of the alleles of *PKD1* or *PKD2* lead to the development of the disease. This raises the question of what initiates cyst development, and why, despite all renal tubule cells having the germline mutation, only some are capable of initiating a cyst or are unable to prevent the cyst from forming. The growth of ADPKD renal cysts is very characteristic. In the renal epithelial cells, a specific trigger induces the cell to begin proliferating. There is an orderly cellular overgrowth in monolayer, forming a sac-like structure that eventually detaches from the tubule, as shown in Figure 5. The formed cyst grows because it proliferates and fills with fluid that enters its interior (Qiu et al., 2023).

Traditionally, four hypotheses have been proposed to explain the triggering of cystogenesis : a gain of function, where the mutation causes excessive expression of the encoded protein, leading to incorrect interactions; dominant negative, where the mutation encodes a dysfunctional protein that interferes with the normal protein; haploinsufficiency, which results in an deficient level of functional protein; and finally, the proposal of recessive behavior at the molecular level, where functional insufficiency is reached when the cell acquires a somatic mutation in the normal allele (the two-hit model)(Qiu et al., 2023).

Currently, the most accepted model is the **"threshold" model**, which posits that cysts begin to form when protein functionality levels fall below a critical threshold. In most cases, this point is reached as a result of the second hit ("**two-hit" model**) (Figure 5), which involves a second mutation occurring in the wild-type allele of *PKD1* or *PKD2* in the cystic epithelium (prone to somatic mutations) (Torres & Harris, 2019). However, any process that leads to a decrease in functionality below the threshold can trigger cyst formation.

Somatic mutations are non-predictable and vary in each cell. However, by understanding the germline mutation, we can understand variable presentations of the disease as the germline mutation itself establishes a starting threshold. The germline genetic factors identified to date that influence ADPKD include the following:

- **Type of mutation.** A truncating variant (frameshift indels, non-sense, and splicing variants) results in a truncated protein product, while a non-truncating variant (missense and in-frame indels) does not affect the complete synthesis of the protein, but its function can be altered. It has been demonstrated that *PKD1* truncating mutations are significantly associated with a lower estimated glomerular filtration rate (eGFR) compared to non-truncating mutations (Heyer et al., 2016). In humans, fully penetrant biallelic pathogenic variants in either *PKD1* or *PKD2* results in lethality (Paterson et al., 2002). However, if at least one of the variants is hypomorphic (non-fully penetrant), it can be compatible with life. The presentation of the disease can be very varied; even two hypomorphic variants can result in early onset ADPKD. These variants are often classified as VUS, making it difficult to prove their involvement in the disease (Gulati et al., 2023; Hopp et al., 2012; Rossetti et al., 2009; Vujic et al., 2010).
- **Interaction with other cystic genes**. Transheterozygosity involving *PKD1* and *PKD2* is not necessarily lethal, but it does result in a more severe form of the disease (Paterson et al., 2002; Pei et al., 2001). Polycystic genes have been suggested to interact with other genes such as *HNF1B*, *PKHD1*, *PRKCSH* or *SEC63*. Studies using mouse mutants have demonstrated that the loss of GIIβ (*Prkcsh*) or Sec63p (*Sec63*) results in reduced levels of the functional PC1-PC2 complex, with PC1 acting as the rate-limiting factor that determines the severity of the cystic phenotype. Furthermore, the expression levels of PC1 can influence the severity of kidney cyst formation caused by mutations in *Pkhd1*(Fedeles et al., 2011).
- There is also the possibility of **mosaicism**, meaning that not all cells in the organism have the germline mutation. This leads to significant variability; however, it is generally associated with a milder phenotype in *PKD1*-mutant cases (Hopp et al., 2020).

A "**three-hit" model** has been proposed by some researchers. It suggests that the delay between the loss of *Pkd1* and cyst onset in adult mice can be accelerated by a third hit, as a renal injury, indicating that changes in the physiological state of the cell may influence the rates of cyst formation(Cordido et al., 2021; Takakura et al., 2009; Weimbs, 2011). This model also explains what has been observed in animal models, in which the moment of gene inactivation can be decisive for cyst development. A difference of just two days in the timing of inactivation can lead to two very different phenotypes (Piontek et al., 2007). It appears that certain factors intrinsic to the cell or its microenvironment may influence the necessity for polycystins expression and functionality.

Another study delves deeper into the initiation and evolution of cysts. Using a mouse model and a methodological approximation that mimics better ADPKD in humans, they observed that the inactivation of the normal allele in some cells is sufficient for the appearance of a few cysts. If a renal injury is applied, the formation of cysts increases, but there are still very few. However, over time, the few cysts present exert stress on the surrounding cells, initiating a "**snowball effect"**. This leads to the appearance of many new cysts, which accelerate the progression of the disease (Leonhard et al., 2015).

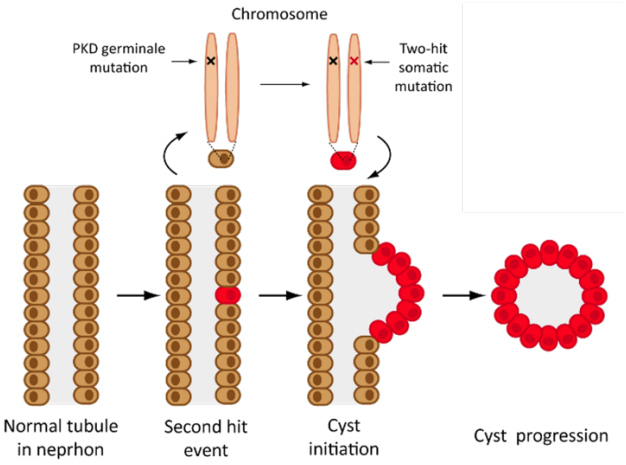

Figure 5. Mechanism of cystogenesis according to the two-hit model and the threshold model. Renal tubular cells all carry the germline mutation. When a second mutation occurs in one of these cells in the cystic gene, the protein functionality drops below a critical threshold, the cell begins to proliferate, eventually forming a fluid-filled cyst that can detach from the tubule. Image modified fromAdrián Cordido Eijo, 2021)

The intrinsic mechanism of the disease is still unknown, with many gaps in the puzzle yet to be filled. What is clear is that the PCs are the root cause, and we already know that non-endogenous re-expression of the *Pkd* genes in ADPKD mice can rapidly reverse the disease (Dong et al., 2021).

1.1.1.5.4. ADPKD metabolism

Cellular metabolism is dysregulated in PKD, and there is growing evidence that its influence on the disease is significant and not just a side effect. Over the years, different dysregulated pathways have been described, and, in some cases, specific therapies have been designed to target this dysregulation at preclinical level.

The focus was placed on energy metabolism when the **Warburg effect** was described in ADPKD, a phenomenon observed in cancer cells that involves the use of aerobic glycolysis under conditions of oxygen availability instead of oxidative phosphorylation, much more energy efficient. Researchers demonstrated an increase in glucose consumption, lactate production, and ATP levels in both *Pkd1*$^{-/-}$ mouse embryonic fibroblasts (MEFs) and in young cystic *Pkd1*-mutant mouse kidneys. Through another methodological approach, they showed that inhibiting glycolysis with a treatment of 2-deoxy-D-glucose (2-DG), a non-metabolizable glucose analog, they achieve a reduction in the kidney:body weight ratio in *Pkd1* mutant mouse models (Chiaravalli et al., 2016; Rowe et al., 2013). Some subsequent studies found that glycolysis was upregulated and that the transcription of key glycolytic genes, hexokinase 1 (*HK1*) and *HK2,* were increased in human ADPKD primary cells in vitro (Riwanto et al., 2016). However, other studies did not observe a significant increase in glycolysis (Menezes et

al., 2016; Warner et al., 2016). The reason for this discrepancy is not known but it is thought that it may lie in the methodology used in the different experiments

Lipid metabolism is also altered in ADPKD. Defects in fatty acid oxidation (FAO) have been reported in cell lines derived from *Pkd1*$^{KO/KO}$ mice (Menezes et al., 2016), and transcriptional profiles of ADPKD kidneys showed a tendency towards the downregulation of key enzymes involved in **fatty acid oxidation** (FAO)(Podrini et al., 2018). Another study demonstrated an upregulation of the miR-17~92 cluster, involved in cyst proliferation and disease progression, in cystic samples from mice and ADPKD patients (Hajarnis et al., 2017). An anti-miR-17 treatment and miR-17 inhibition successfully reduced the cystic growth in human in vitro models and animal models of ADPKD (Hajarnis et al., 2017; Lee et al., 2019). It has been suggested that miR-17 effects are mediated by Pparα (Peroxisome proliferator-activated receptor α), a transcription factor involved in metabolism. miR-17 inhibits Pparα. Therefore, the suppression of miR-17 normalizes the expression of Pparα, reverses the dysregulation in oxidative phosphorylation (OXPHOS) and FAO, and improves the cystic phenotype in ADPKD models (Carney, 2017; Hajarnis et al., 2017). Additionally, a Pparα agonist (fenofibrate) increases the expression levels of Pparα and also FAO, reducing cyst volume in a slow progression model of ADPKD (Lakhia et al., 2018).

A decrease in fatty acid oxidation (FAO) leads to a reduction in **oxidative phosphorylation** (OXPHOS). This is logical because FAO is the primary process that supplies energy to OXPHOS. This fact has been found in ADPKD (Hajarnis et al., 2017; Menezes et al., 2016; Podrini et al., 2018).

Metabolomics studies have found that **glutaminolysis**, an anabolic process providing energy and substrates for biosynthetic reactions, is increased in ADPKD as a compensatory mechanism for the reduced input of glycolysis-derived metabolites into the tricarboxylic acid (TCA) cycle. *Pkd1*$^{-/-}$ MEFs were shown to be dependent on glutamine for energy production, and this glutamine is also processed for use in fatty acid biosynthesis. The authors propose that increased production of fatty acids is necessary for membrane generation in ADPKD proliferative cells. Additionally, it was demonstrated that glutamine utilization in ADPKD is directly related to asparagine metabolism, leading to the upregulation of asparagine synthase (ASNS) to further fuel the TCA cycle (Podrini et al., 2018). Reducing glutamine metabolism effectively slowed the growth of *Pkd1*-mutant cells from young mice. In contrast, adult *Pkd1*-mutant cells did not show a notable decrease in proliferation when deprived of glutamine, behaving similarly to wild-type cells (Flowers et al., 2018; Menezes & Germino, 2019). A proposed therapy to inhibit glutaminase 1(GLS1), the enzyme that catalyzes the hydrolysis of glutamine, led to conflicting results in different models of ADPKD (Soomro et al., 2018).

All these observed metabolic changes may be closely related to the altered signaling pathways in ADPKD: the mTOR (mammalian target of rapamycin) pathway, the cAMP (cyclic AMP) pathway, the Wnt/β-catenin pathway, the AMPK (AMP-activated protein kinase) pathway, calcium signaling, growth factor signaling, and G-protein signaling.

The relationship between these metabolic changes, polycystins and cyst development remains unknown. However, it is evident that metabolic reprogramming is key for the development and progression of the disease. Therefore, further research is essential to understand the factors driving PC1-deficient cells to undergo this metabolic

reprogramming. Moreover, these altered pathways may serve as promising targets for new therapeutic approaches

1.1.1.5.5. Mitochondria in ADPKD

ADPKD causes **mitochondrial abnormalities**, which have been detected in cell models, animal models and tissue samples from ADPKD patients. Studies on cyst-lining cells from Ksp-Cre;*Pkd1*$^{flox/-}$ mice and Han:SPRD$^{Cy/+}$ rats have demonstrated that these mitochondria exhibit increased fragmentation, elevated production of reactive oxygen species (ROS), and a reduced mtDNA copy number compared to wild-type(Ishimoto et al., 2017). Further evidence indicates altered mitochondrial membrane potential and abnormal morphology in *Pkd1* knockout cell lines (C.-C. Lin et al., 2018). Additionally, several mitochondrial alterations, including reduced mass, structural changes, and network fragmentation, were observed in the cystic epithelia of Ksp-Cre;*Pkd1*$^{flox/-}$ mice and a reduced expression of pro-fusion proteins (OPA1 and MFN1) and an increased expression of the pro-fission protein DRP (Cassina et al., 2020).

Polycystins are proteins functionally linked to mitochondria. In 2016, the polycystin complex was associated with the ability to detect and respond to oxygen levels, thus playing a role in the regulation of mitochondrial function. The study showed that, depending on oxygen levels, the subcellular localization and function of the polycystin complex were modified through its interaction with the oxygen-sensing prolyl hydroxylase domain-containing protein EGLN3 (PHD3), which hydroxylates PC1. Additionally, it was observed that cells lacking PC1 expression used less oxygen and had reduced mitochondrial calcium uptake following bradykinin-induced calcium release from the endoplasmic reticulum (ER). Researchers suggest that PC1 responds to low-oxygen (hypoxia) conditions by trafficking from MAMs (mitochondrial-associated membranes) to the plasma membrane, thereby reducing PC-mediated calcium release from the ER, even with normal cytosolic calcium levels, leading to decreased calcium-dependent OXPHOS. According to this model, lacking PC1 expression could mimic conditions of low oxygen, leading to changes in mitochondrial function. These observations link polycystins to mitochondrial function and the altered metabolism we have discussed (Padovano et al., 2017).

It has been identified that some **C-terminal fragments of PC1** (PC1-CTT) have a mitochondrial localization. They directly affect mitochondrial function, as well as indirectly influence cyst formation. In *Pkd1*-deficient cells, a 17 kD PC1-CTT protein construct was observed to translocate to the mitochondrial matrix and rescue the mitochondrial fragmented phenotype (C. C. Lin et al., 2018). Another PC1-CTT construct, this one 200 amino acids long, was able to reduce cell proliferation and cyst size in an in vitro *Pkd1*-KO 3D model (Merrick et al., 2012). And, when studying the transgenic expression of this 200 amino acid PC1-CTT fragment in two *Pkd1*-KO animal models, it was found that it was able to suppress the cystic phenotype and maintain the renal function. Additionally, it was determined that this suppression depended on the interaction of the fragment with the mitochondrial enzyme Nicotinamide Nucleotide Transhydrogenase (NTT) (Onuchic et al., 2023). Of note, although further research is required, a cohort study involving 338 patients (82 families) with *PKD1* mutations indicated that pathogenic non-truncating mutations in the C-terminal tail (CTT) were associated with shorter renal survival (51 years) compared to other mutations of the same type located in upstream positions of the G-protein-coupled receptor proteolytic site

(GPS-upstream domain) (70,2 years) or in transmembrane domains (67 years) (Higashihara et al., 2018).

All these data together, demonstrate that the absence of PC1 leads to structural and functional alterations in the mitochondria. These changes seem to occur close to the initial defect and precede the cascade of events that results due to the loss of polycystins.

PC2 have also been associated with mitochondrial structure and function. A study found that the loss of PC2 increases calcium transfer to the mitochondria and decreases mitochondrial movement, as mitochondria become anchored to ER membranes due to an increased presence of mitofusin-2 (MFN2). Based on their findings, the authors propose that one of the functions of PC2 is to regulate calcium influx into the mitochondria by modulating proteins located in MAMs, enhancing mitochondrial biogenesis, and anchoring mitochondria to the ER via PGC1α (peroxisome proliferator-activated receptor gamma coactivator 1-alpha). Structurally, in PC2 KD (knockdown) cells they observe a high degree of fragmentation (Kuo et al., 2019). Some of their findings conflict with those observed in ADPKD-*PKD1* models, for example, regarding metabolic behavior. However, they attribute these discrepancies to the possibility that PC1- and PC2-mediated cyst development may involve both common and distinct mechanisms.

1.1.1.5.6. Cilia in ADPKD

Polycystins are mainly located in the primary cilium, a hair-like structure that protrudes from the apical membrane of renal epithelial cells into the lumen of the nephron with sensory functions (Bergmann et al., 2018). That is why ADPKD is classified under a group of genetic disorders known as ciliopathies, which are characterized by dysfunction of the primary cilia. The connection between polycystins, cilia, and cyst formation is recognized within the ADPKD scientific community. The role of the cilia is considered one of the most significant mechanisms proposed to date as a trigger for cyst formation. In 2013, using *Pkd1*-mutant mice or *Pkd2*-mutant mice, it was shown that when polycystins were inactivated, if cilia remained intact, cyst growth was accelerated. Conversely, if the cilia were lost or become non-functional shortly after polycystins inactivation, cyst growth was significantly suppressed. This suggests the existence of a mechanism by which polycystins inhibit a **cilia-dependent cyst activation (CDCA)** that controls renal epithelial cell proliferation (Ma et al., 2013). A recent study established *Glis2* as a functional target of CDCA's cyst-promoting activity following polycystin inactivation. In preclinical models, pharmacological targeting of *Glis2* demonstrated suppression of PKD (Zhang et al., 2024).

The trafficking of polycystins to the cilia is crucial to prevent the formation of cysts. The pathogenic mechanism of many mutations in *PKD1* and *PKD2* involves the disruption of polycystin trafficking to the cilia (Cai et al., 2014).

TULP3 (Tubby-related protein 3), a ciliary trafficking protein, was shown to be involved in the regulation of renal cystic disease. In mouse models, loss of *Tulp3* function leads to the development of kidney cysts, like those seen in ADPKD. In models where both *Tulp3* and *Pkd1* are deleted, the severity of cyst formation is reduced, suggesting that *Tulp3* and *Pkd1* interact in complex ways to regulate cystogenesis (Legué & Liem, 2019).

It is interesting to note the bi-directional relationship between autophagy, another process known to be altered in ADPKD, and ciliogenesis. It has been suggested that basal

autophagy regulates ciliary growth through the degradation of proteins required for intraflagellar transport. Thus, the compromised ability to activate the autophagic response may underlie some ciliopathies (Pampliega et al., 2013).

1.1.1.5.7. Autophagy and apoptosis in ADPKD

Autophagy is the cellular process by which cells degrade their own components in order to maintain cellular homeostasis. It degrades anything that is damaged or not needed at the time and is a very important process during development. Autophagy occurs through the formation of vesicles (autophagosomes) around organelles or areas of the cytoplasm. These vesicles subsequently fuse with lysosomes (autophagolysosomes) and their contents are digested by lysosomal enzymes. For the study of autophagy, the proteins ATG (Autophagy-related genes), LC3 (Microtubule-associated protein 1A/1B-light chain 3), Beclin-1, and P62/SQSTM1 are typically used as reference markers. Autophagy has been linked to degenerative diseases and cancer.

In ADPKD, autophagy has also been demonstrated to be an impaired process. Under a stressful condition, such as hypoxia, an increase in LC3-II and beclin-1 has been detected in rat and mouse models of ADPKD (Belibi et al., 2011). Another stress condition experienced by renal cells is altered metabolism. In response to glucose deprivation, Pkd1+/+ cells are capable of activating autophagy, whereas Pkd1−/− cells are unable to do so and exhibit high levels of apoptosis. Treatment with rapamycin can partially restore autophagy (Rowe et al., 2013). In another study, inhibition of autophagy by knocking down the ATG5 protein in an ADPKD zebrafish model promoted cytogenesis. Conversely, activation of autophagy with a Beclin-1 inducer improved the cystic phenotype. It was also confirmed that rapamycin and other autophagy-activating compounds were able to reduce cyst formation and improve renal function (Zhu et al., 2017).

Autophagy is a dynamic process associated with both negative and positive characteristics. The same applies to **apoptosis**, a process of programmed cell death. While inhibiting apoptosis has been shown to slow renal cyst growth in certain animal models of ADPKD, it was also found that, in *Pkd1* mutant mice, promotion of apoptosis in cystic epithelial cells through intrinsic or extrinsic signaling pathways can decrease disease progression, regardless of whether cell proliferation is inhibited (Zhou & Li, 2015).

1.2. ORGANELLE RECYCLING AND DISPOSAL MECHANISMS

Cells possess intricate mechanisms for the recycling and disposal of organelles to sustain homeostasis and operational efficiency. Central to this process are lysosomes, which are membrane-bound organelles endowed with hydrolytic enzymes capable of degrading macromolecules, cellular debris, and impaired organelles. This degradation process is termed autophagy.

1.2.1.1. Mitophagy

Mitophagy is a specialized form of autophagy responsible for eliminating and recycling dysfunctional or unnecessary mitochondria. This essential quality control process helps maintain cellular homeostasis, particularly in metabolically active organs such as the kidney. Maintaining mitochondrial health relies on several mechanisms,

including mitophagy, antioxidant defense, and protein quality control (Held & Houtkooper, 2015).

Mitophagy has proven to be important in chronic kidney disease (CKD) progression and kidney repair after acute kidney injury (AKI) (Jiang et al., 2020; L. Su et al., 2023). It supports healthy mitochondrial function, reduces reactive oxygen species (ROS), and protects renal cells. Renal interstitial fibrosis (RIF) is a late-stage kidney disease change linked to functional impairment. Mitochondrial damage, occurring before inflammation and fibrosis, plays a key role in kidney fibrosis (J. Sun et al., 2023).

Under stressful conditions such as oxidative stress, hypoxia, nutrient deprivation, aging, or the accumulation of mitochondrial DNA mutations, mitochondria become damaged and their membrane potential decreases. Mitophagy involves the tagging of damaged mitochondria for degradation, recognition by the autophagic machinery, engulfment by lysosomes, fusion with phagosomes, and degradation within mitophagolysosomes. This process ensures the maintenance of mitochondrial quality, reduces oxidative stress, regulates apoptosis and cell survival, and assists cells in adapting to metabolic demands and environmental stresses (Fan et al., 2024).

Mitophagy in kidney disease is regulated by several key pathways, with the most well-known being the **PINK1/Parkin pathway**. When mitochondria are damaged and lose their membrane potential, PINK1 (PTEN-induced kinase 1) accumulates on the outer mitochondrial membrane (OMM). This accumulation recruits and activates Parkin, an E3 ubiquitin ligase. Then, Parkin ubiquitinates various mitochondrial surface proteins, marking the damaged mitochondria for degradation. There is evidence that PINK1 may also have functions independent of Parkin (Figure 6). Mitophagy can also be mediated by specific membrane receptors. These mitophagy receptors can be divided into three groups: OMM receptors, such as BCL2 interacting protein 3 (BNIP3) and BCL2 interacting protein 3 Like (NIX/BNIP3L), FUN14 domain containing 1 (FUNDC1), FKBP prolyl isomerase 8 (FKBP8), and BCL2 like 13 (BCL2L13); IMM protein receptors, such as prohibitin 2 (PHB2); and mitochondrial membrane lipid receptor cardiolipin (CL) (J. Sun et al., 2023) (Figure 6).

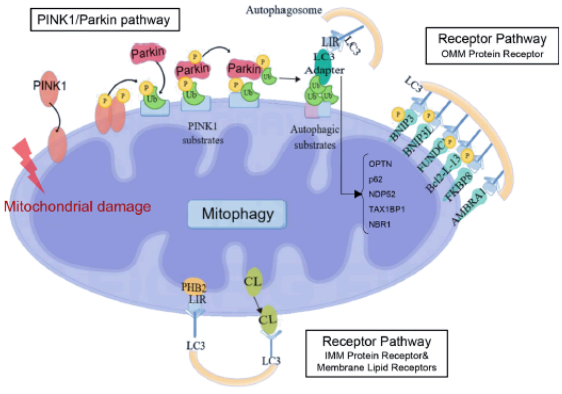

Figure 6. Mechanisms of mitophagy initiation. When mitochondria are damaged and lose membrane potential, PINK1 accumulates on the outer mitochondrial membrane, recruiting and activating Parkin. Parkin ubiquitinates mitochondrial surface proteins, marking the damaged mitochondria for degradation. Mitophagy can also be mediated by specific membrane receptors, which are categorized into three groups: outer mitochondrial membrane (OMM), inner mitochondrial membrane (IMM) protein receptors, and mitochondrial membrane lipid receptor. Image taken from *(J. SUN ET AL., 2023)* with usage rights granted by Springer Nature

2 JUSTIFICATION AND OBJECTIVES

The study of ADPKD has been ongoing for years, with various national and international groups working to understand this disease, each leveraging their own expertise. We all share common goals: improving diagnosis, deciphering the molecular pathology of the disease, and ultimately finding a treatment that improves the health and quality of life of those affected by ADPKD.

The NefroCHUS group is partly dedicated to the genetic diagnosis of kidney diseases. We frequently encounter inconclusive cases, and this is precisely an issue we aimed to address in this thesis. As well, in the group we attempted to investigate the molecular mechanisms implicated in ADPKD. Particularly this thesis will focus on investigating the potential of the mIMCD3 monoclonal cell line for the study of ADPKD. The set objectives we were working on are outlined below:

1 **Diagnose genetically inconclusive cases with candidate variants of uncertain significance (VUS)**. We began by studying two ADPKD families that present two *cis* variants, E3068Q and A1368V, in the *PKD1* gene. These variants are known to segregate with the disease. Our aim was to confirm or rule out the following hypotheses:

   a) One variant is causative, and the other is inherited together due to linkage disequilibrium.

   b) Both variants are causative due to an additive effect, resulting in the synthesized protein failing to meet the threshold of minimal functionality.

   c) There is an undetected causative variant in linkage disequilibrium with the VUS variants.

   d) A pathogenic mutation in a cystic gene, other than *PKD1* or *PKD2,* is responsible for the cystic disease.

2 **Explore new research avenues related to ADPKD, focusing on identifying specific proteins, signaling pathways, and affected processes, prioritizing those that may offer viable therapeutic options,** specifically aiming to:

   a) Conduct a proteomic study using the monoclonal cell line mIMCD3 (WT and *Pkd1*KO) and perform a comparative analysis of the results.

   b) Examine the proteomic results and conduct the necessary experiments to characterize and contextualize the potential findings.

      i. Assessment of cellular and mitochondria status in mIMCD3 cells

   c) Compare our findings with proteomic analyses that were previously carried out on kidney samples from mice to find shared mechanisms of the disease and highlight the strengths and weaknesses of the cellular model.

      i. Deciphering the role of mitophagy in ADPKD.

3 MATERIAL AND METHODS

3.1. FUNCTIONAL VALIDATION OF VARIANTS OF UNCERTAIN SIGNIFICANCE (VUS) IN *PKD1*

3.1.1. Genetic tests

DNA was isolated from peripheral blood of the patients using the QIAamp® DNA Blood Mini Kit (Qiagen, 51104) according to the manufacturer's instructions. Samples for massive sequencing were prepared following the instructions of the TruSeq DNA Exome protocol (Illumina) and sequenced using the Illumina NextSeq 500 (Illumina). The coding region and flanking intronic regions of the 82 genes analyzed were sequenced. Family segregation was performed by Sanger sequencing following a standard protocol and using the 3730xl DNA Analyzer 96-capillary (Applied Biosystems). MLPA was conducted using the SALSA® MLPA® probe mixes P352 *PKD1-PKD2* kit.

3.1.2. Genetic interpretation of the variants

Variants were classified according to the ACMG/AMP criteria using the online tools Varsome (https://varsome.com) and Franklin (https://franklin.genoox.com/clinical-db/home). The ACMG/AMP criteria are based on multiple data types that contribute in varying degrees to an overall score that measures the probability of a variant being pathogenic. The online tools incorporate information from population data, computational and predictive data, functional data, segregation data, de novo data, allelic data, and other supplementary data. Codes are assigned to each variant based on the type of available information (Richards et al., 2015). Additionally, we queried ADPKD variants in the PKD database (https://pkdb.mayo.edu/variants).

3.1.3. *In silico* prediction of splicing variants

In silico prediction tools are computational programs designed to predict the functional effect of genetic variants. There are a multitude of predictors and each of them analyses in a different way, depending on the information they use from different databases and the algorithm they use. To test the functional effect of variants suspected of having an effect on splicing, we have used the following tools: SpliceAI (https://spliceailookup.broadinstitute.org/); SPIDEX, CADD v1.6 (SPIDEX and CADD information comes from the gene panel performed on patients) and NNSplice (https://www.fruitfly.org/seq_tools/splice.html)

3.1.4. Plasmid construction

A splicing assay was performed to assess the predicted splicing effect that *in silico* predicting tools give to one of our variants of interest (*PKD1* c.9202; E3068Q). By polymerase chain reaction (PCR) we amplified a genomic DNA fragment from two of our patients (long range PCR) (Supplemental figure 1). The PCR was done using Platinum™ Taq High Fidelity polymerase (Invitrogen™, 11304011) and BPF6-BPR6 primers (Supplemental table *1*). The amplification program used a temperature gradient for hybridization [95ºC,3min; 80ºC,3min; (95ºC,20s; 70C-Δ0,5ºC,30s)x15; (95ºC,30s; 64ºC,30s; 72ºC,7min)x20; 72ºC,10min]. After that we did serial dilutions to get rid of any possible pseudogene amplification (*PKD1* has 6 pseudogenes on chromosome 16). Using the amplification product as template we performed a second (nested) PCR that amplified

a 2554 bp fragment using Platinum Taq High Fidelity polymerase and PKD1_EX26_SA_F - PKD1_EX26_SA_R4 primers (Supplemental table *1*). This polymerase left single 3'adenine-overhangs for posterior use in TA TOPO cloning. In this PCR we used a conventional PCR program. We used the GeneJET Gel extraction kit (ThermoFisher™, K0691) to extract DNA from the agarose gel bands before cloning.

3.1.5. Cloning and transformation

For cloning, we used the TOPO™ TA Cloning™ kit for subcloning with TOP10 *E.coli* competent cells (Invitrogen™, K4500) following the manufacturer's instructions and using ampicillin selection. This kit allows fast one-step cloning for the direct insertion of Taq polymerase-amplified PCR products into a plasmid vector (pCR 2.1-TOPO) (Figure *7*) and the One Shot chemical transformation to obtain multiple copies of the vector. To purify we used the GeneEluteTM Plasmid Miniprep Kit (Sigma-Aldrich®, PLN70-1KT). Correct plasmid size and orientation was checked by using *ApaI* restriction (NzyTech) enzyme and running an agarose gel. To check which plasmid was WT and which one was mutant Sanger sequencing was performed using PKD1_EX26_SA_F and PKD1_26R (Supplemental table *1*) as sequencing primers. We needed to move the insert from the pCR 2.1-TOPO plasmid to an expression plasmid, for that we cut with *HindIII* (NzyTech, MB07001) and *XhoI* (NzyTech, 07401) restriction enzymes, gel-purified the fragment of interest and ligate it with the expression vector pCDNA5/FRT/TO (Invitrogen™, V6520-20) (Figure *7*) using T4 DNA ligase (ThermoScientific™, EL0011). We used a dephosphorylation step FastAP (ThermoScientific™, EF0652) to avoid recircularization, in case only one cut was done, so only vector an insert are going to ligate and form a functional plasmid.

3.1.6. Cell culture and transfection

We cultured 293HEK cells with Dulbecco's Modified Eagle's Medium (DMEM) (Gibco™, 11965092) supplemented with 10% Fetal Bovine Serum (FBS) (Corning ®, 35-079-CV) and 1% Penicilin-Streptomycin (Gibco™, 11548876). Once they reached 70% of confluency, we transfected the cells with polyethylenimine (PEI) at a proportion 1:3 (ug DNA/ug PEI). 24 hours later expression was induced with Tetracyclin (1µg/mL) and 24 h later, samples were collected in TRI Reagent® (Sigma-Aldrich, T9424).

3.1.7. RNA isolation, DNAase I treatment and reverse transcription

RNA extraction from cell pellet was done following the TRI Reagent® recommended procedure. For that, extra material such as chloroform (Sigma-Aldrich®, C2432) and isopropanol (Sigma-Aldrich®, 650447) is needed. Finally, RNA precipitate was diluted in DEPC water (Ambion®, AM9920) and supplemented with 1% SUPERaseIn RNase inhibitor (Invitrogen™, AM2694). Extracted RNA was treated to degrade possible traces of DNA in the sample with DNase I (Invitrogen™, 18068016). To reverse transcribe, SuperScript® III First-Strand Synthesis System kit (Invitrogen™, 18080051) was used.

3.1.8. RT-PCR and Sanger Sequencing

cDNA was used as template for RT-PCR (reverse transcription polymerase chain reaction) using PKD1_EX26_SA_F PKD1_EX26_SA_R2 primers and Platinum Taq High Fidelity polymerase (PTHF). Amplicons of different sizes were obtained and run on a 2% agarose gel. The bands were extracted with GeneJET Gel extraction kit

(ThermoFisher™, K0691), and the DNA was purified (ThermoFisher™, K0691) for Sanger sequencing (ABI 3730XL, Applied Biosystems). Sanger sequences were aligned using the nucleotide BLAST tool available in the NCBI (National Center for Biotechnology Information) web page (https://blast.ncbi.nlm.nih.gov/Blast.cgi).

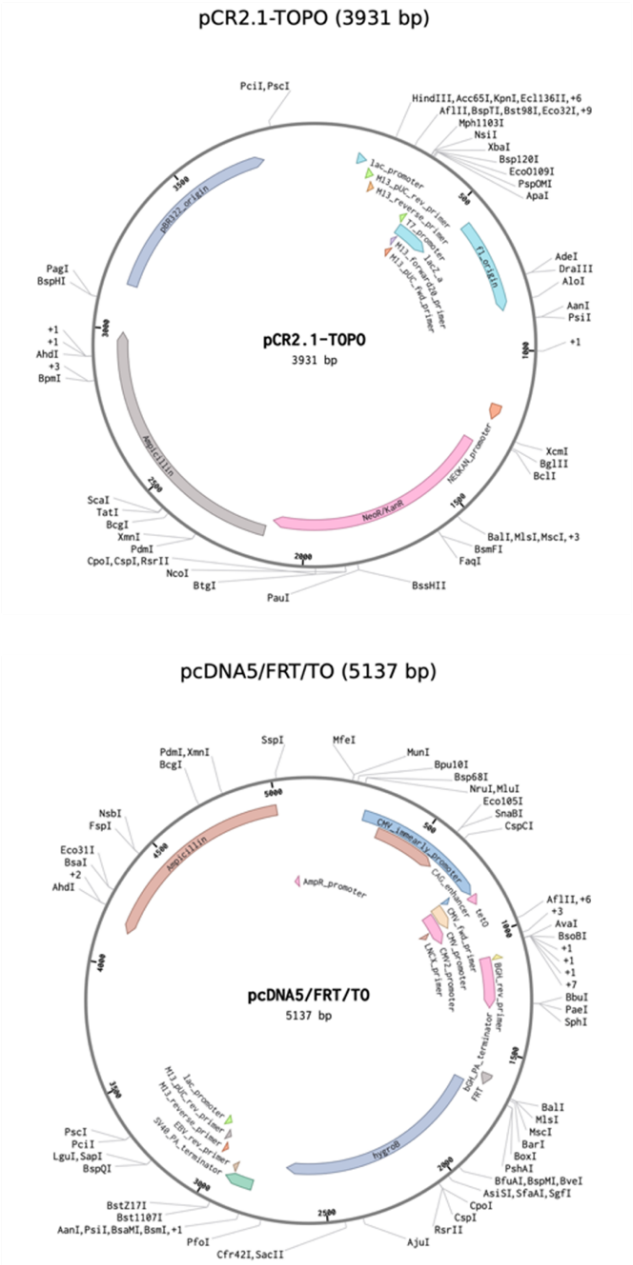

Figure 7. pCR2.1 TOPO and pcDNA5/FRT/TO plasmids structure. Plasmid sequences were downloaded from Addgene and analyzed with Benchling (https://www.benchling.com)

3.2. PROTEOMIC ANALYSIS AND CELLULAR CHARACTERIZATION TECHNIQUES

3.2.1. Cell culture

Murine inner medullary collecting duct (mIMCD3) cells were a gift from Prof. Dr. Michael Köttgen (University of Freiburg, Germany)(Hofherr et al., 2017). We were working with monoclonal cells, one WT clone and 3 *Pkd1* KO clones (derived from the WT after CRISPR-Cas9 editing). Cells were cultured in Dulbecco's Modified Eagle

Medium:Ham's F12 (Lonza™ BioWhittaker®, BE12-719F; Gibco™, 11330-032) supplemented with 10% (v/v) Fetal Bovine Serum (Corning ®, 35-079-CV) and 1% (v/v) Penicillin-Streptomycin (Gibco™, 11548876). For passages cells were wash with Phosphate Buffered Saline (PBS) (provided by the center) and detached with Trypsin-EDTA (Gibco™, 25200056). Seventy-hundred thousand cells were seeded per 100mm plate (Corning®) and grow for 10 days without any passage. Complete medium was change on days 3 and 6 and cells were starved on day 8. This cell culture procedure was utilized in subsequent experiments (Figure *8*)

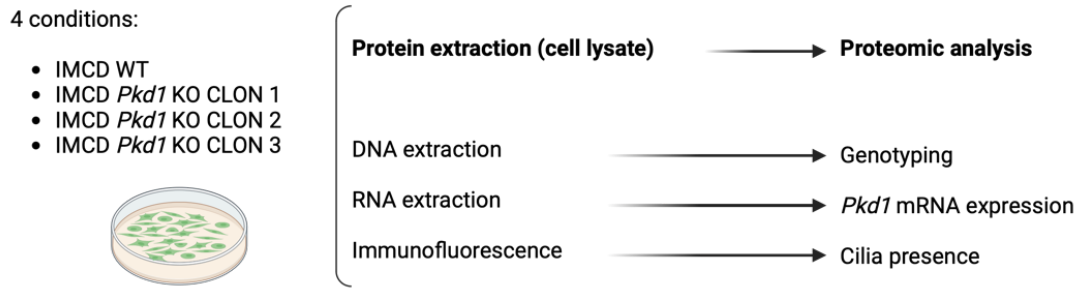

Figure 8. Overview of the procedures to be conducted on cell cultures. Image created with BioRender (https://www.biorender.com)

3.2.2. Proteomic analysis

3.2.2.1. Cell lysate and protein extraction

After removing growth medium from mIMCD3 cells, they were washed three times with ice cold PBS. Cells were scraped off the plates in ice cold PBS and transfer to a 15mL conical tube. They were pelleted at 200g for 5 minutes. Cell pellet was lysate using RIPA buffer (150mM NaCl; 10mM Tris-HCl pH7; 0,1% (v/v) SDS; 1% (v/v) Triton X100; 5mM EDTA pH8; 1% (m/v) sodium deoxycholate), supplemented with 1% (v/v) of protease inhibitor cocktail (Sigma-Aldrich®, P8340) and 1% (v/v) of phosphatase inhibitor cocktail (Sigma-Aldrich®, P0044) and incubated for 30 minutes on ice. Samples were centrifugated at 14000g for 15 minutes at 4ºC. Supernatant was transferred to a new tube and pellet was discarded (Figure *9*). Protein was quantified by a colorimetric assay similar to Lowry assay (DC™ Protein Assay Kit II, 5000112).

Secretomes were also collected; however, this thesis will not present any results related to them (Figure *9*).

3.2.2.2. Mass-spectrometry by LC-MSMS

The proteomic analysis was conducted in collaboration with the Proteomics Platform of the Health Research Institute of Santiago de Compostela, led by Dr. Susana Bravo. We provided 50 µg of total protein per sample, and they handled the subsequent processing, including analysis by liquid chromatography-mass spectrometry, as well as protein identification and quantification. For a more detailed protocol, please refer to (Cordido et al., 2022).

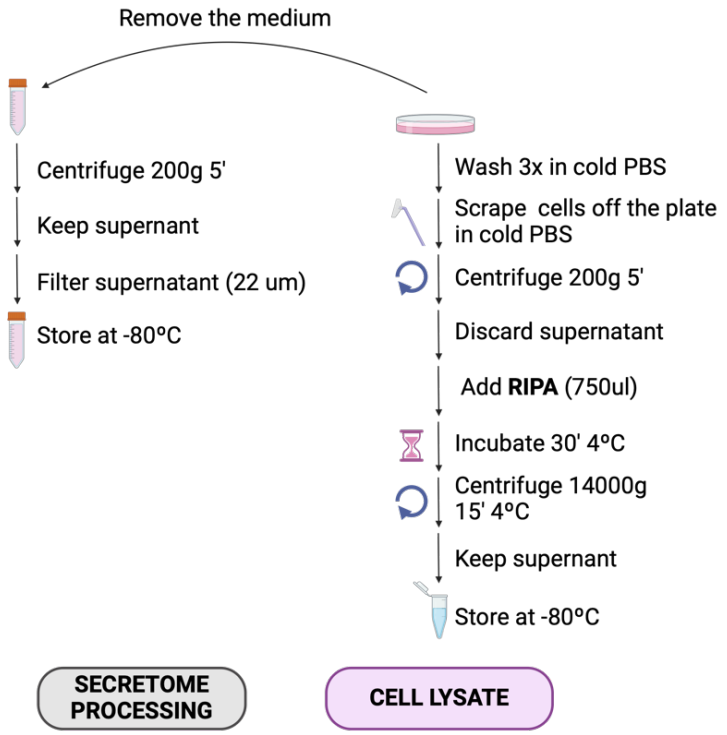

Figure 9. Protocol followed for cell lysate and secretome collection. Image created with BioRender

3.2.2.3. Results filtering

The reported results include both a qualitative analysis based on Data-Dependent Acquisition (DDA) and a quantitative analysis using Sequential Window Acquisition of All Theoretical Mass Spectra (SWATH). The DDA analysis provides a comprehensive list of all proteins identified in all samples under specific conditions. For our analysis, we only consider proteins with a Global False Discovery Rate (FDR) of less than 1%.

The quantitative SWATH analysis, on the other hand, includes a list of quantified proteins that are common across the analyzed conditions, along with their associated fold changes and p-values. For our analysis, we only considered proteins with a p-value of less than 0.05 and a fold change greater than 1.5. The comparison we have conducted was between two groups: the mIMCD3 *Pkd1* KO cell lysates (comprising data from the three *Pkd1* KO clones) and the mIMCD3 WT cell lysate.

3.2.2.4. Bioinformatics analysis tools

To analyze and organize the data, several bioinformatic tools were used. STRING is a tool for predicting and visualizing protein-protein interactions and enrichment analysis. For the enrichment analysis, we set the following "Enrichment display settings": Merge rows by term similarity 0,9; maximum FDR shown ≤0,05; minimum signal shown ≥1; minimum strength shown ≥ 0,01, minimum count on network 2. A heatmap is a visual way to find patterns among samples in large data sets. Using the areas under the curve (AUC) for each protein and for each sample a heatmap was created by using Heatmapper (http://www.heatmapper.ca/expression/). To analyze the overlap between datasets and determine the shared elements and their quantities, we created a Venn diagram with

Interactivenn (https://www.interactivenn.net). We generated the volcano plot using the statistical tool GraphPad Prism 10. The PCA (Principal component analysis) plot presented was derived from the proteomics reports.

3.2.3. DNA extraction and genotyping

DNA extraction from the cell pellet was performed following the recommended procedure for TRI Reagent®. Genotyping consists of a multiplex PCR capable of simultaneously amplifying the WT allele and the *Pkd1* KO alleles. The genotyping strategy can be found in the original paper (Hofherr et al., 2017). The primers required are mPkd1_1, mPkd1_2, and mPkd1_3 (Supplemental table *1*).

3.2.4. RNA extraction and *Pkd1* mRNA expression in mIMCD3 cells

RNA was extracted from the cell pellet following the recommended procedure for TRI Reagent® and reversotranscribed to cDNA as it was mentioned on section 3.1.7. Using the cDNA a RT-PCR was performed using the primers RT_mPkd1_1 y RTmPkd1_2 (Supplemental table *1*) (Hofherr et al., 2017).

3.2.5. Immunofluorescence of the cilia

Cells were cultured on a coverslip placed at the bottom of the wells in a 24-well plate. They were washed with PBS and fixed with 4% paraformaldehyde (Thermo Scientific™, 15424389) for 20 minutes. They were permeabilized with 0.25% Triton™ X-100 (Sigma-Aldrich®, X100-500mL) in PBS for 30 minutes. After washing with PBS, the cells were blocked with 2% BSA (bovine serum albumin) (NZYtech, MB04602) in PBS for 45 minutes. The primary antibody, mouse anti-acetylated α-tubulin (1:10000; Sigma-Aldrich®, T7451), was incubated at 4°C for 16 hours. The cells were washed three times with PBS for 10 minutes before adding the secondary antibody, Alexa Fluor® 488 anti-mouse (1:10000; Invitrogen™, A-11001), which was incubated for 1 hour at RT. The cells were washed three times with PBS for 10 minutes each and the nuclei were stained with DAPI (1:10000; Thermo Scientific™, 62248). Finally, the coverslips were affixed to slides using a fluorescence mounting medium (Dako, S3023). A Leica TCS-SP8 (Leica®) confocal microscopy was used to take the images.

3.2.6. Characterization of cellular and mitochondrial state in mIMCD3

3.2.6.1. Flow cytometry

mIMCD3 cells were washed twice with PBS solution, detached using trypsin (Gibco™, 25200056), and neutralized with complete medium. The cells were washed twice before adding the staining solution, which was diluted in Hanks' Balanced Salt Solution (Gibco™, 14025092). After the incubation period (Table *2*) the cells were centrifuged to remove the supernatant, washed with PBS, and centrifuged again to discard the supernatant. The cell pellet was then resuspended in PBS with 2% FBS. The CitoFlex flow cytometer (Beckman Coulter) was used, and the results were analyzed using the CytoExpert software.

3.2.6.2. Dyes

For flow cytometry and microscopy experiments, we utilized various dyes. Table 2 summarizes the different steps and the target organelles/molecules.

Table 2. Dyes used for flow cytometry and microscopy experiments

Stain	MitoTracker ®Green FM (Invitrogen™, M7514)	Image-iT™ TMRM reagent (Invitrogen™, I34361)	Propidium iodide (Invitrogen™, P1304MP)
Fixation	No	No	Cold methanol at 4C for 24h (add drop by drop)
Working concentration	50nM	50nM	2mg/mL RNAse (Invitrogen™) 1mg/mL Propidium iodide
Incubation	30 minutes in growth conditions	30 minutes in growth conditions	30 minutes in darkness RT
Target	Mitochondria	Active mitochondria= membrane potential	Nucleic acids

For TMRM staining, a control was performed using the membrane uncoupler FCCP (Carbonyl cyanide-p-trifluoromethoxyphenylhydrazone). FCCP (Sigma-Aldrich®, C2920) was added at a concentration of 20 µM prior to TMRM staining. The incubation period was 10 minutes.

3.2.6.3. Confocal microscopy

Cells were cultured for 10 days without passage (10,000 cells/well) in µ-Slide 8 Well high Glass (Ibidi®, 80807). They were washed three times with HSSB before adding MitoTracker Green FM (50 nM) and incubated under growth conditions for 30 minutes. The cells were then washed again before adding Hoechst (1:2000) for 5 minutes. Finally, the staining was washed with HSSB twice, and the cells were prepared for imaging using the confocal microscope Leica TCS SP5 X.

3.3. MITOPHAGY ASSAYS

3.3.1. Mitophagy proteins validation

3.3.1.1. Samples

For the mitophagy assays we used RNA and protein samples from mice and cells. The mouse line used was C57/BL6J *Pkd1*$^{flox/flox}$; TamCre. To induce Cre recombinase expression and inactivate the *Pkd1* gene, at postnatal days 10 and 11, the nursing mothers of the mice under study were injected intraperitoneally with tamoxifen (Sigma-Aldrich®, T5648) (10mg/40g) dissolved in corn oil (Sigma-Aldrich®, C8267). The mice were sacrificed at postnatal days 18 (p18) and 30 (p30). *Pkd1*$^{flox/flox}$;Tam-Cre- mice were considered as Wild Type (WT) and *Pkd1*$^{flox/flox}$;Tam-Cre+ as mutants (*Pkd1* KO). These mice were always handled by qualified personnel. All the experiments were done in a pathogen-free facility (CEBEGA, Centre for experimental biomedicine) following the protocols approved by the ethics committee of the University of Santiago de Compostela (code: #15010/2020/002). We cultured the mIMCD3 cells as it was described in section 3.2.1.

3.3.1.2. Gene expression of mitophagy proteins by qPCR

RNA samples from whole kidney and from cell lysates were treated and reversotranscribed to cDNA as mentioned in section 3.1.8. For quantitative Polymerase

Chain Reaction (qPCR), 14 total cDNA p30 whole kidney lysates samples were used, 7 from WT mice and 7 from *Pkd1* KO mice. Three technical replicates for each sample.

Gene expression was assessed by qPCR following manufacturer's protocol for FastStart Universal SYBR GREEN Master (ROX) (Roche®, 04913914001). PCR system QuantStudio3 (AppliedBiosystems) was employed to run the PCR and the Design and analysis software 2.7.0 (AppliedBiosystems) was the selected tool to visualize and analyse the data. Hypoxanthine Guanine Phosphoribosyltransferase (*Hprt*) gene was set as the endogenous control gene, necessary for normalization of the expression of each sample (Supplemental table *1*). The PCR program consisted of the following steps: 30s denaturation at 95ºC; 45 cycles of 30s denaturation at 95ºC, 1min hybridization at 60ºC and 30s elongation at 72ºC.

3.3.1.3. Mitophagy protein levels by Western Blot

3.3.1.3.1. Protein isolation, SDS-PAGE, Western Blot and ECL detection

Western Blot validation was done with both cell lysates and whole kidney lysates protein samples. The concentration of the protein samples was quantified using DC™ Protein Assay Kit II (Bio-rad, 5000112). To prepare samples for loading, 30ug total protein was mixed with XT sample buffer, 4X (Bio-Rad, 1610791) with 10% ß-mercaptoetanol (Sigma®, M6250). Denaturalization was done for 5 minutes at 95ºC.

Protein samples and standards (Bio-rad, 1610374) were separated by SDS-PAGE using hand casting 12% polyacrilamide gels (Bio-Rad). Proteins were Western-blotted wet on nitrocellulose membranes (Bio-Rad, 1620115). Membranes were blocked with SuperBlock™ blocking buffer (Thermo Scientific™, 37515) for 1 hour at room temperature (RT) and incubated with primary antibodies overnight at 4ºC. Next day, after washing three times with 0,3% Tween-20 (Sigma-Aldrich, P2287-500mL) in PBS membranes were incubated with horseradish peroxidase-labeled antibodies that were detected using SuperSignal™ West Pico PLUS chemiluminescent substrate kit (Thermo Scientific™, 34580). For developing, ChemiDoc™ Imaging System (Bio-Rad) was used. Images were analyzed and quantified using ImageJ® Lab software. Total protein was used as the loading control to normalize protein quantities. Total protein was stained just after transference with Ponceau Red (Thermo Scientific™, A40000279) and scanned with ChemiDoc™ Imaging System.

For NISP1, two protein samples (a WT and a *Pkd1* KO from mice) were run in a 2D-SDS-PAGE gel. A total of 20µg of protein were re-suspended in 250µL of DeStreak™ Buffer (Bio-Rad, 17-6003-19) with ampholytes (0.1% servalyte 3-10 and 2-4, 0.05% servalyte 9-11, SERVA), and subjected for solubilization during 1 hour at RT. The mixture was centrifuged at 18000g for 15 minutes and the pellet was discarded. For the first dimension, samples were load to each strip (Bio-Rad®) and subjected to active rehydration at 50V during 12h before IEF (Isoelectric focusing). IEF was performed in a Protean IEF Cell focusing unit (BioRad) until 20000 V/total h reached. After IEF, the IPG strips were equilibrated for 15 min in 4M urea, 2M thiourea, 50mM Tris pH 6.8, 2% SDS, 12mM DTT and 30% glycerol with 1% DTT and 15 min in 4M urea, 2M thiourea, 50mM Tris pH 6.8, 2% sodium dodecyl sulphate (SDS), 12mM dithiothreitol (DTT) and 30% glycerol with 4% iodoacetamide (all reagents from Sigma-Aldrich®). Second

dimension was performed in a handmade 10-12% SDS-PAGE and followed with Western Blot as previously described.

3.3.1.3.2. Antibodies

For Western Blotting we used the following primary antibodies: Anti-NISP1 (1:2000, Abcam, ab67302),), anti-Fis1(1:1000, Cell Signaling, 32525), anti-Prohibitin (1:10000, Proteintech, 10787-1-AP) and anti-LC3B (1:1000 Cell Signaling®, 2775). The secondary antibodies were Goat anti-rabbit IgG HRP (1:10000, Invitrogen ™, 31460) and Goat anti-mouse IgG-HRP (1:10000, Invitrogen™, 31430).

3.3.2. Mitophagy downregulation validation by other techniques

For evaluating mitophagy and autophagy we create cell lines expressing fluorescent markers of mitophagy and autophagy.

3.3.2.1. Plasmids

Table 3 lists the plasmids used: the plasmids of interest, the fluorescent control plasmids to test transfection efficiency, and the packaging plasmids for each type of transduction. All plasmids were prepared at 1µg/µl.

Table 3. List of plasmids used for transfection of HEK293T cells.

Plasmid		Transduction	Reference
pHAGE-mt-mKeima (Um et al., 2018)	Plasmid of interest (PI)	Lentiviral	Addgene#131626
pBABEpuro GFP-LC3	Plasmid of interest (PI)	Retroviral	Addgene#22405
pCL-Eco	Packaging plasmid (PP)	Retroviral	Addgene #12371
pLP1	Packaging plasmid (PP)	Lentiviral	ViraPowerTM Lentiviral Packaging Mix (Invitrogen)
pLP2	Packaging plasmid (PP)	Lentiviral	ViraPowerTM Lentiviral Packaging Mix (Invitrogen)
pLP-VSVG	Packaging plasmid (PP)	Lentiviral	ViraPowerTM Lentiviral Packaging Mix (Invitrogen)
FUGW	Fluorescent control (FC)	Lentiviral	Addgene #14883
pBABEpuro EGFP	Fluorescent control (FC)	Retroviral	Addgene #128041

3.3.2.2. Cell transfection

The day before transfection, HEK293T cells were seeded in order to get an 80-90% of confluency for transfection. HEK293T cells were transfected with polyethyleneimine (PEI) (Polysciences) at a ratio of 1:6 (DNA:PEI). The DNA plasmid of interest was mixed with retroviral or lentiviral packaging plasmids in a 1:1 ratio (PI:PP(s)). Plasmid mixture and PEI were diluted separately in DMEM-F12 unsupplemented medium. The contents of both tubes were combined, vortexed, and incubated for 10 minutes at RT. The mixture was then added to the plates. After 8-16 hours, the cells were washed with PBS and the medium was replaced with fresh medium.

In our case, we seeded the cells in 100 mm plates, using a total of 5 µg of DNA and 30 µg of PEI (1:6). Both quantities were diluted in 250 µL of unsupplemented

medium, which were then combined to obtain a total volume of 500 µL for transfecting the cells

3.3.2.3. Viral transduction

36 hours after transfection, the medium containing the viral particles was collected and filtered to avoid contamination with cell debris using 20 mL syringes (BD®) and 0.45 µm filters (Jet Biofil). Polybrene (Sigma-Aldrich®, TR-1003) was added to the filtered medium at a concentration of 8 µg/mL. This medium was then used to infect mIMCD3 cells, which had been seeded at a subconfluent level the previous day. Fresh medium was added to the HEK293T cells to maintain viral production. This process was repeated three times in 12–16-hour cycles. After completing the three rounds of infection, the medium of the mIMCD3 cells was changed for fresh medium. Following a 12-hour rest period, the transduction was completed, and the cells were passaged to continue growing. Cells retrovirally transduced with pBABEpuro GFP-LC3 were selected with 1 µg/mL of puromycin for seven days. The puromycin dose was determined based on an MTT viability assay. The cells were analyzed by flow cytometry.

To perform the viability assay, mIMCD3 cells were seeded in 96-well plates. When they reached near confluency, different doses of puromycin (0.5 µg/mL, 1 µg/mL, 2 µg/mL, 3 µg/mL, 4 µg/mL) were added. Viability was measured at 24 hours, 3 days, 5 days, and 7 days. The procedure involved adding 10 µL of MTT (5 mg/mL in PBS) to each well and incubating for 4 hours at 37°C. Subsequently, 100 µL of 10% SDS (in 0.01 M HCl) were added per well and incubated for 14 hours at 37°C. Absorbance was measured using an Infinite M100 Pro plate reader (TECAN) at 590 nm. Data analysis was performed using GraphPad Prism 10. The depicted kill curve will help to select the minimum puromycin concentration at which all non-resistant cells die.

3.3.2.4. Flow cytometry

mIMCD3 cells were washed twice with PBS solution, detached using trypsin (Gibco™, 25200056), and neutralized with complete medium. The cells were washed twice in Hanks' Balanced Salt Solution (Gibco™, 14025092), resuspended in HBSS with 2% FBS. The CitoFlex flow cytometer (Beckman Coulter) was used, and the results were analyzed using the CytoExpert software.

3.3.3. Statistical analysis

Statistical analysis of the data was conducted using GraphPad Prism 10. The normality of the data was first assessed using the Shapiro-Wilk test. If the data were normally distributed, differences between two groups were compared using a two-tailed unpaired t-test. In the absence of normality, the non-parametric Mann-Whitney test was employed. P-values less than 0.05 were considered statistically significant.

4 RESULTS

4.1. FUNCTIONAL VALIDATION OF VARIANTS OF UNCERTAIN SIGNIFICANCE (VUS) IN *PKD1*

4.1.1. Variants of Uncertain Significance in *PKD1* gene: A case study

The NefroCHUS cohort is composed exclusively of patients with suspected genetic kidney diseases. Over the past 20 years, the cohort has grown steadily, primarily due to genetic diagnosis requests from hospitals in Galicia, and to a lesser extent, from other hospitals across Spain. This cohort includes numerous patients who have undergone various diagnostic tests over the years. It must be assumed that certain diagnoses, particularly older negative or inconclusive ones, could be solved today if re-analyzed with current knowledge or re-sequenced using modern technologies.

In the following lines, we will present one of these cases that was previously classified as inconclusive, and we selected for re-evaluation. This case involves two families from the cohort that share two variants in the *PKD1* gene (Table 4), both classified as variants of uncertain significance (VUS)(Table *5*). They co-segregate with the disease in both families (Figure 10) and are therefore inherited together, from which we deduce that they are located on the same allele, in *cis* position. After ruling out the presence of duplications and insertions in *PKD1* and *PKD2* by performing MLPA analysis and testing other known cystic genes by a tNGS panel, those variants were the only candidates to explain the disease. The segregation study could not rule out either of the variants as causal, but neither could it indicate which of the two could be the causal. Given the situation, we proposed several hypotheses to genetically explain the case. The first hypothesis is that one of the variants is causal, while the other is simply co-inherited. The second hypothesis suggests a possible dose effect in *cis*, where each variant alone is harmless (in terms of phenotypic effects), but together on the same allele, they may have an additive effect that does not exceed the threshold of protein functionality, causing the pathology. The third hypothesis posits that there is a causal mutation we have not yet detected, which is inherited in linkage disequilibrium with the two variants. We could propose a fourth hypothesis to encompass all possibilities: a mutation in a cystic gene other than *PKD1* or *PKD2*. However, we consider this to be the least likely scenario given the clinical presentation, as both families were clinically classified as typical ADPKD from the very beginning.

Table 4. Variants of uncertain significance in the *PKD1* gene found in the families under study.
Variant data according to the reference genome HG19 (GRCh37).

Gene	AAChange.RefSeq	Annotation.RefSeq
PKD1	NM_001009944.3: c.9202G>C, p. Glu3068Gln; NM_000296.4: c.9202G>C, p. Glu3068Gln	Missense variant: splice region variant
PKD1	NM_001009944.3: c.4103C>T, p. Ala1368Val; NM_000296.4: c.4103C>T, p. Ala1368Val	Missense variant

Table 5. Classification of the variants according to different variant classification tools. ACMG codes and their meaning: PP3: Computational evidence supports a deleterious effect on the gene or gene product. PM2: The variant is absent from controls (or at extremely low frequency if recessive) in population databases. PM1: Located in a mutational hot spot and/or critical and well-established functional domain without benign variation. BP1: Missense variant in a gene for which primarily truncating variants are known to cause disease.

AA Change	VarSome ACMG	InterVar ACMG	Franklin ACMG	PKD Database
Glu3068Gln (E3068Q)	VUS (PP3_ Strong PM2_Supporting)	VUS (PM2 ,PP3 ,BP1)	VUS (PM2_Moderate PP3_Supporting)	Likely benign
Ala1368Val (A1368V)	VUS (PP3_Moderate PM1_Supporting PM2_Supporting)	VUS (PM1, PM2, BP1)	VUS (PM2_Moderate)	VUS

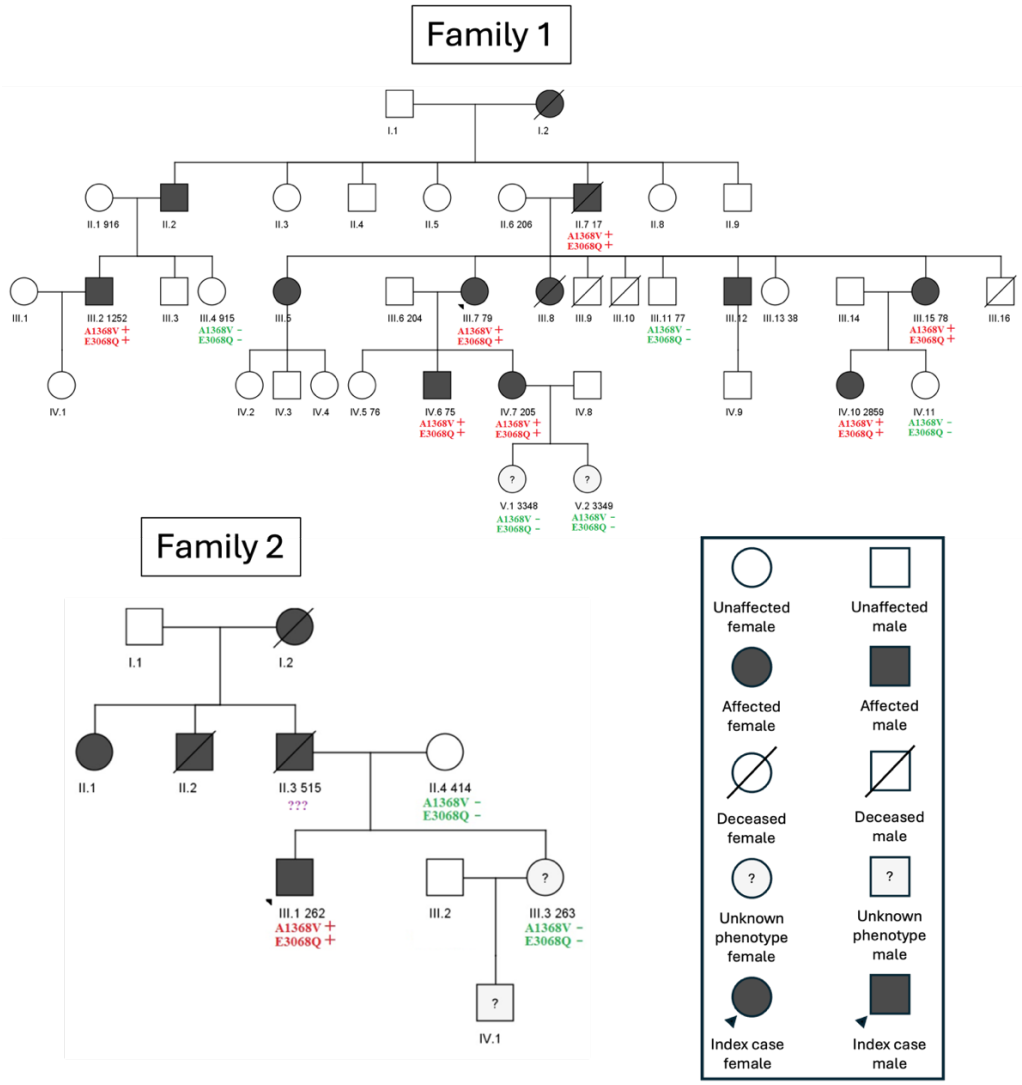

Figure 10. Family trees of the two families under study. It includes the genetic results of the individuals studied. For Family 1, we have clinical information spanning 5 generations, and for Family 2, we have clinical information spanning 4 generations. In both families the E3068Q and A1368V segregate, which means that all affected individuals are positive for the variants while unaffected are negative for them. This figure was created by the author.

As one of the studied variants, E3068Q, was located in the first nucleotide of exon 26 we decided to check the splicing effect of this variant through a minigene assay. Splicing is the process by which non-coding regions (introns) are removed from a newly synthesized precursor messenger RNA (pre-mRNA), and the coding regions (exons) are joined together to form a mature mRNA molecule. Splicing is essential for the correct translation of genetic information into proteins. It increases the diversity of proteins that can be produced by a single gene and plays a significant role in gene regulation. Splicing primarily acts on mRNA to produce mature mRNA molecules, but it can also process other types of RNA, such as rRNA and tRNA, to generate various mature RNA molecules essential for cellular functions.

Our methodological approach involves consulting the variant in an in silico splicing predictor before proceeding with the design of the minigene splicing assay.

4.1.2. *In silico* prediction of splicing variants

In order to understand the information provided by splicing predictors and to design a minigene assay, it is first necessary to understand some basic concepts related to the splicing process.

The spliceosome is the molecular complex responsible for executing splicing. Its initial task is to recognize specific splice sites, which are sequences in the precursor RNA (pre-mRNA) that delineate the limits between exons and introns There are two main types of splice sites: 1) The splice **donor site** is a highly conserved sequence located at the beginning (5' end) of an intron, while 2) the **splice acceptor** site is another conserved sequence found at the end (3' end) of an intron. If a variant alters an existing splice site or creates a novel splice site, it will lead to aberrant splicing. Therefore, there are four possible splice site alterations: **donor loss** (DL), **acceptor loss** (AL), **donor gain** (DG) and **acceptor gain** (AG). Donor and acceptor loss can lead to exon skipping or intron retention and, donor and acceptor gain can create an anomalous mRNA sequence. An aberrant mRNA can have several fates. If quality control mechanisms detect it, the mRNA will be removed by nonsense-mediated decay (NMD), preventing the translation of the protein. However, if these mechanisms fail to detect it, a truncated but potentially functional protein may be produced. So, at a protein level, splicing errors can result in a reduced dosage of the protein or the production of an aberrant protein, which may retain some functionality or have deleterious effect.

In ADPKD, splicing errors are a known mechanism of pathogenicity (Claverie-Martin et al., 2015).The variant, E3068Q, was searched in various web tools specifically designed to predict *in silico* splicing events: SpliceAI, SPIDEX, CADD and NNSplice (Table *6*).

- **SpliceAI** is an open-source deep learning algorithm designed to predict splicing alterations caused by genetic variants. It is accessible through the Broad Institute's web service (https://spliceailookup.broadinstitute.org/) (Jaganathan et al., 2019). SpliceAI delta scores (DS) range from 0 to 1, indicating the probability that a variant will affect splicing. Higher scores suggest a greater likelihood of splicing alteration. It is recommended a threshold value of 0.2 for the DS to differentiate potential splice-altering variants from non-altering ones (de Sainte Agathe et al., 2023). E3068Q shows a DS of 0.2 or higher for three of the splicing alterations, with an

acceptor gain being the most likely outcome. SpliceAI rules out the possibility of a donor gain resulting from the variant (Table *6*).

- **SPIDEX** (SPlicing InDEpendent EXpression) is a computational tool that uses the Percentage of Spliced-In (PSI) metric to assess whether a specific splicing isoform is more prevalent in the presence or absence of a particular variant. Typically, a dPSI score below -5 or above 5 is used as a threshold to indicate a significant impact on splicing, which could be deleterious (Xiong et al., 2015). Our queried variant has a dPSI score of -0.63 (Table *6*). This score alone may not be sufficient to classify the variant as deleterious without additional context or supporting evidence.
- **The Combined Annotation Dependent Depletion (CADD)** tool evaluates the predicted deleteriousness of single nucleotide variants and insertion/deletion variants in the human genome. It integrates multiple annotations, including conservation metrics, functional genomic data, transcript information, and protein-level scores, into a single metric (Rentzsch et al., 2019). CADD version 1.6, also known as Splice-CADD, incorporates specialized splicing prediction scores from SpliceAI and MMSplice, enhancing the prediction of splicing effects (Rentzsch et al., 2021). Consequently, a high CADD score may also indicate a significant impact on RNA splicing. PHRED scores, which range from 1 to 99, measure the likelihood that a variant is deleterious, with higher scores indicating a greater likelihood. A PHRED score of 30 indicates that the variant is highly likely deleterious. E3068Q has a PHRED score of 25 that suggests that the variant could be deleterious, but with moderate certainty (Table *6*).
- **NNSplice (Neural Network Splice).** It is an online tool, available at https://www.fruitfly.org/seq_tools/splice.html, that predicts splicing sites in human genes and *Drosophila melanogaster*. Users need to input a DNA sequence, set the search parameters, and the program will predict the acceptor and donor sites. By inputting the reference sequence and the variant sequence, we found that in the reference sequence NNSplice correctly identifies both the acceptor and donor sites, whereas in the mutated sequence it fails to identify the acceptor site (Table *6*). The inability to identify the acceptor site could indicate a loss of the acceptor site, although the program does not operate in these terms.

Table 6. Predictions made by *in silico* splicing predictors on the E3068Q variant.

Predictor	Score	Interpretation
Splice AI	Acceptor loss Δscore 0.27	ΔScore ranges from 0 to 1 and can be interpreted as the probability of the variant being splice-altering
	Donor loss Δscore 0.20	
	Acceptor gain Δscore 0.49	
	Donor gain Δscore 0.00	
Spidex	dPSI -0.63	dPSI > | 5 | suggests an impact on RNA splicing
CADD GRCh37-v1.6	PHRED 25.3	PHRED>30 "highly likely deleterious; PHRED 20-30 "likely deleterious"
NNSplice	Donor site prediction for E3068: score 0.82 Acceptor site prediction for E3068: score 0.84 Donor site prediction for E3068Q: score 0.82 Acceptor site prediction for E3068Q: score none	Score: probability of being the donor or acceptor site

All these predictive data together suggest that the effect on splicing might be real, although the results do not confirm it conclusively.

4.1.3. Minigene splicing assay

A minigene splicing assay is a functional validation experiment able to reproduce the splicing pattern of the mRNA in vitro. It is called a minigene because we introduce into a vector part of the sequence of the gene under investigation, a sequence that is susceptible to being affected by the defective splicing process.

The entire workflow has 3 main steps (Figure *11*):

1. **Minigene construction**. The *PKD1* minigene (from exon 25 to exon 29) sequence was obtained by PCR from patients' genomic DNA using a high-fidelity Taq polymerase enzyme. One sample from each studied family was used. Initially, we attempted to amplify the minigenes by PCR with specialized primers that had end sequences complementary to those created by the restriction enzymes in the expression vector. However, the DNA yielded was low after the PCR purification process. Thus, the sequence was cloned into the pCR 2.1-TOPO vector to amplify it in competent cells and obtain a large quantity of DNA. The minigene was cut from pCR.21-TOPO and ligated into the expression vector pcDNA5/FRT/TO.
2. **Minigene expression**. Once we had the expression plasmids ready (four plasmids per sample, two with the reference variant and two with the mutant (Figure *12*)), we transfected HEK 293 cells with these plasmids and induced CMV promoter-mediated expression with tetracycline.
3. **RNA collection and splicing pattern analysis**. Cells were lysed and total RNA was extracted from the lysate, treated with DNAase and reverse transcribed to cDNA. RNA is labile and can be easily degraded whereas cDNA is more stable and can better withstand working with it. We then used different pairs of primers to amplify the cDNA sequence (RT-PCR). Amplified DNA fragments (transcribed transcripts) were run on agarose gels, and the resulting bands were purified for sequencing.

Figure 13a shows the DNA bands amplified by RT-PCR. We observed that the expression of E3068 cDNA produced both the canonical transcript (388 bp band) and an alternative transcript with intron retention (513 bp band). However, for E3068Q, **the canonical transcript was absent**, and only the alternative splicing band was present. We do not know the exact nature of the splicing error that occurred. There are several plausible options, such as an acceptor gain, a donor loss, or an acceptor loss that was detected and eliminated by the cell's repair mechanism. Alternatively, it could be that the product of the splicing error is indistinguishable from the product of the alternative splicing, the 513 bp band. In any case, the absence of the canonical transcript can assert that this variant influences the splicing process and, subsequently, the synthesized protein. Both bands were excised from the agarose gel and sequenced (Figure 13b and Supplemental figure 2). Sequencing confirmed that the bands correspond to what we inferred based on their base pair length. Varsome and Franklin, two variant interpretation tools, change their criteria to "**pathogenic**" once we add the functional in vitro information. Following the recommendations of Walker et al. and their decision tree, we assign a PVS1 code keeping the strength level. The PVS1 is applied to variants that are

predicted to cause a loss of function (LoF) in a gene where LoF is a known mechanism of disease. Walker et al. recommend to use it in splicing cases when we have "splicing assay data-assays demonstrating that a variant leads to aberrant splicing profile that can be categorized against a PVS1 decision tree".

We determined E3068Q as a pathogenic variant that affects the splicing process and causes ADPKD. It is therefore the cause of the disease in the two families presented. The A1368V variant remains classified as a VUS, and we cannot rule out that it may have some additive negative effect on the protein functionality.

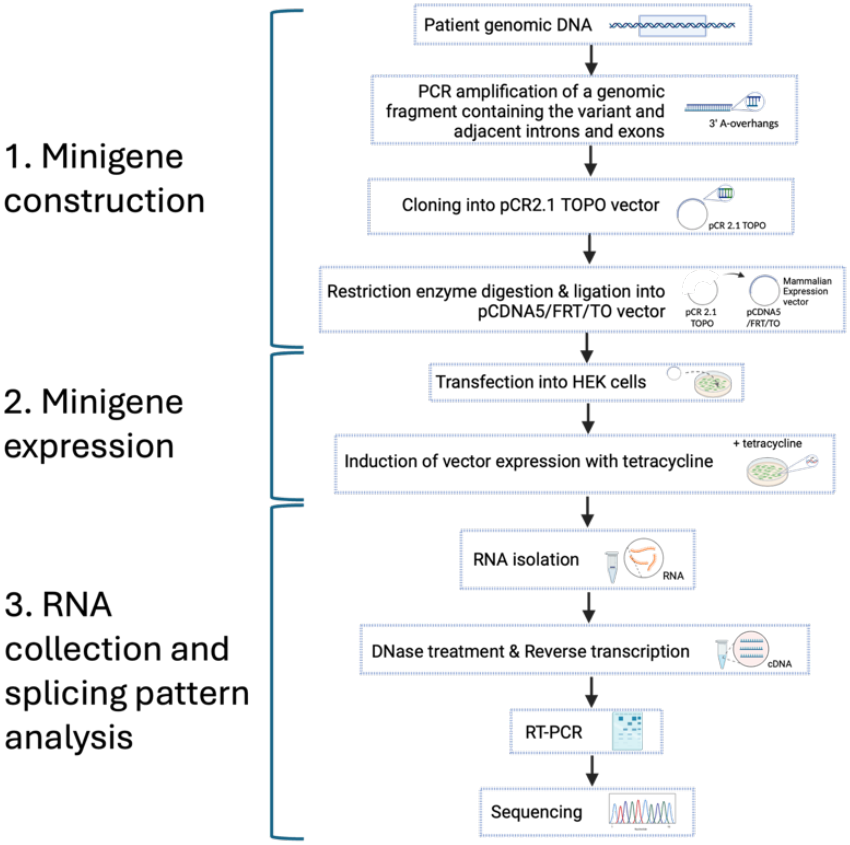

Figure 11. Workflow of the splicing minigene assay. The entire process comprises three main steps: (1) Minigene construction, where patient genomic DNA is amplified by PCR and inserted into an expression vector (minigene). (2) Minigene expression, where the expression of the minigene is induced after transfecting a cell line, in order to (3) collect the RNA and analyze the splicing pattern by RT-PCR and Sanger sequencing. Image created with BioRender by the author.

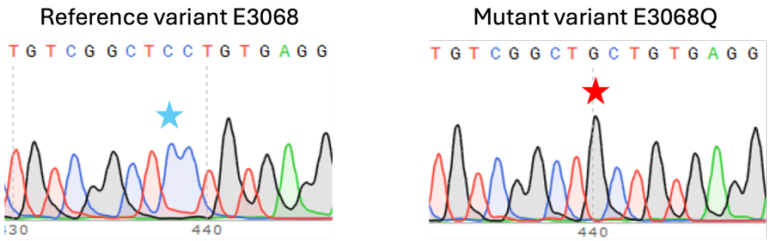

Figure 12. Electropherogram illustrating both the reference variant (E3068) and, the mutant (E3068Q) as identified through Sanger sequencing.

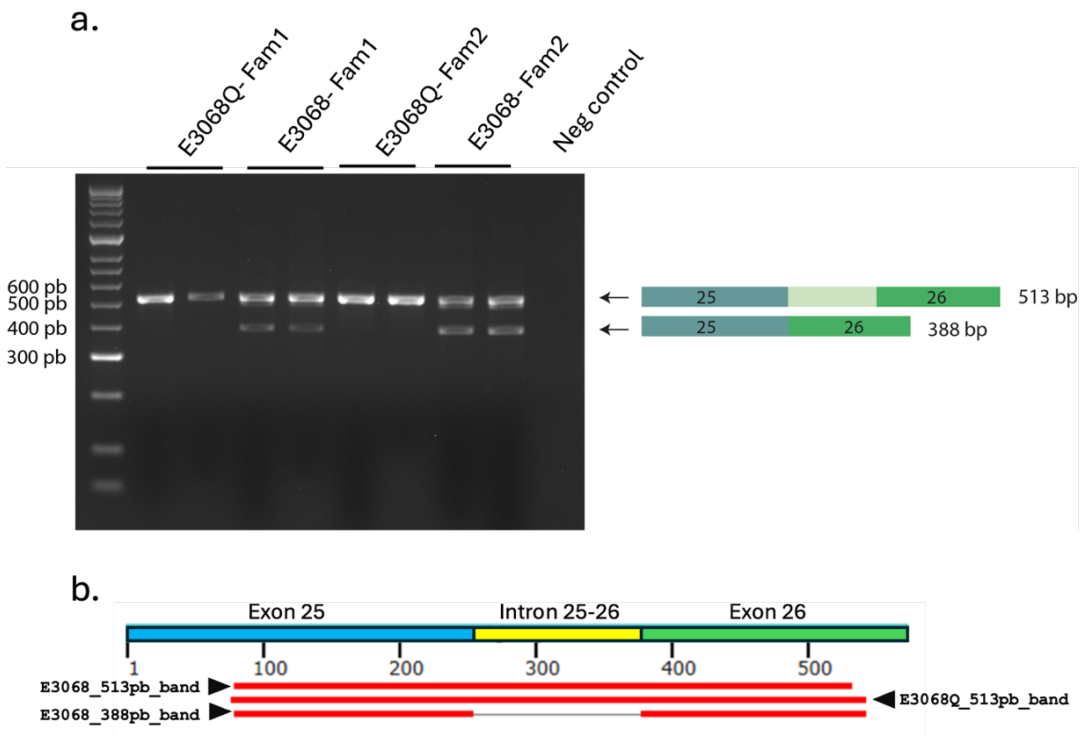

Figure 13. Agarose gel displaying the bands amplified by the same PCR performed on samples containing either the mutant (E3068Q) or reference variant (E3068). a. When the reference variant is present, two bands are amplified; however, only one band is amplified in the case of the mutant variant.**b.**Alignment of the Sanger sequences from the bands confirms that the absent sequence corresponds to the canonical transcript. This figure was created by the author.

4.2. PROTEOMIC ANALYSIS OF MONOCLONAL WT AND *PKD1* MUTANT MIMCD3 CELLS

4.2.1. Characterization of the mIMCD3 monoclonal cell line

mIMCD3 cells are a type of epithelial cells derived from the inner medullary collecting duct of the kidney of an adult mouse. It is one of the most widely used *in vitro* models to study kidney function and kidney diseases. The use of mIMCD-3 cells offers several advantages for the study of ADPKD: (1) These cells are epithelial, which is significant because the cysts in ADPKD are also formed by epithelial cells;(2) mIMCD3 cells can develop cilia, making them useful for studying ADPKD; (3) mIMCD3 cells express the *Pkd1* and *Pkd2* genes, which are implicated in ADPKD and (4) these cells are relatively easy to work with, as they grow well under standard culture conditions without requiring special treatments. Of course, they also present some disadvantages as they are a simplified model that cannot capture the intricate complexity of the entire nephron. Additionally, being a non-human model can lead to genotypic and phenotypic differences, and there is also heterogeneity within the culture itself. To address the aforementioned issue, in this thesis we have utilized monoclonal cells. The mutant clones were derived from a male monoclonal culture to ensure a consistent genetic background, thereby making the results more robust and eliminating the possibility that variations in the outcomes are due to cellular heterogeneity (Hofherr et al., 2017; Westermann et al., 2022). In all experiments presented in this thesis, mIMCD3 cells were cultured for 10 days without passaging. The cells reached confluence from the fourth day of culture onwards. During the last two days, cells were washed with PBS and deprived of serum to remove serum proteins that could alter proteomics results, synchronize cells in G_0-G_1 phase by arresting division, stimulate differentiation and promote primary cilium formation.

We have characterized the cell line to demonstrate some of the mIMCD3 key characteristics to study ADPKD. Firstly, we corroborated that *Pkd1* expression is present exclusively in the WT cells, while it is absent in the *Pkd1* KO cell clones (Figure *14*a). We also observed that the cells, after being cultured according to the described protocol, were able to develop the primary cilium, as shown in Figure *14*c. Cells were routinely genotyped. Figure *14*b presents the correct genotyping results of the biological replicates that were sent to the proteomics service. The genotyping strategy can be consulted in Hofherr et al., 2017. In Figure *14*d the appearance of the cells on day 10 is shown, and the cultures of WT and *Pkd1* KO cells are clearly distinguishable. When stained with crystal violet, the WT cells accumulate more stain, indicating that there are more cells in the WT plate than in the mutant plate under the same conditions. The WT culture appears capable of adapting its cell shape during growth. In contrast, *Pkd1* KO cell cultures are unable to do this, predominantly growing flat in a monolayer (Figure *14*d). It appears that WT cells require less contact with the plate surface compared to *Pkd1* KO cells, thus allowing more WT cells to fit on the same surface area than mutant cells.

4.2.2. General description of the proteomic results

Our objective was to conduct a comprehensive proteomic analysis of a monoclonal cell line whose findings could provide valuable insights into the underlying molecular mechanisms of ADPKD.

We analyzed protein samples collected from monoclonal WT mIMCD3 cells and 3 different clones of *Pkd1 KO* mIMCD3 cells. Biological triplicates were used.

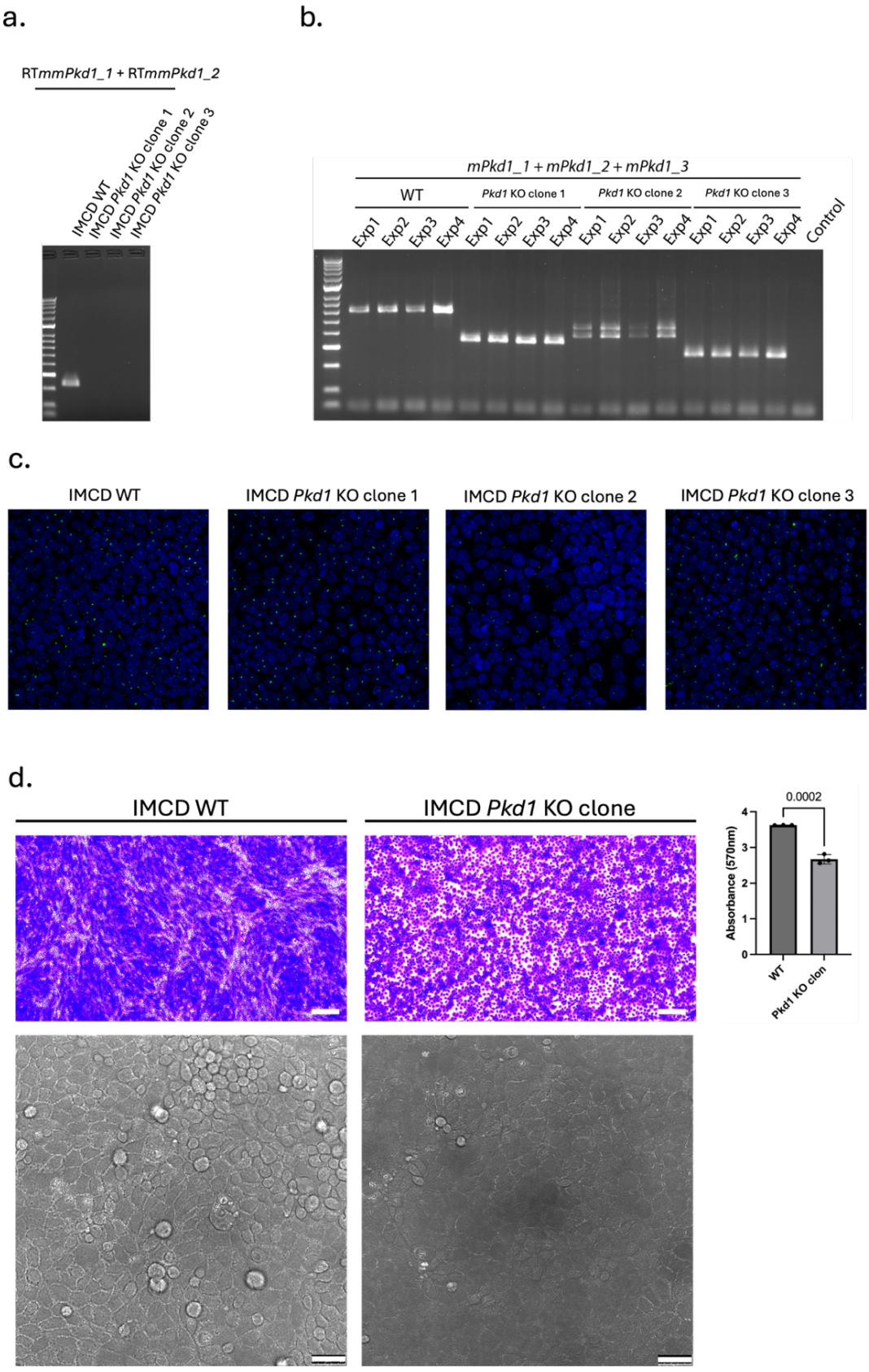

Figure 14. Characterization of the mIMCD3 cell line. a. No *Pkd1* gene expression is detected in the mutant clones.**b.** Genotyping results of the biological replicates that were sent to the proteomics service. ***c.*** Immunofluorescence of the cilia***. d.*** Images of the cultures stained with crystal violet (above), and brightfield images of the cultures at day 10 (below). Scale bar: 100μm (above); 25μm (below)

Samples from the KO group and the WT group clustered so well in the Principal Component Analysis (PCA) (Figure *15*a). The SWATH analysis identified a total of 334 differentially expressed proteins (Supplemental table *2*) after applying filters (p-value < 0.05 and fold-change > 1.5). Among these, 165 proteins were upregulated in the KO condition, 118 were downregulated, and 51 proteins were exclusively present in the KO condition. (Figure *15*b). These proteins were representative of the entire cell. The digestion process has been successful, as we have identified proteins from the mitochondrial matrix, an intracellular compartment protected by two membranes.

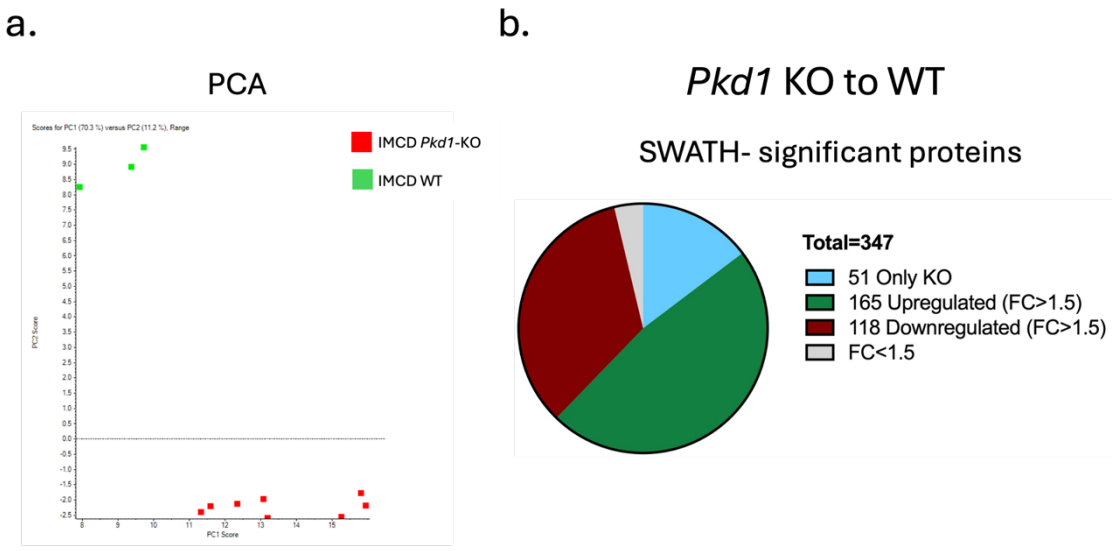

Figure 15. Clustering of the analyzed samples and classification of proteins detected by SWATH based on their abundance in *Pkd1* KO compared to WT mIMCD3 cells.a. Unsupervised PCA where the samples from the WT group (in green) differ from the samples from the mutant group (in red)**. b.** Classificatory pie chart of significant proteins from the SWATH analysis according to their abundance in the mutant group compared to the WT group.

The DDA analysis detected a total of 765 proteins in the cell lysate. In Figure *16*a, a Venn diagram show the overlap between proteins detected by DDA and SWATH, 291 proteins were shared between the two techniques.

The volcano plot represents the differentially expressed proteins (DEPs). In both upregulated and downregulated, some proteins show high statistical significance. In the case of upregulated proteins, some proteins with a high fold-change stand out, they are much more expressed in mutant than in WT group (Figure *16*b). The volcano plot does not contain information about proteins for which we only have data in the KO group, as we cannot calculate a fold-change (Figure *15*b). Top ten most dysregulated proteins of each group (only detected in KO, upregulated and downregulated in KO) are collected in Table *7*, 8, and 9.

The heatmap enables the comparison of protein expression levels for each individual sample. The WT and *Pkd1* mutant samples cluster correctly into their respective groups. Visually, it is evident that the WT samples exhibit less variability in expression among samples compared to the mutants (Figure *16*c).

4.2.2.1. Enrichment analysis

An enrichment analysis was conducted using the online tool STRING. STRING performs enrichment analysis considering various concepts or groups (e.g., cell biology, compartments). Here, we present three different enrichment analyses applied to three different datasets: all dysregulated proteins, upregulated proteins, and downregulated proteins. The parameter we focus on is the signal, which takes into account both the False Discovery Rate (FDR) and the observed/expected ratio. The signal parameter aims to balance both metrics. We have grouped the terms by similarity to reduce the redundancy of terms and provide a clearer mental picture of the situation.

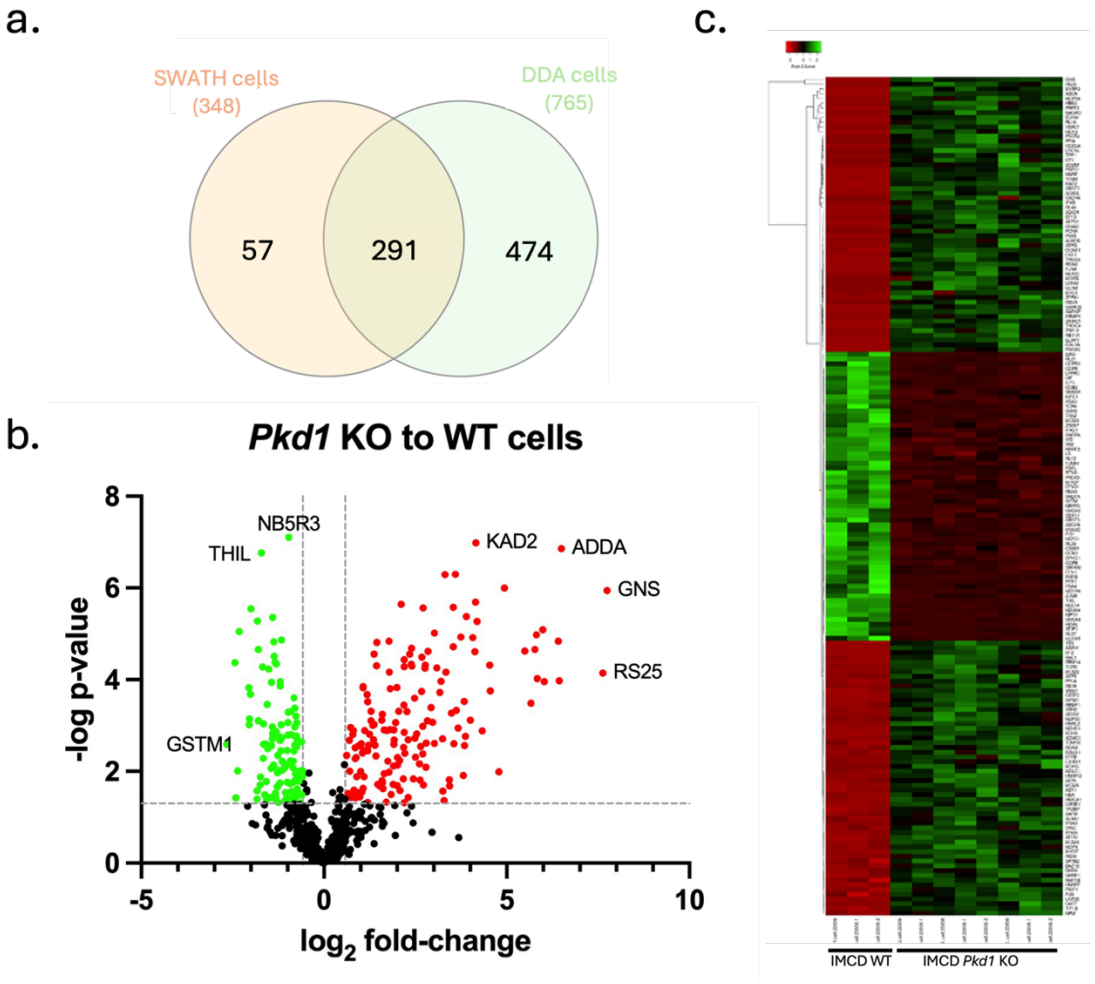

Figure 16. General characterization of the LC-MS/MS results a. Venn diagram illustrating the significant shared proteins between those detected in the SWATH analysis and the DDA analysis. **b.** Volcano plot representing all the proteins found in the SWATH analysis. Black dots represent non-significant proteins (p-value > 0.05). Red dots represent significantly upregulated proteins (FC > 1.5, p-value < 0.05). Green dots represent significantly downregulated proteins. **c.** Heatmap illustrating the differential expression levels of proteins (FC>1,5) across the samples. The color gradient represents the range of expression levels, with red indicating higher expression and green indicating lower expression.

Table 7. Top ten proteins only identified in the *Pkd1* KO group

Uniprot code	Uniprot name	Group	p-value	FC WT to Mut	1/FC	Abundance
O55022	PGRC1_MOUSE	Membrane-associated progesterone receptor component 1	4,55E-08	N/A	N/A	Only KO
Q8CCH2	NHLC3_MOUSE	NHL repeat-containing protein 3	1,37E-06	N/A	N/A	Only KO
Q99KP6	PRP19_MOUSE	Pre-mRNA-processing factor 19	9,51E-06	N/A	N/A	Only KO
Q8VDP4	CCAR2_MOUSE	Cell cycle and apoptosis regulator protein 2	2,94E-05	N/A	N/A	Only KO
Q61033	LAP2A_MOUSE	Lamina-associated polypeptide 2, isoforms alpha/zeta	3,14E-05	N/A	N/A	Only KO
Q60931	VDAC3_MOUSE	Voltage-dependent anion-selective channel protein 3	5,00E-05	N/A	N/A	Only KO
Q9CQA3	SDHB_MOUSE	Succinate dehydrogenase [ubiquinone] iron-sulfur subunit, mitochondrial	5,82E-05	N/A	N/A	Only KO
Q571E4	GALNS_MOUSE	N-acetylgalactosamine-6-sulfatase	7,06E-05	N/A	N/A	Only KO
P60122	RUVB1_MOUSE	RuvB-like 1	0,00012519	N/A	N/A	Only KO
Q99JY0	ECHB_MOUSE	Trifunctional enzyme subunit beta, mitochondrial	0,00014519	N/A	N/A	Only KO

Table 8. Top ten upregulated proteins (*Pkd1* KO to WT group)

Uniprot code	Uniprot name	Group	p-value	FC WT to Mut	1/FC	Abundance
Q8BFR4	GNS_MOUSE	N-acetylglucosamine-6-sulfatase	1,13E-06	0,004663939	214,411	Upreg
P62852	RS25_MOUSE	40S ribosomal protein S25	7,16E-05	0,005048796	198,067	Upreg
Q9QYC0	ADDA_MOUSE	Alpha-adducin	1,39E-07	0,011062375	90,396	Upreg
Q9D6Z1	NOP56_MOUSE	Nucleolar protein 56	0,0001053	0,011557849	86,521	Upreg
Q8C854	MYEF2_MOUSE	Myelin expression factor 2	1,45E-05	0,011751527	85,095	Upreg
Q9QWR8	NAGAB_MOUSE	Alpha-N-acetylgalactosaminidase	0,00010982	0,015272976	65,475	Upreg
Q922U1	PRPF3_MOUSE	U4/U6 small nuclear ribonucleoprotein Prp3	8,11E-06	0,015765106	63,431	Upreg
P02089	HBB2_MOUSE	Hemoglobin subunit beta-2	9,52E-05	0,017537813	57,019	Upreg
P20060	HEXB_MOUSE	Beta-hexosaminidase subunit beta	1,06E-05	0,017774534	56,260	Upreg
Q8BH95	ECHM_MOUSE	Enoyl-CoA hydratase, mitochondrial	2,21E-05	0,018332827	54,546	Upreg

Table 9. Top ten downregulated proteins (*Pkd1* KO to WT group)

Uniprot code	Uniprot name	Group	p-value	FC WT to Mut	1/FC	Abundance
P47758	SRPRB_MOUSE	Signal recognition particle receptor subunit beta	0,03996826	3,561178597	0,280	Downreg
O55125	NIPS1_MOUSE	Protein NipSnap homolog 1	2,88E-06	3,999596813	0,250	Downreg
Q3TKT4	SMCA4_MOUSE	Transcription activator BRG1	0,00020748	4,043668971	0,247	Downreg
P10518	HEM2_MOUSE	Delta-aminolevulinic acid dehydratase	0,0007225	4,110385197	0,243	Downreg
O55029	COPB2_MOUSE	Coatomer subunit beta'	0,00096738	4,125774048	0,242	Downreg
Q60864	STIP1_MOUSE	Stress-induced-phosphoprotein 1	0,0001503	4,153526837	0,240	Downreg
O09167	RL21_MOUSE	60S ribosomal protein L21	8,91E-06	5,005130493	0,199	Downreg
Q6A068	CDC5L_MOUSE	Cell division cycle 5-like protein	0,00975727	5,140121475	0,194	Downreg
Q9CXW3	CYBP_MOUSE	Calcyclin-binding protein	0,03774168	5,321273161	0,187	Downreg
Q61545	EWS_MOUSE	RNA-binding protein EWS	4,26E-05	5,42558213	0,184	Downreg
P10649	GSTM1_MOUSE	Glutathione S-transferase Mu 1	0,00255615	6,317736517	0,158	Downreg

1. **Enrichment of biological processes** (Gene Ontology). After analyzing all proteins, the 15 most significantly enriched Gene Ontology terms have been categorized into 4 distinct groups. The primary enriched group encompasses terms such as cellular respiration, aerobic respiration, precursor metabolites and energy production, the tricarboxylic acid cycle, oxidative phosphorylation, and dicarboxylic acid metabolism. Essentially, the first enriched group provides insights into mitochondria and mitochondrial metabolism. The remaining enriched terms, while organized into 3 groups, are closely interconnected; they pertain to RNA, its processing, the regulation of its processing, as well as its localization, transport, and translation (Figure *17*).

   If we only analyze the upregulated proteins, the picture is very similar, but it is worth noting the appearance of the terms: apoptotic mitochondrial changes, electron transport chain or proton transmembrane transport. They all refer to mitochondria.

   Finally, the downregulated proteins are classified in more diverse and less related terms such as cytoplasmic translation, amide biosynthesis process, cellular amide metabolic process, cellular nitrogen compound metabolic process, translation, peptide metabolic process and cellular nitrogen compound biosynthesis process. It is noteworthy that metabolism and biosynthesis are repeated in several of these terms.

2. **Subcellular location enrichment**. When analyzing all the proteins according to their subcellular location, we can observe a consistent relationship with what has been described in the section on biological processes, since they are expected locations when talking about mitochondrial metabolism, such as mitochondrial envelope, mitochondrion, mitochondrial protein complex, mitochondrial matrix or mitochondrial nucleoid. And, in relation to RNA, we found terms such as ribonucleoprotein complex, ribosome, cytosolic small ribosomal subunit, ribosomal subunit or polysome. There are also some general terms such as organelle inner membrane, organelle envelope or intracellular organelle lumen. The most disappointing term might be myelin sheath as it has the highest FDR and no direct relation with the kidney. If we analyze the upregulated proteins, we still find some terms related to mitochondrion and RNA, but the most remarkable is the appearance of terms related to the nucleus, such as nuclear lumen, nucleoplasm or nuclear periphery. Among the downregulated proteins, the most prominent compartments in terms of signal strength are those related to the ribosome, followed by the nucleus, the mitochondrion and the cytosol (Figure *18*).

3. **Tissue expression enrichment**. The enrichment analysis did not find any terms related to the kidney or to the epithelial nature of the cells analyzed. The terms it does find relate to other organs and systems, such as the cardiovascular or nervous system, embryonic tissue or fibroblasts, and even cancer cells (Figure *19*).

Based on the enrichment analysis, we can conclude that the mutant cell is undergoing a global change, with many processes being affected, and the mitochondrion playing a central role.

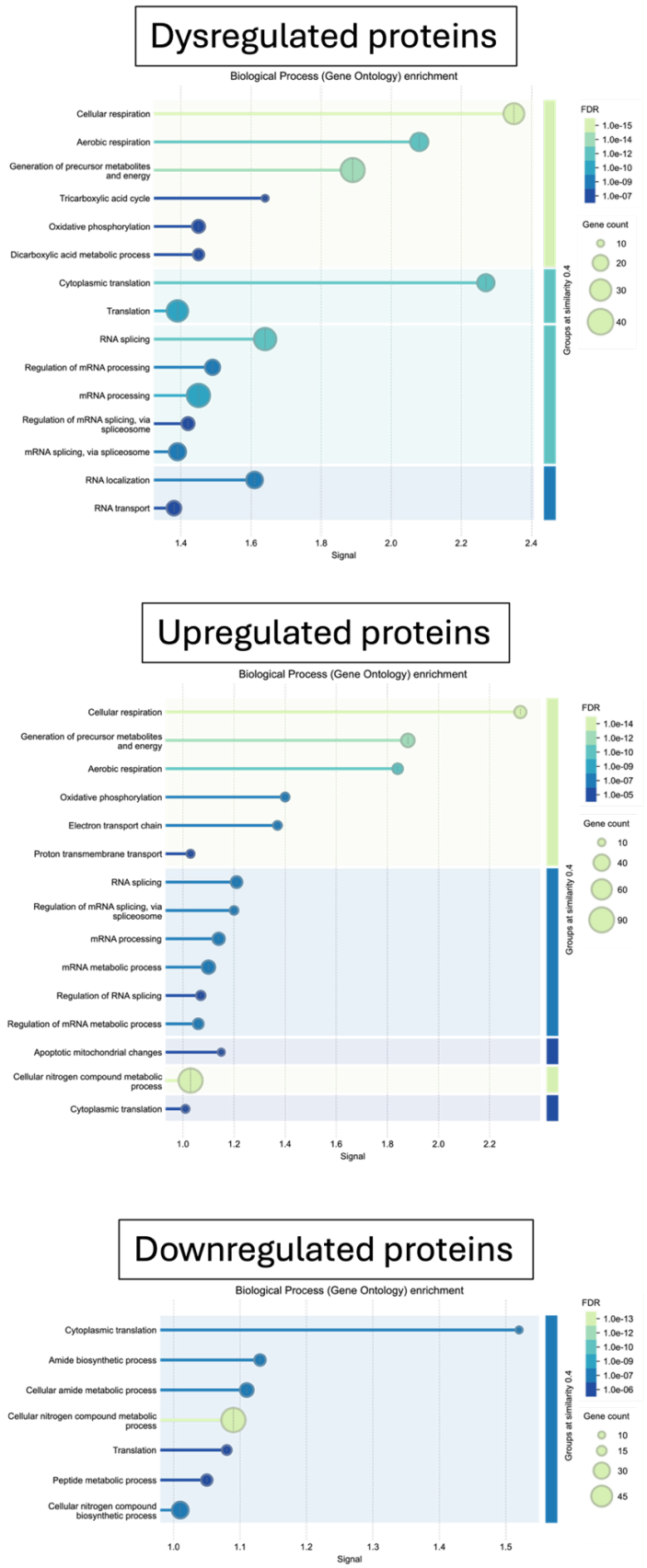

Figure 17. Enrichment analysis illustrating the significantly represented terms from Biological Process (Gene Ontology), created using STRING. The analysis was applied individually to total dysregulated proteins, upregulated proteins, and downregulated proteins. The terms with the highest signal values are shown.

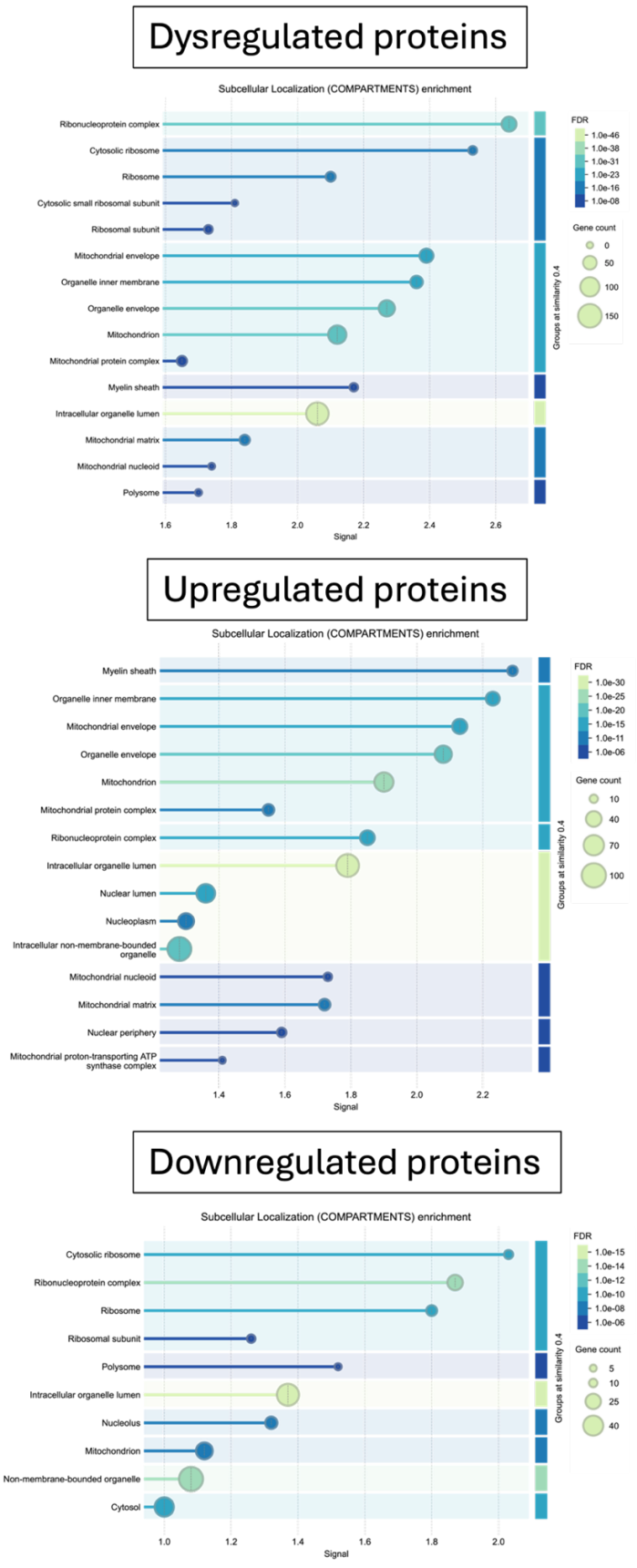

Figure 18. Enrichment analysis illustrating the significantly represented terms from subcellular localization (compartments), created using STRING. The analysis was applied individually to total dysregulated proteins, upregulated proteins, and downregulated proteins. The terms with the highest signal values are shown.

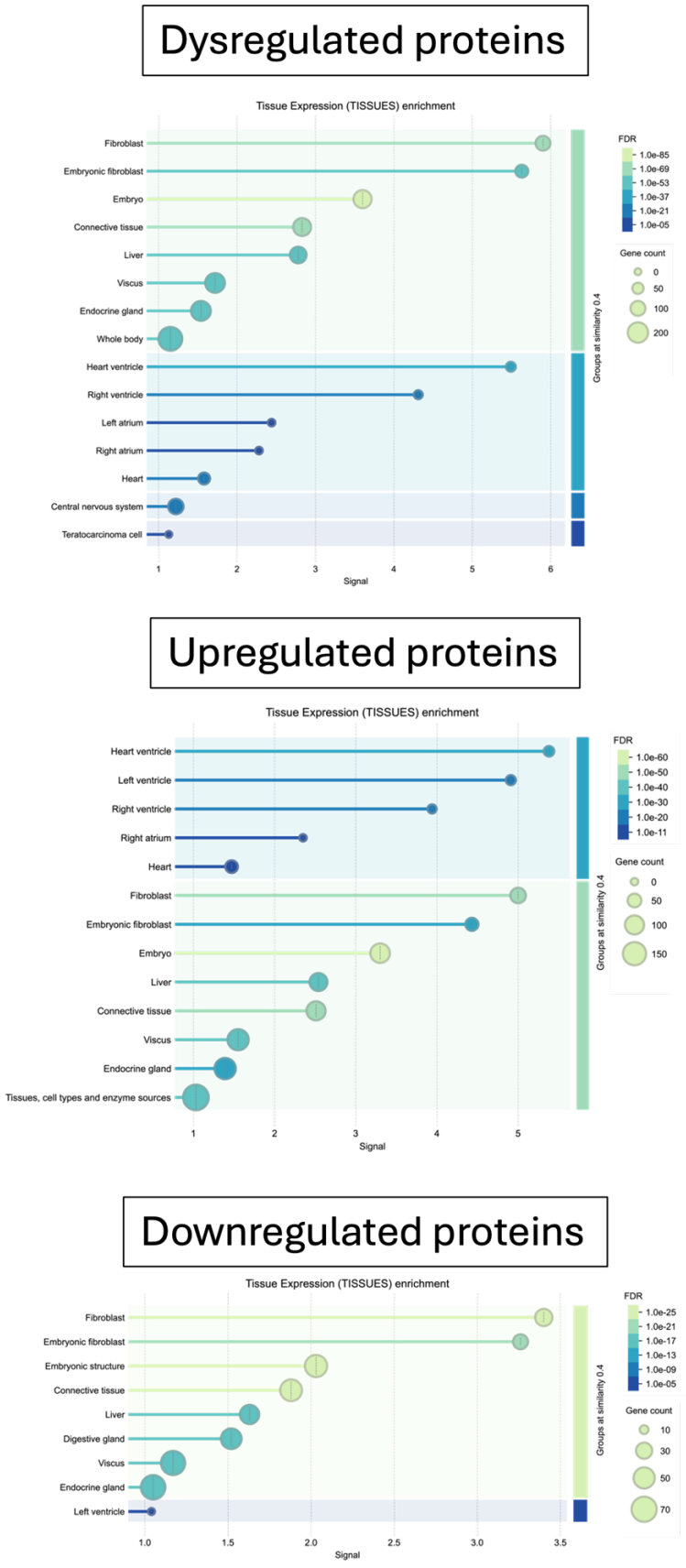

Figure 19. Enrichment analysis illustrating the significantly represented terms from tissue expression (Tissues), created using STRING. The analysis was applied individually to total dysregulated proteins, upregulated proteins, and downregulated proteins. The terms with the highest signal values are shown.

4.2.3. Metabolism in mIMCD3 cells

The proteomic analysis provides us with a lot of information; we have a large list of dysregulated proteins and most of these proteins do have multiple functions in very different processes. It is very difficult to analyze what is happening in each specific pathway by only looking at the global protein map. Therefore, we decided to start by conducting a manual analysis for certain specific pathways, to compare them with what was already published and as a way to learn about our model.

The proteomic analysis has detected only two **glycolytic** proteins: Glyceraldehyde-3-phosphate dehydrogenase (GAPDH) and Phosphoglycerate kinase 1 (PGK1). GAPDH is upregulated, while PGK1 is downregulated. Since they are behaving in opposite ways and both are reversible enzymes, we cannot determine how glycolysis is altered. We could infer that if glycolysis is occurring normally, pyruvate is not being directed to the TCA cycle, because Pyruvate dehydrogenase E1 component subunit beta (PDHB) is downregulated (Figure *20*a). However, these are assumptions, as we would need more proteins to confirm this.

Regarding **fatty acid oxidation**, it appears to be upregulated in *Pkd1* KO cells. We have identified several enzymes involved in this process that are upregulated: Enoyl-CoA hydratase, mitochondrial (ECHM; *Echs1*), Long-chain specific acyl-CoA dehydrogenase, mitochondrial (ACADL; *Acadl*), Short-chain specific acyl-CoA dehydrogenase, mitochondrial (ACADS; *Acads*), and Trifunctional enzyme subunit alpha, mitochondrial (ECHA; *Hadha*). Additionally, we found that Trifunctional enzyme subunit beta, mitochondrial (ECHB; *Hadhb*) is only detected in mutants. On the other hand, 3-ketoacyl-CoA thiolase, mitochondrial (THIM; *Acaa2*) and Acetyl-CoA acetyltransferase, mitochondrial (THIL; *Acat1*) are downregulated. These downregulated enzymes are both involved in ketone body formation. The function of both enzymes can be substituted by the trifunctional enzyme (Figure *20*b).

Interpreting the events occurring in the **tricarboxylic acid (TCA) cycle** is challenging, despite the identification of several enzymes. The Isocitrate dehydrogenase [NAD] subunit alpha, mitochondrial (IDH3A; *Idh3a*) is upregulated and is responsible for an irreversible reaction. However, the 2-oxoglutarate dehydrogenase, mitochondrial (ODO1; *Ogdh*), which is part of a complex also responsible for an irreversible reaction, is downregulated. The Succinate-CoA ligase [ADP-forming] subunit beta, mitochondrial (SUCB1; *Sucla2*) is upregulated. Both hydrophilic subunits of the mitochondrial Succinate dehydrogenase were detected: SDHA; *Sdha* and SDHB; *Sdhb*. SDHB appears only in the KO group, while SDHA is downregulated. The fumarate hydratase (FUMH; Fh) is downregulated. With this data, we cannot determine what is happening with the TCA cycle; it may be functioning correctly, but certain enzymes might have modified activities due to intrinsic cellular factors (Figure *20*c).

The functioning of **oxidative phosphorylation** appears to be more straightforward to interpret compared to other metabolic pathways because there are many dysregulated proteins, all of which tend to be upregulated, with a few exceptions. Under the applied conditions, it seems that mIMCD3 cells are still capable of using oxygen to generate energy. We can also infer that the *Pkd1* KO cells are experiencing a period of high energy demand.

- Three proteins were found belonging to Complex I: the upregulated protein NADH-ubiquinone oxidoreductase 75 kDa subunit (NDUS1; *Nduf1*), a subunit

that catalyzes the transfer of electrons from NADH; the downregulated NADH dehydrogenase [ubiquinone] 1 alpha subcomplex subunit 8 (NDUA8; *Ndufa8*), a non-catalytic subunit and, additionally, the Complex I assembly factor ACAD9 (ACAD9; *Acad9*) found only in the KO group.

- From Complex II, as mentioned in the TCA cycle, SDHB was found only in the KO group, and SDHA was downregulated. It is worth mentioning that TRAP1, a mitochondrial chaperone protein, is upregulated and plays a crucial role in maintaining mitochondrial function and polarization. TRAP1 can influence mitochondrial spare respiratory capacity (SRC) by inhibiting succinate dehydrogenase (SDHA), acting as a negative regulator of mitochondrial respiration (Yoshida et al., 2013). This could be one explanation for the downregulation of SDHA, but we have not yet observed the metabolic switch, at least at the protein level.
- Two upregulated cytochromes were listed: Cytochrome c somatic (CYC; *Cycs*) and Cytochrome c1, heme protein (CY1; *Cyc1*).
- In Complex IV, we found two upregulated subunits of cytochrome oxidase: Cytochrome c oxidase subunit 5A (COX5A; *Cox5a*) and Cytochrome c oxidase subunit 4 isoform 1 (COX41; *Cox4i1*), and one downregulated subunit, Cytochrome c oxidase subunit 6B1 (CX6B1; *Cox6b1*).
- From Complex V, we found the ATP synthase F(0) complex subunit B1 (AT5F1; Atp5pb) only in the KO group, and the rest of the ATP synthase subunits are upregulated (ATP5H; *Atp5pd*, ATPG; *Atp5f1c*, ATPB; *Atp5f1b*, ATPA; *Atp5f1a*, ATPD; *Atp5f1d*). The ADP/ATP translocase 1 (ADT1; *Slc25a4*) is also upregulated (Figure *20*d).

The metabolism in mutant mIMCD3 cells is highly dysregulated. It seems that the cells have a high energy demand and are able to use oxygen to produce it

4.2.4. Stress and apoptosis

Our database containing proteomics results was enriched with additional information from UniProt. Upon searching in the database for the keyword "**stress**," we identified a series of upregulated and downregulated proteins indicative of an increased stress state, particularly in the mitochondria. We observed both active responses combating the stress situation and potentially inhibited responses. Supplemental table *4* lists some of these proteins, which we believe are functioning in relation to cellular stress. The mitochondrial superoxide dismutase (SODM; *Sod2*) and cytosolic superoxide dismutase (SODC; *Sod1*) enzymes were detected as upregulated and downregulated in mutant cells, respectively. SODM has a fold change (FC) of 16, indicating its abundant presence and suggesting the need to eliminate reactive oxygen species (ROS) in the mitochondria. The thioredoxin-dependent peroxide reductase (PRDX3; *Prdx3*) enzyme, which detoxifies peroxides, is upregulated and plays a crucial role in protecting the cell against oxidative stress. Notably, Peroxiredoxin-5 (PRDX5; *Prdx5*) is downregulated. Finally, glutathione S-transferase Mu 1 (GSTM1; Gstm1), the most downregulated protein on the list, detoxifies by catalyzing the conjugation of glutathione to toxic compounds or oxidative stress products. These conjugates are water-soluble and easier to eliminate. To interpret these results, we must consider that the WT cells are also under a state of stress (confluency and serum starvation) and it is possible that the change in the abundance of stress-related proteins is influenced by this condition.

We also searched for the keyword "**apoptosis**" and obtained several results, with the most relevant ones presented in Supplemental table *5*.The proteins have various functions and, in certain states, can influence apoptosis. What we want to highlight here is that pro-apoptotic proteins are upregulated, while anti-apoptotic proteins are downregulated. Whether they are fulfilling their role in apoptosis is unknown.

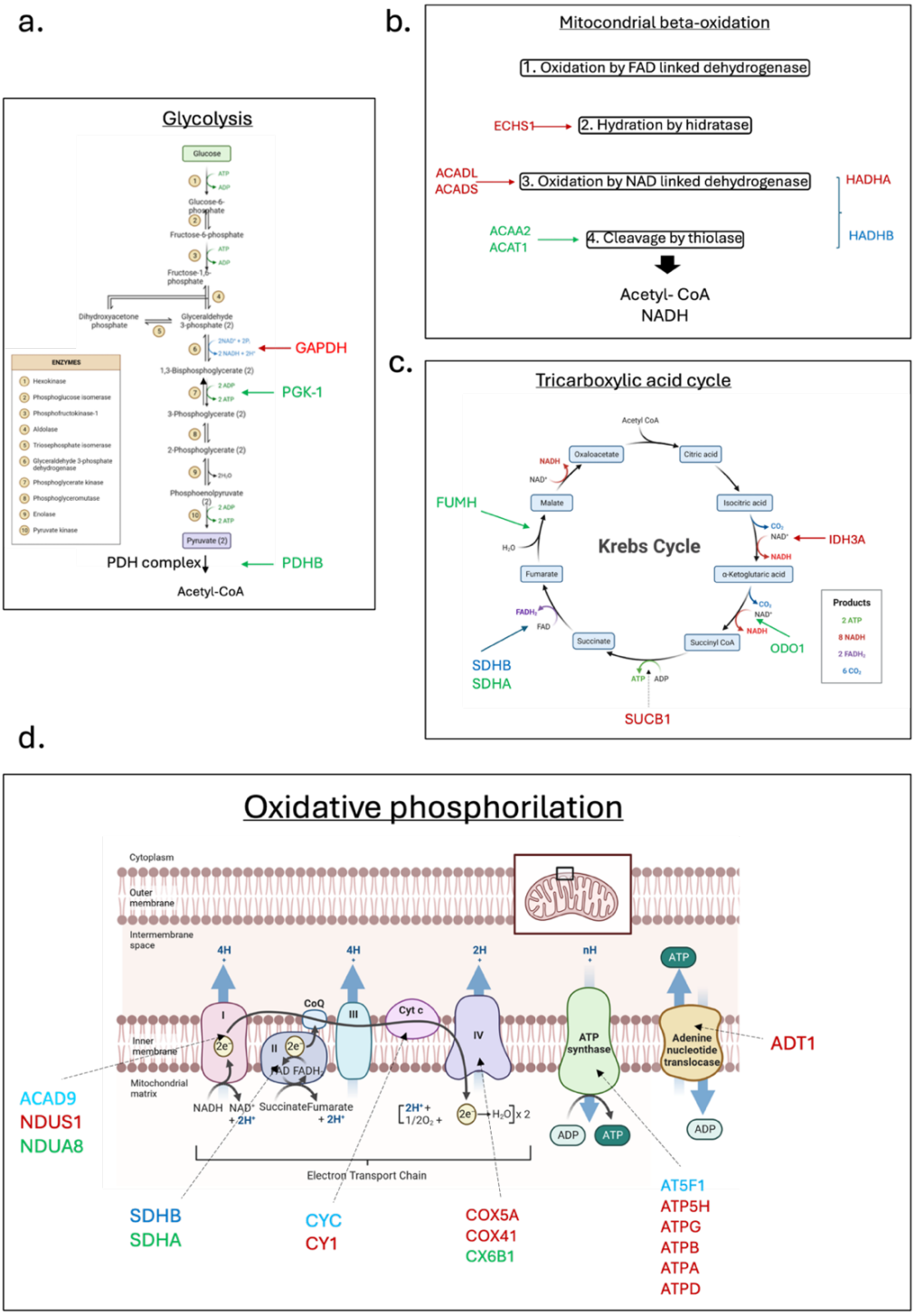

Figure 20. Metabolic pathways dysregulated in mIMCD3 *Pkd1*-KO according to proteomic analysis. Proteins found to be dysregulated in glycolysis (a), fatty acid oxidation (b), the tricarboxylic acid cycle (c), and oxidative phosphorylation (d) are shown. Proteins written in blue are those found only in the KO group, red indicates upregulated proteins, and green indicates downregulated proteins. Images created with BioRender.

4.2.5. Cell cycle

In the proteomics data, we identified two notable proteins related to the cell cycle: CDK1 (Cyclin Dependent Kinase 1), which is upregulated, and CDC5L (Cell division cycle 5-like protein), which is downregulated. The *Cdk1* gene was found to be upregulated in transcriptomic studies and validated as an early driver of cyst proliferation (Zhang et al., 2021). CDC5L functions as a DNA-binding protein involved in cell cycle control. The expression of *Cdc5l* has been observed in transcriptomic data from animal models of ADPKD, both *Pkd1* and *Pkd2* ((Zhang et al., 2024; (https://pkdgenesandmetabolism.org/expression/Cdc5l)). The gene appears downregulated in male *Pkd1* mutant mice (mIMCD3 cells are male) at week 7 but not in females (the differences do not seem to be significant).

From the upregulated CDK1 data, we can infer that the mIMCD3 *Pkd1* KO cells could be proliferating.

4.2.6. Assessment of cellular and mitochondrial status in mIMCD3 cells

4.2.6.1. Description of the cell population

We performed various flow cytometry experiments using different dyes to assess the cellular and mitochondrial status. In a flow cytometer, cells pass one by one through a laser beam, and the detectors measure the scattered light. There are two main types of scatter: forward scatter (FSC), which provides information about cell size, and side scatter (SSC), which provides information about cell complexity and structures. When we plot both parameters (FSC and SSC) on a graph, we obtain a comprehensive view of the size and complexity of the cell line we are analyzing.

In our flow cytometry experiments with mIMCD3 cells, we observed that the cells exhibited a **characteristic cellular profile**, mutant cells exhibit a clearly identifiable second cell population, as shown in Figure *21*a. In all our flow cytometry analyses, we exclude potential doublets, as our experience with these cells had shown that they have some difficulty dissociating. If we analyze the SSC (Figure *21*b) and FSC (Figure *21*c) parameters individually, the differences between WT and *Pkd1* KO are mainly focused on the FSC level, which corresponds to cell size. The range of cell sizes is the same in WT and *Pkd1* KO cells. The WT cells exhibit a Gaussian distribution with a tail, indicating the presence of few cells of higher sizes. In contrast, the mutants display a bimodal distribution. The main population is slightly smaller than the WT, while the secondary population consists of larger cells (Figure *21*c). We divided the cells into a main population and a secondary population using the point where the slope changes as the boundary. Based on this, the primary population of WT cells comprises approximately 70% of the cells, while the secondary population comprises 30%. In the case of the mutant line, the distribution is different: approximately 57% of the cells are included in the main population, and 43% are included in the secondary population (Figure *21*c).

4.2.6.2. Cell cycle profile

We aimed to determine if there was a difference between the cell cycle of WT and *Pkd1* KO cells. For this purpose, we use propidium iodide, a DNA fluorescent stain, which allows to determine the DNA content of cells by flow cytometry. This approach enables the identification of 2N cells in the G_1 phase, cells between 2N and 4N in the S phase, and 4N cells in the G_2/M phase. In an FSC-Width vs B690-A graph, we can observe how the cells are organized according to their size and signal intensity. The first

peak of smaller cells corresponds to 2N cells, and the second peak of larger cells corresponds to 4N cells. Cells in the S phase are located between these two peaks. As shown in Figure *22*b, **the number of cells in the S phase significantly decreases in the mutant condition**. Although not significant, there is a **trend towards a decrease in G_1 phase cells and an increase in G_2/M phase cells in the mutant condition** compared to the WT.

Throughout the different phases of the cell cycle, there are checkpoints that ensure the cell's DNA is in the proper condition to progress and divide. If any damage is detected in the DNA, these checkpoints stop the cell's progression in the cycle, preventing its division. Therefore, the decrease in cells synthesizing DNA and the accumulation of *Pkd1*KO cells in the G_2/M phases could be a consequence of increased genetic instability and the corresponding response mediated by the cell cycle checkpoints. Another interpretation is that cells are proliferating, something reasonable considering ADPKD is a disease characterized by increased proliferation for cyst formation but quite unlikely due to the high confluence situation of the culture.

In the last graph of Figure *22*a, when selecting the cycling population, we can observe that this population represents different percentages relative to the total population, 85,25% in mIMCD3 WT and 63,82% in mIMCD3 *Pkd1*KO cells. When considering the total cell population, polyploid cells (which have larger amounts of DNA than 2N or 4N cells) are included. When analyzing all the cells together, we observe that there are **more polyploid cells in *Pkd1* KO cells than in WT cells** (Figure *22*c). Another factor supporting the presence of genetic instability in the mutant cells.

4.2.6.3. Mitochondrial mass

To assess mitochondrial mass, we used MitoTracker Green FM, a fluorescent dye that labels mitochondria in live cells. This dye diffuses across the plasma membrane and accumulates in mitochondria. Although we did not find a significant difference (p value=0.0529) in the fluorescent signal between conditions, there is a clear trend (Figure *23*b). The fluorescent intensity in mIMCD3 *Pkd1* KO cells is higher than in WT cells, indicating an **increased mitochondrial mass in mutant cells**. When we analyzed the MitoTracker signal by subpopulations, we found that in both conditions, the second population exhibited higher intensity. This indicates that the second population has an increased mitochondrial mass compared to the main population. In this case the larger the cell, the greater the mitochondrial mass (Figure *23*a,b).

4.2.6.4. Mitochondrial membrane potential

To assess the functional status of the mitochondria, we measured the mitochondrial membrane potential using TMRM (Tetramethylrhodamine). TMRM is a fluorescent dye that measures mitochondrial membrane potential in live cells. As a cationic dye, it accumulates in active mitochondria due to their negative membrane potential. The intensity of TMRM fluorescence correlates with the membrane potential.

In both conditions, we included a control with FCCP (Carbonyl cyanide-p-trifluoromethoxyphenylhydrazone) to depolarize the membrane, which was used to gate the positive TMRM population. As shown in Figure *24*, the addition of FCCP resulted in the loss of membrane potential in both conditions. **A trend towards a higher membrane potential was observed in mutant cells** (Figure 25). Similar to the findings for

mitochondrial mass, analysis by subpopulations revealed that the second population in both conditions exhibited a higher mitochondrial membrane potential. Thus, the second population is larger, has greater mitochondrial mass and higher membrane potential (Figure 25).

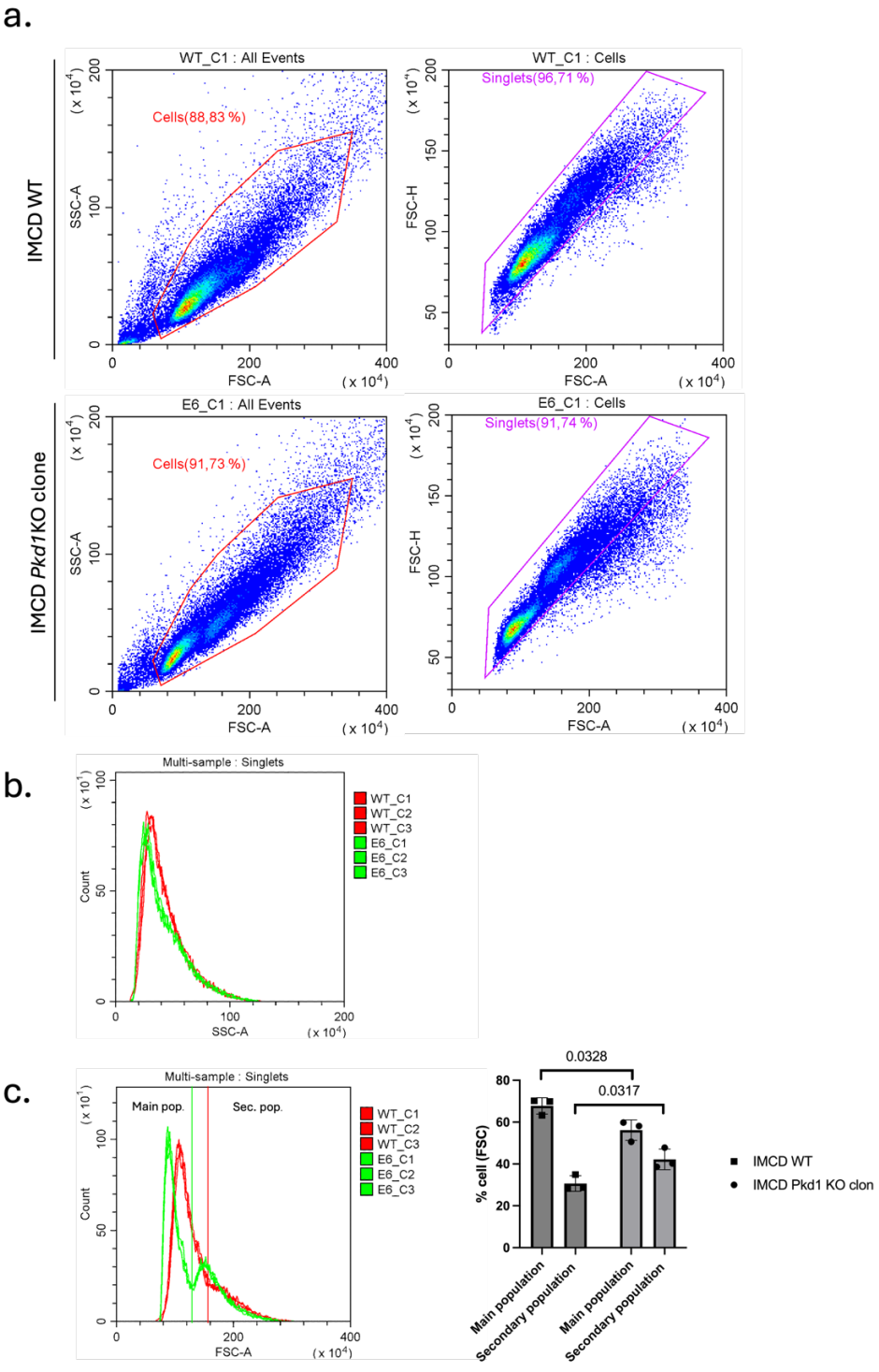

Figure 21. Flow cytometry analysis of mIMCD3 cells. a. Dot plots showing cell population gating and doublet exclusion. **b.** Histograms of the singlets populations plotted individually based on size (FSC-A) and **c.** complexity (SSC-A). **c.** For each condition, a different FSC-A value was considered to establish the delimitation between populations. The red vertical bar indicates the delimitation between populations for the WT condition, while the green bar indicates the delimitation for the mutant condition. Statistical significance was determined by unpaired t-test (two-tailed) and presented as the mean ± SEM.

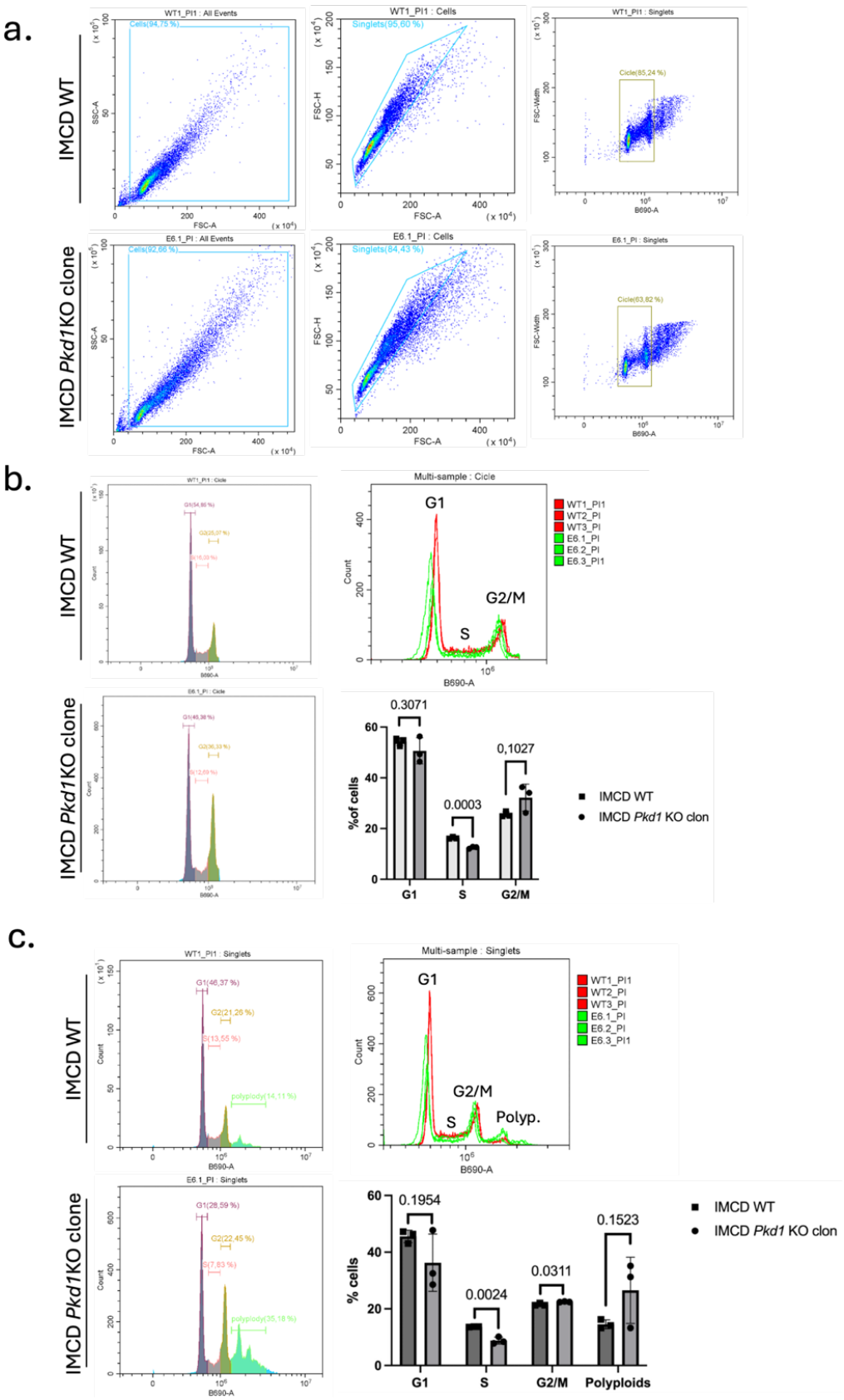

Figure 22. Flow cytometry analysis of mIMCD3 cells stained with propidium iodide. a. Dot plots showing cell population gating, doublet exclusion, and selection of cycling cells. **b.** Cell cycle profile and representation of the proportion of cells in each phase of the cycle. **c.** Total population profile (singlets) and representation of the proportion of cells in each cell cycle phase/ploidy peak. Statistical significance was determined by unpaired t-test (two-tailed) and presented as the mean ± SEM.

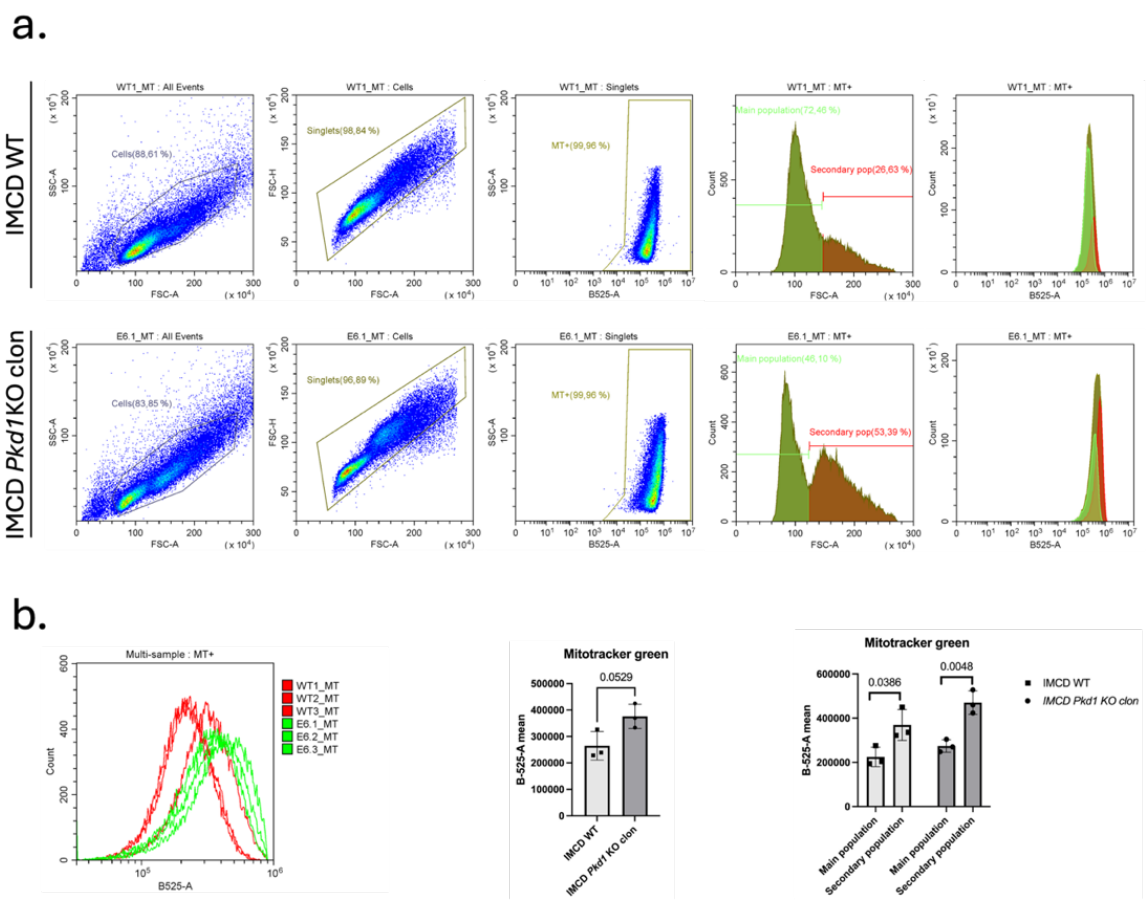

Figure 23. Flow cytometry analysis of mIMCD3 cells stained with MitoTracker Green FM. a. Dot plots showing population gating, doublet exclusion, gating of fluorescent signal-positive cells, histogram subpopulation gating based on FSC-A, and fluorescent signal intensity comparisons of the conditions and subpopulations. **b.** Histogram comparing the signal intensity of triplicates for the two conditions. Plots depicting the mean signal intensity per group (WT and *Pkd1* KO clone) and per subpopulation. Statistical significance was determined by unpaired t-test (two-tailed) and presented as the mean ± SEM.

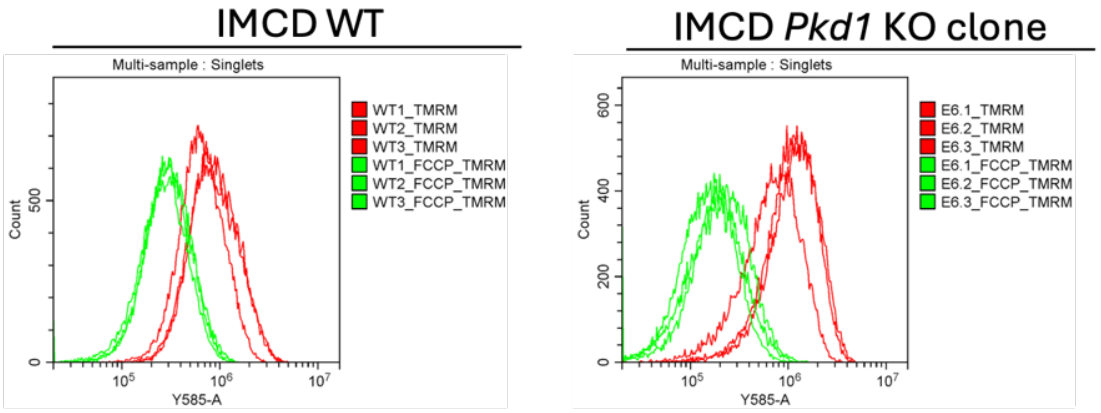

Figure 24. Flow cytometry analysis of mIMCD3 cells stained TMRM. Control experiment using FCCP to assess mitochondria membrane depolarization.

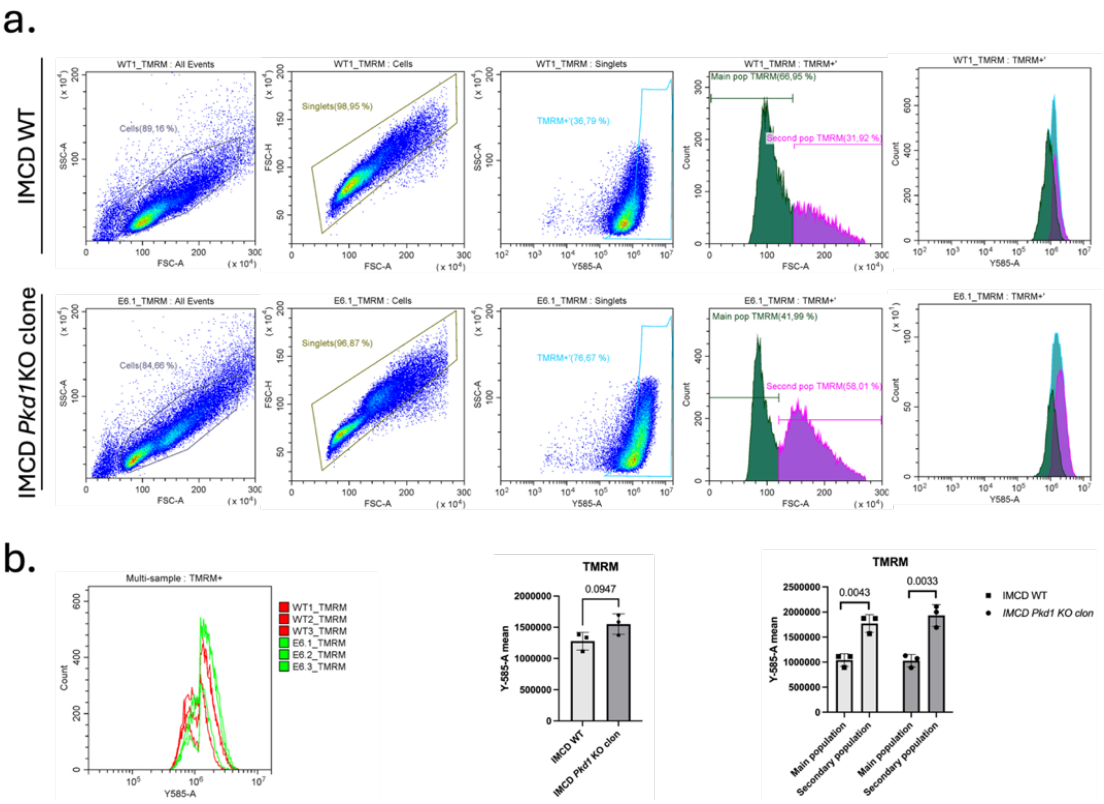

Figure 25. Flow cytometry analysis of mIMCD3 cells stained TMRM. a. Dot plots showing population gating, doublet exclusion, gating of fluorescent signal-positive cells, histogram subpopulation gating, and fluorescent signal intensity comparisons. **b.** Histogram comparing the signal intensity of triplicates for the two conditions. Plots depicting the mean signal intensity per group (WT and *Pkd1* KO clone) and per subpopulation. Statistical significance was determined by unpaired t-test (two-tailed).

4.2.6.5. Mitochondrial morphology

On the 10th day of culture, we stained the mitochondria with Mitotracker Green FM to examine their morphology and subcellular localization. The mIMCD3 WT cells were highly confluent, making it difficult to achieve good magnification under the microscope to determine the size and morphology of the mitochondria due to the cells being closely packed together (Figure *26*). In contrast, the mIMCD *Pkd1*-KO cells allowed for more detailed observation of the mitochondria. Interestingly, in the KO culture, where cells grow flattened, we observed areas similar to the WT cells with closely packed cells (Figure *26*). Additionally, there were regions with noticeably larger cells, where we could distinguish mitochondria with **normal morphology, fragmented mitochondria, and mitochondria with different intensity signals** (Figure *26*). These results are consistent with our flow cytometry findings, which identified a second population of larger cells.

Furthermore, DAPI staining revealed **multinucleated cells**. The cells previously referred as polyploid cells, based on the microscopy results, could be multinucleated cells. It was not possible to conduct a comparative analysis between the mitochondria of mIMCD3 WT and *Pkd1*-KO cells. To achieve this, the culture would need to be analyzed at a different time point, without that much confluency.

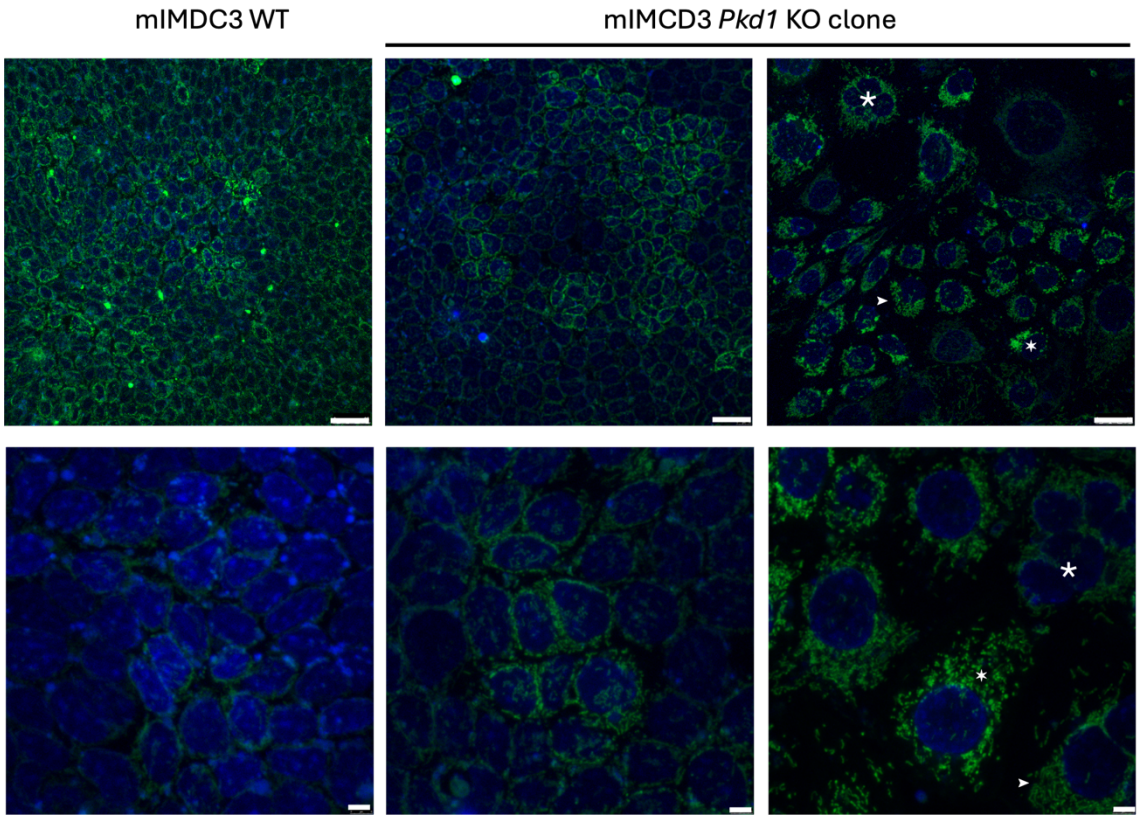

Figure 26. Confocal microscopy images of IMCD3 cells at day 10. Mitochondria stained with Mitotracker Green FM (green) and nuclei stained with DAPI (blue). Scale bar: 25μm upper images; 5μm bottom images. Asterisk: multinucleated cell; arrowhead: healthy mitochondria shape; star: fragmented mitochondria.

4.2.7. Comparison of cells and mice proteomics

The amount of information generated by the proteomic analysis was massive, and understanding it is a laborious task dependent on many factors. It is true that the only difference between the cells we are comparing, is the deletion of the *Pkd1* gene, but given the complexity of the disease and the external factors that can be influencing, such as culture conditions or the timing of the analysis, it is totally impossible to understand completely the results. Thus, the most common approach in this type of analysis is to focus on a particular protein or pathway and study it thoroughly through experimental assays. In our case, we decided to select a specific pathway to study by comparing the proteomics of the mIMCD3 cells with the proteomics of whole kidneys from C57/BL6J *Pkd1*$^{flox/flox}$; TamCre mice sacrificed at day 18 and 30. In this manner, we aim to identify and emphasize pathways or proteins that may be overlooked and give them more robustness, as they would be independent of the model and the timing.

4.2.7.1. Description of the mice model

Proteomic analysis of mice kidneys was previously conducted in the NefroCHUS group, and the results were presented in the thesis of Marta Vizoso González (Vizoso-González, 2023). Briefly, mice were treated with tamoxifen to inactivate the *Pkd1* gene at postnatal days 10-11 and were sacrificed at postnatal days 18 (p18) and 30 (p30) (Figure *27*). The C57/BL6J *Pkd1*$^{flox/flox}$; TamCre model, is defined as a rapid progression

model when *Pkd1* is inactivated before postnatal day 12 (Piontek et al., 2007). For the LC-MS/MS a number of 3 per group was submitted to analysis due to be a consanguineous model. C57/BL6J *Pkd1*$^{flox/flox}$; TamCre+ are the mutant group, while C57/BL6J *Pkd1*$^{flox/flox}$; TamCre- serve as the control mice, and they are referred as WT in this document.

The structural and functional state of the kidneys of WT and *Pkd1*-mutant mice at different sacrifice times is described below. Hematoxylin-eosin staining of the histological sections of the kidneys allowed us to calculate the cystic index (percentage of the total tissue area that is occupied by cysts) and the total number of cysts. *Pkd1*-mutant p30 mice exhibited high cystic index (Figure 28c) and a high number of cysts (Figure 28b,d), which correlated with an increased renal volume (Figure 28e) comparing to WT p30 mice. The measurement of BUN (Blood Urea Nitrogen), indicative of renal function, showed high variability in mutant samples, and thus renal function was not significantly differential compared to normal kidneys (Figure 28f). On the other hand, mice sacrificed at p18 displayed a debutant cystic phenotype (Figure 28a,c,d) without an increase in total kidney size (Figure 28e), although some degree of renal function loss was already apparent (Figure 28f).

The use of total kidney samples from mice sacrificed at day 30 has the advantage of a higher representation of cystic cells, but as the disease is quite advanced many secondary pathways to cystogenesis may be dysregulated. Conversely, kidneys from mice sacrificed at day 18 have fewer cystic cells, making it more challenging to detect differences in proteomic analysis, but any differences found could be related to the early stages of the cystogenesis.

We assessed the expression level of *Pkd1* in mice at days p18 and p30 using qPCR. As expected, in both cases, we observed a decreased expression of *Pkd1* in *Pkd1*-mutant mice (Figure *29*).

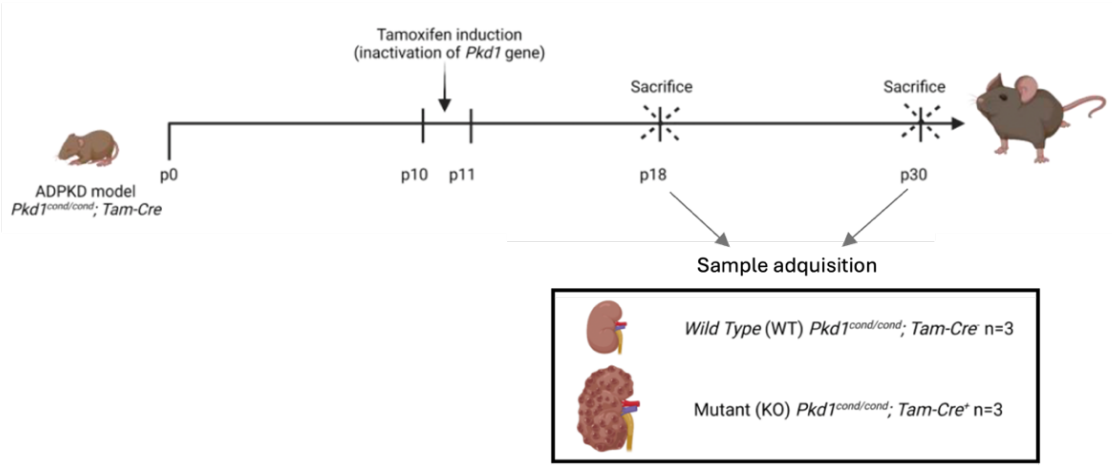

Figure 27. Illustrative timeline showing the events that occur during the animal´s life. Using C57/BL6J *Pkd1*$^{flox/flox}$; TamCre model, *Pkd1* gene was inactivated at day 10-11 to obtain cystic (Cre+) and no-cystic (Cre-) kidney phenotype. The mice were sacrificed at two different time points, postnatal day 18 (p18) and postnatal day 30 (p30), and samples were collected. Image modified fromVizoso-González, 2023.

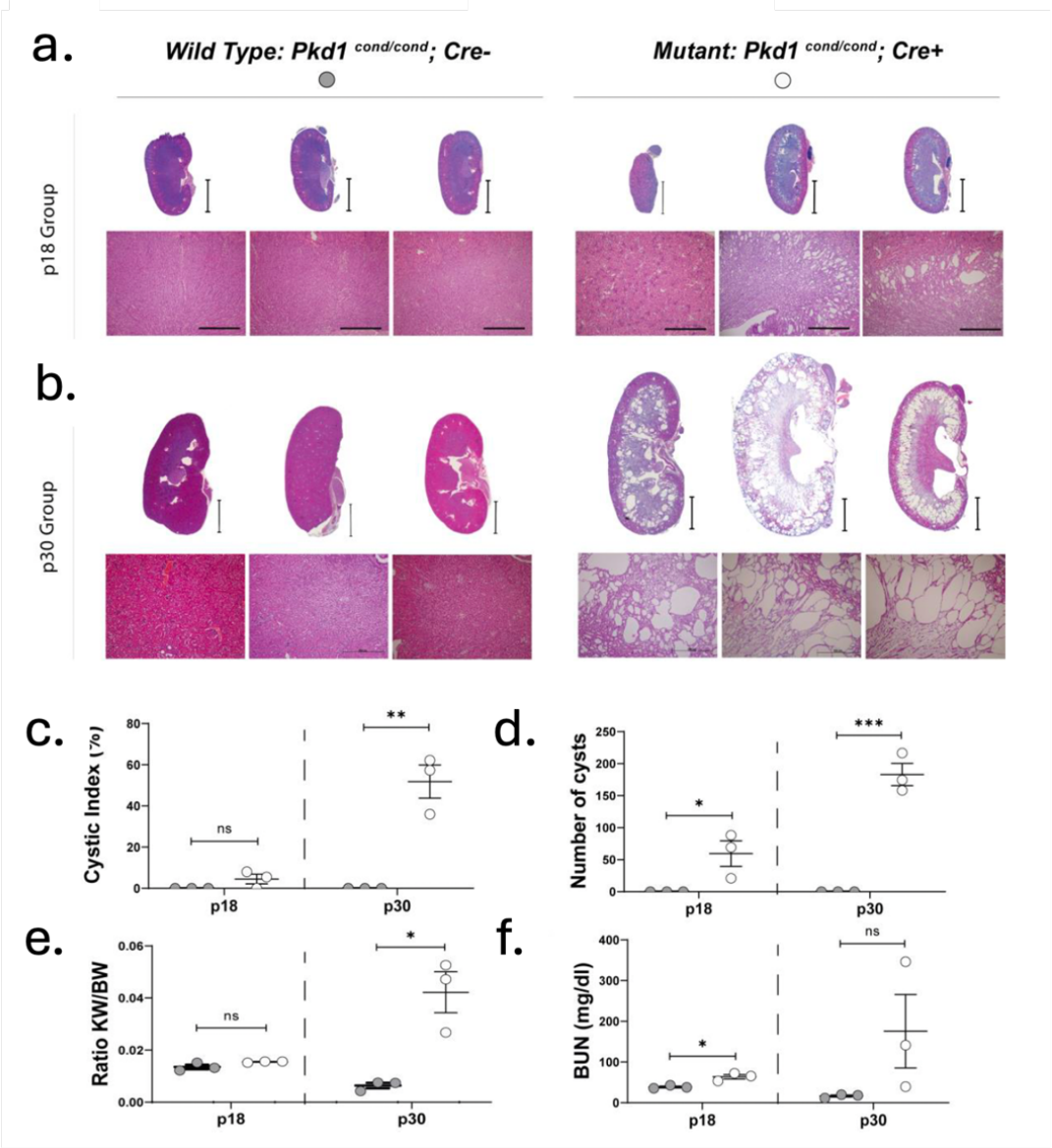

Figure 28. Characterization of the cystic kidney phenotype at postnatal days 18 and 30. Representative macroscopic and microscopic images of hematoxylin-eosin stained kidneys from WT and Mutant mice sacrificed at day 18 (a) and day 30 (b) are shown. Three samples per group were used. Panels (c) and (d) display the renal cystic index and the number of cysts for the different phenotypes. Panels (e) and (f) show the kidney weight to body weight ratios and Blood Urea Nitrogen (BUN) concentrations for the different groups. Bars represent means ± SEM. Statistical significance was determined using Student's t-test (two-tailed), with $p<0.05$ considered significant: ns indicates not significant; * $p<0.05$; ** $p<0.01$; *** $p<0.001$. The scale bars represent 2 mm (upper panel) and 100 µm (lower panel). Image taken from Vizoso-González, 2023.

4.2.7.2. SWATH comparison and results analysis

We compared the SWATH results of mIMCD3 cells with the renal proteomics of C57/BL6J *Pkd1*$^{flox/flox}$; TamCre mice sacrificed at p18 and p30. For this comparison, we only considered proteins with a p-value < 0.05 and they were classified according to their trend without setting a specific FC threshold. The SWATH analyses comprised 348 proteins for mIMCD3 cells and 248 proteins for p18 mice kidneys. Regarding the renal proteomics of p30, it is important to clarify that we have two different SWATH analyses. Both were conducted on the same samples but analyzed against two different reference spectral libraries. Therefore, there may be differences in the peptides/proteins that each

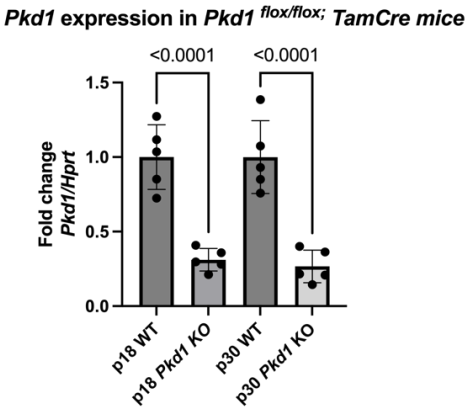

Figure 29. Expression of the *Pkd1* gene in whole kidney samples from *Pkd1*$^{flox/flox}$; TamCre mice at p18 and p30. A statistically significant reduction in *Pkd1* expression was confirmed at both time points. Statistical significance was determined by unpaired t-test (two-tailed) and presented as the mean ± SEM.

analysis could identify. The larger SWATH will be named as p30# and the other as just p30. The SWATH analyses comprised 1414 proteins for p30# mice kidneys and 914 proteins for p30 mice kidneys. Figure *30*a shows the number of proteins shared among each of the described groups.

There were 228 proteins shared between the SWATH of cells and some of the other SWATHs (Figure *30*b). By examining the levels of each protein, we can categorize them into those that are upregulated in cells and in some other condition, or those that are downregulated in cells and in some other condition, i.e. they exhibit the same behavior. It is not necessary for the same pattern to occur in all conditions, as it would be possible for a protein to be upregulated or downregulated on day 18 and show the opposite trend on day 30. There are many days and changes in between that could influence the abundance of the proteins. Additionally, there are shared proteins that are upregulated or downregulated in cells but exhibit the opposite behavior in other conditions. 109 proteins exhibited opposite behavior, while 119 proteins showed behavior consistent with what was observed in the SWATH for cells. Of these 119 proteins, 101 were upregulated and 18 were downregulated. Upon reviewing the downregulated proteins (Supplemental table 3), we found that 17 out of the 18 were mitochondrial proteins, 10 were metabolic enzymes, 3 were structural proteins, 2 were related to stress management, and 4 were associated with mitophagy (Figure 30b and Table *10*).

We decided to focus our attention in the **mitophagy** process, as it has never been explored in ADPKD and considering the important role of mitochondria in the disease. There were 4 proteins that we found downregulated in relation to mitophagy: Protein NipSnap homolog 1 (NIPS1), Mitochondrial fission 1 protein (FIS1), Prohibitin 1 (PHB1) and MICOS complex subunit Mic60 (MIC60) (Table *10* and Table *11*). All proteins pass the significance filter, in fact all changes are highly significant in both cells and mice. However, as mentioned above, no FC filter was considered for the cell-mouse comparison, and several of the proteins do not reach a minimum fold-change of 1.5.

NIPS1 was one of the most significant proteins found in cell proteomics. It is a protein with a tissue-specific expression pattern, being expressed almost exclusively in the brain, kidney and liver according to GTEx (https://gtexportal.org/home/). NIPS1is a mitochondrial matrix protein that accumulates on the mitochondria surface in response to mitochondrial depolarization and acts as a 'eat me' signal by recruiting proteins involved

in selective autophagy, such as autophagy receptors (ATG8 proteins and showed GABARAPs as preferred interacting partners). It is only required for PARKIN-dependent mitophagy. This research was made in human cells (Abudu et al., 2019).

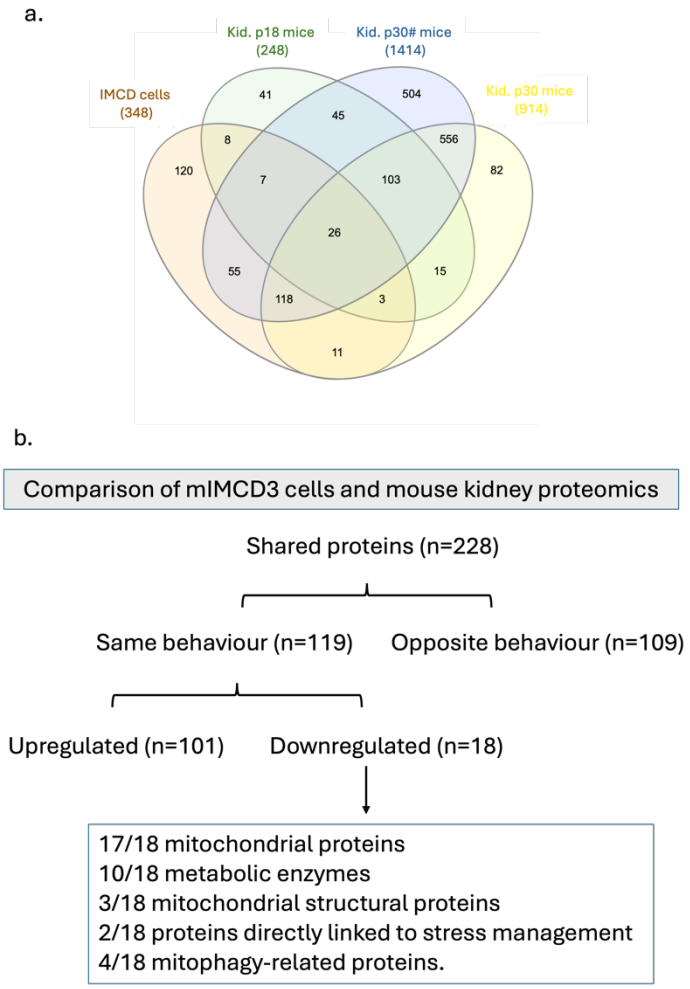

Figure 30. Schematic breakdown of the results obtained after comparing mIMCD3 cells and mouse kidney proteomics (SWATH analysis). a. Venn diagram illustrating the significant shared proteins between the SWATH analyses compared. **b.** Subclassification of shared proteins.

FIS1 participates in the fragmentation of the mitochondrial network and its perinuclear clustering, and it is its main role known. However, FIS1 has other functions, including participation in mitophagy. We find FIS1 interesting because we have found publications associating it with development, oxidative stress, and metabolism. In a 2021 publication, it was described how the ablation of *Fis1* in male germ cells causes disruption of mitochondrial morphology and mitophagy, and halts spermatid development (Varuzhanyan et al., 2021). In other study, in mouse hepatocytes, researchers described how a high-fat diet (HFD) induces oxidative stress, defective mitophagy, and an increased type I interferon (IFN-I) response, contributing to metabolic inflammation. By using adenoviral vectors to overexpress *Fis1* in the liver, oxidative damage was reduced, and glucose balance was improved in HFD-fed mice (Liou et al., 2022).

PHB1 forms complexes with PHB2 in the IMM. Prohibitin complexes have a role as mitophagic receptors, marking mitochondria for lysosomal degradation. Prohibitins are essential proteins in the maintenance of proper mitochondrial function and are part of mitochondrial quality control mechanisms. (Alula et al., 2023; Coates et al., 2001; García-Chávez et al., 2024). PHB1 is also interesting because, according to Uniprot (www.uniprot.org), throughout gestation, PHB1 is highly expressed in developing renal tubules among other tissues.

MIC60 is an IMM protein that is part of the MICOS complex, whose main function is to maintain mitochondrial cristae, IMM structure and contacts with the OMM. This subunit has been shown to block mitophagy in response to high levels of stress (Li

et al., 2021). As it is a protein that does not exceed the FC of 1.5, we will first validate and focus on the other proteins.

We hypothesize that mitophagy is blocked because it has surpassed a stress threshold. At that point, other mechanisms of cellular damage control, such as apoptosis, must be activated.

Table 10. List of proteins that are downregulated in mIMCD cells and mouse kidney proteomics (SWATH analysis). Mitophagy proteins are highlighted in blue.

Uniprot code	Uniprot name	Protein names	Gene Names	Mice p18	Mice p30	Mice p30#	Cells
P99029	PRDX5_MOUSE	Peroxiredoxin-5, mitochondrial	Prdx5 Prdx6	down FC<1,5	down	down	down
Q9JHI5	IVD_MOUSE	Isovaleryl-CoA dehydrogenase, mitochondrial	Ivd	Not found	down FC<1,5	down	down
Q9D051	ODPB_MOUSE	Pyruvate dehydrogenase E1 component subunit beta, mitochondrial	Pdhb	Not found	down	down FC<1,5	down
P56391	CX6B1_MOUSE	Cytochrome c oxidase subunit 6B1	Cox6b1 Cox6b	Not found	down	down FC<1,5	down
O55125	NIPS1_MOUSE	Protein NipSnap homolog 1 (NipSnap1)	Nipsnap 1	Not found	down	down FC<1,5	down
P53395	ODB2_MOUSE	Lipoamide acyltransferase component of branched-chain alpha-keto acid dehydrogenase complex, mitochondrial	Dbt	Not found	down	down FC<1,5	down
Q8BWT1	THIM_MOUSE	3-ketoacyl-CoA thiolase, mitochondrial	Acaa2	Not found	down	down	down
Q8QZT1	THIL_MOUSE	Acetyl-CoA acetyltransferase, mitochondrial	Acat1	Not found	down	down	down
Q9DCJ5	NDUA8_MOUSE	NADH dehydrogenase [ubiquinone] 1 alpha subcomplex subunit 8 (Complex I-19kD)	Ndufa8	up FC<1,5	Not found	down	down
Q8CAQ8	MIC60_MOUSE	MICOS complex subunit Mic60 (Mitochondrial inner membrane protein) (Mitofilin)	Immt Mic60	Not found	down FC<1,5	down FC<1,5	down FC<1,5
Q9CQ92	FIS1_MOUSE	Mitochondrial fission 1 protein (FIS1 homolog)	Fis1 Ttc11	Not found	down FC<1,5	down FC<1,5	down
P97807	FUMH_MOUSE	Fumarate hydratase, mitochondrial (Fumarase)	Fh Fh1	Not found	down FC<1,5	down FC<1,5	down
P08228	SODC_MOUSE	Superoxide dismutase [Cu-Zn]	Sod1	Not found	Not found	down FC<1,5	down
Q6PB66	LPPRC_MOUSE	Leucine-rich PPR motif-containing protein, mitochondrial	Lrpprc Lrp130	Not found	Not found	down FC<1,5	down
Q8VEM8	S25A3_MOUSE	Solute carrier family 25 member 3, mitochondrial	Slc25a3	Not found	Not found	down FC<1,5	down
P67778	PHB1_MOUSE	Prohibitin 1	Phb1 Phb	Not found	Not found	down FC<1,5	down
Q60597	ODO1_MOUSE	2-oxoglutarate dehydrogenase complex component E1	Ogdh Kiaa4192	Not found	Not found	down FC<1,5	down
Q8K2B3	SDHA_MOUSE	Succinate dehydrogenase [ubiquinone] flavoprotein subunit, mitochondrial	Sdha	Not found	Not found	down FC<1,5	down

Table 11. Mitophagy proteins with their corresponding p-values and fold change (FC) values, as determined by SWATH analysis.

Uniprot code	Uniprot name	p-value mIMCD3	FC IMCD WT to KO mIMCD3	p-value mice p30#	FC IMCD WT to KO p30#
O55125	NIPS1_MOUSE	2,88E-06	3,999596813	4,46E-05	1,464144702
Q9CQ92	FIS1_MOUSE	0,001813557	2,488858166	3,21E-07	1,313991521
P67778	PHB1_MOUSE	0,011242116	1,718579425	0,000189095	1,320021414
Q8CAQ8	MIC60_MOUSE	0,027702647	1,388269841	3,92E-05	1,43429954

4.3. DECIPHERING THE ROLE OF MITOPHAGY IN ADPKD

4.3.1. Gene expression of mitophagy-related genes

NISP1, FIS1, Prohibitin1, MIC60 are mitophagy-related proteins found downregulated in both cell and mice proteomics. ABCE1(ATP-binding cassette sub-family E member 1) and ATG7 (Ubiquitin-like modifier-activating enzyme ATG7) are proteins related to mitophagy only found in mice proteomics and PINK (Serine/threonine-protein kinase PINK1, mitochondrial), Parkin (E3 ubiquitin-protein ligase parkin) and NIX (BCL2/adenovirus E1B 19 kDa protein-interacting protein 3-like) are some of the most known proteins related to mitophagy. Quantitative PCR (qPCR) was used to test the expression levels of the genes encoding the proteins mentioned before in total kidney samples from mice p30 and mIMCD3 cells. When comparing the expression levels between WT and mutant mIMCD3 cells, we found no significant differences, with the data showing a wide dispersion (Figure *31*). However, in kidney samples from mice, the studied genes showed significant differences, with a **decrease in expression observed in the *Pkd1* KO condition**, with the exception of *Atg7* (Figure *32*).

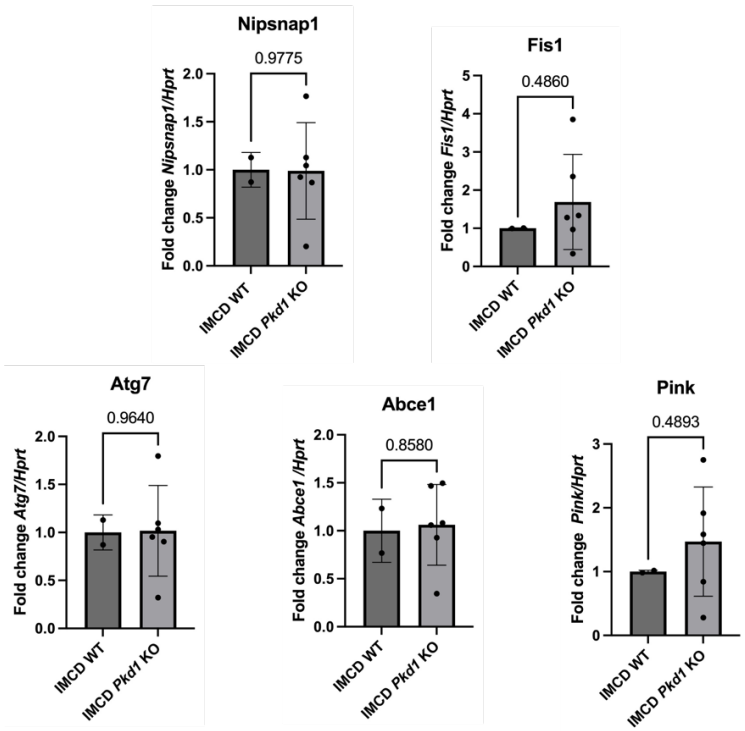

Figure 31. Gene expression of mitophagy-related genes in mIMCD3 cells. None of the genes were differentially expressed in mIMCD3 cells. Statistical significance was determined by unpaired t-test (two-tailed) and presented as the mean ± SEM.

4.3.2. Protein levels of mitophagy-related proteins

Using Western Blot technique, we validated that the levels of the proteins related to mitophagy were indeed decreased. It is important to mention that after testing several loading controls (HSP90 and β-actin), we decided that the most appropriate method to normalize the results was total protein, quantified by Ponceau staining.

The Western Blot results for the proteins FIS1 and PHB1 were not significant in the cell samples (Figure 33a) but were significant in the mouse samples (Figure 33b).

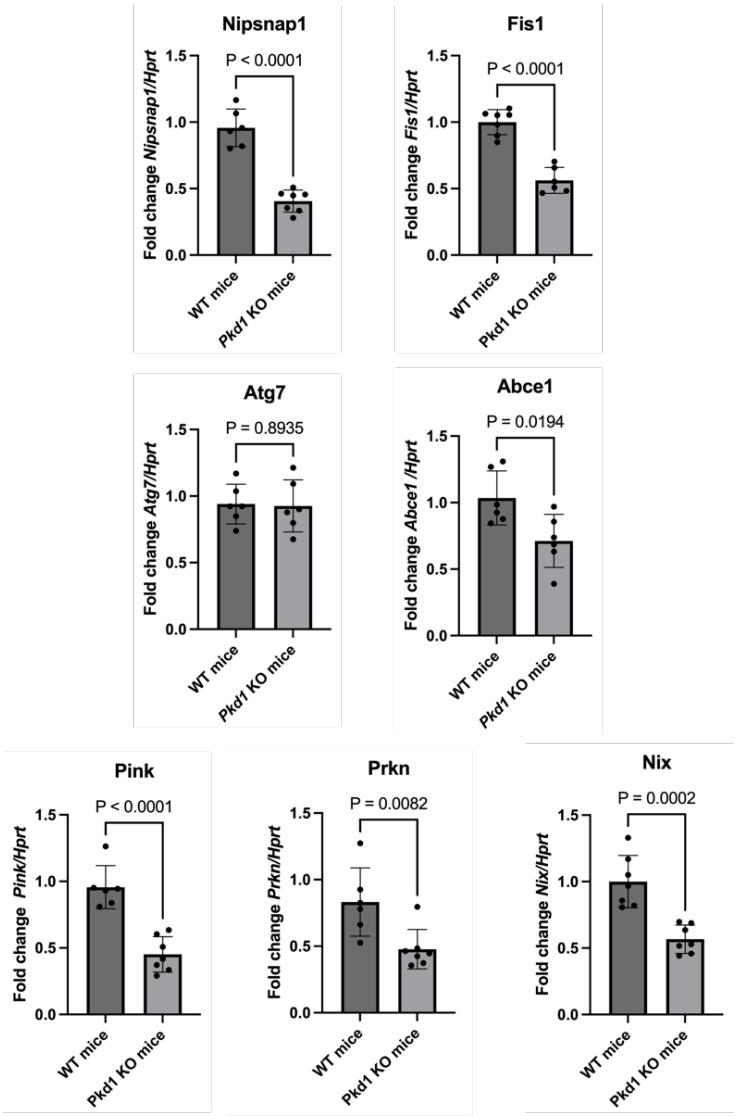

Figure 32. Gene expression of mitophagy-related genes in *Pkd1*$^{flox/flox}$; TamCre (p30). For *Prkn*, a non-parametric Mann Whitney test was used. All genes were differentially expressed except *Atg7*. Statistical significance was determined by unpaired t-test (two-tailed) and presented as the mean ± SEM.

Both proteins were downregulated in the *Pkd1*-mutant mice. The validation of the NISP1 protein was more complicated, as the antibody reacted at multiple points on the membrane in both cell lysate and tissue lysate samples (Figure *34*a). The theoretical weight of the protein is 30 kDa, and the densitometry of that bands did not show significant differences between conditions (data not shown). However, upon studying the pattern, we thought that the extra bands might not be due to non-specificity but rather to isoforms of the protein or post-translational modifications. For this reason, we decided to perform a 2D SDS-PAGE gel (Figure *34*b), separating the proteins in two dimensions: first by their isoelectric point and then by their molecular weight. This method provides information about the different variants of the protein and helps rule out possible non-specificities. **NISP1 is a modified protein and is differentially modified between the WT and *Pkd1*-mutant conditions**. The disadvantage of the 2D gel is that it does not allow for quantification of the protein, so we could not verify the downregulation of the protein.

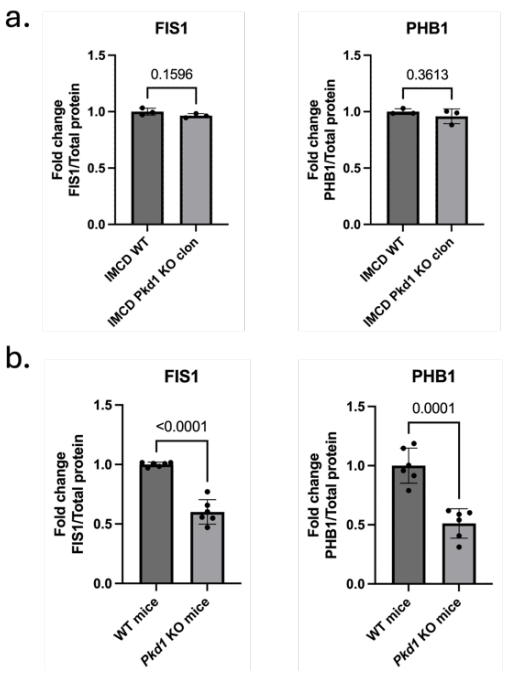

Figure 33. Statistical analysis of densitometry data from Western Blot for proteins related to mitophagy in mIMCD3 and *Pkd1*$^{flox/flox}$; TamCre (p30) mice. The differences in protein abundance in cells were not statistically significant (***a.***) however, significant differences were observed in the mouse tissue samples (***b.***). Statistical significance was determined by unpaired t-test (two-tailed) and presented as the mean ± SEM.

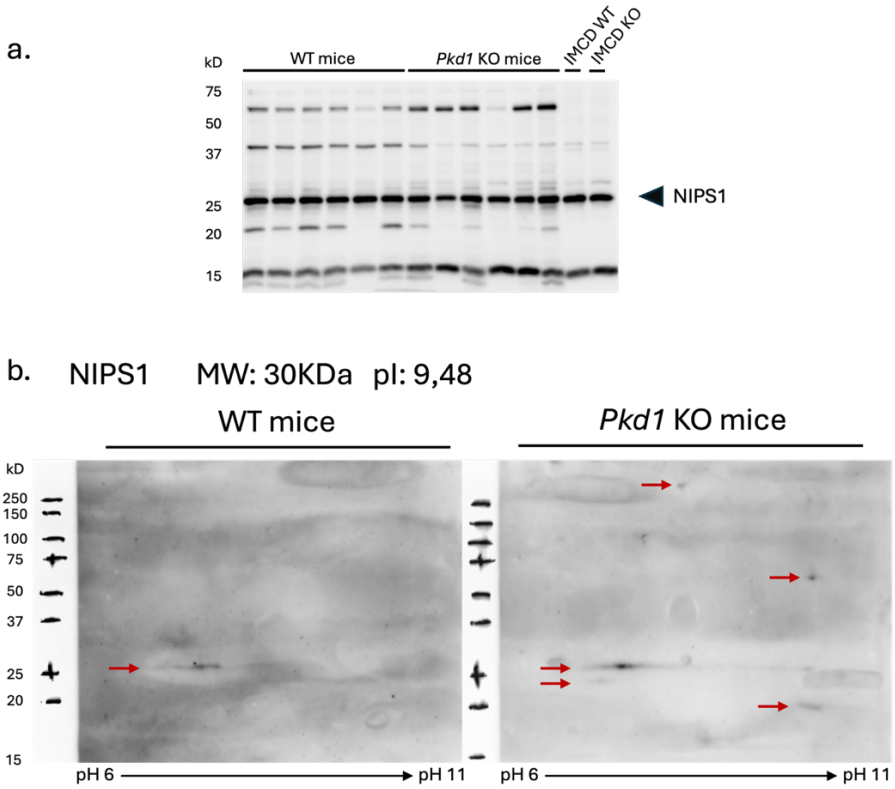

Figure 34. Validation of the NISP1 protein levels. a. Western Blot membrane incubated with anti-NISP1 antibody reveals multiple bands in addition to the theoretical band at 30 kDa. **b.** Validation of the NISP1 protein using a 2D approximation, which shows multiple protein modifications in *Pkd1* KO mice comparing to WT (red arrows).

4.3.3. Mitophagy and autophagy

4.3.3.1. Assessment of mitophagy by mt-m-keima

To measure the level of mitophagy we used mt-mKeima, a pH-sensitive fluorescent protein. Mt-mKeima enters the mitochondria because it contains a targeting sequence derived from subunit VIII of cytochrome c oxidase (Karantanou & Bibli, 2024). Mt-mKeima, along with its targeting sequence, is imported into the mitochondrial matrix through the translocation complexes TOM (Translocase of the Outer Membrane) and TIM (Translocase of the Inner Membrane). Mitochondrial peptidases recognize and remove the targeting sequence, leaving mt-mKeima free in the matrix. In a neutral environment (pH7) such as the mitochondrial matrix, mt-mKeima is predominantly excited at 440 nm. However, when mitochondria are degraded in lysosomes, the environment becomes acidic (pH4), and mt-mKeima is predominantly excited at 585 nm. This change in excitation allows for the distinction between intact mitochondria and those being degraded, facilitating the monitoring of mitophagy.

In the mIMDC3 WT condition, there are fewer mitochondria and therefore less mitophagy, while in the mutant condition, there are a greater number of mitochondria and more mitophagy (Figure *35*a,b). An increase in mitochondrial mass is consistent with the results obtained with Mitotracker Green FM staining (section 4.2.6.1). **The relative level of mitophagy in both conditions was calculated** (degrading mitochondria/active mitochondria) **and found to be very similar** (Figure *35*c). We suggest that these results might be due to a certain level of stress in both conditions. These data do not provide sufficient evidence to confirm the downregulation of mitophagy. Further experimentation is required, and the use of mt-m-keima has proven to be an excellent basis for this purpose.

4.3.3.2. Assessment of autophagy by LC3-GFP

Autophagy was also examined due to the inherent interest in understanding its status, its relation to mitophagy, and its ability to indicate the current state of the cell. The pBABEpuro-LC3-GFP plasmid allows for the study of autophagy in living cells. Cells infected with this plasmid express the LC3-GFP fusion protein. The GFP (Green Fluorescent Protein) signal can be detected by flow cytometry or microscopy. By flow cytometry we observe **a higher number of mutant cells expressing LC3-GFP compared to WT cells.** Additionally, **mutant cells emit a higher signal than WT cells** (Figure 36a,b).

The results presented show significant differences between the two conditions studied but do not specifically indicate the state of autophagy in the cells. Further experimentation is required.

To note, the cells positively expressing pBABEpuro-LC3-GFP were selected with 1μg/mL of puromycin for 7 days. When performing the MTT viability assay to establish the puromycin kill curve for mIMCD3 WT and *Pkd1* KO cells, we observed that the mutants were more resistant to the antibiotic. On day 7, with 0.5g/mL of puromycin, mutant cells remained viable, similar to the condition without the antibiotic (Figure 37).

Autophagy was also tested by Western Blot, using cell lysate and mouse kidney protein samples. **Only in the mouse samples were we able to confirm a significant decrease in autophagy based on the LC3II/LC3I ratio** (Figure 38 and Supplemental figure *3*).

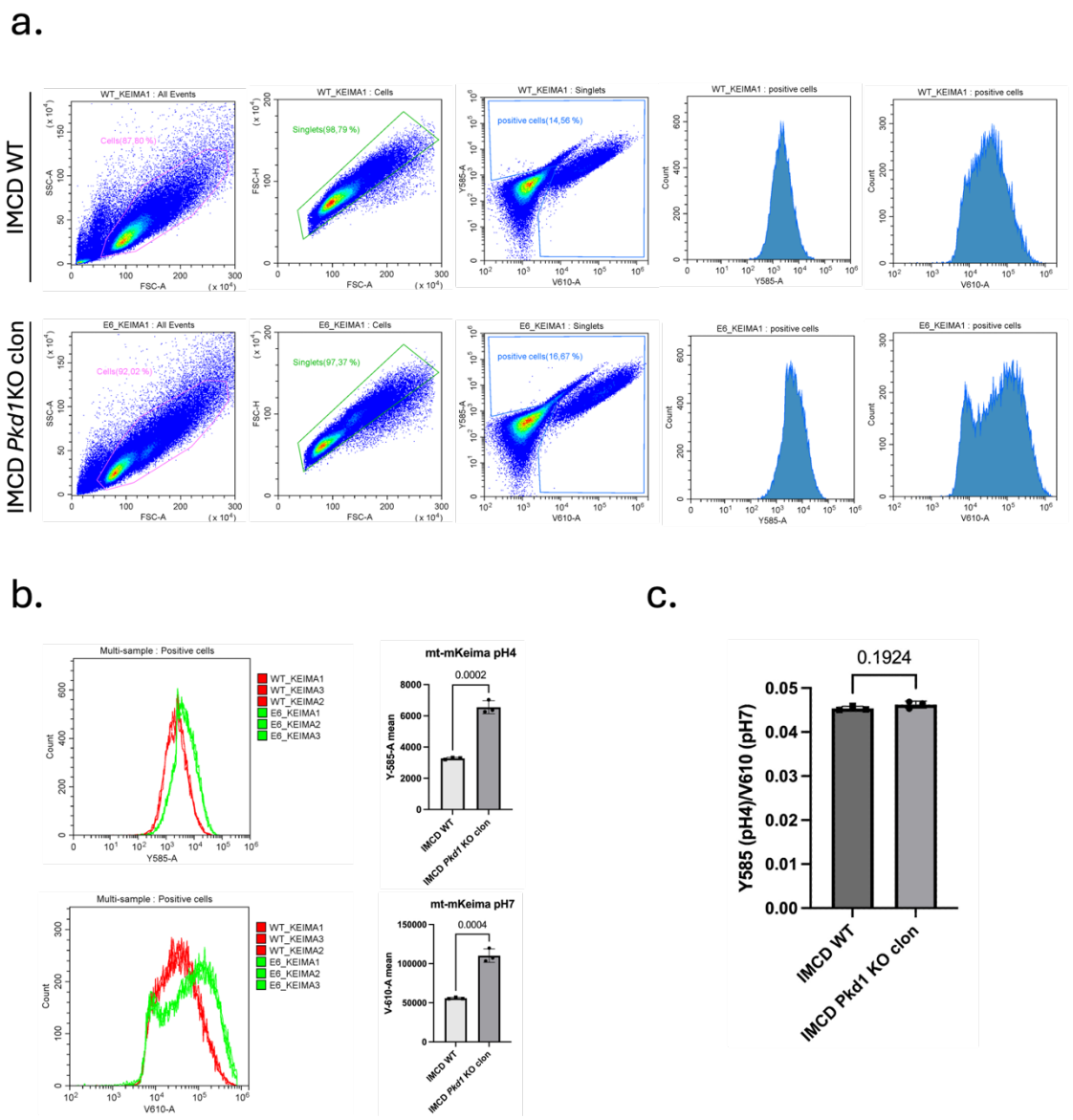

Figure 35. Flow cytometry analysis of mIMCD3-mt-mKeima cells a. Dot plots showing population gating, doublet exclusion, gating of fluorescent signal-positive cells, and signal intensity measurements. **b.** Plots depicting the mean signal intensity at pH4 and pH7 per group (WT and *Pkd1* KO clone). **c.** Ratio of degrading mitochondria (Y585) to active mitochondria (V610) to determine the mitophagy rate. Statistical significance was determined by unpaired t-test (two-tailed) and presented as the mean ± SEM.

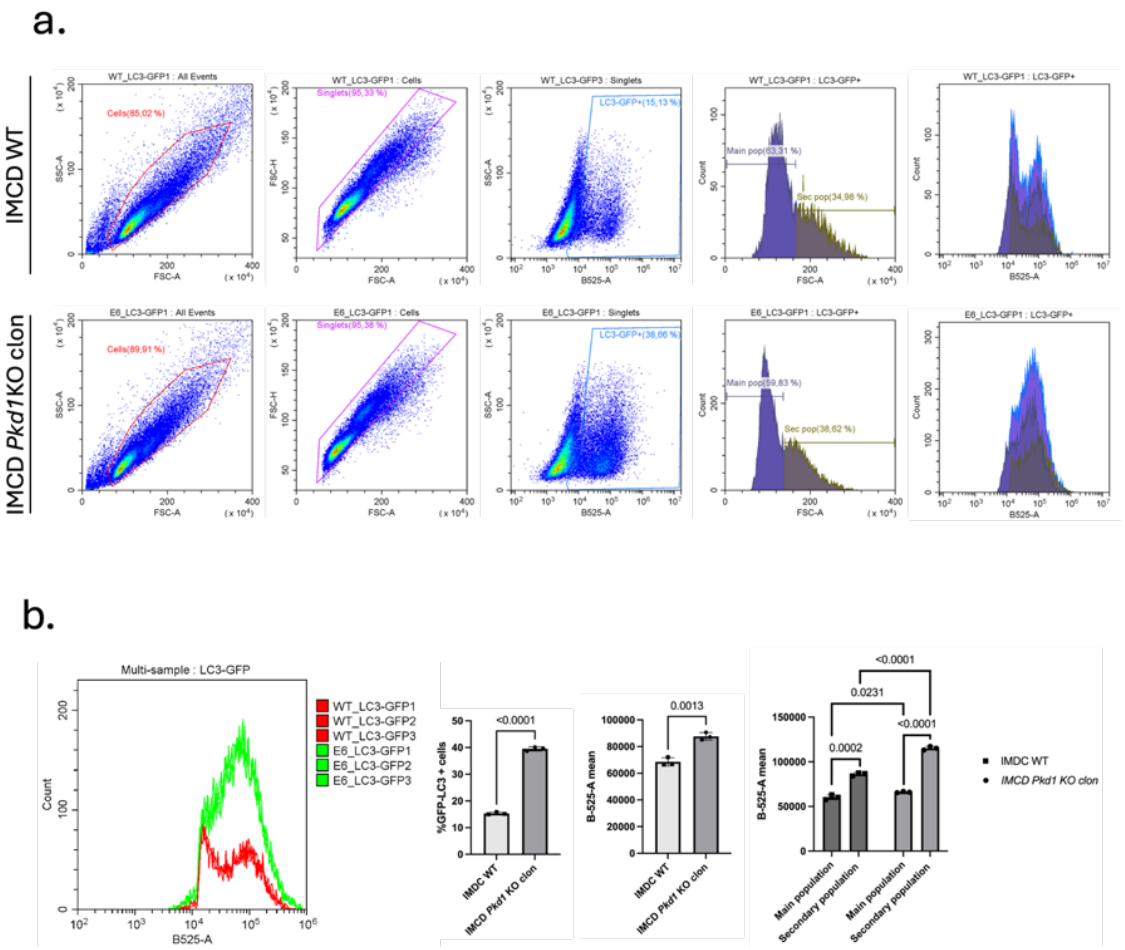

Figure 36. Flow cytometry analysis of mIMCD3-LC3-GFP cells a. Dot plots showing population gating, doublet exclusion, gating of fluorescent signal-positive cells, subpopulation gating, and signal intensity measurements. **b.** Plots depicting the percentage of GFP-LC3 positive cells, mean signal intensity per group (WT and *Pkd1* KO clone) and per subpopulation. Statistical significance was determined by unpaired t-test (two-tailed) and presented as the mean ± SEM.

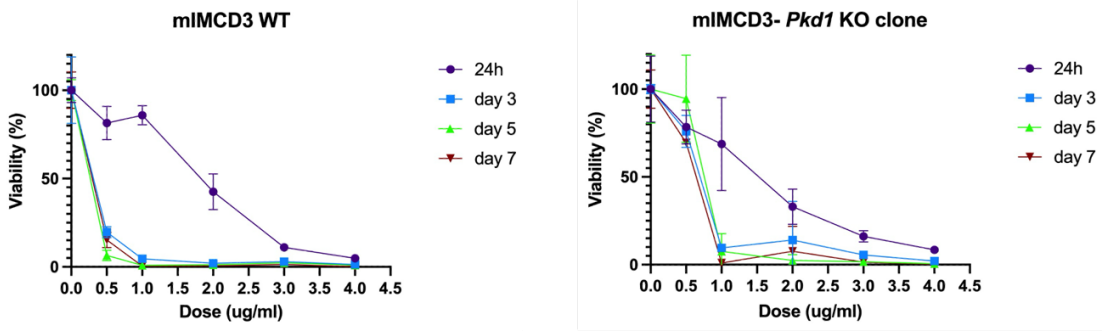

Figure 37. MTT viability assay. mIMCD3 cells were treated for 7 days with different doses of puromycin. mIMCD3 *Pkd1* KO cells were more resistant to puromycin than WT. The graphs were created using GraphPad Prism.

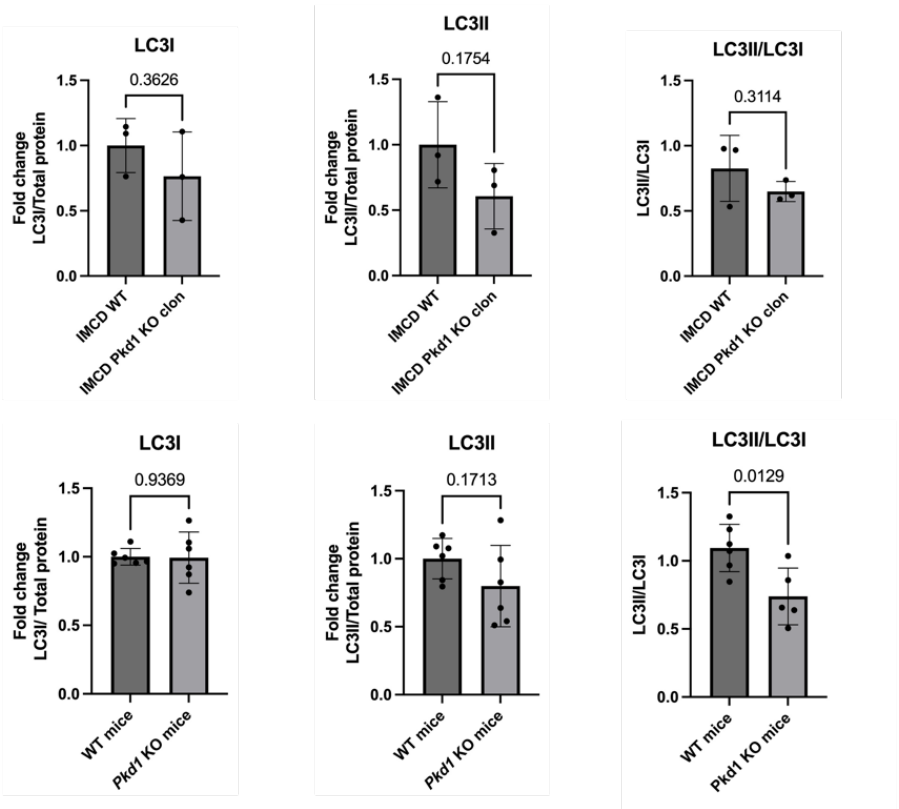

Figure 38. Statistical analysis of densitometry data from Western Blot for LC3. In cell samples, the data was dispersed and not significant; however, in mouse samples, a reduction in autophagy was confirmed. Statistical significance was determined by unpaired t-test (two-tailed) and presented as the mean ± SEM.

5 DISCUSSION

5.1. FUNCTIONAL VALIDATION OF VARIANTS OF UNCERTAIN SIGNIFICANCE (VUS) IN *PKD1*

ADPKD is a monogenic disorder that, although classified as a rare disease, has a relatively high prevalence, affecting approximately 1 in 400 to 1 in 1,000 individuals. In a nephrology genetics laboratory, it is one of the most frequently diagnosed conditions. This thesis addressed inconclusive cases of ADPKD, where, despite finding potential justifications for the disease, there was insufficient or not robust enough evidence to support causality.

Two families in our PKD cohort had two variants (E3068Q and A1368V) in the *PKD1* gene in *cis*, classified as variants of uncertain significance (VUS) by variant classification tools. We were convinced that these variants were important for the diagnosis of the families as they segregated in both. We proposed several hypotheses and began by validating the simplest one: the E3068Q variant, located at the first nucleotide of exon 26, could be a splicing variant. It is worth mentioning that during this thesis, the verdict on this variant changed three times in Varsome and there was a time when it indicated pathogenicity due to its proximity to a splicing region. We conducted a search in splicing predictors and designed a splicing minigene assay, which was successful. We demonstrated that if the mutant variant was present in the cDNA, the canonical transcript was not detected after transcription. The absence of the canonical transcript indicates that the variant indeed affects the splicing process. However, we do not know the exact error in splicing that occurs.

The classification of the variant E3068Q as pathogenic can improve the assessment of rapid progression in ADPKD. This is based on the PROPKD score, a prognostic model that predicts renal outcomes in ADPKD patients using genetic and clinical data (Gall et al., 2016). As one of the criteria for prescribing tolvaptan is being identified as a rapid progressor, patients from both families have an increased likelihood of accessing tolvaptan treatment.

Recently, the relevance of splicing variants in ADPKD has been emphasized. A paper published in 2023 (Hort et al., 2023), aimed to study undiagnosed patients from an ADPKD Australian cohort. The authors employed an approach that combined short- and long-read genomic sequencing and RNA analysis to investigate ADPKD families without a diagnosis after standard testing. In the small cohort studied (n=9), they found that in families with a typical ADPKD phenotype, the most likely variants to be found are those impacting splicing. This is also what we have observed in our case. One advantage of their study is that they have optimized a protocol and are able to use blood samples from patients to extract RNA. This significantly reduces the analysis time and makes it more feasible as a routine test, although it requires the design of highly specific primers for *PKD1* that avoid amplification of pseudogenes. Another noteworthy factor is their successful use of a new splicing predictor, Introme (Sullivan et al., 2023), which considers the effect of both coding and non-coding variants in splicing.

Splicing has also been a subject to the ClinGen (Clinical Genome Resource) SVI Splicing subgroup, a group of experts designated to refine recommendations for applying ACMG/AMP codes relating to splicing data and computational prediction. They emphasize the role of bioinformatic tools for splicing variant prediction, but they admit

that it is challenging, due to the increasing number of tools and the variability of the results. Curators analyze various possible scenarios based on the available information about the candidate splicing variant (splicing predictors and functional data) and specific gene considerations (eg. if a loss of function (LoF) of the gene is a known mechanism of disease) to provide guidance on which ACMG/AMP code is most appropriate to use and the level of strength that should be attributed. Doing this correctly can make a significant difference in the final verdict (Walker et al., 2023). It was following these indications that got a final verdict to E3068Q of "pathogenic" according to Varsome and Franklin. As it was mentioned, the classification of E3068Q has change over the years, presumably due to changes in the considered predictors or changes in the criteria or the level of strength assigned to the criteria. Currently, a Kidney Cystic and Ciliopathy Disorders Variant Curation Expert Panel is working to adapt the ACMG/AMP guidelines to the specific causality of cystic diseases, with an initial focus on the *PKD1* gene (https://clinicalgenome.org/affiliation/50066/). This expert perspective could represent a significant advancement in the classification of VUS and in the approach to splicing variants, thereby in the diagnosis of ADPKD.

Fortunately, one of the variants that we were studying was a candidate for a splicing assay, but most VUS are not of this type. Had we continued our investigation, we would have encountered the challenge of designing an original, innovative, and exclusive functional study for the variants under examination, without any indication of which phenotype to study. For instance, in 2014, a study was conducted to examine the functional expression and cilia-trafficking properties of mutant forms of murine PC1 and human PC2 *in vitro*, as well as PC1 *in vivo*. It was discovered that certain pathogenic amino acid substitution mutations in PC1 and PC2, along with mutations affecting GPS cleavage in PC1, hindered the polycystins from trafficking to cilia. The authors proposed that evaluating cilia trafficking as an *in vitro* functional study could be a useful method for testing the pathogenicity of a subset of PC1 mutations (Cai et al., 2014). However, a "universal" functional model to test the pathogenicity of any variant in *PKD1* or *PKD2* does not yet exist. What does exist is the need, and therefore the search for a differential phenotype WT-mutant *in vitro* has been a research objective. This is a complex objective given that commonly used cell lines, such as mIMCD3, have been shown to be heterogeneous and exhibit clonal variability and, the same may be occurring with other cell lines (Westermann et al., 2022). The development of a good *in vitro* model (clear and measurable phenotype) for ADPKD is an ongoing effort, not only for variant testing but also for studying the disease's pathophysiology and drug screening. Ideally, this model would represent the entire human kidney and the adjacent structures, and current endeavors are promising (Garreta et al., 2024).

In this thesis, we aimed to collaborate in the search for an effective functional assay to test the pathogenicity of *PKD1* variants. The results of the proteomic study that we develop, could help to identify a biomarker directly related to PC1 function, serving as an indicator of pathogenicity. It may not be necessary to rely on a single marker; instead, we might need to look for a proteomic fingerprint based on the levels of several proteins to assess the pathogenicity. Even though we did not focus on that task during the course of the thesis we have data that could be further explored for this purpose.

5.2. PROTEOMIC ANALYSIS OF MONOCLONAL WT AND *PKD1* MUTANT MIMCD3 CELLS

Despite the significant advances made by the scientific community studying ADPKD in recent decades, there remains considerable uncertainty about the molecular pathology of the disease. Specifically, the function of polycystins and why their absence or dysfunction dysregulates the cellular system is not fully understood. In this thesis, we adopted a molecular approach to study the disease, opting to conduct a comparative proteomic analysis using an immortalized and monoclonal cell model. The mIMCD3 cell line, commonly used in the study of renal diseases and ADPKD, offers the advantage of being monoclonal, which helps reduce variability in the cultures (Westermann et al., 2022). The cells grow in a monolayer for several days until they reach confluence. WT cells adapt their shape as they grow, whereas mutant cells are unable to do so and require more space to grow. This phenomenon could be related to the cellular morphological changes described by Dong et al. in 2021. They observed that the flattened cells of cysts present in a *Pkd2* mutant mice, after the re-expression of PC2, progressively reverted to a cuboidal morphology. Therefore, the fact that we observed a higher number of cells per plate in the WT condition does not imply increased proliferation but rather that their morphology allows them to occupy less space compared to the flattened mutant cells. The polycystins may be related with cell shape.

We compared mIMCD3 WT and *Pkd1* KO cells at the proteomic level to describe their differences in protein abundance and to understand the molecular mechanisms underlying the disease. The enrichment analysis of the dysregulated identified proteins revealed the importance of mitochondria and metabolism, which is not surprising given their known role in the disease (Cassina et al., 2020; Padovano et al., 2018). Additionally, terms related to RNA were highlighted, possibly associated with the cellular adaptation occurring in the cells, which requires gene expression and the synthesis of new proteins. The enrichment analysis did not indicate the kidney among the potential tissues, which we suggest may be due to the pathological state of the cells and the expression of proteins under stress conditions that are typically found in other tissues of the body. These same cells were subjected to a proteomic study by other researchers, and the enrichment results were totally different. In their case, the most enriched terms were related to cell substrate and junction assembly, integrin-mediated signaling, and cell-matrix adhesion. We believe that the differences may be due to the way the cells were cultured, sample collection or mass spectrometry analysis (Busch et al., 2024).

Metabolism was found to be dysregulated, but not in the way most frequently described. We could not validate the Warburg effect in our cells; we do not know if glycolysis is altered, but what we have clearly observed is that the cells are capable of using fats as an energy source. Other authors had proposed that proliferative cells needed fatty acids to synthesize new membranes (Podrini et al., 2018). However, in an *in vitro* model like the one we have used, where the cells are confluent for several days (6 days), they do not need to synthesize membranes because they do not have much more space to grow. Another discrepancy with the literature is the apparent elevated oxidative phosphorylation. We found many subunits of the electron transport chain complexes to be upregulated. The mIMCD3 *Pkd1* KO cells seem capable of using oxygen for energy production. Searching through the entire protein list in the gene ontology category for "lipid" and "fatty," we did not find any terms associated with anabolism, only catabolism. Therefore, we suggest that in our confluent culture, fatty acid synthesis is not needed, and

the cells can efficiently use the available fatty acids for energy production. We can conclude that the metabolism in mIMCD3 *Pkd1* KO cells is significantly altered.

Stress and apoptosis were also discussed. Starting with stress, we found key proteins for the control of stress caused by ROS or toxic agents to be both upregulated and downregulated, although we cannot explain why this occurs. The mitochondrial superoxide dismutase (SODM; *Sod2*) and cytosolic superoxide dismutase (SODC; *Sod1*) enzymes were detected as upregulated and downregulated in mutant cells, respectively. SODM has a high fold change, indicating its abundant presence and suggesting the need to eliminate reactive oxygen species (ROS) in the mitochondria. The thioredoxin-dependent peroxide reductase, mitochondrial (PRDX3; *Prdx3*) enzyme, which detoxifies peroxides, is upregulated and plays a crucial role in protecting the cell against oxidative stress, while, Peroxiredoxin-5, mitochondrial (PRDX5; *Prdx5*) is downregulated. PRDX5 has previously been reported as downregulated in association with ADPKD, linked to cyst formation and growth (Agborbesong et al., 2022). It is not known why enzymes with the same purpose can be both upregulated and downregulated. Perhaps the damage and stress control mechanisms are at their limit. Currently, some of the proposed treatments for ADPKD involve using antioxidants (melanin nanoparticles), and the results are promising (CassinaLaura & BolettaAlessandra, 2024; Y. Sun et al., 2024). Regarding apoptosis, we cannot say that an apoptosis process is occurring based solely on proteomics, because the proteins we found related to apoptosis have many other functions. We can only emphasize that we found pro-apoptotic proteins to be upregulated while anti-apoptotic proteins were downregulated. This will need to be confirmed with specific tests. There are specific kits that can easily differentiate among living, dead, and apoptotic cells by flow cytometry.

The proteomic analysis identified two dysregulated proteins associated with cell division: CDK1 (Cyclin-dependent kinase 1) and CDC5L (Cell division cycle 5-like protein). A TRAP (translating ribosome affinity purification) RNASeq experiment, conducted with total kidney samples, described an enrichment of dysregulated genes related to the cell cycle, involving 167 differentially dysregulated genes linked to CDCA. This finding was observed only in male mice, which progress more rapidly than females. Additionally, the study's authors noted that this cell cycle-related transcriptional signature is present at 7 weeks but not at 10 weeks. They argue that the increased proliferation in males correlates with faster progression, while in females, this signature appears at a later stage. *Cdk1* and *Cdc5l* show the same trend in this study as in our proteomic data, upregulated and downregulated, respectively. For *Cdk1*, the results were replicated at weeks 7 and 10 in both males and females, but *Cdc5l* only coincided in males at week 7. Sexual dimorphism appears to be very relevant in mice, both *in vivo* and *in vitro (*https://pkdgenesandmetabolism.org/) (Zhang et al., 2024).

We can conclude that in mIMCD3 *Pkd1* KO cells, there is significant metabolic dysregulation. However, it is difficult to connect what is happening actively. With proteomics, we are observing a static moment, and the cell is likely undergoing dynamic changes, making some of the results difficult to interpret.

Once the fundamental role of the mitochondria was revealed, we proceeded to study it *in vitro*. We wanted to determine the state of the cell and the mitochondria in mIMCD3 cells under the same conditions we used for proteomics. We examined the cell cycle profile, mitochondrial mass, mitochondrial membrane potential, and mitochondrial morphology. Firstly, in the flow cytometry experiments, we found something very

interesting: the cell populations were different between WT and *Pkd1* KO. Although the range of complexity and size was almost the same, there was a well-defined population (second population) with a larger size in the mutant condition (Figure *21*). Regarding the cell cycle profile, we observed that the synthesis phase was significantly decreased in the mutants, with a tendency towards a decrease in the G_1 phase and an increase in the G_2/M phase. These data suggest increased cell proliferation or a certain genetic instability, which is further confirmed when we analyze the total cell population. We found that the mutant cells have many more polyploid cells, cells with a DNA content different from 2N or 4N. Polyploidy may be an adaptive response to stress (Burbridge et al., 2021). In fact, in organs as the liver, hepatocytes include both diploid and polyploid populations. In mice livers, the greater the number of polyploid hepatocytes, the lower the likelihood of developing liver cancer following severe liver damage. Moreover, polyploid hepatocytes retain the ability to regenerate liver tissues during chronic damage without causing mitotic errors (Y. H. Lin et al., 2020). There are tissues where polyploidy is regulated and beneficial, and others where it can contribute to genetic instability.

The study of cell proliferation was not addressed in this work. However, we recognize this as a significant limitation that warrants further investigation. Proteomic data indicating an increase in CKD1, the cell cycle assay showing an elevation in the G_2/M phase in mutants, and the characteristic proliferative increase associated with ADPKD all suggest potential cell division. Nevertheless, the high cell confluence observed suggests otherwise. Serum deprivation was employed to eliminate protein residues from the cell medium that could interfere with our assays. But also, serum deprivation was combined with high confluence to induce the development of the primary cilium, which occurs in non-dividing cells (G_0-G_1) (Tucker et al., 1979). Despite our efforts, synchronization of the cells in the G_0-G_1 phase was not achieved under any condition, as both conditions continued to exhibit cell division. We consider the verification of the proliferative state of the cells to be of fundamental importance.

The mIMCD3 *Pkd1* KO cells exhibited an increased mitochondrial mass compared to the WT cells, which could be related to a higher energy demand of the cells or an attempt to compensate for some mitochondrial defect. The population of larger cells has a greater mitochondrial mass. A two-fold increase in mitochondrial mass had been described in cyst-lining cells in human ADPKD kidneys (Kuo et al., 2019). Additionally, the membrane potential has a tendency to increase in the mutant condition, which makes sense given the higher number of mitochondria in that condition. However, given that there are also more mitochondria per cell, we would like to determine whether this is simply due to a higher number of mitochondria or if these mitochondria inherently have a higher membrane potential. Ideally, a ratio between the membrane potential and the number of mitochondria should be established. Since the staining were done separately, we cannot calculate the TMRM/MitoTracker Green ratio. Measurements of membrane potential and mitochondrial mass should be performed on the very same cells. A TMRM and MitoTracker Green co-staining would also be useful for microscopy imaging. Another aspect to improve in this experiment is the control with FCCP that we used for gating the TMRM-positive populations. We should increase the FCCP dose to ensure that the percentage of the TMRM-positive population does not significantly differ between the WT and mutants (Figure *24*). The literature describes that the membrane potential in ADPKD does not change between WT and *Pkd1*$^{-/-}$ cells (Rowe et al., 2013). However, it also reports a significant increase in membrane potential in mutants from three conditional *Pkd1* cell lines compared to their controls, using TMRM (C. C. Lin et al., 2018).

The microscopy images we obtained using only MitoTracker Green showed the WT cells to be highly confluent, with cells having minimal cytoplasm where the mitochondria were located. Due to the high confluence of the culture, we could not obtain magnified images of these mitochondria. In the case of the mutant cells, we observed cells with similar characteristics, but in some areas, we also observed larger cells with more extensive cytoplasm. In these areas, we could observe cells with normal mitochondrial networks, others with more fragmented and globular mitochondria, some cells with mitochondria showing high signal intensity, and others with low signal intensity. The presence of multinucleated cells was also notable. Our intention was to make a comparison between the two conditions; however, given the situation of the WT cells, we were unable to do so. If we perform a TMRM and MitoTracker Green co-staining, we could verify, for example, whether the more fragmented cells have a lower or higher membrane potential.

Our data show that the mIMCD3 mutant cells have a greater mitochondrial mass, as evidenced by the staining with MitoTracker Green and the experiment with mt-mKeima; and that the membrane potential has a trend to be higher than in WT cells. Likewise, the second population revealed by flow cytometry, compared to the first population, has larger cells, greater mitochondrial mass and higher membrane potential. This second population includes a greater number of cells in the *Pkd1* KO condition than in the WT condition.

With the intention of identifying a protein or pathway that could be interesting as a disease marker, therapeutic target, or as a connection to the process of cystogenesis and the function of polycystins, we conducted a comparative analysis between the proteomics of mIMCD3 cells and the renal proteomics of *Pkd1*$^{flox/flox}$; TamCre mice sacrificed at postnatal day p18 (early cystogenesis) and p30 (advanced cystogenesis).We found that many of the proteins were shared, although not all had the same abundance trend. Therefore, we restricted our analysis to those that showed the same trend. Among the downregulated proteins, we found that most were mitochondrial, which is not surprising given our previous findings. Four of these proteins (NISP1, FIS1, PHB1 and MIC60) were related to mitophagy, an essential process that we deemed necessary to study, as autophagy has been shown to be beneficial for ADPKD (Dong et al., 2021). We believe that mitophagy may represent a significant part of this macroautophagy, given the workload on the mitochondria and the resulting stress. For this reason, we continued the line of research by validating the proteins found in the proteomics associated with mitophagy and setting up experiments to study mitophagy in ADPKD.

These proteins are both crucial as components of the mitophagy pathway and individually in mitochondrial function. Their roles include regulating metabolism and maintaining mitochondrial structure. *Fis1* overexpression in adenoviral-mediated acute hepatic conditions is sufficient to reduce oxidative damage and improve glucose homeostasis in high-fat diet-fed mice (Liou et al., 2022). Additionally, *Fis1* is essential for regulating mitochondrial shape and turnover, which is critical for spermatid maturation. Disruption of the *Fis1* gene in male mice causes early arrest of spermatids, leading to increased mitochondrial content and the formation of multinucleated giant cells. These cells accumulate abnormal mitochondria and intermediates of mitophagy and autophagy, indicating a defect in mitophagy (H. Liu et al., 2022; Varuzhanyan et al., 2021). NISP1 has been shown to integrate with lipid metabolism. Specific ablation of *Nipsnap1* in brown adipose tissue (BAT) results in severe defects in beta-oxidation capacity when exposed to cold environmental challenges. This highlights the importance

of NISP1 in regulating energy metabolism and adaptation to cold (Y. Liu et al., 2023). Furthermore, the loss of PHB1 leads to alterations in mitochondrial integrity and function, thereby regulating the release of mitochondrial DNA and subsequent inflammatory responses. This suggests that PHB1 plays a vital role in maintaining mitochondrial homeostasis and modulating immune responses (H. Liu et al., 2022).

We consider mitophagy to be relevant in the context of ADPKD. Based on proteomic results and existing literature on autophagy in ADPKD, we hypothesize that mitophagy is inhibited while apoptosis becomes active once a certain level of stress is exceeded. Our research aims to investigate this hypothesis by first validating the proteins associated with mitophagy. Subsequently, we studied mitophagy in the same cellular model using a well-designed experimental approach. Understanding the events occurring in mitochondria prior to the initiation of mitophagy, the signals that trigger mitophagy in ADPKD, and the mechanisms by which mitophagy is blocked is crucial. If we can uncover the mitochondrial stress factors leading to such conditions, we may be able to develop appropriate treatments. Alternatively, restoring mitophagy could potentially help cells manage stress more effectively. This investigation is an attempt to prevent the "third hit" phenomenon discussed in the introduction.

5.3. DECIPHERING THE ROLE OF MITOPHAGY IN ADPKD

When we decided to validate the proteins related to mitophagy (NISP1, PHB1, and FIS1) that we had identified in the proteomics, we were only able to do so in mouse samples and not in mIMCD3 cells, nor in qPCR or Western Blot. We validated the downregulation for PHB1 and FIS1. Other mitophagy related proteins as PINK or Parkin were found also downregulated in mice samples. *Nipsnap1* gene downregulation was validated by qPCR but for Western Blot we had to do a 2D SDS-PAGE electrophoresis to avoid nonspecificities and detect possible isoforms and modifications The results of the 2D approach showed that there were indeed differences between the WT and mutant samples. NISP1 emerged as one of the most significant proteins on the proteomics list. It would be interesting to determine what modifications it undergoes, whether any of them are directed towards the activation or inhibition of mitophagy, and what causes them.

To verify mitophagy using an alternative methodology, we utilized the fluorophore mt-mKeima. The results showed that there were more mitochondria in the *Pkd1* KO condition, corroborating the MitoTracker results. We calculated a ratio between degrading mitochondria and active mitochondria to accurately normalize the level of mitophagy. We found that the level of mitophagy between WT and mutants was very similar, with no significant differences. This could be due to the WT cells also being under stress conditions, with high confluence and serum deprivation, making it logical for mitophagy to be activated. The approach with mt-mKeima opens up new avenues for exploration.

We were unable to corroborate the decrease in mitophagy in this assay. We believe the reasons may be minimal changes in the culture conditions, which could have resulted in a lower stress level in the new cultures compared to those used for proteomics, and therefore, mitophagy was still functioning. This experiment could be improved by adding controls to overcome some limitations and address some gaps: 1) Control with bafilomycin A1, which prevents the fusion of autophagosomes with lysosomes, thereby blocking degradation, to assess if the increased signal at pH7 in the *Pkd1*KO condition is only due to a higher number of mitochondria or a blockage in the mitophagosome

degradation. 2) Check the results by fluorescent microscopy to locate where the mitochondria are. The healthy mitochondria should be in the cytosol and the degrading mitochondria inside a mitophagolysosome. It exists the possibility of mitochondria in acidic environments by other reasons, as matrix acidification. 3) Test different levels of stress and evaluate how WT and *Pkd1* KO cells react to it. This could be done with a membrane uncoupler or hypoxia, for example.

In conclusion, the preliminary results show that there is more mitophagy, more mitochondria degrading, in mIMCD3 *Pkd1* KO cells compared to WT cells, but the level of mitophagy activation is similar under both conditions.

We also examined the process of autophagy and created an mIMCD3 cell line that stably expresses a fluorophore, in this case, GFP linked to LC3. The resulting data indicate a difference related to autophagy between the two conditions. However, further experimentation is necessary due to several limitations that need to be addressed: 1) By flow cytometry, we are detecting the signal of total LC3B. LC3B exists in two distinct forms based on its function: LC3I, the non-lipidated cytoplasmic form, and LC3II, the lipidated form associated with autophagosomes. To accurately assess autophagy, LC3I and LC3II must be evaluated separately. The proposed solutions will be to observe the cultures using fluorescence microscopy and quantify the LC3 puncta, which are indicative of autophagosomes, and to perform a Western Blot against GFP to discriminate between LC3I and LC3II. 2)LC3II levels could be increased due to enhanced autophagy or a blockage in autophagosome degradation. The solution will be to use a control with bafilomycin A1. If the addition of bafilomycin A1 results in a change in the LC3II/LC3I ratio observed by Western Blot, it would indicate no pre-existing blockage. Conversely, if no change is observed, it would suggest a pre-existing blockage. Currently we have the cell line and we can continue designing experiments and strategies to study autophagy.

We could not know the state of autophagy *in vitro* but it was found decreased by Western Blot using kidney mouse p30 samples. *In vivo* validation has proven to be the most robust, even when validating results from a proteomic analysis of cell samples cultured *in vitro*. We suggest that slight changes in the culture conditions may be the reason. The *in vivo* context appears to be more stable than the *in vitro* one.

Interestingly, related to this approach, it was observed that mutant cells were more resistant to antibiotic treatment, which is reminiscent of what happens with resistance to certain treatments in some cancers.

While there is still much to explore in the study of mitophagy in ADPKD, this thesis has laid the groundwork for future research. We have established foundational methodologies and proposed new experiments to further investigate this area. Our work provides a basis for understanding the mechanisms of mitophagy in ADPKD and sets the stage for subsequent studies aimed at uncovering the intricate details of mitochondrial stress responses and potential therapeutic interventions. By continuing this line of research, we hope to contribute to the development of effective treatments for ADPKD.

6 CONCLUSIONS

1. The inconclusive case studied was finally **genetically diagnosed**. The VUS variant of *PKD1* studied in the functional minigene assay, E3068Q, **affects the splicing process** as the canonical transcript is absent in the presence of the variant. Thanks to the functional information, the variant E3068Q now has a verdict of "**pathogenic**" according to variant classification tools.

2. The proteomic study of mIMCD3 cells has revealed **substantial changes in protein expression,** indicating significant **metabolic alterations in *Pkd1* KO cells**, particularly related to **mitochondrial metabolism**. *Pkd1* KO cells exhibited genetic instability, as evidenced by an altered cell cycle and increased polyploidy. Additionally, these cells showed greater mitochondrial mass and higher mitochondrial membrane potential compared to WT cells. Flow cytometry assays and confocal microscopy confirmed distinct cellular population profiles, with a larger population being predominant in the mutant cells. This suggests that the loss of *Pkd1* leads to profound **genetic, morphological** and **functional changes**.

   Comparative proteomic analysis of mIMCD3 cells with *Pkd1* $^{flox/flox}$; TamCre mice suggested a potential downregulation of mitophagy-related proteins, validated by qPCR and Western Blot in *Pkd1* mutant mice. Preliminary results indicate upregulated mitophagy in mIMCD3 *Pkd1* KO cells compared to WT cells, although the activation level remains similar. While the results obtained so far are inconclusive, the proposed approach emphasizes the **need for further investigation into the role of mitophagy** in the pathogenesis of ADPKD.

7 BIBLIOGRAPHY

Adrián Cordido Eijo. (2021). *New insights and therapeutic approaches of Polycystic Kidney and Liver Disease*. University of Santiago de Compostela (USC).

Agborbesong, E., Zhou, J. X., Li, L. X., Calvet, J. P., & Li, X. (2022). Antioxidant enzyme peroxiredoxin 5 regulates cyst growth and ciliogenesis via modulating Plk1 stability. *FASEB Journal*, *36*(1). https://doi.org/10.1096/FJ.202101270RR

Ars, E., Bernis, C., Fraga, G., Furlano, M., Martínez, V., Martins, J., Ortiz, A., Pérez-Gómez, M. V., Rodríguez-Pérez, J. C., Sans, L., & Torra, R. (2022). Consensus document on autosomal dominant polycystic kindey disease from the Spanish Working Group on Inherited Kindey Diseases. Review 2020. *Nefrología (English Edition)*, *42*(4), 367–389. https://doi.org/10.1016/J.NEFROE.2022.11.011

Audrézet, M. P., Cornec-Le Gall, E., Chen, J. M., Redon, S., Quéré, I., Creff, J., Bénech, C., Maestri, S., Le Meur, Y., & Férec, C. (2012). Autosomal dominant polycystic kidney disease: comprehensive mutation analysis of PKD1 and PKD2 in 700 unrelated patients. *Human Mutation*, *33*(8), 1239–1250. https://doi.org/10.1002/HUMU.22103

Belibi, F., Zafar, I., Ravichandran, K., Segvic, A. B., Jani, A., Ljubanovic, D. G., & Edelstein, C. L. (2011). Hypoxia-inducible factor-1α (HIF-1α) and autophagy in polycystic kidney disease (PKD). *American Journal of Physiology - Renal Physiology*, *300*(5), 1235–1243. https://doi.org/10.1152/AJPRENAL.00348.2010/SUPPL_FILE/REVISEDFIG3.PDF

Bergmann, C., Guay-Woodford, L. M., Harris, P. C., Horie, S., Peters, D. J. M., & Torres, V. E. (2018). Polycystic kidney disease. *Nature Reviews. Disease Primers*, *4*(1). https://doi.org/10.1038/S41572-018-0047-Y

Burbridge, K., Holcombe, J., & Weavers, H. (2021). *Metabolically active and polyploid renal tissues rely on graded cytoprotection to drive developmental and homeostatic stress resilience*. https://doi.org/10.1242/dev.197343

Busch, T., Neubauer, B., Schmitt, L., Cascante, I., Knoblich, L., Wegehaupt, O., Schöler, F., Tholen, S., Hofherr, A., Schell, C., Schilling, O., Westermann, L., & Köttgen, M. (2024). The role of the co-chaperone DNAJB11 in polycystic kidney disease: Molecular mechanisms and cellular origin of cyst formation. *The FASEB Journal*, *38*(21), e70162. https://doi.org/10.1096/FJ.202401763R

Cai, Y., Fedeles, S. V., Dong, K., Anyatonwu, G., Onoe, T., Mitobe, M., Gao, J. D., Okuhara, D., Tian, X., Gallagher, A. R., Tang, Z., Xie, X., Lalioti, M. D., Lee, A. H., Ehrlich, B. E., & Somlo, S. (2014). Altered trafficking and stability of polycystins underlie polycystic kidney disease. *The Journal of Clinical Investigation*, *124*(12), 5129–5144. https://doi.org/10.1172/JCI67273

Carney, E. F. (2017). MicroRNA-17: a new drug target for ADPKD. *Nature Reviews Nephrology 2017 13:5*, *13*(5), 260–260. https://doi.org/10.1038/nrneph.2017.33

Carrera, P., Calzavara, S., Magistroni, R., Den Dunnen, J. T., Rigo, F., Stenirri, S., Testa, F., Messa, P., Cerutti, R., Scolari, F., Izzi, C., Edefonti, A., Negrisolo, S., Benetti, E., Alibrandi, M. T. S., Manunta, P., Boletta, A., & Ferrari, M. (2016). Deciphering Variability of PKD1 and PKD2 in an Italian Cohort of 643 Patients with Autosomal Dominant Polycystic Kidney Disease (ADPKD). *Scientific Reports*, *6*. https://doi.org/10.1038/SREP30850

Cassina, L., Chiaravalli, M., & Boletta, A. (2020). Increased mitochondrial fragmentation in polycystic kidney disease acts as a modifier of disease

progression. *The FASEB Journal*, *34*(5), 6493–6507. https://doi.org/10.1096/FJ.201901739RR

CassinaLaura, & BolettaAlessandra. (2024). Melanin-like nanoparticles as a potential novel therapeutic approach in ADPKD. *EMBO Molecular Medicine*. https://doi.org/10.1038/S44321-024-00173-4

Chapman, A. B., Devuyst, O., Eckardt, K. U., Gansevoort, R. T., Harris, T., Horie, S., Kasiske, B. L., Odland, D., Pei, Y., Perrone, R. D., Pirson, Y., Schrier, R. W., Torra, R., Torres, V. E., Watnick, T., Wheeler, D. C., Ahn, C., Alam, A., Aussilhou, B., … Winston, K. Y. (2015). Autosomal-dominant polycystic kidney disease (ADPKD): executive summary from a Kidney Disease: Improving Global Outcomes (KDIGO) Controversies Conference. *Kidney International*, *88*(1), 17–27. https://doi.org/10.1038/KI.2015.59

Chiaravalli, M., Rowe, I., Mannella, V., Quilici, G., Canu, T., Bianchi, V., Gurgone, A., Antunes, S., D'Adamo, P., Esposito, A., Musco, G., & Boletta, A. (2016). 2-Deoxy-D-glucose ameliorates PKD progression. *Journal of the American Society of Nephrology*, *27*(7), 1958–1969. https://doi.org/10.1681/ASN.2015030231/-/DCSUPPLEMENTAL

Claverie-Martin, F., Gonzalez-Paredes, F. J., & Ramos-Trujillo, E. (2015). Splicing defects caused by exonic mutations in PKD1 as a new mechanism of pathogenesis in autosomal dominant polycystic kidney disease. *RNA Biology*, *12*(4), 369–374. https://doi.org/10.1080/15476286.2015.1014291

Cordido, A., Besada-Cerecedo, L., & García-González, M. A. (2017). The Genetic and Cellular Basis of Autosomal Dominant Polycystic Kidney Disease—A Primer for Clinicians. *Frontiers in Pediatrics*, *5*. https://doi.org/10.3389/fped.2017.00279

Cordido, A., Nunez-Gonzalez, L., Martinez-Moreno, J. M., Lamas-Gonzalez, O., Rodriguez-Osorio, L., Perez-Gomez, M. V., Martin-Sanchez, D., Outeda, P., Chiaravalli, M., Watnick, T., Boletta, A., Diaz, C., Carracedo, A., Sanz, A. B., Ortiz, A., & Garcia-Gonzalez, M. A. (2021). Tweak signaling pathway blockade slows cyst growth and disease progression in autosomal dominant polycystic kidney disease. *Journal of the American Society of Nephrology*, *32*(8), 1913–1932. https://doi.org/10.1681/ASN.2020071094/-/DCSUPPLEMENTAL

Cordido, A., Vizoso-Gonzalez, M., Nuñez-Gonzalez, L., Molares-Vila, A., Chantada-Vazquez, M. D. P., Bravo, S. B., & Garcia-Gonzalez, M. A. (2022). Quantitative Proteomic Study Unmasks Fibrinogen Pathway in Polycystic Liver Disease. *Biomedicines*, *10*(2), 290. https://doi.org/10.3390/BIOMEDICINES10020290/S1

Cornec-Le Gall, E., Alam, A., & Perrone, R. D. (2019). Autosomal dominant polycystic kidney disease. *The Lancet*, *393*(10174), 919–935. https://doi.org/10.1016/S0140-6736(18)32782-X/ASSET/1D394F43-7EDF-453C-9E07-59F7C73C85F3/MAIN.ASSETS/GR3.SML

Cornec-Le Gall, E., Torres, V. E., & Harris, P. C. (2018). Genetic complexity of autosomal dominant polycystic kidney and liver diseases. In *Journal of the American Society of Nephrology* (Vol. 29, Issue 1, pp. 13–23). American Society of Nephrology. https://doi.org/10.1681/ASN.2017050483

de Sainte Agathe, J. M., Filser, M., Isidor, B., Besnard, T., Gueguen, P., Perrin, A., Van Goethem, C., Verebi, C., Masingue, M., Rendu, J., Cossée, M., Bergougnoux, A., Frobert, L., Buratti, J., Lejeune, É., Le Guern, É., Pasquier, F., Clot, F., Kalatzis, V., … Baux, D. (2023). SpliceAI-visual: a free online tool to improve SpliceAI splicing variant interpretation. *Human Genomics*, *17*(1), 1–16. https://doi.org/10.1186/S40246-023-00451-1/FIGURES/9

Devuyst, O., Ahn, C., Barten, T. R. M., Brosnahan, G., Cadnapaphornchai, M. A., Chapman, A. B., Cornec-Le Gall, E., Drenth, J. P. H., Gansevoort, R. T., Harris, P. C., Harris, T., Horie, S., Liebau, M. C., Liew, M., Mallett, A. J., Mei, C., Mekahli, D., Odland, D., Ong, A. C. M., … Torres, V. E. (2025). KDIGO 2025 Clinical Practice Guideline for the Evaluation, Management, and Treatment of Autosomal Dominant Polycystic Kidney Disease (ADPKD). *Kidney International*, *107*(2), S1–S239. https://doi.org/10.1016/J.KINT.2024.07.009/ASSET/2EDF5AC3-D05D-4FB7-BE14-7CE3F85AF852/MAIN.ASSETS/GR2.JPG

Dong, K., Zhang, C., Tian, X., Coman, D., Hyder, F., Ma, M., & Somlo, S. (2021). Renal plasticity revealed through reversal of polycystic kidney disease in mice. *Nature Genetics*, *53*(12), 1649–1663. https://doi.org/10.1038/S41588-021-00946-4

Fedeles, S. V., Tian, X., Gallagher, A. R., Mitobe, M., Nishio, S., Lee, S. H., Cai, Y., Geng, L., Crews, C. M., & Somlo, S. (2011). A genetic interaction network of five genes for human polycystic kidney and liver diseases defines polycystin-1 as the central determinant of cyst formation. *Nature Genetics 2011 43:7*, *43*(7), 639–647. https://doi.org/10.1038/ng.860

Flowers, E. M., Sudderth, J., Zacharias, L., Mernaugh, G., Zent, R., Deberardinis, R. J., & Carroll, T. J. (2018). Lkb1 deficiency confers glutamine dependency in polycystic kidney disease. *Nature Communications 2018 9:1*, *9*(1), 1–11. https://doi.org/10.1038/s41467-018-03036-y

Fowler, D. M., & Rehm, H. L. (2024). Will variants of uncertain significance still exist in 2030? *American Journal of Human Genetics*, *111*(1), 5–10. https://doi.org/10.1016/j.ajhg.2023.11.005

Gall, E. C. Le, Audrézet, M. P., Chen, J. M., Hourmant, M., Morin, M. P., Perrichot, R., Charasse, C., Whebe, B., Renaudineau, E., Jousset, P., Guillodo, M. P., Grall-Jezequel, A., Saliou, P., Férec, C., & Le Meur, Y. (2013). Type of PKD1 mutation influences renal outcome in ADPKD. *Journal of the American Society of Nephrology*, *24*(6), 1006–1013. https://doi.org/10.1681/ASN.2012070650/-/DCSUPPLEMENTAL

Gall, E. C. Le, Audrézet, M. P., Rousseau, A., Hourmant, M., Renaudineau, E., Charasse, C., Morin, M. P., Moal, M. C., Dantal, J., Wehbe, B., Perrichot, R., Frouget, T., Vigneau, C., Potier, J., Jousset, P., Guillodo, M. P., Siohan, P., Terki, N., Sawadogo, T., … Le Meur, Y. (2016). The PROPKD score: A new algorithm to predict renal survival in autosomal dominant polycystic kidney disease. *Journal of the American Society of Nephrology*, *27*(3), 942–951. https://doi.org/10.1681/ASN.2015010016

Garreta, E., Moya-Rull, D., Marco, A., Amato, G., Ullate-Agote, A., Tarantino, C., Gallo, M., Esporrín-Ubieto, D., Centeno, A., Vilas-Zornoza, A., Mestre, R., Kalil, M., Gorroñogoitia, I., Zaldua, A. M., Sanchez, S., Izquierdo Reyes, L., Fernández-Santos, M. E., Prosper, F., & Montserrat, N. (2024). Natural Hydrogels Support Kidney Organoid Generation and Promote In Vitro Angiogenesis. *Advanced Materials*, *36*(34), 2400306. https://doi.org/10.1002/ADMA.202400306

Gimpel, C., Bergmann, C., Bockenhauer, D., Breysem, L., Cadnapaphornchai, M. A., Cetiner, M., Dudley, J., Emma, F., Konrad, M., Harris, T., Harris, P. C., König, J., Liebau, M. C., Marlais, M., Mekahli, D., Metcalfe, A. M., Oh, J., Perrone, R. D., Sinha, M. D., … Schaefer, F. (2019). International consensus statement on the diagnosis and management of autosomal dominant polycystic kidney disease in children and young people. *Nature Reviews Nephrology 2019 15:11*, *15*(11), 713–726. https://doi.org/10.1038/s41581-019-0155-2

Gulati, A., Dahl, N. K., Hartung, E. A., Clark, S. L., Moudgil, A., Goodwin, J., & Somlo, S. (2023). Hypomorphic PKD1 Alleles Impact Disease Variability in Autosomal Dominant Polycystic Kidney Disease. *Kidney360*, *4*(3), 387–392. https://doi.org/10.34067/KID.0000000000000064

Gulati, A., Sevillano, A. M., Praga, M., Gutierrez, E., Alba, I., Dahl, N. K., Besse, W., Choi, J., & Somlo, S. (2020). Collagen IV Gene Mutations in Adults With Bilateral Renal Cysts and CKD. *Kidney International Reports*, *5*(1), 103–108. https://doi.org/10.1016/J.EKIR.2019.09.004

Hajarnis, S., Lakhia, R., Yheskel, M., Williams, D., Sorourian, M., Liu, X., Aboudehen, K., Zhang, S., Kersjes, K., Galasso, R., Li, J., Kaimal, V., Lockton, S., Davis, S., Flaten, A., Johnson, J. A., Holland, W. L., Kusminski, C. M., Scherer, P. E., … Patel, V. (2017). MicroRNA-17 family promotes polycystic kidney disease progression through modulation of mitochondrial metabolism. *Nature Communications*, *8*. https://doi.org/10.1038/ncomms14395

Held, N. M., & Houtkooper, R. H. (2015). Mitochondrial quality control pathways as determinants of metabolic health. *BioEssays : News and Reviews in Molecular, Cellular and Developmental Biology*, *37*(8), 867–876. https://doi.org/10.1002/BIES.201500013

Heyer, C. M., Sundsbak, J. L., Abebe, K. Z., Chapman, A. B., Torres, V. E., Grantham, J. J., Bae, K. T., Schrier, R. W., Perrone, R. D., Braun, W. E., Steinman, T. I., Mrug, M., Yu, A. S. L., Brosnahan, G., Hopp, K., Irazabal, M. V, Bennett, W. M., Flessner, M. F., Moore, C. G., … HALT PKD and CRISP Investigators. (2016). Predicted Mutation Strength of Nontruncating PKD1 Mutations Aids Genotype-Phenotype Correlations in Autosomal Dominant Polycystic Kidney Disease. *Journal of the American Society of Nephrology : JASN*, *27*(9), 2872–2884. https://doi.org/10.1681/ASN.2015050583

Higashihara, E., Horie, S., Kinoshita, M., Harris, P. C., Okegawa, T., Tanbo, M., Hara, H., Yamaguchi, T., Shigemori, K., Kawano, H., Miyazaki, I., Kaname, S., & Nutahara, K. (2018). A potentially crucial role of the PKD1 C-terminal tail in renal prognosis. *Clinical and Experimental Nephrology*, *22*(2), 395–404. https://doi.org/10.1007/S10157-017-1477-7/TABLES/4

Hofherr, A., Busch, T., Huber, N., Nold, A., Bohn, A., Viau, A., Bienaimé, F., Kuehn, E. W., Arnold, S. J., & Köttgen, M. (2017). Efficient genome editing of differentiated renal epithelial cells. *Pflugers Archiv : European Journal of Physiology*, *469*(2), 303–311. https://doi.org/10.1007/S00424-016-1924-4

Hopp, K., Cornec-Le Gall, E., Senum, S. R., te Paske, I. B. A. W., Raj, S., Lavu, S., Baheti, S., Edwards, M. E., Madsen, C. D., Heyer, C. M., Ong, A. C. M., Bae, K. T., Fatica, R., Steinman, T. I., Chapman, A. B., Gitomer, B., Perrone, R. D., Rahbari-Oskoui, F. F., Torres, V. E., & Harris, P. C. (2020). Detection and characterization of mosaicism in autosomal dominant polycystic kidney disease. *Kidney International*, *97*(2), 370–382. https://doi.org/10.1016/j.kint.2019.08.038

Hopp, K., Ward, C. J., Hommerding, C. J., Nasr, S. H., Tuan, H.-F., Gainullin, V. G., Rossetti, S., Torres, V. E., & Harris, P. C. (2012). Functional polycystin-1 dosage governs autosomal dominant polycystic kidney disease severity. *The Journal of Clinical Investigation*, *122*(11), 4257. https://doi.org/10.1172/JCI64313

Hort, Y., Sullivan, P., Wedd, L., Fowles, L., Stevanovski, I., Deveson, I., Simons, C., Mallett, A., Patel, C., Furlong, T., Cowley, M. J., Shine, J., & Mallawaarachchi, A. (2023). Atypical splicing variants in PKD1 explain most undiagnosed typical familial ADPKD. *NPJ Genomic Medicine*, *8*(1). https://doi.org/10.1038/S41525-023-00362-Z

Ishimoto, Y., Inagi, R., Yoshihara, D., Kugita, M., Nagao, S., Shimizu, A., Takeda, N., Wake, M., Honda, K., Zhou, J., & Nangaku, M. (2017). Mitochondrial Abnormality Facilitates Cyst Formation in Autosomal Dominant Polycystic Kidney Disease. *Molecular and Cellular Biology*, *37*(24). https://doi.org/10.1128/MCB.00337-17

Jaganathan, K., Kyriazopoulou Panagiotopoulou, S., McRae, J. F., Darbandi, S. F., Knowles, D., Li, Y. I., Kosmicki, J. A., Arbelaez, J., Cui, W., Schwartz, G. B., Chow, E. D., Kanterakis, E., Gao, H., Kia, A., Batzoglou, S., Sanders, S. J., & Farh, K. K. H. (2019). Predicting Splicing from Primary Sequence with Deep Learning. *Cell*, *176*(3), 535-548.e24. https://doi.org/10.1016/J.CELL.2018.12.015/ATTACHMENT/CDE3A9F2-4502-4B23-9516-A1F40805F15D/MMC4.XLSX

Jiang, M., Bai, M., Lei, J., Xie, Y., Xu, S., Jia, Z., & Zhang, A. (2020). Mitochondrial dysfunction and the AKI-to-CKD transition. *American Journal of Physiology - Renal Physiology*, *319*(6), F1105–F1116. https://doi.org/10.1152/AJPRENAL.00285.2020/ASSET/IMAGES/LARGE/AJ-AFLU200026F004.JPEG

Karantanou, C., & Bibli, S. I. (2024). Monitoring Mitophagy Dynamics in Live Cells. *Methods in Molecular Biology*, *2845*, 161–175. https://doi.org/10.1007/978-1-0716-4067-8_13

Kuo, I. Y., Brill, A. L., Lemos, F. O., Jiang, J. Y., Falcone, J. L., Kimmerling, E. P., Cai, Y., Dong, K., Kaplan, D. L., Wallace, D. P., Hofer, A. M., & Ehrlich, B. E. (2019). Polycystin 2 regulates mitochondrial Ca2+ signaling, bioenergetics, and dynamics through mitofusin 2. *Science Signaling*, *12*(580). https://doi.org/10.1126/SCISIGNAL.AAT7397/SUPPL_FILE/AAT7397_SM.PDF

Kurbegovic, A., Kim, H., Xu, H., Yu, S., Cruanès, J., Maser, R. L., Boletta, A., Trudel, M., & Qian, F. (2014). Novel functional complexity of polycystin-1 by GPS cleavage in vivo: role in polycystic kidney disease. *Molecular and Cellular Biology*, *34*(17), 3341–3353. https://doi.org/10.1128/MCB.00687-14

Lakhia, R., Yheskel, M., Flaten, A., Quittner-Strom, E. B., Holland, W. L., & Patel, V. (2018). PPARα agonist fenofibrate enhances fatty acid β-oxidation and attenuates polycystic kidney and liver disease in mice. *American Journal of Physiology - Renal Physiology*, *314*(1), F122–F131. https://doi.org/10.1152/AJPRENAL.00352.2017/ASSET/IMAGES/LARGE/ZH20101783570006.JPEG

Lanktree, M. B., Haghighi, A., Guiard, E., Iliuta, I. A., Song, X., Harris, P. C., Paterson, A. D., & Pei, Y. (2018). Prevalence estimates of polycystic kidney and liver disease by population sequencing. *Journal of the American Society of Nephrology*, *29*(10), 2593–2600. https://doi.org/10.1681/ASN.2018050493

Lee, E. C., Valencia, T., Allerson, C., Schairer, A., Flaten, A., Yheskel, M., Kersjes, K., Li, J., Gatto, S., Takhar, M., Lockton, S., Pavlicek, A., Kim, M., Chu, T., Soriano, R., Davis, S., Androsavich, J. R., Sarwary, S., Owen, T., … Patel, V. (2019). Discovery and preclinical evaluation of anti-miR-17 oligonucleotide RGLS4326 for the treatment of polycystic kidney disease. *Nature Communications*, *10*(1), 1–14. https://doi.org/10.1038/s41467-019-11918-y

Legué, E., & Liem, K. F. (2019). Tulp3 Is a Ciliary Trafficking Gene that Regulates Polycystic Kidney Disease. *Current Biology : CB*, *29*(5), 803-812.e5. https://doi.org/10.1016/j.cub.2019.01.054

Leonhard, W. N., Zandbergen, M., Veraar, K., Van Den Berg, S., Van Der Weerd, L., Breuning, M., De Heer, E., & Peters, D. J. M. (2015). Scattered deletion of PKD1

in kidneys causes a cystic snowball effect and recapitulates polycystic kidney disease. *Journal of the American Society of Nephrology*, *26*(6), 1322–1333. https://doi.org/10.1681/ASN.2013080864

Lin, C. C., Kurashige, M., Liu, Y., Terabayashi, T., Ishimoto, Y., Wang, T., Choudhary, V., Hobbs, R., Liu, L. K., Lee, P. H., Outeda, P., Zhou, F., Restifo, N. P., Watnick, T., Kawano, H., Horie, S., Prinz, W., Xu, H., Menezes, L. F., & Germino, G. G. (2018). A cleavage product of Polycystin-1 is a mitochondrial matrix protein that affects mitochondria morphology and function when heterologously expressed. *Scientific Reports*, *8*(1), 2743. https://doi.org/10.1038/S41598-018-20856-6

Lin, Y. H., Zhang, S., Zhu, M., Lu, T., Chen, K., Wen, Z., Wang, S., Xiao, G., Luo, D., Jia, Y., Li, L., MacConmara, M., Hoshida, Y., Singal, A. G., Yopp, A., Wang, T., & Zhu, H. (2020). Mice With Increased Numbers of Polyploid Hepatocytes Maintain Regenerative Capacity But Develop Fewer Hepatocellular Carcinomas Following Chronic Liver Injury. *Gastroenterology*, *158*(6), 1698-1712.e14. https://doi.org/10.1053/J.GASTRO.2020.01.026/ATTACHMENT/993F7CE8-5321-4A23-94A8-7461137A70DA/MMC1.XLSX

Liu, H., Fan, H., He, P., Zhuang, H., Liu, X., Chen, M., Zhong, W., Zhang, Y., Zhen, C., Li, Y., Jiang, H., Meng, T., Xu, Y., Zhao, G., & Feng, D. (2022). Prohibitin 1 regulates mtDNA release and downstream inflammatory responses . *The EMBO Journal*, *41*(24). https://doi.org/10.15252/EMBJ.2022111173/SUPPL_FILE/EMBJ2022111173-SUP-0006-SDATAEV.ZIP

Liu, Y., Qu, Y., Cheng, C., Tsai, P. Y., Edwards, K., Xue, S., Pandit, S., Eguchi, S., Sanghera, N., & Barrow, J. J. (2023). Nipsnap1—A regulatory factor required for long-term maintenance of non-shivering thermogenesis. *Molecular Metabolism*, *75*, 101770. https://doi.org/10.1016/J.MOLMET.2023.101770

Ma, M., Tian, X., Igarashi, P., Pazour, G. J., & Somlo, S. (2013). Loss of cilia suppresses cyst growth in genetic models of autosomal dominant polycystic kidney disease. *Nature Genetics*, *45*(9), 1004–1012. https://doi.org/10.1038/ng.2715

Martínez, V., Comas, J., Arcos, E., Díaz, J. M., Muray, S., Cabezuelo, J., Ballarín, J., Ars, E., & Torra, R. (2013). Renal replacement therapy in ADPKD patients: A 25-year survey based on the Catalan registry. *BMC Nephrology*, *14*(1), 1–8. https://doi.org/10.1186/1471-2369-14-186/FIGURES/4

Menezes, L. F., & Germino, G. G. (2019). The pathobiology of polycystic kidney disease from a metabolic viewpoint. *Nature Reviews Nephrology 2019 15:12*, *15*(12), 735–749. https://doi.org/10.1038/s41581-019-0183-y

Menezes, L. F., Lin, C. C., Zhou, F., & Germino, G. G. (2016). Fatty Acid Oxidation is Impaired in An Orthologous Mouse Model of Autosomal Dominant Polycystic Kidney Disease. *EBioMedicine*, *5*, 183–192. https://doi.org/10.1016/J.EBIOM.2016.01.027

Merrick, D., Chapin, H., Baggs, J. E., Yu, Z., Somlo, S., Sun, Z., Hogenesch, J. B., & Caplan, M. J. (2012). The γ-Secretase Cleavage Product of Polycystin-1 Regulates TCF and CHOP-Mediated Transcriptional Activation through a p300-Dependent Mechanism. *Developmental Cell*, *22*(1), 197–210. https://doi.org/10.1016/J.DEVCEL.2011.10.028/ATTACHMENT/9752CB02-1853-477F-B3F1-450CE465A784/MMC5.MP4

Onuchic, L., Padovano, V., Schena, G., Rajendran, V., Dong, K., Shi, X., Pandya, R., Rai, V., Gresko, N. P., Ahmed, O., Lam, T. K. T., Wang, W., Shen, H., Somlo, S., & Caplan, M. J. (2023). The C-terminal tail of polycystin-1 suppresses cystic

disease in a mitochondrial enzyme-dependent fashion. *Nature Communications*, *14*(1). https://doi.org/10.1038/S41467-023-37449-1

Padovano, V., Kuo, I. Y., Stavola, L. K., Aerni, H. R., Flaherty, B. J., Chapin, H. C., Ma, M., Somlo, S., Boletta, A., Ehrlich, B. E., Rinehart, J., & Caplan, M. J. (2017). The polycystins are modulated by cellular oxygen-sensing pathways and regulate mitochondrial function. *Molecular Biology of the Cell*, *28*(2), 261–269. https://doi.org/10.1091/MBC.E16-08-0597/ASSET/IMAGES/LARGE/261FIG5.JPEG

Padovano, V., Podrini, C., Boletta, A., & Caplan, M. J. (2018). Metabolism and mitochondria in polycystic kidney disease research and therapy. *Nature Reviews Nephrology 2018 14:11*, *14*(11), 678–687. https://doi.org/10.1038/s41581-018-0051-1

Pampliega, O., Orhon, I., Patel, B., Sridhar, S., Díaz-Carretero, A., Beau, I., Codogno, P., Satir, B. H., Satir, P., & Cuervo, A. M. (2013). Functional interaction between autophagy and ciliogenesis. *Nature 2013 502:7470*, *502*(7470), 194–200. https://doi.org/10.1038/nature12639

Paterson, A. D., Wang, K. R., Lupea, D., St. George-Hyslop, P., & Pei, Y. (2002). Recurrent fetal loss associated with bilineal inheritance of type 1 autosomal dominant polycystic kidney disease. *American Journal of Kidney Diseases*, *40*(1), 16–20. https://doi.org/10.1053/ajkd.2002.33908

Pei, Y., Paterson, A. D., Rong Wang, K., He, N., Hefferton, D., Germino, G. G., Parfrey, P., Somlo, S., & St. George-Hyslop, P. (2001). Bilineal disease and trans-heterozygotes in autosomal dominant polycystic kidney disease. *American Journal of Human Genetics*, *68*(2), 355–363. https://doi.org/10.1086/318188

Pierides, A., Voskarides, K., Athanasiou, Y., Ioannou, K., Damianou, L., Arsali, M., Zavros, M., Pierides, M., Vargemezis, V., Patsias, C., Zouvani, I., Elia, A., Kyriacou, K., & Deltas, C. (2009). Clinico-pathological correlations in 127 patients in 11 large pedigrees, segregating one of three heterozygous mutations in the COL4A3/ COL4A4 genes associated with familial haematuria and significant late progression to proteinuria and chronic kidney disease from focal segmental glomerulosclerosis. *Nephrology Dialysis Transplantation*, *24*(9), 2721–2729. https://doi.org/10.1093/NDT/GFP158

Piontek, K., Menezes, L. F., Garcia-Gonzalez, M. A., Huso, D. L., & Germino, G. G. (2007). A critical developmental switch defines the kinetics of kidney cyst formation after loss of Pkd1. *Nature Medicine*, *13*(12), 1490–1495. https://doi.org/10.1038/nm1675

Podrini, C., Rowe, I., Pagliarini, R., Costa, A. S. H., Chiaravalli, M., Di Meo, I., Kim, H., Distefano, G., Tiranti, V., Qian, F., di Bernardo, D., Frezza, C., & Boletta, A. (2018). Dissection of metabolic reprogramming in polycystic kidney disease reveals coordinated rewiring of bioenergetic pathways. *Communications Biology 2018 1:1*, *1*(1), 1–14. https://doi.org/10.1038/s42003-018-0200-x

Qian, F. (2015). The Role of G-protein Coupled Receptor Proteolytic Site (GPS) Cleavage in Polycystin-1 Biogenesis, Trafficking and Function. In *Polycystic Kidney Disease*. Codon Publications. https://doi.org/10.15586/CODON.PKD.2015.CH11

Qiu, J., Germino, G. G., & Menezes, L. F. (2023). Mechanisms of Cyst Development in Polycystic Kidney Disease. *Advances in Kidney Disease and Health*, *30*(3), 209–219. https://doi.org/10.1053/J.AKDH.2023.03.001

Ratnam, S., & Nauli, S. M. (2010). Hypertension in Autosomal Dominant Polycystic Kidney Disease: A Clinical and Basic Science Perspective. *International Journal*

of Nephrology & Urology, *2*(2), 294. https://pmc.ncbi.nlm.nih.gov/articles/PMC4215423/

Reeders, S. T., Gal, A., Propping, P., Waldherr, R., Davies, K. E., Zerres, K., Hogenkamp, T., Schmidt, W., Dolata, M. M., & Weatherall, D. J. (1986). Prenatal diagnosis of autosomal dominant polycystic kidney disease with a DNA probe. *Lancet (London, England)*, *2*(8497), 6–8. https://doi.org/10.1016/S0140-6736(86)92557-2

Rentzsch, P., Schubach, M., Shendure, J., & Kircher, M. (2021). CADD-Splice—improving genome-wide variant effect prediction using deep learning-derived splice scores. *Genome Medicine*, *13*(1), 1–12. https://doi.org/10.1186/S13073-021-00835-9/FIGURES/4

Rentzsch, P., Witten, D., Cooper, G. M., Shendure, J., & Kircher, M. (2019). CADD: predicting the deleteriousness of variants throughout the human genome. *Nucleic Acids Research*, *47*(D1), D886–D894. https://doi.org/10.1093/NAR/GKY1016

Richards, S., Aziz, N., Bale, S., Bick, D., Das, S., Gastier-Foster, J., Grody, W. W., Hegde, M., Lyon, E., Spector, E., Voelkerding, K., & Rehm, H. L. (2015). Standards and guidelines for the interpretation of sequence variants: a joint consensus recommendation of the American College of Medical Genetics and Genomics and the Association for Molecular Pathology. *Genetics in Medicine : Official Journal of the American College of Medical Genetics*, *17*(5), 405–424. https://doi.org/10.1038/GIM.2015.30

Riwanto, M., Kapoor, S., Rodriguez, D., Edenhofer, I., Segerer, S., & Wüthrich, R. P. (2016). Inhibition of Aerobic Glycolysis Attenuates Disease Progression in Polycystic Kidney Disease. *PLOS ONE*, *11*(1), e0146654. https://doi.org/10.1371/JOURNAL.PONE.0146654

Rossetti, S., Kubly, V. J., Consugar, M. B., Hopp, K., Roy, S., Horsley, S. W., Chauveau, D., Rees, L., Barratt, T. M., van't Hoff, W. G., Niaudet, P., Niaudet, W. P., Torres, V. E., & Harris, P. C. (2009). Incompletely penetrant PKD1 alleles suggest a role for gene dosage in cyst initiation in polycystic kidney disease. *Kidney International*, *75*(8), 848–855. https://doi.org/10.1038/ki.2008.686

Rowe, I., Chiaravalli, M., Mannella, V., Ulisse, V., Quilici, G., Pema, M., Song, X. W., Xu, H., Mari, S., Qian, F., Pei, Y., Musco, G., & Boletta, A. (2013). Defective glucose metabolism in polycystic kidney disease identifies a new therapeutic strategy. *Nature Medicine 2013 19:4*, *19*(4), 488–493. https://doi.org/10.1038/nm.3092

Sevillano, A. M., Gutierrez, E., Morales, E., Hernandez, E., Molina, M., Gonzalez, E., & Praga, M. (2014). Multiple kidney cysts in thin basement membrane disease with proteinuria and kidney function impairment. *Clinical Kidney Journal*, *7*(3), 251–256. https://doi.org/10.1093/CKJ/SFU033

Soomro, I., Sun, Y., Li, Z., Diggs, L., Hatzivassiliou, G., Thomas, A. G., Rais, R., Slusher, B. S., Somlo, S., & Skolnik, E. Y. (2018). Glutamine metabolism via glutaminase 1 in autosomal-dominant polycystic kidney disease. *Nephrology Dialysis Transplantation*, *33*(8), 1343–1353. https://doi.org/10.1093/NDT/GFX349

Su, L., Zhang, J., Gomez, H., Kellum, J. A., & Peng, Z. (2023). Mitochondria ROS and mitophagy in acute kidney injury. *Autophagy*, *19*(2), 401–414. https://doi.org/10.1080/15548627.2022.2084862

Su, Q., Hu, F., Ge, X., Lei, J., Yu, S., Wang, T., Zhou, Q., Mei, C., & Shi, Y. (2018). Structure of the human PKD1-PKD2 complex. *Science*, *361*(6406). https://doi.org/10.1126/science.aat9819

Sullivan, P. J., Gayevskiy, V., Davis, R. L., Wong, M., Mayoh, C., Mallawaarachchi, A., Hort, Y., McCabe, M. J., Beecroft, S., Jackson, M. R., Arts, P., Dubowsky, A., Laing, N., Dinger, M. E., Scott, H. S., Oates, E., Pinese, M., & Cowley, M. J. (2023). Introme accurately predicts the impact of coding and noncoding variants on gene splicing, with clinical applications. *Genome Biology*, *24*(1). https://doi.org/10.1186/S13059-023-02936-7

Sun, J., Liu, C., Liu, Y. Y., & Guo, Z. A. (2023). Mitophagy in renal interstitial fibrosis. *International Urology and Nephrology 2023 56:1*, *56*(1), 167–179. https://doi.org/10.1007/S11255-023-03686-Y

Sun, Y., Zou, Q., Yu, H., Yi, X., Dou, X., Yang, Y., Liu, Z., Yang, H., Jia, J., Chen, Y., Sun, S. K., & Zhang, L. (2024). Melanin-like nanoparticles slow cyst growth in ADPKD by dual inhibition of oxidative stress and CREB. *EMBO Molecular Medicine*. https://doi.org/10.1038/S44321-024-00167-2/SUPPL_FILE/44321_2024_167_MOESM9_ESM.PDF

Suwabe, T., Shukoor, S., Chamberlain, A. M., Killian, J. M., King, B. F., Edwards, M., Senum, S. R., Madsen, C. D., Chebib, F. T., Hogan, M. C., Le Gall, E. C., Harris, P. C., & Torres, V. E. (2020). Epidemiology of autosomal dominant polycystic kidney disease in Olmsted county. *Clinical Journal of the American Society of Nephrology*, *15*(1), 69–79. https://doi.org/10.2215/CJN.05900519/-/DCSUPPLEMENTAL

Takakura, A., Contrino, L., Zhou, X., Bonventre, J. V., Sun, Y., Humphreys, B. D., & Zhou, J. (2009). Renal injury is a third hit promoting rapid development of adult polycystic kidney disease. *Human Molecular Genetics*, *18*(14), 2523–2531. https://doi.org/10.1093/HMG/DDP147

Torres, V. E., Chapman, A. B., Devuyst, O., Gansevoort, R. T., Perrone, R. D., Dandurand, A., Ouyang, J., Czerwiec, F. S., & Blais, J. D. (2018). Multicenter, open-label, extension trial to evaluate the long-term efficacy and safety of early versus delayed treatment with tolvaptan in autosomal dominant polycystic kidney disease: the TEMPO 4:4 Trial. *Nephrology Dialysis Transplantation*, *33*(3), 477–489. https://doi.org/10.1093/NDT/GFX043

Torres, V. E., Chapman, A. B., Devuyst, O., Gansevoort, R. T., Perrone, R. D., Koch, G., Ouyang, J., McQuade, R. D., Blais, J. D., Czerwiec, F. S., & Sergeyeva, O. (2017). Tolvaptan in Later-Stage Autosomal Dominant Polycystic Kidney Disease. *New England Journal of Medicine*, *377*(20), 1930–1942. https://doi.org/10.1056/NEJMOA1710030/SUPPL_FILE/NEJMOA1710030_DISCLOSURES.PDF

Torres, V. E., & Harris, P. C. (2019). Progress in the understanding of polycystic kidney disease. *Nature Reviews Nephrology 2019 15:2*, *15*(2), 70–72. https://doi.org/10.1038/s41581-018-0108-1

Torres, V. E., Higashihara, E., Devuyst, O., Chapman, A. B., Gansevoort, R. T., Grantham, J. J., Perrone, R. D., Ouyang, J., Blais, J. D., & Czerwiec, F. S. (2016). Effect of tolvaptan in autosomal dominant polycystic kidney disease by CKD stage: Results from the TEMPO 3:4 trial. *Clinical Journal of the American Society of Nephrology*, *11*(5), 803–811. https://doi.org/10.2215/CJN.06300615/-/DCSUPPLEMENTAL

Tucker, R. W., Pardee, A. B., & Fujiwara, K. (1979). Centriole ciliation is related to quiescence and DNA synthesis in 3T3 cells. *Cell*, *17*(3), 527–535. https://doi.org/10.1016/0092-8674(79)90261-7

Um, J.-H., Kim, Y. Y., Finkel, T., & Yun, J. (2018). Sensitive Measurement of Mitophagy by Flow Cytometry Using the pH-dependent Fluorescent Reporter mt-Keima. *Journal of Visualized Experiments*, *138*. https://doi.org/10.3791/58099-V

Varuzhanyan, G., Ladinsky, M. S., Yamashita, S. I., Abe, M., Sakimura, K., Kanki, T., & Chan, D. C. (2021). Fis1 ablation in the male germline disrupts mitochondrial morphology and mitophagy, and arrests spermatid maturation. *Development (Cambridge)*, *148*(18). https://doi.org/10.1242/dev.199686

Vizoso-González, M. (2023). *New molecular mechanisms and novel biomarkers associated with Extracellular Vesicles in Polycystic Kidney Disease: from preclinical models to patients*. Universidad de Santiago de Compostela.

Vujic, M., Heyer, C. M., Ars, E., Hopp, K., Markoff, A., Orndal, C., Rudenhed, B., Nasr, S. H., Torres, V. E., Torra, R., Bogdanova, N., & Harris, P. C. (2010). Incompletely penetrant PKD1 alleles mimic the renal manifestations of ARPKD. *Journal of the American Society of Nephrology : JASN*, *21*(7), 1097–1102. https://doi.org/10.1681/ASN.2009101070

Walker, L. C., Hoya, M. de la, Wiggins, G. A. R., Lindy, A., Vincent, L. M., Parsons, M. T., Canson, D. M., Bis-Brewer, D., Cass, A., Tchourbanov, A., Zimmermann, H., Byrne, A. B., Pesaran, T., Karam, R., Harrison, S. M., Spurdle, A. B., Biesecker, L. G., Tayoun, A. A., Berg, J. S., … Topper, S. (2023). Using the ACMG/AMP framework to capture evidence related to predicted and observed impact on splicing: Recommendations from the ClinGen SVI Splicing Subgroup. *American Journal of Human Genetics*, *110*(7), 1046–1067. https://doi.org/10.1016/j.ajhg.2023.06.002

Warner, G., Hein, K. Z., Nin, V., Edwards, M., Chini, C. C. S., Hopp, K., Harris, P. C., Torres, V. E., & Chini, E. N. (2016). Food Restriction Ameliorates the Development of Polycystic Kidney Disease. *Journal of the American Society of Nephrology : JASN*, *27*(5), 1437–1447. https://doi.org/10.1681/ASN.2015020132

Weimbs, T. (2011). Third-hit signaling in renal cyst formation. *Journal of the American Society of Nephrology*, *22*(5), 793–795. https://doi.org/10.1681/ASN.2011030284

Westermann, L., Li, Y., Göcmen, B., Niedermoser, M., Rhein, K., Jahn, J., Cascante, I., Schöler, F., Moser, N., Neubauer, B., Hofherr, A., Behrens, Y. L., Göhring, G., Köttgen, A., Köttgen, M., & Busch, T. (2022). Wildtype heterogeneity contributes to clonal variability in genome edited cells. *Scientific Reports 2022 12:1*, *12*(1), 1–13. https://doi.org/10.1038/s41598-022-22885-8

Willey, C. J., Blais, J. D., Hall, A. K., Krasa, H. B., Makin, A. J., & Czerwiec, F. S. (2017). Prevalence of autosomal dominant polycystic kidney disease in the European Union. *Nephrology Dialysis Transplantation*, *32*(8), 1356–1363. https://doi.org/10.1093/NDT/GFW240

Xiong, H. Y., Alipanahi, B., Lee, L. J., Bretschneider, H., Merico, D., Yuen, R. K. C., Hua, Y., Gueroussov, S., Najafabadi, H. S., Hughes, T. R., Morris, Q., Barash, Y., Krainer, A. R., Jojic, N., Scherer, S. W., Blencowe, B. J., & Frey, B. J. (2015). The human splicing code reveals new insights into the genetic determinants of disease. *Science*, *347*(6218). https://doi.org/10.1126/SCIENCE.1254806/SUPPL_FILE/XIONG.SM-CORRECTED.PDF

Yoshida, S., Tsutsumi, S., Muhlebach, G., Sourbier, C., Lee, M. J., Lee, S., Vartholomaiou, E., Tatokoro, M., Beebe, K., Miyajima, N., Mohney, R. P., Chen, Y., Hasumi, H., Xu, W., Fukushima, H., Nakamura, K., Koga, F., Kihara, K., Trepel, J., … Neckers, L. (2013). Molecular chaperone TRAP1 regulates a metabolic switch between mitochondrial respiration and aerobic glycolysis.

Proceedings of the National Academy of Sciences of the United States of America, *110*(17), E1604–E1612. https://doi.org/10.1073/PNAS.1220659110/SUPPL_FILE/PNAS.201220659SI.PDF

Zhang, C., Balbo, B., Ma, M., Zhao, J., Tian, X., Kluger, Y., & Somlo, S. (2021). Cyclin-dependent kinase 1 activity is a driver of cyst growth in polycystic kidney disease. *Journal of the American Society of Nephrology*, *32*(1), 41–51. https://doi.org/10.1681/ASN.2020040511/-/DCSUPPLEMENTAL

Zhang, C., Rehman, M., Tian, X., Pei, S. L. C., Gu, J., Bell, T. A., Dong, K., Tham, M. S., Cai, Y., Wei, Z., Behrens, F., Jetten, A. M., Zhao, H., Lek, M., & Somlo, S. (2024). Glis2 is an early effector of polycystin signaling and a target for therapy in polycystic kidney disease. *Nature Communications 2024 15:1*, *15*(1), 1–19. https://doi.org/10.1038/s41467-024-48025-6

Zhou, J. X., & Li, X. (2015). Apoptosis in Polycystic Kidney Disease: From Pathogenesis to Treatment. *Exon Publications*, 197–230. https://doi.org/10.15586/CODON.PKD.2015.CH9

Zhu, P., Sieben, C. J., Xu, X., Harris, P. C., & Lin, X. (2017). Autophagy activators suppress cystogenesis in an autosomal dominant polycystic kidney disease model. *Human Molecular Genetics*, *26*(1), 158–172. https://doi.org/10.1093/hmg/ddw376

8 SUPPLEMENTAL DATA

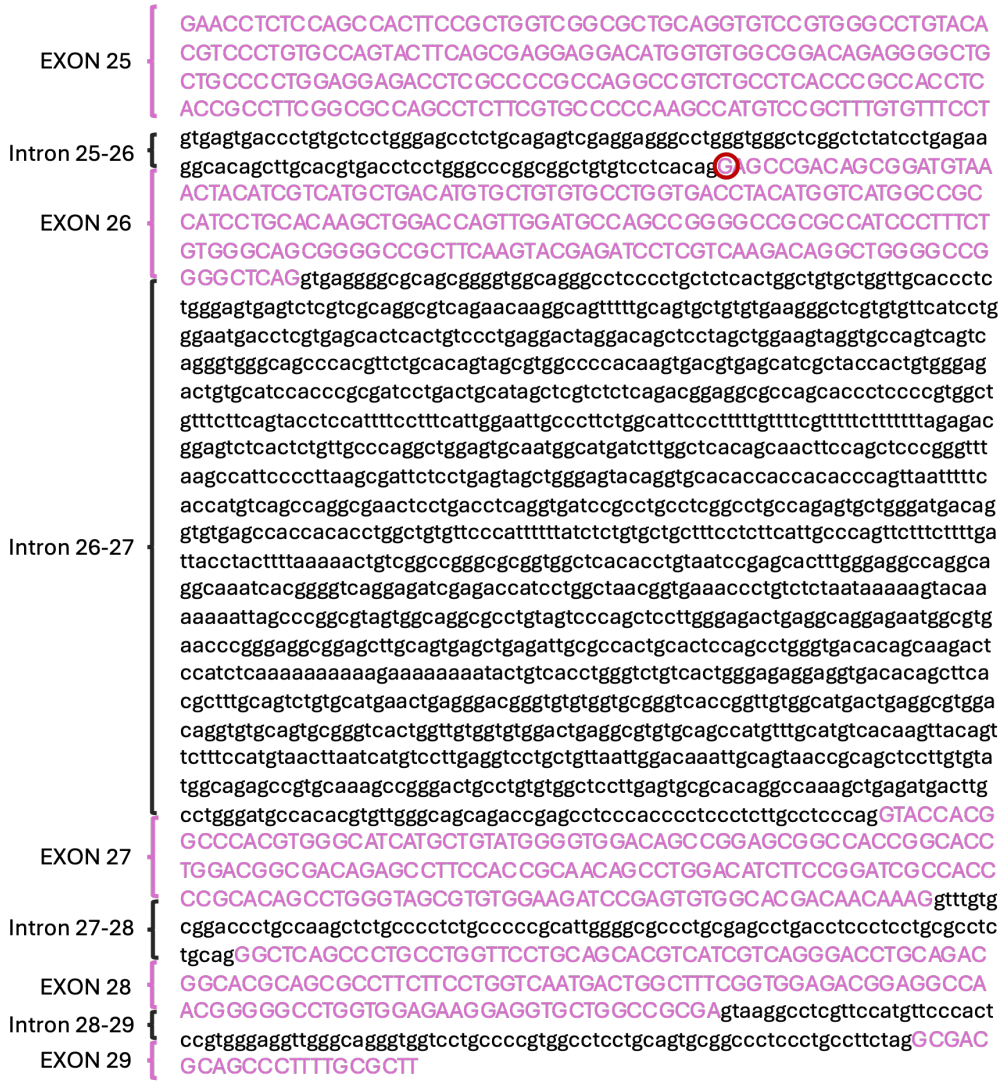

Supplemental figure 1. DNA 'minigene' fragment for the splicing assay. The red circle indicates the position of the mutant variant (E3068Q).

EXON 25 INTRON 25-26 EXON 26

Alignments:

```
>E3068_513pb_band
Length: 467
Range 1: 2 to 454
Score:793 bits (429), Expect:0.0,
Identities:444/454(98%), Gaps:2/454(0%), Strand: Plus/Plus

Query  80   CTGTACACGTCCCTGTGCCAGTACTTCAGCGAGGAGGACATGGTGTGGCGGACAGAGGGG  139
            ||||||  ||||||||||||||||||||||||||||||||||||||||||||||||||||
Sbjct  2    CTGTAC-CGTCCCTGTGCCAGTACTTCAGCGAGGAGGACATGGTGTGGCGGACAGAGGGG  60

Query  140  CTGCTGCCCCTGGAGGAGACCTCGCCCCGCCAGGCCGTCTGCCTCACCCGCCACCTCACC  199
            ||||||||||||  ||||||||||||||||||||  ||||||||||||||||||||||||
Sbjct  61   CTGCTGCCCCTGAAGGAGACCTCGCCCCGCCAGGSCGTCTGCCTCACCCGCCACCTCACC  120

Query  200  GCCTTCGGCGCCAGCCTCTTCGTGCCCCCAAGCCATGTCCGCTTTGTGTTTCCTGTGAGT  259
            ||||||||||||||||||||||||||||||||||||||||||||||||||||||||||||
Sbjct  121  GCCTTCGGCGCCAGCCTCTTCGTGCCCCCAAGCCATGTCCGCTTTGTGTTTCCTGTGAGT  180

Query  260  GACCCTGTGCTCCTGGGAGCCTCTGCAGAGTCGAGGAGGGCCTGGGTGGGCTCGGCTCTA  319
            |||||||||||||||||||||||||  |||  ||||||  ||||||||||||||||||||
Sbjct  181  GACCCTGTGCTCCTGGGAGCCTCTGCRGAGKCGAGGARGGCCTGGGTGGGCTCGGCTCTA  240

Query  320  TCCTGAGAAGGCACAGCTTGCACGTGACCTCCTGGGCCCGGCGGCTGTGTCCTCACAGGA  379
            ||||||||||||||||||||||||||||||||||||||||||||||||||||||||||||
Sbjct  241  TCCTGAGAAGGCACAGCTTGCACGTGACCTCCTGGGCCCGGCGGCTGTGTCCTCACAGGA  300

Query  380  GCCGACAGCGGATGTAAACTACATCGTCATGCTGACATGTGCTGTGTGCCTGGTGACCTA  439
            |||||||||||||||||||||||||||||||||||||  ||||||||||||||||||||
Sbjct  301  GCCGACAGCGGATGTAAACTACATCGTCATGCTGACATGWGCTGTGTGCCTGGTGACCTA  360

Query  440  CATGGTCATGGCCGCCATCCTGCACAAGCTGGACCAGTTGGATGCCAGCCGGGGCCGCGC  499
            ||||||||||||||||||||||||||||||||||||||||||||||||||||||||||||
Sbjct  361  CATGGTCATGGCCGCCATCCTGCACAAGCTGGACCAGTTGGATGCCAGCCGGGGCCGCGC  420

Query  500  CATCCCTTTCTGTGGGC-AGCGGGGCCGCTTCAA  532
            ||||||||||  |||||  ||||||||||||||||
Sbjct  421  CATCCCTTTCKGTGGGGSAGCGGGGCCGCTTCAA  454
```

```
>E3068Q_513pb_band
Length: 467
Range 1: 2 to 466
Score:769 bits (416), Expect:0.0,
Identities:446/466(96%), Gaps:2/466(0%), Strand: Plus/Plus

Query  78   GCCTGTACACGTCCCTGTGCCAGTACTTCAGCGAGGAGGACATGGTGTGGCGGACAGAGG  137
            ||||||  ||||||||||||||||||||||||||||||||||||||||||||||||||||
Sbjct  2    GCCTGT-CACGTCCCTGTGCCAGTACTTCAGCGAGGAGGACATGGTGTGGCGGACAGAGG  60

Query  138  GGCTGCTGCCCCTGGAGGAGACCTCGCCCCGCCAGGCCGTCTGCCTCACCCGCCACCTCA  197
            ||||||||||||||||||||||||||||||||||||||||||||||||||||||||||||
Sbjct  61   GGCTGCTGCCCCTGGAGGAGACCTCGCCCCGCCAGGCCGTCTGCCTCACCCGCCACCTCA  120

Query  198  CCGCCTTCGGCGCCAGCCTCTTCGTGCCCCCAAGCCATGTCCGCTTTGTGTTTCCTGTGA  257
            ||||||||||||||||||||||||||||||||||||||||||||||||  |||||||||
Sbjct  121  CCGCCTTCGGCGCCAGCCTCTTCGTGCCCCCAAGCCATGTCCGCTTTGTCCTTCCTGTGA  180

Query  258  GTGACCCTGTGCTCCTGGGAGCCTCTGCAGAGTCGAGGAGGGCCTGGGTGGGCTCGGCTC  317
            ||||||||||||||||||||||||||||||||||||||||||||||||||||||||||||
Sbjct  181  GTGACCCTGTGCTCCTGGGAGCCTCTGCAGAGTCGAGGAGGGCCTGGGTGGGCTCGGCTC  240

Query  318  TATCCTGAGAAGGCACAGCTTGCACGTGACCTCCTGGGCCCGGCGGCTGTGTCCTCACAG  377
            ||||||||||||||||||||||||||||||||||||||||||||||||||||||||||||
Sbjct  241  TATCCTGAGAAGGCACAGCTTGCACGTGACCTCCTGGGCCCGGCGGCTGTGTCCTCACAG  300
```

```
Query  378  GAGCCGACAGCGGATGTAAACTACATCGTCATGCTGACATGTGCTGTGTGCCTGGTGACC  437
            ||||||||||| ||||||||||||||||||||||||||||||||||||||||||||||||
Sbjct  301  CAGCCGACAGCGRATGTAAACTACATCGTCATGCTGACATGTGCTGTGTGCCTGGTGACC  360

Query  438  TACATGGTCATGGCCGCCATCCTGCACAAGCTGGACCAGTTGGATGCCAGCCGGGGCCGC  497
            ||||||| |||||||||| ||||| |||||||||||||| |||||| | ||||||||||
Sbjct  361  TACATGGYCATGGCCGCCMTCCTGYACAAGCTGGACCAGYTGGATGMCGGCCGGGGCCGC  420

Query  498  GCCATCCCTTTCTGTGGGCAGCGGG-GCCGCTTCAAGTACGAGATC  542
            |||||||||||| ||| | |||||  | || ||||||||| | |||
Sbjct  421  GCCATCCCTTTCGGTGTGGAGCGGSTGMCGYTTCAAGTACRAKATC  466
```

```
>E3068_388pb_band
Length: 457
Range 1: 1 to 174
Score:311 bits(168), Expect:1e-88,
Identities:173/175(99%), Gaps:1/175(0%), Strand: Plus/Plus

Query  80   CTGTACACGTCCCTGTGCCAGTACTTCAGCGAGGAGGACATGGTGTGGCGGACAGAGGGG  139
            ||||| ||||||||||||||||||||||||||||||||||||||||||||||||||||||
Sbjct  1    CTGTA-ACGTCCCTGTGCCAGTACTTCAGCGAGGAGGACATGGTGTGGCGGACAGAGGGG  59

Query  140  CTGCTGCCCCTGGAGGAGACCTCGCCCCGCCAGGCCGTCTGCCTCACCCGCCACCTCACC  199
            |||||||||||| ||||||||||||||||||||||||||||||||||||||||||||||
Sbjct  60   CTGCTGCCCCTGAAGGAGACCTCGCCCCGCCAGGCCGTCTGCCTCACCCGCCACCTCACC  119

Query  200  GCCTTCGGCGCCAGCCTCTTCGTGCCCCCAAGCCATGTCCGCTTTGTGTTTCCT  253
            |||||||||||||||||||||||||||||||||||||||||||||||||||||||
Sbjct  120  GCCTTCGGCGCCAGCCTCTTCGTGCCCCCAAGCCATGTCCGCTTTGTGTTTCCT  173



Range 2: 174 to 338
Score:291 bits(157), Expect:2e-82,
Identities:161/165(98%), Gaps:0/165(0%), Strand: Plus/Plus

Query  378  GAGCCGACAGCGGATGTAAACTACATCGTCATGCTGACATGTGCTGTGTGCCTGGTGACC  437
            |||||||||||||||||||||||||||||||| ||||||||||||||||||||||||||
Sbjct  174  GAGCCGACAGCGGATGTAAACTACATCGTCATGSTGACATGTGCTGTGTGCCTGGTGACC  233

Query  438  TACATGGTCATGGCCGCCATCCTGCACAAGCTGGACCAGTTGGATGCCAGCCGGGGCCGC  497
            ||||||||||||||||||||||||||||||||||||||||||||||||||||||||||||
Sbjct  234  TACATGGTCATGGCCGCCATCCTGCACAAGCTGGACCAGTTGGATGCCAGCCGGGGCCGC  293

Query  498  GCCATCCCTTTCTGTGGGCAGCGGGGCCGCTTCAAGTACGAGATC  542
            |||||||||||||||||||||||||||||||  |||| |||
Sbjct  294  GCCATCCCTTTCTGTGGGCAGCGGGGCCGCTTCAAKWACGARATC  338
```

Supplemental figure 2. Alignment of the Sanger sequences from the splicing assay. Agarose gel bands (**Figure 13**) were extracted and sequenced. The resulting sequences were aligned with a query sequence encompassing exon 25 (blue), intron 25-26 (yellow), and exon 26 (green). The alignment process was performed automatically using the BLAST tool.

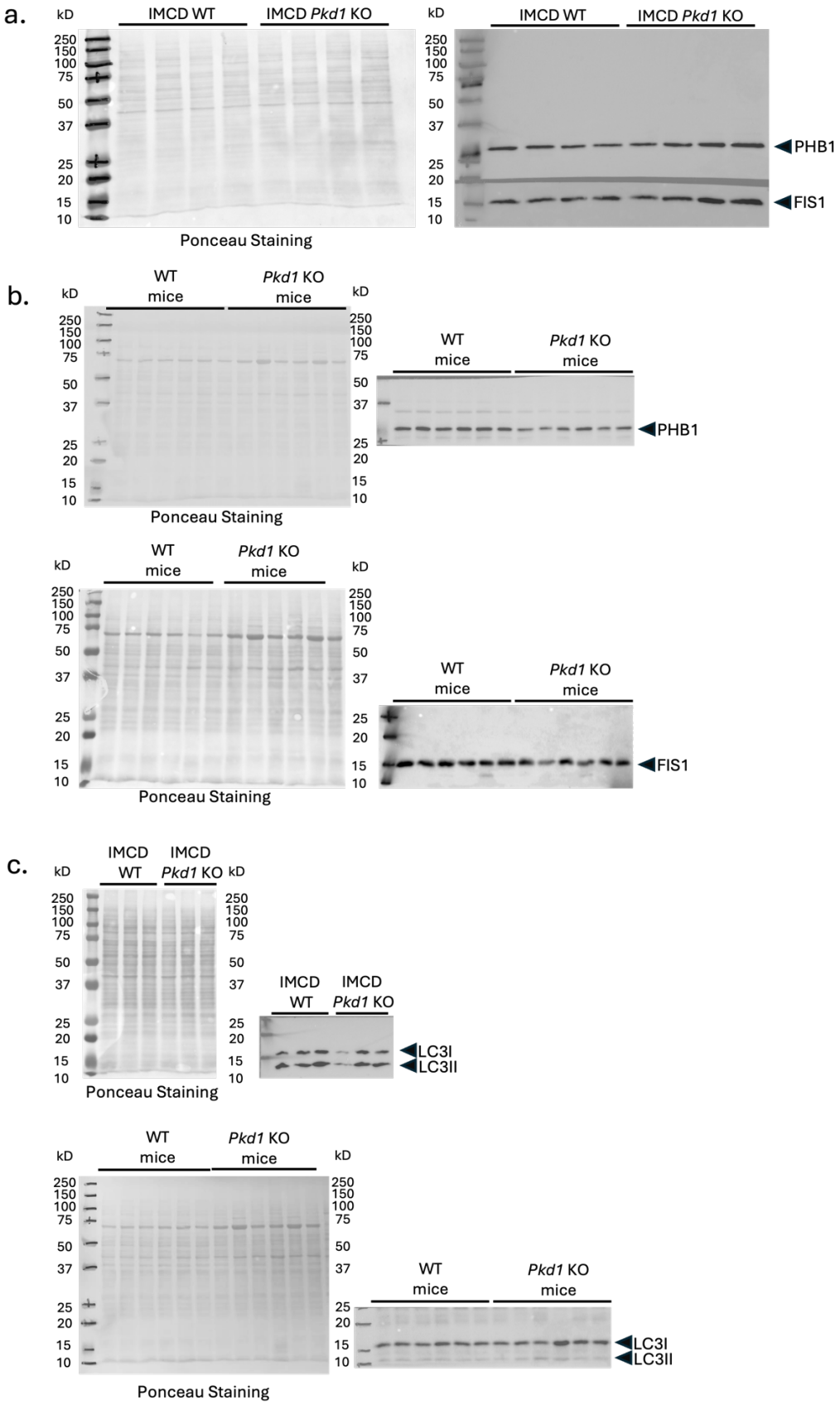

Supplemental figure 3. Membranes used for Western Blot densitometry. As a loading control we used total protein stained with Ponceau. Mitophagy proteins PHB1 and FIS1 abundance was measure in cell samples (**a**) and kidney samples from p30 mice (**b**). **c.** LC3B measure in cell samples and kidney samples from p30 mice.

Supplemental table 1. Primers list

Purpose	PCR	Gene	Primer name	Primers sequence (5'-3')
Splicing assay	PCR	*PKD1* (human)	BPF6	CCCCGTCCTCCCCGTCCTTTTGTC
			BPR6	AAGCGCAAAAGGGCTGCGTCG
			PKD1_EX26_SA_F	GAACCTCTCCAGCCACTTCC
			PKD1_EX26_SA_R1	ATGTAGGTCACCAGGCACAC
			PKD1_EX26_SA_R2	GATCTCGTACTTGAAGCGGC
			PKD1_EX26_SA_R3	TGTCCACCCCATACAGCAT
			PKD1_EX26_SA_R4	AAGCGCAAAAGGGCTGC
			PKD1_26R	TGGTAGCGATGCTCACGTCACTT
Genotyping mIMCD3 cells	PCR	*Pkd1* (mouse)	mPkd1_1	AGATGGCCATCCTGGTAGGT
			mPkd1_2	CTAGGTGGGAGCACAACTGG
			mPkd1_3	CCACCTACAGCCAACTTGGA
Pkd1 expression in mIMCD3 cells	RT-PCR	cDNA *Pkd1* (mouse)	RT_mPkd1_1	GTGGAAAGCAGGTCGGAAG
			RT_mPkd1_2	TCGTCTCGTTCAGCACCAG
Gene expression of mitophagy proteins	RT-qPCR	cDNA *Nipsnap1* (mouse)	Nipsnap1_mmRT_F	CACTCCACTCTGCTGTCCAA
			Nipsnap1_mmRT_R	AACCGCCATAGGTGTACTGC
		cDNA *Fis1* (mouse)	Fis1_mmRT_F	CCGGCTCAAGGAATATGAAA
			Fis1_mmRT_	ACAGCCAGTCCAATGAGTCC
		cDNA *Atg7* (mouse)	Atg7_mmRT_F	TCCGTTGAAGTCCTCTGCTT
			Atg7_mmRT_R	CCACTGAGGTTCACCATCCT
		cDNA *Abce1* (mouse)	Abce1__mmRT_F	CAACCACGACAAATGCAAAC
			Abce1__mmRT_R	CGCCAAAGGGACATTTCTTA
		cDNA *Pink* (mouse)	Pink_mmRT_F	CCCACACCCTAACATCATCC
			Pink_mmRT_R	ACTGGGAGTCTGCTCCTCAA
		cDNA Nix (mouse)	Nix__mmRT_F	CTACCCATGAACAGCAGCAA
			Nix__mmRT_R	ATCTGCCCATCTTCTTGTGG
		cDNA *Prkn* (mouse)	mm_RT_Prkn_2F	CACGATGCTCAACTTGGCTA
			mm_RT_Prkn_2R	CTTCGCAGGTGACTTTCCTC
		cDNA *Hprt1* (mouse)	Hprtr_R	CAATGCAAACTTTGCTTTCCC
			Hprtr_F	TCCTTTTCACCAGCAAGCTTG

Supplemental table 2. Significant proteins (p-value<0.05) in the differential proteomics of mIMCD3 cells

Uniprot code	Isoform	Uniprot name	Group	Gene name	p-value	Mean WT	Mean KO	FC (WT to KO)	1/FC (KO to WT)	Abundance
O55022		PGRC1_MOUSE	Membrane-associated progesterone receptor component 1	Pgrmc1	4,55E-08	0	41360,542	NA	NA	Only in KO
Q8CCH2		NHLC3_MOUSE	NHL repeat-containing protein 3	Nhlrc3	1,37E-06	0	12449,437	NA	NA	Only in KO
Q99KP6		PRP19_MOUSE	Pre-mRNA-processing factor 19	Prpf19	9,51E-06	0	1019,641	NA	NA	Only in KO
Q8VDP4		CCAR2_MOUSE	Cell cycle and apoptosis regulator protein 2	Ccar2	2,94E-05	0	11743,327	NA	NA	Only in KO
Q61033		LAP2A_MOUSE	Lamina-associated polypeptide 2, isoforms alpha/zeta	Tmpo	3,14E-05	0	59692,377	NA	NA	Only in KO
Q60931		VDAC3_MOUSE	Voltage-dependent anion-selective channel protein 3	Vdac3	5,00E-05	0	15386,956	NA	NA	Only in KO
Q9CQA3		SDHB_MOUSE	Succinate dehydrogenase [ubiquinone] iron-sulfur subunit, mitochondrial	Sdhb	5,82E-05	0	6261,318	NA	NA	Only in KO
Q571E4		GALNS_MOUSE	N-acetylgalactosamine-6-sulfatase	Galns	7,06E-05	0	6433,696	NA	NA	Only in KO
P60122		RUVB1_MOUSE	RuvB-like 1	Ruvbl1	0,00012519	0	24448,048	NA	NA	Only in KO
Q99JY0		ECHB_MOUSE	Trifunctional enzyme subunit beta, mitochondrial	Hadhb	0,00014519	0	102014,857	NA	NA	Only in KO
Q791V5		MTCH2_MOUSE	Mitochondrial carrier homolog 2	Mtch2	0,0001617	0	5690,944	NA	NA	Only in KO
Q62190		RON_MOUSE	Macrophage-stimulating protein receptor	Mst1r	0,00017131	0	8230,440	NA	NA	Only in KO
Q9ERG0		LIMA1_MOUSE	LIM domain and actin-binding protein 1	Lima1	0,00017213	0	9449,317	NA	NA	Only in KO
P97300		NPTN_MOUSE	Neuroplastin	Nptn	0,0001764	0	18181,566	NA	NA	Only in KO
O70378		EMC8_MOUSE	ER membrane protein complex subunit 8	Emc8	0,00018396	0	7428,163	NA	NA	Only in KO
Q9QXS1		PLEC_MOUSE	Plectin	Plec	0,00031447	0	6156,194	NA	NA	Only in KO

Q99K01		PDXD1_MOUSE	Pyridoxal-dependent decarboxylase domain-containing protein 1	Pdxdc1	0,00031935	0	16140,233	NA	NA	Only in KO
Q8JZN5		ACAD9_MOUSE	Complex I assembly factor ACAD9, mitochondrial	Acad9	0,00042298	0	6966,569	NA	NA	Only in KO
P17225		PTBP1_MOUSE	Polypyrimidine tract-binding protein 1	Ptbp1	0,00047593	0	32050,342	NA	NA	Only in KO
O88712		CTBP1_MOUSE	C-terminal-binding protein 1	Ctbp1	0,00048381	0	12901,257	NA	NA	Only in KO
Q9CQL1		MGN2_MOUSE	Protein mago nashi homolog 2	Magohb	0,00063426	0	8246,792	NA	NA	Only in KO
Q9WUQ2		PREB_MOUSE	Prolactin regulatory element-binding protein	Preb	0,00067944	0	5489,246	NA	NA	Only in KO
Q99KF1		TMED9_MOUSE	Transmembrane emp24 domain-containing protein 9	Tmed9	0,0007653	0	2860,733	NA	NA	Only in KO
Q8K411		PREP_MOUSE	Presequence protease, mitochondrial	Pitrm1	0,001084	0	3915,673	NA	NA	Only in KO
P63280		UBC9_MOUSE	SUMO-conjugating enzyme UBC9	Ube2i	0,00121191	0	890,284	NA	NA	Only in KO
O55131		SEPT7_MOUSE	Septin-7	Septin7	0,00162784	0	416,350	NA	NA	Only in KO
Q60930		VDAC2_MOUSE	Voltage-dependent anion-selective channel protein 2	Vdac2	0,00179118	0	35640,561	NA	NA	Only in KO
Q8BWY3		ERF1_MOUSE	Eukaryotic peptide chain release factor subunit 1	Etf1	0,00181707	0	6565,532	NA	NA	Only in KO
Q8BM55		TM214_MOUSE	Transmembrane protein 214	Tmem214	0,00188727	0	7110,386	NA	NA	Only in KO
Q99JR8		SMRD2_MOUSE	SWI/SNF-related matrix-associated actin-dependent regulator of chromatin subfamily D member 2	Smarcd2	0,00190877	0	3199,116	NA	NA	Only in KO
Q02248		CTNB1_MOUSE	Catenin beta-1	Ctnnb1	0,00204911	0	13935,353	NA	NA	Only in KO
Q91V61		SFXN3_MOUSE	Sideroflexin-3	Sfxn3	0,00239801	0	8137,505	NA	NA	Only in KO
P07724		ALBU_MOUSE	Albumin	Alb	0,00279656	0	5938,922	NA	NA	Only in KO
P26369		U2AF2_MOUSE	Splicing factor U2AF 65 kDa subunit	U2af2	0,00419417	0	3170,647	NA	NA	Only in KO
Q9CQU0		TXD12_MOUSE	Thioredoxin domain-containing protein 12	Txndc12	0,0049709	0	1282,370	NA	NA	Only in KO

Q9JMA1		UBP14_MOUSE	Ubiquitin carboxyl-terminal hydrolase 14	Usp14	0,00530088	0	2585,813	NA	NA	Only in KO
P11440		CDK1_MOUSE	Cyclin-dependent kinase 1	Cdk1	0,00540064	0	5681,219	NA	NA	Only in KO
P46471		PRS7_MOUSE	26S proteasome regulatory subunit 7	Psmc2	0,00574841	0	2292,804	NA	NA	Only in KO
O88844		IDHC_MOUSE	Isocitrate dehydrogenase [NADP] cytoplasmic	Idh1	0,00699779	0	1015,901	NA	NA	Only in KO
Q6PFD9		NUP98_MOUSE	Nuclear pore complex protein Nup98-Nup96	Nup98	0,00759683	0	12833,315	NA	NA	Only in KO
Q9CQQ7		AT5F1_MOUSE	ATP synthase F(0) complex subunit B1, mitochondrial	Atp5pb	0,00954235	0	27560,887	NA	NA	Only in KO
P51660		DHB4_MOUSE	Peroxisomal multifunctional enzyme type 2	Hsd17b4	0,00994815	0	25672,165	NA	NA	Only in KO
Q9EQ06		DHB11_MOUSE	Estradiol 17-beta-dehydrogenase 11	Hsd17b11	0,01076031	0	2760,907	NA	NA	Only in KO
P97298		PEDF_MOUSE	Pigment epithelium-derived factor	Serpinf1	0,01277311	0	2387,700	NA	NA	Only in KO
Q9CQC9		SAR1B_MOUSE	GTP-binding protein SAR1b	Sar1b	0,01367952	0	1678,415	NA	NA	Only in KO
Q60715	2	P4HA1_MOUSE	Isoform 2 of Prolyl 4-hydroxylase subunit alpha-1	P4ha1	0,01405136	0	4840,380	NA	NA	Only in KO
A2APB8		TPX2_MOUSE	Targeting protein for Xklp2	Tpx2	0,02540483	0	1511,860	NA	NA	Only in KO
Q8R0W0		EPIPL_MOUSE	Epiplakin	Eppk1	0,03061253	0	1328,677	NA	NA	Only in KO
Q3U186		SYRM_MOUSE	Probable arginine--tRNA ligase, mitochondrial	Rars2	0,03245371	0	1428,621	NA	NA	Only in KO
P62897		CYC_MOUSE	Cytochrome c, somatic	Cycs	0,0327724	0	778,462	NA	NA	Only in KO
P32233		DRG1_MOUSE	Developmentally-regulated GTP-binding protein 1	Drg1	0,03783854	0	2211,578	NA	NA	Only in KO
Q8BFR4		GNS_MOUSE	N-acetylglucosamine-6-sulfatase	Gns	1,13E-06	171,748	36824,617	0,005	214,411	Upregulated in KO
P62852		RS25_MOUSE	40S ribosomal protein S25	Rps25	7,16E-05	187,241	37086,192	0,005	198,067	Upregulated in KO
Q9QYC0		ADDA_MOUSE	Alpha-adducin	Add1	1,39E-07	250,171	22614,600	0,011	90,397	Upregulated in KO
Q9D6Z1		NOP56_MOUSE	Nucleolar protein 56	Nop56	0,0001053	69,046	5973,980	0,012	86,521	Upregulated in KO

Q8C854		MYEF2_MOUSE	Myelin expression factor 2	Myef2	1,45E-05	175,690	14950,375	0,012	85,095	Upregulated in KO
Q9QWR8		NAGAB_MOUSE	Alpha-N-acetylgalactosaminidase	Naga	0,00010982	308,781	20217,469	0,015	65,475	Upregulated in KO
Q922U1		PRPF3_MOUSE	U4/U6 small nuclear ribonucleoprotein Prp3	Prpf3	8,11E-06	542,622	34419,169	0,016	63,431	Upregulated in KO
P02089		HBB2_MOUSE	Hemoglobin subunit beta-2	Hbb-b2	9,52E-05	3927,774	223960,309	0,018	57,020	Upregulated in KO
P20060		HEXB_MOUSE	Beta-hexosaminidase subunit beta	Hexb	1,06E-05	320,583	18036,072	0,018	56,260	Upregulated in KO
Q8BH95		ECHM_MOUSE	Enoyl-CoA hydratase, mitochondrial	Echs1	2,21E-05	258,437	14096,976	0,018	54,547	Upregulated in KO
Q60932	2	VDAC1_MOUSE	Isoform Mt-VDAC1 of Voltage-dependent anion-selective channel protein 1	Vdac1	0,00032682	2231,939	112885,912	0,020	50,578	Upregulated in KO
P35980		RL18_MOUSE	60S ribosomal protein L18	Rpl18	2,38E-05	808,231	36434,641	0,022	45,079	Upregulated in KO
P62984		RL40_MOUSE	Ubiquitin-60S ribosomal protein L40	Uba52	1,00E-06	5483,093	167778,839	0,033	30,599	Upregulated in KO
Q9CQN1		TRAP1_MOUSE	Heat shock protein 75 kDa, mitochondrial	Trap1	0,01021142	956,532	26452,721	0,036	27,655	Upregulated in KO
Q8BGD9		IF4B_MOUSE	Eukaryotic translation initiation factor 4B	Eif4b	0,00017629	532,715	12533,354	0,043	23,527	Upregulated in KO
P51174		ACADL_MOUSE	Long-chain specific acyl-CoA dehydrogenase, mitochondrial	Acadl	4,84E-05	303,452	7033,574	0,043	23,179	Upregulated in KO
P97326		CADH6_MOUSE	Cadherin-6	Cdh6	0,00129884	448,595	9018,562	0,050	20,104	Upregulated in KO
Q8BL97		SRSF7_MOUSE	Serine/arginine-rich splicing factor 7	Srsf7	5,35E-06	2269,792	41247,840	0,055	18,173	Upregulated in KO
Q9WTP6		KAD2_MOUSE	Adenylate kinase 2, mitochondrial	Ak2	1,04E-07	7132,573	127238,929	0,056	17,839	Upregulated in KO
Q8K4Z3		NNRE_MOUSE	NAD(P)H-hydrate epimerase	Naxe	2,05E-06	363,908	6424,172	0,057	17,653	Upregulated in KO
P40630		TFAM_MOUSE	Transcription factor A, mitochondrial	Tfam	2,46E-05	1390,671	24293,109	0,057	17,469	Upregulated in KO
Q8R326		PSPC1_MOUSE	Paraspeckle component 1	Pspc1	1,21E-05	1640,084	27560,575	0,060	16,804	Upregulated in KO

P09671		SODM_MOUSE	Superoxide dismutase [Mn], mitochondrial	Sod2	0,00076645	1137,518	18305,100	0,062	16,092	Upregulated in KO
P12787		COX5A_MOUSE	Cytochrome c oxidase subunit 5A, mitochondrial	Cox5a	4,22E-06	1647,405	24563,347	0,067	14,910	Upregulated in KO
P17742		PPIA_MOUSE	Peptidyl-prolyl cis-trans isomerase A	Ppia	0,00173276	2163,190	31707,130	0,068	14,658	Upregulated in KO
Q9D0M3		CY1_MOUSE	Cytochrome c1, heme protein, mitochondrial	Cyc1	0,00274858	1684,513	24186,712	0,070	14,358	Upregulated in KO
O89023		TPP1_MOUSE	Tripeptidyl-peptidase 1	Tpp1	0,00029793	1236,578	17688,241	0,070	14,304	Upregulated in KO
Q99P72		RTN4_MOUSE	Reticulon-4	Rtn4	0,01223503	2956,158	41482,451	0,071	14,033	Upregulated in KO
P61957		SUMO2_MOUSE	Small ubiquitin-related modifier 2	Sumo2	1,18E-05	1796,486	24093,292	0,075	13,411	Upregulated in KO
Q922Q4		P5CR2_MOUSE	Pyrroline-5-carboxylate reductase 2	Pycr2	0,00114612	390,592	4972,402	0,079	12,730	Upregulated in KO
Q3UVK0		ERMP1_MOUSE	Endoplasmic reticulum metallopeptidase 1	Ermp1	0,00046872	1530,888	18829,125	0,081	12,299	Upregulated in KO
Q9D1J3		SARNP_MOUSE	SAP domain-containing ribonucleoprotein	Sarnp	5,07E-07	3955,083	47874,296	0,083	12,104	Upregulated in KO
Q922Q8		LRC59_MOUSE	Leucine-rich repeat-containing protein 59	Lrrc59	0,00249788	1966,926	23116,194	0,085	11,752	Upregulated in KO
O08583		THOC4_MOUSE	THO complex subunit 4	Alyref	1,91E-05	8315,560	96754,600	0,086	11,635	Upregulated in KO
P97496		SMRC1_MOUSE	SWI/SNF complex subunit SMARCC1	Smarcc1	2,63E-06	1536,394	17846,115	0,086	11,616	Upregulated in KO
Q69Z99		ZN512_MOUSE	Zinc finger protein 512	Znf512	0,00053551	1159,339	13020,919	0,089	11,231	Upregulated in KO
P51859		HDGF_MOUSE	Hepatoma-derived growth factor	Hdgf	0,02076185	1213,118	13143,120	0,092	10,834	Upregulated in KO
P19783		COX41_MOUSE	Cytochrome c oxidase subunit 4 isoform 1, mitochondrial	Cox4i1	0,01517754	730,841	7852,073	0,093	10,744	Upregulated in KO
Q4VA53		PDS5B_MOUSE	Sister chromatid cohesion protein PDS5 homolog B	Pds5b	6,83E-05	2503,876	25254,273	0,099	10,086	Upregulated in KO
P70372		ELAV1_MOUSE	ELAV-like protein 1	Elavl1	5,11E-07	11192,021	111093,617	0,101	9,926	Upregulated in KO
P29758		OAT_MOUSE	Ornithine aminotransferase, mitochondrial	Oat	0,04314742	182,363	1775,907	0,103	9,738	Upregulated in KO

Q6P5F9		XPO1_MOUSE	Exportin-1	Xpo1	0,02708231	584,603	5591,811	0,105	9,565	Upregulated in KO
P14206		RSSA_MOUSE	40S ribosomal protein SA	Rpsa	0,00196089	5278,770	50068,622	0,105	9,485	Upregulated in KO
Q9D172		GAL3A_MOUSE	Glutamine amidotransferase-like class 1 domain-containing protein 3A, mitochondrial	Gatd3a	0,00010865	2449,249	22543,608	0,109	9,204	Upregulated in KO
P62492		RB11A_MOUSE	Ras-related protein Rab-11A	Rab11a	0,00018848	2312,655	20846,287	0,111	9,014	Upregulated in KO
Q9DCX2		ATP5H_MOUSE	ATP synthase subunit d, mitochondrial	Atp5pd	5,52E-05	1753,822	14932,827	0,117	8,514	Upregulated in KO
Q9R112		SQOR_MOUSE	Sulfide:quinone oxidoreductase, mitochondrial	Sqor	9,62E-06	3417,253	27807,152	0,123	8,137	Upregulated in KO
P17918		PCNA_MOUSE	Proliferating cell nuclear antigen	Pcna	0,00243833	2032,679	16483,492	0,123	8,109	Upregulated in KO
P57776		EF1D_MOUSE	Elongation factor 1-delta	Eef1d	0,00084481	2419,320	18999,048	0,127	7,853	Upregulated in KO
P08752		GNAI2_MOUSE	Guanine nucleotide-binding protein G(i) subunit alpha-2	Gnai2	0,00040461	2501,278	19071,320	0,131	7,625	Upregulated in KO
Q8VHR5		P66B_MOUSE	Transcriptional repressor p66-beta	Gatad2b	2,42E-05	1106,597	7970,452	0,139	7,203	Upregulated in KO
Q07417		ACADS_MOUSE	Short-chain specific acyl-CoA dehydrogenase, mitochondrial	Acads	0,00078379	4005,825	28423,348	0,141	7,096	Upregulated in KO
Q6PDN3		MYLK_MOUSE	Myosin light chain kinase, smooth muscle	Mylk	0,00240227	1673,697	11627,336	0,144	6,947	Upregulated in KO
P16858		G3P_MOUSE	Glyceraldehyde-3-phosphate dehydrogenase	Gapdh	0,00817835	5932,265	40917,142	0,145	6,897	Upregulated in KO
Q8BTM8		FLNA_MOUSE	Filamin-A	Flna	4,81E-05	2599,736	17788,475	0,146	6,842	Upregulated in KO
Q9ET30		TM9S3_MOUSE	Transmembrane 9 superfamily member 3	Tm9sf3	5,63E-05	4446,721	30093,695	0,148	6,768	Upregulated in KO
P63260		ACTG_MOUSE	Actin, cytoplasmic 2	Actg1	0,01973434	32542,813	214406,178	0,152	6,588	Upregulated in KO
O88569		ROA2_MOUSE	Heterogeneous nuclear ribonucleoproteins A2/B1	Hnrnpa2b1	2,74E-06	170885,271	1118637,480	0,153	6,546	Upregulated in KO

Q8CGK3		LONM_MOUSE	Lon protease homolog, mitochondrial	Lonp1	0,00411513	2524,984	16488,876	0,153	6,530	Upregulated in KO
Q8R0G9		NU133_MOUSE	Nuclear pore complex protein Nup133	Nup133	0,00103526	2437,075	15879,059	0,153	6,516	Upregulated in KO
Q9CRD0		OCAD1_MOUSE	OCIA domain-containing protein 1	Ociad1	3,23E-05	3645,533	23342,937	0,156	6,403	Upregulated in KO
Q61584		FXR1_MOUSE	Fragile X mental retardation syndrome-related protein 1	Fxr1	0,00018073	4388,044	27973,206	0,157	6,375	Upregulated in KO
Q9CZN7		GLYM_MOUSE	Serine hydroxymethyltransferase, mitochondrial	Shmt2	0,00286616	58512,959	366880,466	0,159	6,270	Upregulated in KO
Q922K7		NOP2_MOUSE	Probable 28S rRNA (cytosine-C(5))-methyltransferase	Nop2	0,01548449	1036,541	6417,697	0,162	6,191	Upregulated in KO
Q9JKR6		HYOU1_MOUSE	Hypoxia up-regulated protein 1	Hyou1	0,00690712	2897,600	17702,150	0,164	6,109	Upregulated in KO
Q91VR2		ATPG_MOUSE	ATP synthase subunit gamma, mitochondrial	Atp5f1c	0,00151932	5992,981	34781,725	0,172	5,804	Upregulated in KO
P26041		MOES_MOUSE	Moesin	Msn	0,00486552	1262,994	7160,310	0,176	5,669	Upregulated in KO
Q62511		ZFP91_MOUSE	E3 ubiquitin-protein ligase ZFP91	Zfp91	0,00187773	2259,962	12670,689	0,178	5,607	Upregulated in KO
P63001		RAC1_MOUSE	Ras-related C3 botulinum toxin substrate 1	Rac1	0,00025422	4935,717	27457,108	0,180	5,563	Upregulated in KO
Q8R0X7		SGPL1_MOUSE	Sphingosine-1-phosphate lyase 1	Sgpl1	0,01457843	1955,099	10644,862	0,184	5,445	Upregulated in KO
Q8C2Q3		RBM14_MOUSE	RNA-binding protein 14	Rbm14	5,04E-05	32175,294	170372,206	0,189	5,295	Upregulated in KO
Q9WV54		ASAH1_MOUSE	Acid ceramidase	Asah1	2,08E-05	6360,378	33462,417	0,190	5,261	Upregulated in KO
Q04736		YES_MOUSE	Tyrosine-protein kinase Yes	Yes1	4,60E-05	1699,077	8911,179	0,191	5,245	Upregulated in KO
P15864		H12_MOUSE	Histone H1.2	H1-2	2,76E-05	67837,661	344411,959	0,197	5,077	Upregulated in KO
P20029		BIP_MOUSE	Endoplasmic reticulum chaperone BiP	Hspa5	0,03689516	69946,431	345383,903	0,203	4,938	Upregulated in KO
Q91YP0		L2HDH_MOUSE	L-2-hydroxyglutarate dehydrogenase, mitochondrial	L2hgdh	0,00204537	1245,771	6142,982	0,203	4,931	Upregulated in KO

P97310		MCM2_MOUSE	DNA replication licensing factor MCM2	Mcm2	0,0004981	16665,686	80486,270	0,207	4,829	Upregulated in KO
P14152		MDHC_MOUSE	Malate dehydrogenase, cytoplasmic	Mdh1	0,00399	682,635	3154,898	0,216	4,622	Upregulated in KO
P80315		TCPD_MOUSE	T-complex protein 1 subunit delta	Cct4	0,00140654	3575,118	16422,899	0,218	4,594	Upregulated in KO
P30681		HMGB2_MOUSE	High mobility group protein B2	Hmgb2	0,04813866	12260,090	56232,026	0,218	4,587	Upregulated in KO
Q9Z0X1		AIFM1_MOUSE	Apoptosis-inducing factor 1, mitochondrial	Aifm1	3,67E-05	7467,265	34190,219	0,218	4,579	Upregulated in KO
Q9CSN1		SNW1_MOUSE	SNW domain-containing protein 1	Snw1	5,22E-05	1474,407	6741,270	0,219	4,572	Upregulated in KO
Q9DBR1		XRN2_MOUSE	5'-3' exoribonuclease 2	Xrn2	0,00035964	2005,435	9112,180	0,220	4,544	Upregulated in KO
P56480		ATPB_MOUSE	ATP synthase subunit beta, mitochondrial	Atp5f1b	0,00300971	39846,737	180253,242	0,221	4,524	Upregulated in KO
P40142		TKT_MOUSE	Transketolase	Tkt	0,01451125	3440,808	15497,871	0,222	4,504	Upregulated in KO
Q8BIQ5		CSTF2_MOUSE	Cleavage stimulation factor subunit 2	Cstf2	2,29E-06	8819,696	38033,169	0,232	4,312	Upregulated in KO
Q91WJ8		FUBP1_MOUSE	Far upstream element-binding protein 1	Fubp1	0,02623645	4683,922	19821,943	0,236	4,232	Upregulated in KO
Q9Z315		SNUT1_MOUSE	U4/U6.U5 tri-snRNP-associated protein 1	Sart1	0,0057615	2049,354	8596,081	0,238	4,195	Upregulated in KO
Q99PL5		RRBP1_MOUSE	Ribosome-binding protein 1	Rrbp1	0,00048902	1481,231	6124,886	0,242	4,135	Upregulated in KO
Q8BJ71		NUP93_MOUSE	Nuclear pore complex protein Nup93	Nup93	0,00498923	10429,117	42077,080	0,248	4,035	Upregulated in KO
Q9QXX4		CMC2_MOUSE	Calcium-binding mitochondrial carrier protein Aralar2	Slc25a13	0,0073023	16059,201	64614,160	0,249	4,023	Upregulated in KO
Q9D880		TIM50_MOUSE	Mitochondrial import inner membrane translocase subunit TIM50	Timm50	0,02032712	2731,426	10925,834	0,250	4,000	Upregulated in KO
P62137		PP1A_MOUSE	Serine/threonine-protein phosphatase PP1-alpha catalytic subunit	Ppp1ca	0,00014679	3558,098	14196,758	0,251	3,990	Upregulated in KO

Q00PI9		HNRL2_MOUSE	Heterogeneous nuclear ribonucleoprotein U-like protein 2	Hnrnpul2	0,00085962	14383,680	55977,822	0,257	3,892	Upregulated in KO
O55143		AT2A2_MOUSE	Sarcoplasmic/endoplasmic reticulum calcium ATPase 2	Atp2a2	0,00208565	11506,904	43666,885	0,264	3,795	Upregulated in KO
Q9DCW4		ETFB_MOUSE	Electron transfer flavoprotein subunit beta	Etfb	0,00124822	7294,325	27517,918	0,265	3,773	Upregulated in KO
Q9CZX8		RS19_MOUSE	40S ribosomal protein S19	Rps19	0,00255826	4487,458	16873,153	0,266	3,760	Upregulated in KO
Q61753		SERA_MOUSE	D-3-phosphoglycerate dehydrogenase	Phgdh	0,00761275	16235,952	60677,551	0,268	3,737	Upregulated in KO
Q8BXZ1		TMX3_MOUSE	Protein disulfide-isomerase TMX3	Tmx3	0,01925873	2215,957	8232,407	0,269	3,715	Upregulated in KO
Q9Z2D8		MBD3_MOUSE	Methyl-CpG-binding domain protein 3	Mbd3	0,03176739	1558,964	5572,030	0,280	3,574	Upregulated in KO
Q8BMD8		SCMC1_MOUSE	Calcium-binding mitochondrial carrier protein SCaMC-1	Slc25a24	0,00015802	35416,783	124055,745	0,285	3,503	Upregulated in KO
Q61543		GSLG1_MOUSE	Golgi apparatus protein 1	Glg1	0,00123492	1123,638	3919,081	0,287	3,488	Upregulated in KO
Q91VD9		NDUS1_MOUSE	NADH-ubiquinone oxidoreductase 75 kDa subunit, mitochondrial	Ndufs1	6,90E-05	6508,548	22432,273	0,290	3,447	Upregulated in KO
O08795		GLU2B_MOUSE	Glucosidase 2 subunit beta	Prkcsh	0,01032434	26015,846	89093,618	0,292	3,425	Upregulated in KO
Q8BMS1		ECHA_MOUSE	Trifunctional enzyme subunit alpha, mitochondrial	Hadha	1,46E-05	40015,913	136968,843	0,292	3,423	Upregulated in KO
Q3U9G9		LBR_MOUSE	Delta(14)-sterol reductase LBR	Lbr	0,00602263	7015,000	23512,289	0,298	3,352	Upregulated in KO
Q9R069		BCAM_MOUSE	Basal cell adhesion molecule	Bcam	0,0012866	2990,219	9832,312	0,304	3,288	Upregulated in KO
Q9WTM5		RUVB2_MOUSE	RuvB-like 2	Ruvbl2	0,04654432	1189,940	3873,323	0,307	3,255	Upregulated in KO
P62281		RS11_MOUSE	40S ribosomal protein S11	Rps11	0,011161	5928,557	18560,409	0,319	3,131	Upregulated in KO
Q9CZW5		TOM70_MOUSE	Mitochondrial import receptor subunit TOM70	Tomm70	0,00124146	3004,793	9389,978	0,320	3,125	Upregulated in KO
P01899		HA11_MOUSE	H-2 class I histocompatibility antigen, D-B alpha chain	H2-D1	0,02374394	2338,697	7161,415	0,327	3,062	Upregulated in KO

P21614		VTDB_MOUSE	Vitamin D-binding protein	Gc	0,01791725	1281,876	3879,642	0,330	3,027	Upregulated in KO
Q69ZN7		MYOF_MOUSE	Myoferlin	Myof	0,0005721	36556,584	110466,268	0,331	3,022	Upregulated in KO
P48678		LMNA_MOUSE	Prelamin-A/C	Lmna	0,01592969	15599,201	46879,578	0,333	3,005	Upregulated in KO
P60867		RS20_MOUSE	40S ribosomal protein S20	Rps20	0,00076731	4360,410	12995,345	0,336	2,980	Upregulated in KO
P04104		K2C1_MOUSE	Keratin, type II cytoskeletal 1	Krt1	0,02074606	1675,373	4818,245	0,348	2,876	Upregulated in KO
Q8VDM4		PSMD2_MOUSE	26S proteasome non-ATPase regulatory subunit 2	Psmd2	0,02002671	354,160	1013,137	0,350	2,861	Upregulated in KO
P63038		CH60_MOUSE	60 kDa heat shock protein, mitochondrial	Hspd1	0,01925566	348400,542	965073,226	0,361	2,770	Upregulated in KO
Q8VDN2		AT1A1_MOUSE	Sodium/potassium-transporting ATPase subunit alpha-1	Atp1a1	1,56E-05	82770,992	225189,304	0,368	2,721	Upregulated in KO
O35691		PININ_MOUSE	Pinin	Pnn	4,95E-05	12532,569	34002,574	0,369	2,713	Upregulated in KO
P37040		NCPR_MOUSE	NADPH--cytochrome P450 reductase	Por	0,00459014	31404,001	83902,073	0,374	2,672	Upregulated in KO
Q9JLJ2		AL9A1_MOUSE	4-trimethylaminobutyraldehyde dehydrogenase	Aldh9a1	0,00270167	3308,450	8695,043	0,380	2,628	Upregulated in KO
Q921F2		TADBP_MOUSE	TAR DNA-binding protein 43	Tardbp	2,77E-05	28263,447	73305,225	0,386	2,594	Upregulated in KO
P01942		HBA_MOUSE	Hemoglobin subunit alpha	Hba	0,00095372	5180,932	13421,794	0,386	2,591	Upregulated in KO
Q64727		VINC_MOUSE	Vinculin	Vcl	0,00203713	7985,873	20357,298	0,392	2,549	Upregulated in KO
P49717		MCM4_MOUSE	DNA replication licensing factor MCM4	Mcm4	0,00099605	17697,073	44752,690	0,395	2,529	Upregulated in KO
P14733		LMNB1_MOUSE	Lamin-B1	Lmnb1	0,00078867	16596,115	40475,442	0,410	2,439	Upregulated in KO
P48962		ADT1_MOUSE	ADP/ATP translocase 1	Slc25a4	0,0004906	3060,578	7463,533	0,410	2,439	Upregulated in KO
P05202		AATM_MOUSE	Aspartate aminotransferase, mitochondrial	Got2	0,00154427	136858,312	324734,849	0,421	2,373	Upregulated in KO

Q03265		ATPA_MOUSE	ATP synthase subunit alpha, mitochondrial	Atp5f1a	0,00267124	64668,748	150713,167	0,429	2,331	Upregulated in KO
Q9Z2I9		SUCB1_MOUSE	Succinate--CoA ligase [ADP-forming] subunit beta, mitochondrial	Sucla2	0,04714632	5439,025	12460,592	0,436	2,291	Upregulated in KO
Q91VC3		IF4A3_MOUSE	Eukaryotic initiation factor 4A-III	Eif4a3	0,00354453	4295,143	9832,319	0,437	2,289	Upregulated in KO
P17095		HMGA1_MOUSE	High mobility group protein HMG-I/HMG-Y	Hmga1	0,00030523	7703,207	17599,015	0,438	2,285	Upregulated in KO
P49718		MCM5_MOUSE	DNA replication licensing factor MCM5	Mcm5	0,00020951	25424,966	57655,079	0,441	2,268	Upregulated in KO
Q7TMK9	2	HNRPQ_MOUSE	Isoform 2 of Heterogeneous nuclear ribonucleoprotein Q	Syncrip	0,00128831	21997,831	47432,980	0,464	2,156	Upregulated in KO
Q6PDQ2		CHD4_MOUSE	Chromodomain-helicase-DNA-binding protein 4	Chd4	0,01308817	8277,615	17667,948	0,469	2,134	Upregulated in KO
P56959		FUS_MOUSE	RNA-binding protein FUS	Fus	0,00342537	16844,707	35505,368	0,474	2,108	Upregulated in KO
P08249		MDHM_MOUSE	Malate dehydrogenase, mitochondrial	Mdh2	0,02360026	88758,966	186556,168	0,476	2,102	Upregulated in KO
Q62318		TIF1B_MOUSE	Transcription intermediary factor 1-beta	Trim28	0,00014041	37957,127	79754,191	0,476	2,101	Upregulated in KO
Q61029		LAP2B_MOUSE	Lamina-associated polypeptide 2, isoforms beta/delta/epsilon/gamma	Tmpo	0,00014924	51674,249	108379,330	0,477	2,097	Upregulated in KO
E9Q5C9		NOLC1_MOUSE	Nucleolar and coiled-body phosphoprotein 1	Nolc1	0,00396392	9726,267	20188,845	0,482	2,076	Upregulated in KO
P10126		EF1A1_MOUSE	Elongation factor 1-alpha 1	Eef1a1	0,02814974	14057,508	28822,049	0,488	2,050	Upregulated in KO
Q8BI72		CARF_MOUSE	CDKN2A-interacting protein	Cdkn2aip	0,00249004	3176,773	6435,802	0,494	2,026	Upregulated in KO
Q61656		DDX5_MOUSE	Probable ATP-dependent RNA helicase DDX5	Ddx5	0,01009151	92103,681	184491,428	0,499	2,003	Upregulated in KO
Q9DB15		RM12_MOUSE	39S ribosomal protein L12, mitochondrial	Mrpl12	0,03595805	6829,566	13445,457	0,508	1,969	Upregulated in KO
Q62261		SPTB2_MOUSE	Spectrin beta chain, non-erythrocytic 1	Sptbn1	0,00275454	14733,937	28423,785	0,518	1,929	Upregulated in KO
P35564		CALX_MOUSE	Calnexin	Canx	0,03580668	10066,451	19410,867	0,519	1,928	Upregulated in KO

Q9D0K2		SCOT1_MOUSE	Succinyl-CoA:3-ketoacid coenzyme A transferase 1, mitochondrial	Oxct1	0,02927942	14457,139	27616,449	0,523	1,910	Upregulated in KO
Q9D6R2		IDH3A_MOUSE	Isocitrate dehydrogenase [NAD] subunit alpha, mitochondrial	Idh3a	0,02908853	11063,803	20915,460	0,529	1,890	Upregulated in KO
Q60749		KHDR1_MOUSE	KH domain-containing, RNA-binding, signal transduction-associated protein 1	Khdrbs1	0,01306484	30880,718	57344,826	0,539	1,857	Upregulated in KO
Q61937		NPM_MOUSE	Nucleophosmin	Npm1	0,00499215	13135,267	24178,927	0,543	1,841	Upregulated in KO
Q9Z277		BAZ1B_MOUSE	Tyrosine-protein kinase BAZ1B	Baz1b	0,00304174	19255,191	34861,698	0,552	1,811	Upregulated in KO
Q811D0	3	DLG1_MOUSE	Isoform 3 of Disks large homolog 1	Dlg1	0,03748643	4608,816	8336,510	0,553	1,809	Upregulated in KO
P16546		SPTN1_MOUSE	Spectrin alpha chain, non-erythrocytic 1	Sptan1	0,00532686	22075,673	39891,424	0,553	1,807	Upregulated in KO
P20108		PRDX3_MOUSE	Thioredoxin-dependent peroxide reductase, mitochondrial	Prdx3	0,02558295	17623,553	31137,551	0,566	1,767	Upregulated in KO
Q99JF8		PSIP1_MOUSE	PC4 and SFRS1-interacting protein	Psip1	0,0012847	14264,195	24919,452	0,572	1,747	Upregulated in KO
Q9D3D9		ATPD_MOUSE	ATP synthase subunit delta, mitochondrial	Atp5f1d	0,03017281	4004,047	6973,045	0,574	1,741	Upregulated in KO
Q9R190		MTA2_MOUSE	Metastasis-associated protein MTA2	Mta2	0,03156218	25364,836	43873,759	0,578	1,730	Upregulated in KO
Q9Z2X1		HNRPF_MOUSE	Heterogeneous nuclear ribonucleoprotein F	Hnrnpf	0,00156506	59281,201	102409,027	0,579	1,728	Upregulated in KO
P97461		RS5_MOUSE	40S ribosomal protein S5	Rps5	0,03726722	18863,617	31531,896	0,598	1,672	Upregulated in KO
Q99JI6		RAP1B_MOUSE	Ras-related protein Rap-1b	Rap1b	0,00110826	6357,647	10520,974	0,604	1,655	Upregulated in KO
Q8VIJ6		SFPQ_MOUSE	Splicing factor, proline- and glutamine-rich	Sfpq	0,00998762	157172,277	256665,488	0,612	1,633	Upregulated in KO
Q8VDF2		UHRF1_MOUSE	E3 ubiquitin-protein ligase UHRF1	Uhrf1	0,00210698	39619,299	64340,932	0,616	1,624	Upregulated in KO
P07356		ANXA2_MOUSE	Annexin A2	Anxa2	0,03039366	11316,569	17894,867	0,632	1,581	Upregulated in KO

P50171		DHB8_MOUSE	Estradiol 17-beta-dehydrogenase 8	Hsd17b8	0,00444773	14556,103	22328,069	0,652	1,534	Upregulated in KO
P28667		MRP_MOUSE	MARCKS-related protein	Marcksl1	0,04004364	8177,250	12195,210	0,671	1,491	FC<1,5
Q9CX86		ROA0_MOUSE	Heterogeneous nuclear ribonucleoprotein A0	Hnrnpa0	0,00721622	19363,952	28624,923	0,676	1,478	FC<1,5
O35737		HNRH1_MOUSE	Heterogeneous nuclear ribonucleoprotein H	Hnrnph1	0,03915192	59259,845	84406,608	0,702	1,424	FC<1,5
Q99LC5		ETFA_MOUSE	Electron transfer flavoprotein subunit alpha, mitochondrial	Etfa	0,03537505	4278,377	5894,679	0,726	1,378	FC<1,5
Q99LD8		DDAH2_MOUSE	N(G),N(G)-dimethylarginine dimethylaminohydrolase 2	Ddah2	0,02500958	14902,457	20124,919	0,740	1,350	FC<1,5
Q9DB20		ATPO_MOUSE	ATP synthase subunit O, mitochondrial	Atp5po	0,03719492	32481,870	43260,516	0,751	1,332	FC<1,5
Q64436		ATP4A_MOUSE	Potassium-transporting ATPase alpha chain 1	Atp4a	0,04734545	44760,779	58872,432	0,760	1,315	FC<1,5
Q61941		NNTM_MOUSE	NAD(P) transhydrogenase, mitochondrial	Nnt	0,02912502	6146,705	7249,860	0,848	1,179	FC<1,5
P09055		ITB1_MOUSE	Integrin beta-1	Itgb1	0,04755162	36279,458	28600,487	1,268	0,788	FC<1,5
O88286	3	WIZ_MOUSE	Isoform 2 of Protein Wiz	Wiz	0,01080985	20818,117	15665,788	1,329	0,753	FC<1,5
Q9DC51		GNAI3_MOUSE	Guanine nucleotide-binding protein G(i) subunit alpha-3	Gnai3	0,02523864	15985,258	11553,980	1,384	0,723	FC<1,5
Q8CAQ8	3	MIC60_MOUSE	Isoform 3 of MICOS complex subunit Mic60	Immt	0,02770265	102208,186	73622,709	1,388	0,720	FC<1,5
P63276		RS17_MOUSE	40S ribosomal protein S17	Rps17	0,01830375	14206,361	9686,125	1,467	0,682	FC<1,5
Q99K48		NONO_MOUSE	Non-POU domain-containing octamer-binding protein	Nono	0,00960346	85795,112	57159,915	1,501	0,666	Downregulated in KO
Q91ZW3		SMCA5_MOUSE	SWI/SNF-related matrix-associated actin-dependent regulator of chromatin subfamily A member 5	Smarca5	0,01295086	96992,757	64617,197	1,501	0,666	Downregulated in KO
P32261		ANT3_MOUSE	Antithrombin-III	Serpinc1	0,03252866	4738,396	3116,795	1,520	0,658	Downregulated in KO
Q9D1L0		CHCH2_MOUSE	Coiled-coil-helix-coiled-coil-helix domain-containing protein 2	Chchd2	0,00226464	46278,620	30322,415	1,526	0,655	Downregulated in KO

Q60597		ODO1_MOUSE	2-oxoglutarate dehydrogenase, mitochondrial	Ogdh	0,03235625	73300,395	47356,947	1,548	0,646	Downregulated in KO
Q8K019		BCLF1_MOUSE	Bcl-2-associated transcription factor 1	Bclaf1	0,01360318	47308,778	30460,985	1,553	0,644	Downregulated in KO
P47962		RL5_MOUSE	60S ribosomal protein L5	Rpl5	0,00973096	23601,168	15185,939	1,554	0,643	Downregulated in KO
Q8BH04		PCKGM_MOUSE	Phosphoenolpyruvate carboxykinase [GTP], mitochondrial	Pck2	0,01344843	92367,514	58382,301	1,582	0,632	Downregulated in KO
Q922R8		PDIA6_MOUSE	Protein disulfide-isomerase A6	Pdia6	0,04788868	77664,960	48682,080	1,595	0,627	Downregulated in KO
P58252		EF2_MOUSE	Elongation factor 2	Eef2	0,01647336	26344,721	16396,353	1,607	0,622	Downregulated in KO
O70133		DHX9_MOUSE	ATP-dependent RNA helicase A	Dhx9	0,01000042	19611,025	12123,251	1,618	0,618	Downregulated in KO
P09405		NUCL_MOUSE	Nucleolin	Ncl	0,0108578	43852,947	26836,686	1,634	0,612	Downregulated in KO
Q9CU62		SMC1A_MOUSE	Structural maintenance of chromosomes protein 1A	Smc1a	0,02785434	17925,502	10928,368	1,640	0,610	Downregulated in KO
P97807		FUMH_MOUSE	Fumarate hydratase, mitochondrial	Fh	0,00209895	10369,002	6305,120	1,645	0,608	Downregulated in KO
P23591		FCL_MOUSE	GDP-L-fucose synthase	Gfus	0,02420459	2282,104	1375,031	1,660	0,603	Downregulated in KO
P62317		SMD2_MOUSE	Small nuclear ribonucleoprotein Sm D2	Snrpd2	0,01262023	14151,167	8503,828	1,664	0,601	Downregulated in KO
P35550		FBRL_MOUSE	rRNA 2'-O-methyltransferase fibrillarin	Fbl	0,00292611	31181,466	18606,992	1,676	0,597	Downregulated in KO
P30999		CTND1_MOUSE	Catenin delta-1	Ctnnd1	0,00087555	67634,560	40329,836	1,677	0,596	Downregulated in KO
P47963		RL13_MOUSE	60S ribosomal protein L13	Rpl13	0,02620601	4710,425	2808,115	1,677	0,596	Downregulated in KO
Q8VEM8		MPCP_MOUSE	Phosphate carrier protein, mitochondrial	Slc25a3	0,00169599	418677,512	247580,083	1,691	0,591	Downregulated in KO
Q501J6		DDX17_MOUSE	Probable ATP-dependent RNA helicase DDX17	Ddx17	0,00062919	49641,436	29300,775	1,694	0,590	Downregulated in KO
Q61881		MCM7_MOUSE	DNA replication licensing factor MCM7	Mcm7	0,03791129	72380,244	42182,902	1,716	0,583	Downregulated in KO

P67778		PHB_MOUSE	Prohibitin	Phb	0,01124212	15661,386	9112,984	1,719	0,582	Downregulated in KO
P32067		LA_MOUSE	Lupus La protein homolog	Ssb	0,00266651	35334,973	20398,761	1,732	0,577	Downregulated in KO
Q9ES97		RTN3_MOUSE	Reticulon-3	Rtn3	0,00041983	27839,183	16056,398	1,734	0,577	Downregulated in KO
P35979		RL12_MOUSE	60S ribosomal protein L12	Rpl12	0,00170255	11816,964	6803,515	1,737	0,576	Downregulated in KO
Q9JHL1		NHRF2_MOUSE	Na(+)/H(+) exchange regulatory cofactor NHE-RF2	Slc9a3r2	0,00106854	12926,422	7433,671	1,739	0,575	Downregulated in KO
P25976		UBF1_MOUSE	Nucleolar transcription factor 1	Ubtf	0,01609023	20164,544	11542,633	1,747	0,572	Downregulated in KO
P84104		SRSF3_MOUSE	Serine/arginine-rich splicing factor 3	Srsf3	0,00358528	26003,122	14688,143	1,770	0,565	Downregulated in KO
P99029		PRDX5_MOUSE	Peroxiredoxin-5, mitochondrial	Prdx5	0,00025049	7605,790	4293,790	1,771	0,565	Downregulated in KO
P14131		RS16_MOUSE	40S ribosomal protein S16	Rps16	0,00596324	4161,997	2334,460	1,783	0,561	Downregulated in KO
Q61703		ITIH2_MOUSE	Inter-alpha-trypsin inhibitor heavy chain H2	Itih2	0,01731054	9140,247	5121,544	1,785	0,560	Downregulated in KO
Q9EQU5		SET_MOUSE	Protein SET	Set	0,03258425	3548,706	1975,793	1,796	0,557	Downregulated in KO
Q8K2B3		SDHA_MOUSE	Succinate dehydrogenase [ubiquinone] flavoprotein subunit, mitochondrial	Sdha	0,00839852	22769,305	12669,645	1,797	0,556	Downregulated in KO
P27773		PDIA3_MOUSE	Protein disulfide-isomerase A3	Pdia3	0,02714903	402520,024	216716,809	1,857	0,538	Downregulated in KO
Q9D0Q7		RM45_MOUSE	39S ribosomal protein L45, mitochondrial	Mrpl45	0,00158371	5872,184	3137,933	1,871	0,534	Downregulated in KO
Q3TWW8		SRSF6_MOUSE	Serine/arginine-rich splicing factor 6	Srsf6	0,00651133	10138,046	5405,624	1,875	0,533	Downregulated in KO
P62821		RAB1A_MOUSE	Ras-related protein Rab-1A	Rab1A	0,0004941	11127,963	5922,633	1,879	0,532	Downregulated in KO
O08553		DPYL2_MOUSE	Dihydropyrimidinase-related protein 2	Dpysl2	0,00587847	7092,542	3744,921	1,894	0,528	Downregulated in KO
P62754		RS6_MOUSE	40S ribosomal protein S6	Rps6	0,01848437	16280,269	8528,946	1,909	0,524	Downregulated in KO
P18760		COF1_MOUSE	Cofilin-1	Cfl1	0,04049218	5349,560	2793,728	1,915	0,522	Downregulated in KO

Q9DCN2		NB5R3_MOUSE	NADH-cytochrome b5 reductase 3	Cyb5r3	7,86E-08	84981,663	43643,898	1,947	0,514	Downregulated in KO
Q3UQ84		SYTM_MOUSE	Threonine--tRNA ligase, mitochondrial	Tars2	0,00050956	18033,993	9165,799	1,968	0,508	Downregulated in KO
P25206		MCM3_MOUSE	DNA replication licensing factor MCM3	Mcm3	0,0016109	108970,051	54951,598	1,983	0,504	Downregulated in KO
Q6NZJ6		IF4G1_MOUSE	Eukaryotic translation initiation factor 4 gamma 1	Eif4g1	0,00086178	3991,569	2012,157	1,984	0,504	Downregulated in KO
P50580		PA2G4_MOUSE	Proliferation-associated protein 2G4	Pa2g4	0,0071263	3215,689	1612,846	1,994	0,502	Downregulated in KO
P29699		FETUA_MOUSE	Alpha-2-HS-glycoprotein	Ahsg	0,0171493	2757,903	1374,707	2,006	0,498	Downregulated in KO
Q9JMD0		ZN207_MOUSE	BUB3-interacting and GLEBS motif-containing protein ZNF207	Znf207	0,00350418	9375,866	4637,320	2,022	0,495	Downregulated in KO
Q61838		PZP_MOUSE	Pregnancy zone protein	Pzp	0,03753477	1645,553	809,370	2,033	0,492	Downregulated in KO
P05201		AATC_MOUSE	Aspartate aminotransferase, cytoplasmic	Got1	0,02901876	5300,950	2553,644	2,076	0,482	Downregulated in KO
P23927		CRYAB_MOUSE	Alpha-crystallin B chain	Cryab	0,04273506	2729,570	1303,701	2,094	0,478	Downregulated in KO
O70435		PSA3_MOUSE	Proteasome subunit alpha type-3	Psma3	0,00838242	1077,528	511,176	2,108	0,474	Downregulated in KO
Q9WTQ5		AKA12_MOUSE	A-kinase anchor protein 12	Akap12	0,00667205	8309,330	3870,994	2,147	0,466	Downregulated in KO
Q3THS6		METK2_MOUSE	S-adenosylmethionine synthase isoform type-2	Mat2a	0,00598479	7558,631	3414,980	2,213	0,452	Downregulated in KO
P10639		THIO_MOUSE	Thioredoxin	Txn	0,00947626	5572,146	2514,963	2,216	0,451	Downregulated in KO
Q9QWT9		KIFC1_MOUSE	Kinesin-like protein KIFC1	Kifc1	0,00187245	29237,161	13165,150	2,221	0,450	Downregulated in KO
P09411		PGK1_MOUSE	Phosphoglycerate kinase 1	Pgk1	1,37E-05	2978,178	1333,907	2,233	0,448	Downregulated in KO
Q8BWT1		THIM_MOUSE	3-ketoacyl-CoA thiolase, mitochondrial	Acaa2	0,00096184	8132,238	3620,668	2,246	0,445	Downregulated in KO
Q62189		SNRPA_MOUSE	U1 small nuclear ribonucleoprotein A	Snrpa	0,00352219	11363,712	5008,788	2,269	0,441	Downregulated in KO
Q8BJS4		SUN2_MOUSE	SUN domain-containing protein 2	Sun2	0,00011014	25567,338	11176,603	2,288	0,437	Downregulated in KO

Q61191		HCFC1_MOUSE	Host cell factor 1	Hcfc1	0,000138	12640,069	5521,867	2,289	0,437	Downregulated in KO
P62301		RS13_MOUSE	40S ribosomal protein S13	Rps13	0,01819187	2413,546	1047,979	2,303	0,434	Downregulated in KO
Q6P5D8		SMHD1_MOUSE	Structural maintenance of chromosomes flexible hinge domain-containing protein 1	Smchd1	0,00211582	3069,189	1330,529	2,307	0,434	Downregulated in KO
Q9JHI5		IVD_MOUSE	Isovaleryl-CoA dehydrogenase, mitochondrial	Ivd	0,00180421	18496,577	7969,213	2,321	0,431	Downregulated in KO
P47915		RL29_MOUSE	60S ribosomal protein L29	Rpl29	0,0017468	28764,116	12318,199	2,335	0,428	Downregulated in KO
Q9JMG1		EDF1_MOUSE	Endothelial differentiation-related factor 1	Edf1	0,04714429	2117,935	894,863	2,367	0,423	Downregulated in KO
Q3TIX9		SNUT2_MOUSE	U4/U6.U5 tri-snRNP-associated protein 2	Usp39	0,00949824	1120,681	466,076	2,405	0,416	Downregulated in KO
P56391		CX6B1_MOUSE	Cytochrome c oxidase subunit 6B1	Cox6b1	0,00445517	1871,075	777,655	2,406	0,416	Downregulated in KO
Q8C1A5		THOP1_MOUSE	Thimet oligopeptidase	Thop1	0,010676	3386,948	1401,704	2,416	0,414	Downregulated in KO
Q99MD9		NASP_MOUSE	Nuclear autoantigenic sperm protein	Nasp	0,02157459	4504,929	1862,053	2,419	0,413	Downregulated in KO
Q61646		HPT_MOUSE	Haptoglobin	Hp	0,02131346	2321,737	955,411	2,430	0,412	Downregulated in KO
Q9Z1X4	3	ILF3_MOUSE	Isoform 3 of Interleukin enhancer-binding factor 3	Ilf3	4,53E-05	11309,111	4574,700	2,472	0,405	Downregulated in KO
Q8BTI8		SRRM2_MOUSE	Serine/arginine repetitive matrix protein 2	Srrm2	0,00134201	3169,126	1278,243	2,479	0,403	Downregulated in KO
Q9CQ92		FIS1_MOUSE	Mitochondrial fission 1 protein	Fis1	0,00181356	562,857	226,151	2,489	0,402	Downregulated in KO
Q61792		LASP1_MOUSE	LIM and SH3 domain protein 1	Lasp1	0,04082037	843,185	337,890	2,495	0,401	Downregulated in KO
P08228		SODC_MOUSE	Superoxide dismutase [Cu-Zn]	Sod1	0,03681356	9378,115	3757,235	2,496	0,401	Downregulated in KO
Q61879		MYH10_MOUSE	Myosin-10	Myh10	0,03011844	3718,560	1483,169	2,507	0,399	Downregulated in KO
Q91Z49		UIF_MOUSE	UAP56-interacting factor	Fyttd1	4,20E-05	12068,774	4783,038	2,523	0,396	Downregulated in KO

Q6PB66		LPPRC_MOUSE	Leucine-rich PPR motif-containing protein, mitochondrial	Lrpprc	3,10E-05	26471,928	10275,433	2,576	0,388	Downregulated in KO
P62242		RS8_MOUSE	40S ribosomal protein S8	Rps8	1,50E-05	16718,817	6466,888	2,585	0,387	Downregulated in KO
Q8C570		RAE1L_MOUSE	mRNA export factor	Rae1	0,00725085	8056,334	3096,220	2,602	0,384	Downregulated in KO
P39749		FEN1_MOUSE	Flap endonuclease 1	Fen1	0,00165495	4934,033	1891,445	2,609	0,383	Downregulated in KO
B2RQC6		PYR1_MOUSE	CAD protein	Cad	0,0015064	6874,410	2599,677	2,644	0,378	Downregulated in KO
P53395		ODB2_MOUSE	Lipoamide acyltransferase component of branched-chain alpha-keto acid dehydrogenase complex, mitochondrial	Dbt	4,38E-06	26042,741	9827,915	2,650	0,377	Downregulated in KO
O35295		PURB_MOUSE	Transcriptional activator protein Pur-beta	Purb	0,00106407	13129,475	4931,622	2,662	0,376	Downregulated in KO
P11983		TCPA_MOUSE	T-complex protein 1 subunit alpha	Tcp1	0,00194083	3288,160	1234,370	2,664	0,375	Downregulated in KO
Q9JIF7		COPB_MOUSE	Coatomer subunit beta	Copb1	0,00011466	3620,347	1339,213	2,703	0,370	Downregulated in KO
Q91VU0		FAM3C_MOUSE	Protein FAM3C	Fam3c	0,00272343	7414,663	2738,325	2,708	0,369	Downregulated in KO
Q9WUM3		COR1B_MOUSE	Coronin-1B	Coro1b	0,00860382	2365,000	868,241	2,724	0,367	Downregulated in KO
Q61581		IBP7_MOUSE	Insulin-like growth factor-binding protein 7	Igfbp7	0,03691261	3004,852	1087,335	2,764	0,362	Downregulated in KO
Q9JHU4		DYHC1_MOUSE	Cytoplasmic dynein 1 heavy chain 1	Dync1h1	5,86E-05	6295,988	2207,509	2,852	0,351	Downregulated in KO
P19324		SERPH_MOUSE	Serpin H1	Serpinh1	0,00319567	16181,813	5571,148	2,905	0,344	Downregulated in KO
E9PVA8		GCN1_MOUSE	eIF-2-alpha kinase activator GCN1	Gcn1	0,00034938	6240,816	2121,255	2,942	0,340	Downregulated in KO
Q6GQT1		A2MG_MOUSE	Alpha-2-macroglobulin-P	A2m	0,0404839	5365,331	1811,255	2,962	0,338	Downregulated in KO
O70400		PDLI1_MOUSE	PDZ and LIM domain protein 1	Pdlim1	0,01678638	4495,859	1507,182	2,983	0,335	Downregulated in KO

Q9R1P0		PSA4_MOUSE	Proteasome subunit alpha type-4	Psma4	0,00254692	2353,106	783,527	3,003	0,333	Downregulated in KO
P46935		NEDD4_MOUSE	E3 ubiquitin-protein ligase NEDD4	Nedd4	0,03249227	2794,460	908,503	3,076	0,325	Downregulated in KO
P09450		JUNB_MOUSE	Transcription factor jun-B	Junb	0,00091343	20333,580	6444,702	3,155	0,317	Downregulated in KO
Q9QUI0		RHOA_MOUSE	Transforming protein RhoA	Rhoa	0,00519364	1885,522	596,721	3,160	0,316	Downregulated in KO
Q9D051		ODPB_MOUSE	Pyruvate dehydrogenase E1 component subunit beta, mitochondrial	Pdhb	5,26E-05	14118,892	4411,387	3,201	0,312	Downregulated in KO
Q8QZT1		THIL_MOUSE	Acetyl-CoA acetyltransferase, mitochondrial	Acat1	1,73E-07	36226,023	11074,617	3,271	0,306	Downregulated in KO
P16110		LEG3_MOUSE	Galectin-3	Lgals3	0,01330288	2208,977	664,331	3,325	0,301	Downregulated in KO
Q9CPR4		RL17_MOUSE	60S ribosomal protein L17	Rpl17	0,0197354	1061,468	316,447	3,354	0,298	Downregulated in KO
P61358		RL27_MOUSE	60S ribosomal protein L27	Rpl27	0,00079348	3613,074	1041,384	3,469	0,288	Downregulated in KO
Q80U93		NU214_MOUSE	Nuclear pore complex protein Nup214	Nup214	2,20E-05	3509,756	1008,265	3,481	0,287	Downregulated in KO
Q9DCJ5		NDUA8_MOUSE	NADH dehydrogenase [ubiquinone] 1 alpha subcomplex subunit 8	Ndufa8	5,28E-06	33462,887	9492,369	3,525	0,284	Downregulated in KO
Q60604		ADSV_MOUSE	Adseverin	Scin	0,02641812	9148,254	2576,133	3,551	0,282	Downregulated in KO
P47758		SRPRB_MOUSE	Signal recognition particle receptor subunit beta	Srprb	0,03996826	15676,866	4402,157	3,561	0,281	Downregulated in KO
O55125		NIPS1_MOUSE	Protein NipSnap homolog 1	Nipsnap1	2,88E-06	5889,931	1472,631	4,000	0,250	Downregulated in KO
Q3TKT4		SMCA4_MOUSE	Transcription activator BRG1	Smarca4	0,00020748	6911,877	1709,308	4,044	0,247	Downregulated in KO
P10518		HEM2_MOUSE	Delta-aminolevulinic acid dehydratase	Alad	0,0007225	5097,110	1240,057	4,110	0,243	Downregulated in KO
O55029		COPB2_MOUSE	Coatomer subunit beta'	Copb2	0,00096738	3349,028	811,733	4,126	0,242	Downregulated in KO
Q60864		STIP1_MOUSE	Stress-induced-phosphoprotein 1	Stip1	0,0001503	3876,327	933,261	4,154	0,241	Downregulated in KO

O09167		RL21_MOUSE	60S ribosomal protein L21	Rpl21	8,91E-06	6450,719	1288,821	5,005	0,200	Downregulated in KO
Q6A068		CDC5L_MOUSE	Cell division cycle 5-like protein	Cdc5l	0,00975727	2008,380	390,726	5,140	0,195	Downregulated in KO
Q9CXW3		CYBP_MOUSE	Calcyclin-binding protein	Cacybp	0,03774168	6458,306	1213,677	5,321	0,188	Downregulated in KO
Q61545		EWS_MOUSE	RNA-binding protein EWS	Ewsr1	4,26E-05	7369,650	1358,315	5,426	0,184	Downregulated in KO
P10649		GSTM1_MOUSE	Glutathione S-transferase Mu 1	Gstm1	0,00255615	8630,765	1366,117	6,318	0,158	Downregulated in KO

Supplemental table 3. Common downregulated proteins in the differential proteomics of mIMCD3 cells and total kidney samples of *Pkd1* $^{flox/flox}$; TamCre mice.

Uniprot code	Entry Name	Protein names	Gene Names	Mice p18	Mice p30	Cells
P99029	PRDX5_MOUSE	Peroxiredoxin-5, mitochondrial	Prdx5 Prdx6	down FC<1,5	down	down
Q9JHI5	IVD_MOUSE	Isovaleryl-CoA dehydrogenase, mitochondrial	Ivd	Not found	down	down
Q9D051	ODPB_MOUSE	Pyruvate dehydrogenase E1 component subunit beta, mitochondrial	Pdhb	Not found	down FC<1,5	down
P56391	CX6B1_MOUSE	Cytochrome c oxidase subunit 6B1	Cox6b1 Cox6b	Not found	down FC<1,5	down
O55125	NIPS1_MOUSE	Protein NipSnap homolog 1 (NipSnap1)	Nipsnap1	Not found	down FC<1,5	down
P53395	ODB2_MOUSE	Lipoamide acyltransferase component of branched-chain alpha-keto acid dehydrogenase complex, mitochondrial	Dbt	Not found	down FC<1,5	down
Q8BWT1	THIM_MOUSE	3-ketoacyl-CoA thiolase, mitochondrial	Acaa2	Not found	down	down
Q8QZT1	THIL_MOUSE	Acetyl-CoA acetyltransferase, mitochondrial	Acat1	Not found	down	down
Q9DCJ5	NDUA8_MOUSE	NADH dehydrogenase [ubiquinone] 1 alpha subcomplex subunit 8 (Complex I-19kD)	Ndufa8	up FC<1,5	down	down
Q8CAQ8	MIC60_MOUSE	MICOS complex subunit Mic60 (Mitochondrial inner membrane protein) (Mitofilin)	Immt Mic60	Not found	down FC<1,5	down FC<1,5
Q9CQ92	FIS1_MOUSE	Mitochondrial fission 1 protein (FIS1 homolog)	Fis1 Ttc11	Not found	down FC<1,5	down
P97807	FUMH_MOUSE	Fumarate hydratase, mitochondrial (Fumarase)	Fh Fh1	Not found	down FC<1,5	down
P08228	SODC_MOUSE	Superoxide dismutase [Cu-Zn]	Sod1	Not found	down FC<1,5	down
Q6PB66	LPPRC_MOUSE	Leucine-rich PPR motif-containing protein, mitochondrial	Lrpprc Lrp130	Not found	down FC<1,5	down
Q8VEM8	S25A3_MOUSE	Solute carrier family 25 member 3, mitochondrial	Slc25a3	Not found	down FC<1,5	down
P67778	PHB1_MOUSE	Prohibitin 1	Phb1 Phb	Not found	down FC<1,5	down
Q60597	ODO1_MOUSE	2-oxoglutarate dehydrogenase complex component E1	Ogdh Kiaa4192	Not found	down FC<1,5	down
Q8K2B3	SDHA_MOUSE	Succinate dehydrogenase [ubiquinone] flavoprotein subunit, mitochondrial	Sdha	Not found	down FC<1,5	down

Supplemental table 4. Stress-related proteins dysregulated in the differential proteomics of mIMCD3 cells

Uniprot code	Entry Name	Protein names	Gene Names	FC (WT to KO)	1/FC (KO to WT)	Function [CC]
Q8BM55	TM214_MOUSE	Transmembrane protein 214	Tmem214	ONLY KO	ONLY KO	Required or the activation of CASP4 following endoplasmic reticulum stress
Q8R0W0	EPIPL_MOUSE	Epiplakin	Eppk1 EPPK	ONLY KO	ONLY KO	Cytoskeletal linker protein that connects to intermediate filaments and controls their reorganization in response to stress In response to mechanical stress like wound healing, is associated with the machinery for cellular motility by slowing down keratinocyte migration and proliferation and accelerating keratin bundling in proliferating keratinocytes thus contributing to tissue architecture. However in wound healing in corneal epithelium also positively regulates cell differentiation and proliferation and negatively regulates migration thereby controlling corneal epithelium morphogenesis and integrity. In response to cellular stress, plays a role in keratin filament reorganization, probably by protecting keratin filaments against disruption.During liver and pancreas injuries, plays a protective role by chaperoning disease-induced intermediate filament reorganization
P09671	SODM_MOUSE	Superoxide dismutase [Mn], mitochondrial	Sod2 Sod-2	0,06214214	16,0921393	Destroys superoxide anion radicals which are normally produced within the cells and which are toxic to biological systems.
Q922Q4	P5CR2_MOUSE	Pyrroline-5-carboxylate reductase 2 (P5C reductase 2)	Pycr2	0,07855204	12,7304145	Involved in cellular response to oxidative stress.
Q8CGK3	LONM_MOUSE	Lon protease homolog, mitochondrial	Lonp1 Prss15	0,15313258	6,53028908	ATP-dependent serine protease that mediates the selective degradation of misfolded, unassembled or oxidatively damaged polypeptides as well as certain short-lived regulatory proteins in the mitochondrial matrix.
Q8BMD8	SCMC1_MOUSE	Mitochondrial adenyl nucleotide antiporter SLC25A24	Slc25a24 Scamc1	0,28549087	3,50273893	May play a role in protecting cells against oxidative stress-induced cell death, by buffering calcium levels in the mitochondrial matrix through the formation of calcium-phosphate precipitates.
Q69ZN7	MYOF_MOUSE	Myoferlin	Myof Fer1l3 Kiaa1207	0,33092983	3,0217886	Calcium/phospholipid-binding protein that plays a role in the plasmalemma repair mechanism of endothelial cells that permits rapid resealing of membranes disrupted by mechanical stress. Involved in endocytic recycling.
Q9Z277	BAZ1B_MOUSE	Tyrosine-protein kinase BAZ1B	Baz1b Wbscr9 Wstf	0,55233083	1,81050911	Involved in DNA damage response by phosphorylating 'Tyr-142' of histone H2AX (H2AXY142ph) (PubMed:19092802). H2AXY142ph plays a central role in DNA repair and acts as a mark that distinguishes between apoptotic and repair responses to genotoxic stress.

P20108	PRDX3_MOUSE	Thioredoxin-dependent peroxide reductase, mitochondrial (peroxiredoxin 3)	Prdx3 Aop1 Mer5	0,56599033	1,76681464	Thiol-specific peroxidase that catalyzes the reduction of hydrogen peroxide and organic hydroperoxides to water and alcohols, respectively. Plays a role in cell protection against oxidative stress by detoxifying peroxides.
Q99JF8	PSIP1_MOUSE	PC4 and SFRS1-interacting protein (Lens epithelium-derived growth factor) (mLEDGF)	Psip1 Ledgf	0,57241206	1,74699325	Transcriptional coactivator involved in neuroepithelial stem cell differentiation and neurogenesis. Involved in particular in lens epithelial cell gene regulation and stress responses. May play an important role in lens epithelial to fiber cell terminal differentiation. May play a protective role during stress-induced apoptosis.
P99029	PRDX5_MOUSE	Peroxiredoxin-5, mitochondrial	Prdx5 Prdx6	1,77134658	0,56454226	Thiol-specific peroxidase that catalyzes the reduction of hydrogen peroxide and organic hydroperoxides to water and alcohols, respectively. Plays a role in cell protection against oxidative stress by detoxifying peroxides and as sensor of hydrogen peroxide-mediated signaling events.
P08228	SODC_MOUSE	Superoxide dismutase [Cu-Zn]	Sod1	2,49601484	0,40063864	Destroys radicals which are normally produced within the cells and which are toxic to biological systems.
P10649	GSTM1_MOUSE	Glutathione S-transferase Mu 1	Gstm1	6,31773652	0,15828454	FUNCTION: Conjugation of reduced glutathione to a wide number of exogenous and endogenous hydrophobic electrophiles. Involved in the formation of glutathione conjugates of both prostaglandin A2 (PGA2) and prostaglandin J2 (PGJ2).
Q60864	STIP1_MOUSE	Stress-induced-phosphoprotein 1	Stip1	4,15352684	0,24075925	Acts as a co-chaperone for HSP90AA1. Mediates the association of the molecular chaperones HSPA8/HSC70 and HSP90

Supplemental table 5. Apoptosis-related proteins dysregulated in the differential proteomics of mIMCD3 cells

Uniprot code	Accesion name	Group	Gene name	FC (WT to KO)	1/FC (KO to WT)	Uniprot Function [CC]
Pro-apoptotic proteins						
Q8VDP4	CCAR2_MOUSE	Cell cycle and apoptosis regulator protein 2	Ccar2	ONLY KO	ONLY KO	Inhibits SIRT1 deacetylase activity leading to increasing levels of p53/TP53 acetylation and p53-mediated apoptosis.
Q791V5	MTCH2_MOUSE	Mitochondrial carrier homolog 2	Mtch2	ONLY KO	ONLY KO	Acts as a receptor for the truncated form of pro-apoptotic BH3-interacting domain death agonist (p15 BID) and has therefore a critical function in apoptosis.
P62897	CYC_MOUSE	Cytochrome c, somatic	Cycs	ONLY KO	ONLY KO	Plays a role in apoptosis. Suppression of the anti-apoptotic members or activation of the pro-apoptotic members of the Bcl-2 family leads to altered mitochondrial membrane permeability resulting in release of cytochrome c into the cytosol. Binding of cytochrome c to Apaf-1 triggers the activation of caspase-9, which then accelerates apoptosis by activating other caspases.
Q60932-2	VDAC1_MOUSE	Isoform Mt-VDAC1 of Voltage-dependent anion-selective channel protein 1	Vdac1	0,01977163	50,5775183	In depolarized mitochondria, acts downstream of PRKN and PINK1 to promote mitophagy or prevent apoptosis; polyubiquitination by PRKN promotes mitophagy, while monoubiquitination by PRKN decreases mitochondrial calcium influx which ultimately inhibits apoptosis. May participate in the formation of the permeability transition pore complex (PTPC) responsible for the release of mitochondrial products that triggers apoptosis
P17742	PPIA_MOUSE	Peptidyl-prolyl cis-trans isomerase A	Ppia	0,0682241	14,6575767	Induces apoptosis in ECs by promoting the FOXO1-dependent expression of CCL2 and BCL2L11 which are involved in EC chemotaxis and apoptosis (By similarity). In response to oxidative stress, initiates proapoptotic and antiapoptotic signaling in ECs via activation of NF-kappa-B and AKT1 and up-regulation of antiapoptotic protein BCL2.
Q9Z0X1	AIFM1_MOUSE	Apoptosis-inducing factor 1, mitochondrial	Aifm1	0,21840355	4,57868012	FUNCTION: Functions both as NADH oxidoreductase and as regulator of apoptosis (By similarity). In response to apoptotic stimuli, it is released from the mitochondrion intermembrane space into the cytosol and to the nucleus, where it functions as a proapoptotic factor in a caspase-independent pathway.
Q8BMS1	ECHA_MOUSE	Trifunctional enzyme subunit alpha, mitochondrial	Hadha	0,2921534	3,42285934	Independently of the subunit beta, the trifunctional enzyme subunit alpha/HADHA also has a monolysocardiolipin acyltransferase activity. It acylates monolysocardiolipin into cardiolipin, a major mitochondrial membrane phospholipid which plays a key role in apoptosis and supports mitochondrial respiratory chain complexes in the generation of ATP.

Anti-apoptotic proteins						
Q62511	ZFP91_MOUSE	E3 ubiquitin-protein ligase ZFP91	Zfp91	0,17836139	5,60659448	May also play an important role in cell proliferation and/or anti-apoptosis.
Q9EQU5	SET_MOUSE	Protein SET	Set	1,79609168	0,55676445	Multitasking protein, involved in apoptosis, transcription, nucleosome assembly and histone chaperoning. Isoform 2 anti-apoptotic activity is mediated by inhibition of the GZMA-activated DNase, NME1. In the course of cytotoxic T-lymphocyte (CTL)-induced apoptosis, GZMA cleaves SET, disrupting its binding to NME1 and releasing NME1 inhibition. Isoform 1 and isoform 2 are potent inhibitors of protein phosphatase 2A. Isoform 1 and isoform 2 inhibit EP300/CREBBP and PCAF-mediated acetylation of histones (HAT) and nucleosomes, most probably by masking the accessibility of lysines of histones to the acetylases. The predominant target for inhibition is histone H4. HAT inhibition leads to silencing of HAT-dependent transcription and prevents active demethylation of DNA. Both isoforms stimulate DNA replication of the adenovirus genome complexed with viral core proteins; however, isoform 2 specific activity is higher (By similarity). {ECO:0000250}.
P50580	PA2G4_MOUSE	Proliferation-associated protein 2G4	Pa2g4	1,99379802	0,50155532	Regulates cell proliferation, differentiation, and survival. Isoform 1 suppresses apoptosis whereas isoform 2 promotes cell differentiation
Q8BWT1	THIM_MOUSE	3-ketoacyl-CoA thiolase, mitochondrial	Acaa2	2,24605984	0,44522411	Abolishes BNIP3-mediated apoptosis and mitochondrial damage

Autosomal Dominant Polycystic Kidney Disease (ADPKD) is the most common hereditary kidney disease, mainly caused by mutations in the PKD1 (80%) and PKD2 (15%) genes. Patients develop renal cysts over time, which can lead to kidney failure and the need for renal replacement therapy.
This thesis aimed to improve the genetic diagnosis of ADPKD, especially in cases with variants of uncertain significance (VUS). It also explored the molecular mechanisms of ADPKD through comparative proteomic analysis. The identification of pathogenic variants and insights into the molecular dysregulation of ADPKD provide a foundation for developing targeted therapeutic strategies.
Continued research is essential for advancing the diagnosis, treatment, and overall understanding of ADPKD.